

International Journal of Antennas and Propagation

Recent Advances in Synthetic Aperture Radar Data Processing and Application

Guest Editors: Gui Gao, Deren Li, and Alejandro C. Frery





Recent Advances in Synthetic Aperture Radar Data Processing and Application

International Journal of Antennas and Propagation

**Recent Advances in Synthetic Aperture Radar
Data Processing and Application**

Guest Editors: Gui Gao, Deren Li, and Alejandro C. Frery



Copyright © 2013 Hindawi Publishing Corporation. All rights reserved.

This is a special issue published in "International Journal of Antennas and Propagation." All articles are open access articles distributed under the Creative Commons Attribution License, which permits unrestricted use, distribution, and reproduction in any medium, provided the original work is properly cited.

Editorial Board

M. Ali, USA
Charles Bunting, USA
Felipe Cátedra, Spain
Dau-Chyrh Chang, Taiwan
Deb Chatterjee, USA
Z. N. Chen, Singapore
Michael Yan Wah Chia, Singapore
Shyh-Jong Chung, Taiwan
Lorenzo Crocco, Italy
Tayeb A. Denidni, Canada
Antonije R. Djordjevic, Serbia
Karu P. Esselle, Australia
Francisco Falcone, Spain
Miguel Ferrando, Spain
Vincenzo Galdi, Italy
Wei Hong, China
Hon Tat Hui, Singapore
Tamer S. Ibrahim, USA
Mandeep Singh Jit Singh, Malaysia
Nemai Karmakar, Australia

Se-Yun Kim, Republic of Korea
Ahmed A. Kishk, Canada
Selvan T. Krishnasamy, India
Tribikram Kundu, USA
Ju-Hong Lee, Taiwan
Byungje Lee, Republic of Korea
L. Li, Singapore
Yilong Lu, Singapore
Atsushi Mase, Japan
Andrea Massa, Italy
Giuseppe Mazzarella, Italy
Derek McNamara, Canada
C. F. Mecklenbräuker, Austria
Michele Midrio, Italy
Mark Mirotznik, USA
Ananda S. Mohan, Australia
P. Mohanan, India
Pavel Nikitin, USA
A. D. Panagopoulos, Greece
Matteo Pastorino, Italy

Massimiliano Pieraccini, Italy
Sadasiva M. Rao, USA
Sembiam R. Rengarajan, USA
Ahmad Safaai-Jazi, USA
Safieddin Safavi-Naeini, Canada
Magdalena Salazar-Palma, Spain
Stefano Selleri, Italy
Zhongxiang Shen, Singapore
John J. Shynk, USA
Seong-Youp Suh, USA
Parveen Wahid, USA
Yuanxun Ethan Wang, USA
Daniel S. Weile, USA
Tat Soon Yeo, Singapore
Young J. Yoon, Republic of Korea
Jong-Won Yu, Republic of Korea
Wenhua Yu, USA
Anping Zhao, China

Contents

Recent Advances in Synthetic Aperture Radar Data Processing and Application, Gui Gao, Deren Li, and Alejandro C. Frery

Volume 2013, Article ID 231560, 1 page

Analysis for Resolution of Bistatic SAR Configuration with Geosynchronous Transmitter and UAV Receiver, Yicheng Jiang and Zhuoqun Wang

Volume 2013, Article ID 237463, 10 pages

Rotating Parabolic-Reflector Antenna Target in SAR Data: Model, Characteristics, and Parameter Estimation, Bin Deng, Hong-Qiang Wang, Yu-Liang Qin, Sha Zhu, and Xiang Li

Volume 2013, Article ID 583865, 13 pages

Junction Point Detection Algorithm for SAR Image, Jun Zhang, Tingjin Luo, Gui Gao, and Lin Lian

Volume 2013, Article ID 357379, 9 pages

Using Open-Source Components to Process Interferometric TerraSAR-X Spotlight Data,

Michael Jendryke, Timo Balz, Houjun Jiang, Mingsheng Liao, and Uwe Stilla

Volume 2013, Article ID 275635, 13 pages

Modeling Multilook Magnitude and Phase in Extremely Heterogeneous Clutter, Gui Gao, Gongtao Shi, and Shilin Zhou

Volume 2013, Article ID 468380, 5 pages

Ship Detection in High-Resolution Dual-Polarization SAR Amplitude Images, Gui Gao, Gongtao Shi, and Shilin Zhou

Volume 2013, Article ID 519296, 5 pages

The Design and Experiments on Corner Reflectors for Urban Ground Deformation Monitoring in Hong Kong, Yuxiao Qin, Daniele Perissin, and Ling Lei

Volume 2013, Article ID 191685, 8 pages

Characterizing the Statistical Properties of SAR Clutter by Using an Empirical Distribution, Gui Gao, Gongtao Shi, Huanxin Zou, and Shilin Zhou

Volume 2013, Article ID 109145, 8 pages

A Wide-Beam Scanning Mode for Near-Space Passive SARs, Peng Zhou, Peng Ren, and Yongshou Dai

Volume 2012, Article ID 930137, 7 pages

Road Extraction from High-Resolution SAR Images via Automatic Local Detecting and Human-Guided Global Tracking, Jianghua Cheng, Wenxia Ding, Xishu Ku, and Jixiang Sun

Volume 2012, Article ID 989823, 10 pages

Editorial

Recent Advances in Synthetic Aperture Radar Data Processing and Application

Gui Gao,¹ Deren Li,² and Alejandro C. Frery³

¹ Department of Information Engineering, School of Electronic Science and Engineering, National University of Defense Technology, Changsha, Hunan 410073, China

² Key Laboratory of Photogrammetry and Remote Sensing, Wuhan University, Wuhan, Hubei 430079, China

³ Laboratório de Computação Científica e Análise Numérica (LaCCAN), Universidade Federal de Alagoas, Avendia Lourival de Melo Mota s/n, 57072-900 Maceió, AL, Brazil

Correspondence should be addressed to Gui Gao; dellar@126.com

Received 26 November 2013; Accepted 26 November 2013

Copyright © 2013 Gui Gao et al. This is an open access article distributed under the Creative Commons Attribution License, which permits unrestricted use, distribution, and reproduction in any medium, provided the original work is properly cited.

Spaceborne synthetic aperture Radar (SAR) sensors have been intensively applied to map, monitor, and analyze the Earth: new operational modes increase the flexibility of SAR sensors that are now able to obtain microwave 2D images as well as 3D interferometry products within a wide range of space and time resolution and coverage. However, the SAR data processing is challenging due to the changing properties of targets (such as vehicles, ships, and buildings) and terrains for the electromagnetic waves with various bands, views, polarimetric modes, and configurations. Hence, the definition of new techniques and algorithms for SAR data usage as well as assessment of existing methods for SAR products exploitation is required. Main purpose of this special issue is to provide an international forum for the researchers, as well as to advance the exploitation of their data for monitoring applications.

This special issue received twenty-two submissions, of which ten of outstanding quality were selected for publication. Among the topics covered by these contributions, the readers will find original and innovative results in image understanding included in the papers entitled “Road extraction from high-resolution SAR images via automatic local detecting and human-guided global tracking,” “Ship detection in high-resolution dual polarization SAR amplitude images,” “Characterizing the statistical properties of SAR clutter by using an empirical distribution,” “Modeling multilook magnitude and phase in extremely heterogeneous clutter,” and “junction point detection algorithm for SAR image”.

The Guest Editors wish to thank the authors for their contributions and offer this special issue to the SAR community in the hope that it constitutes a valuable venue for advances in the knowledge of this important area.

Gui Gao
Deren Li
Alejandro C. Frery

Research Article

Analysis for Resolution of Bistatic SAR Configuration with Geosynchronous Transmitter and UAV Receiver

Yicheng Jiang and Zhuoqun Wang

Research Institute of Electronic Engineering Technology, Harbin Institute of Technology, Number 714, Harbin 150001, China

Correspondence should be addressed to Zhuoqun Wang; wentingwangzhuoqun@126.com

Received 31 October 2012; Accepted 4 January 2013

Academic Editor: Gui Gao

Copyright © 2013 Y. Jiang and Z. Wang. This is an open access article distributed under the Creative Commons Attribution License, which permits unrestricted use, distribution, and reproduction in any medium, provided the original work is properly cited.

Bistatic SAR with geosynchronous illuminator and unmanned aerial vehicle receiver (GEO-UAV BiSAR) has significant potential advantages in the field of continuous local observation under a dangerous environment within nearly 24 h. Due to the extreme platform velocity differences, the ellipse orbital movement of GEOSAR makes this BiSAR configuration not like the conventional spaceborne BiSAR. In this paper, based on the orbital kinetic characteristic of GEOSAR, we theoretically analyze the variations of bistatic configuration effect on common azimuth coverage and coherent accumulated time. In addition, two-dimension the resolution is deduced by geometrical configuration on the basis of gradient method. The simulations show that the appropriate selection of initial bistatic configuration can restrain from the appearance of the dead zone in common coverage. And the image results are obtained by frequency domain RD based on Method of Series Reversion (MSR). It is shown that GEO-UAV BiSAR has the high resolution ability.

1. Introduction

Spaceborne synthetic aperture radar (SAR) has been applied to the wide fields such as landform measurement, ocean observation, earthquake monitor, and digital elevation model (DEM) [1]. For decades, lots of low-orbit (LEO) satellite emitted have high-resolution capability. However, beam irradiation extent of LEO is limited in dozens of kilometers near the nadir, and the revisit time is much longer. To this aspect, geosynchronous SAR (GEOSAR) can overcome the shortcomings aforementioned [2–4].

Geosynchronous orbits have the unique characteristic that their orbital period is nearly 24 h. It makes GEOSAR suitable for the continuous imaging on the specific partial region within 24 h [5]. And the ground coverage provided by a GEOSAR can be nearly one third of the globe for a highly inclined orbit, and it can be as small as few hundred kilometers for a SAR placed in a slightly inclined orbit [6].

Nevertheless, it requires a larger antenna to overcome the energy attenuation of the ionosphere and stratosphere [7–9]. There exists difficulties to hardware realization. In addition, imaging accumulation time, which reaches a few

hours, makes the imaging quality quite easier to be affected by unstable factors in larger ground coverage. To solve these problems, the literature [10] derives a space-based radar surveillance concept employing geosynchronous illumination and bistatic reception on either unmanned aerial vehicles (UAVs) or LEO. Due to the wide beam coverage of GEOSAR, it is easy to realize distributed imaging configuration with illuminator GEOSAR and multiple receivers (aircraft, UAV, LEO, and MEO satellites). Not only the wide imaging area is achieved, but also the requirements for the transmitted power and antenna size are reduced [11, 12].

In particular, bistatic geometrical configuration of GEOSAR illuminator and UAVSAR receiver (GEO-UAV BiSAR) may realize local observation in a dangerous environment. However, since the orbital characteristics of GEOSAR, we need to control the attitude of UAVSAR in the ground station for high resolution. Hence, it is different from other configurations, for example, GEO illumination and LEO receiver; GEO illumination and airborne receiver.

A key factor in determining the performance of GEO-UAV BiSAR systems is the two-dimensional resolution, but performance analysis of BiSAR characterized for any

configuration is usually complex. The literature [13] describes comprehensive knowledge regarding the resolution of BiSAR with geostationary illuminator and UAV receiver, which can be obtained from the gradient method in terms of time delay and the Doppler shift [14, 15]. Yet, it does not consider the variation of geometrical configuration as a function of time effect on resolution. In this case, the geostationary orbit is just a special one of geosynchronous orbit, and it ignores orbital motion and earth rotation effect on GEOSAR velocity, when orbit inclination is not equal to zero.

Before the imaging study for GEO-UAV BiSAR, its two-dimensional spectrum is demanded to discuss. Currently, the traditional method has two kinds, Loffeld's bistatic formula (LBF) [16, 17] and Method of Series Reversion (MSR) [18, 19]. The former mainly applies the Taylor expansion on phase histories of transmitter and receiver individually. The latter considers a power series method to count the stationary point of bistatic phase histories, and its accuracy is scalable in a sense. To this end, MSR is more applicable to the imaging study of GEO-UAV BiSAR.

This paper is organized as follows. It begins with a description of GEOSAR ground track in local ground coordinate system. Section 3 discusses the relative movement of two platforms effect on common coverage and coherent accumulated time owing to the extreme platform velocity differences. In Section 4, the formulas of two-dimensional resolution are deduced from the geometrical relationship of GEOSAR and UAVSAR based on gradient method. In Section 5, we analyze GEO-UAV BiSAR configuration influences on range and azimuth resolution by simulations. And proper initial selecting configuration can avoid the appearance of dead zone in the swath. Then, the imaging results by frequency domain RD method based on MSR are presented and analyzed.

2. Analyses to Movement Model of GEOSAR

2.1. Movement Track of GEOSAR. Suppose that GEOSAR runs on the ellipse orbit and the earth is uniform sphere, orbital inclination is i , right ascension of ascending node is Ω_0 , and argument of perigee is W_0 . The satellite position equation can be expressed in earth fixed coordinate system:

$$\begin{bmatrix} X_s(t_0 + t_a) \\ Y_s(t_0 + t_a) \\ Z_s(t_0 + t_a) \end{bmatrix} = RW_B(t_0 + t_a) W_A W_C(t_0 + t_a), \quad (1)$$

where

$$W_A = \begin{bmatrix} \cos \Omega_0 & -\sin \Omega_0 & 0 \\ \sin \Omega_0 & \cos \Omega_0 & 0 \\ 0 & 0 & 1 \end{bmatrix} \begin{bmatrix} 1 & 0 & 0 \\ 0 & \cos i & -\sin i \\ 0 & \sin i & \cos i \end{bmatrix} \\ \times \begin{bmatrix} \cos W_0 & -\sin W_0 & 0 \\ \sin W_0 & \cos W_0 & 0 \\ 0 & 0 & 1 \end{bmatrix},$$

$$W_B(t_0 + t_a) = \begin{bmatrix} \cos(\omega_e \cdot (t_0 + t_a)) & \sin(\omega_e \cdot (t_0 + t_a)) & 0 \\ -\sin(\omega_e \cdot (t_0 + t_a)) & \cos(\omega_e \cdot (t_0 + t_a)) & 0 \\ 0 & 0 & 1 \end{bmatrix} \\ W_C(t_0 + t_a) = \begin{bmatrix} \cos f(t_0 + t_a) & -\sin f(t_0 + t_a) & 0 \\ \sin f(t_0 + t_a) & \cos f(t_0 + t_a) & 0 \\ 0 & 0 & 1 \end{bmatrix} \quad (2)$$

t_0 is the center time point of time range, ω_e is the earth rotation angular velocity and R is the geocenter distance of the satellite.

In the time range foregoing, the velocity of GEOSAR related to the earth is given by

$$\vec{V}_{ST.EF}(t_0 + t_a) = \sqrt{\frac{\mu}{a}} W_A(t_0 + t_a) W_B \begin{bmatrix} -\sin f(t_0 + t_a) \\ \cos f(t_0 + t_a) \\ 0 \end{bmatrix} \\ + \begin{bmatrix} \omega_e Y_s(t_0 + t_a) \\ -\omega_e X_s(t_0 + t_a) \\ 0 \end{bmatrix}, \quad (3)$$

where a is a semimajor axis, μ is a gravitation constant, R_e is the earth radius, and H_T is a GEOSAR distance of ground.

Thus, when $i = 0$, GEOSAR is the stationary state and GEO-UAV BiSAR images in the local area near the equator. With the increase of i , \vec{V}_{ST} goes up gradually, and the variation of latitude is $[-i, i]$ in "Figure 8" imaging area. For maximum irradiation of Chinese territory, we choose $i = 60^\circ$. Based on GEOSAR basic parameters (see Table 1), the ground track of GEOSAR ($i \neq 0$) is shown in Figure 1.

Due to higher altitude of GEOSAR [20], the rate \vec{V}_{ST} at which the spacecraft moves along its orbital path is unequal to the rate \vec{V}_{eT} at which the footprint of the antenna beam moves along the surface of the earth: $\vec{V}_{eT} = R_e \vec{V}_{ST} / (R_e + H_T)$.

2.2. GEOSAR Velocity in Local Ground Coordinate System.

In general, GEOSAR is described in earth-fixed coordinate system as well as UAVSAR in local ground coordinate system. We will convert GEOSAR into the local ground coordinate system in which the original point O represents the intersection between the satellite line of sight and the ground, the Ox -axis corresponds with track direction of GEOSAR, the Oz -axis corresponds with the connection between satellite and subpoint, and the Oy -axis is determined according to the right-hand rule (see Figure 2).

GEOSAR runs around the earth within a periodical time, T_s . In T_s , the range (Oy -axis) and the azimuth (Ox -axis) acceleration of GEOSAR ground track is shown in Figure 3.

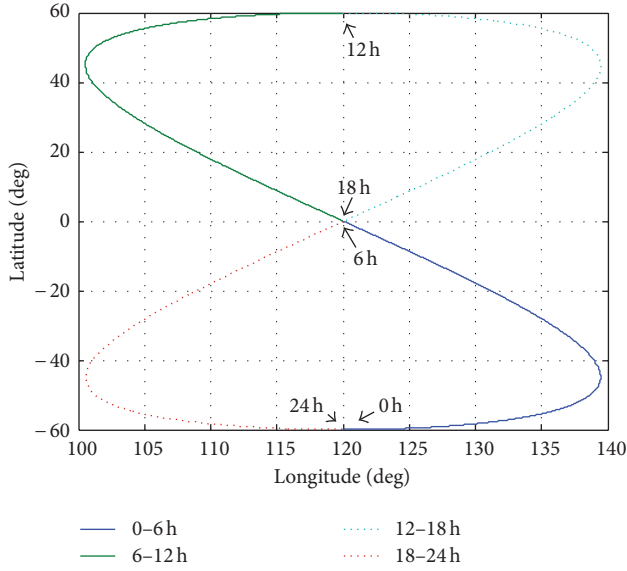


FIGURE 1: Ground track of 60° inclined geosynchronous orbit.

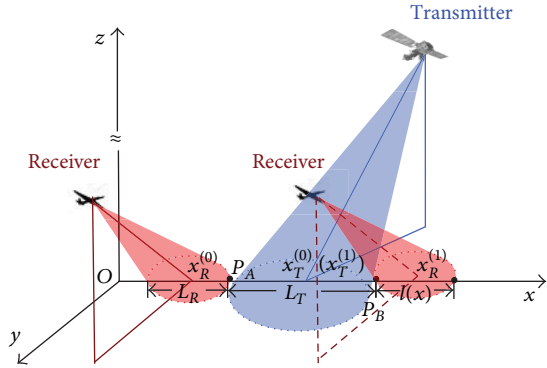


FIGURE 2: The GEOSAR and UAVSAR are in the local ground coordinate system, where the red region represents beam irradiation coverage of UAVSAR, and the blue is GEOSAR.

The trend of range acceleration is similar to a cosine curve whose period is $T_s/2$. The peak value is $2.236 \times 10^{-2} \text{ m/s}^2$, and the valley value is $3.9 \times 10^{-4} \text{ m/s}^2$. Furthermore, the trend of azimuth acceleration is similar to a sine curve whose period is $T_s/4$. The maximum is $9.0088 \times 10^{-3} \text{ m/s}^2$, and the minimum is $5.395 \times 10^{-4} \text{ m/s}^2$.

The range coverage of GEOSAR ground track $C_{tr} = R_{tc} \theta_{tran} / \sin(\theta_{tin}) = 3.75 \times 10^5 \text{ m}$ and the azimuth coverage $C_{ta} = R_{tc} \theta_{taim} / \cos(\varphi_{tsq}) = 1.25 \times 10^5 \text{ m}$ where θ_{tran} and θ_{taim} are the range and azimuth bandwidth of GEOSAR separately; θ_{tin} is an incidence angle, φ_{tsq} is a squint angle, when range acceleration a_a reaches peak, the surface coverage will deviate from the Ox -axis for $T_v > 4.0952 \times 10^3 \text{ s}$ (T_v represents common irradiation time, of two platforms; the limited time length T_{vlim} is calculated by the formula $C_{tr}/2 = \vec{V}_{eT} T_{vlim} + 1/2 a_a T_{vlim}^2$). Besides, for the azimuth acceleration is much smaller, the ground track velocity of GEOSAR is considered

uniform motion as $\vec{V}_{eT}(t_0)$ in the condition of $T_v < 4.0952 \times 10^3 \text{ s}$.

3. Coherent Integration Time and Azimuth Common Coverage

Based on the theoretical research of resolution [21], the coherent integration time and azimuth common coverage influence azimuth resolution capability of GEO-UAV BiSAR.

Coherent integration time T_{sar} and azimuth coverage C_a are relative to GEOSAR azimuth coverage L_T , UAVSAR azimuth coverage L_R , and antenna footprint velocity of two platforms. Movement of GEOSAR is described as the uniform motion in T_v under the aforementioned study. While UAV is difficult to control motion stability in aerodynamic interference (roll angle, pitch angle, and heading angle of UAVSAR are variable). In this case, the accurate calculation is very troubling. To simplify calculation, we consider that roll angle, pitch angle and heading angle of UAVSAR are all constants, and UAV is a uniform motion in a straight line, \vec{V}_R . Therefore, the antenna footprint velocity ratio k can be shown as

$$k = \frac{\vec{e} \cdot \vec{V}_{eT}}{\vec{e} \cdot \vec{V}_R}, \quad (4)$$

where $\vec{e} = [1 \ 0 \ 0]^T$ is the azimuth unit vector.

- (1) If $k = 0$, GEOSAR is the stationary station.
- (2) If $k > 0$, UAV flies the same direction with transmitter. When $V_{eT} < V_R$, $k \in (0, 1)$, otherwise $k \in (1, +\infty)$.
- (3) If $k < 0$, UAV flies the opposite direction with transmitter.

Assume that footprint middle points of GEOSAR and UAVSAR are given by x_T and x_R , respectively, on the Ox -axis in Figure 2. Left and right edges of GEOSAR is P_A and P_B ; $P_A = [x_A \ 0 \ 0]^T$ and $P_B = [x_B \ 0 \ 0]^T$. If two platforms intersect at P_A , $x_T = x_T^{(0)}$ and $x_R = x_R^{(0)}$; if they intersect at P_B , $x_T = x_T^{(1)}$ and $x_R = x_R^{(1)}$. Then, $x_T^{(0)} = x_A + L_T/2$, $x_R^{(0)} = x_A - L_R/2$, $x_T^{(1)} = x_B - L_T/2$, and $x_R^{(1)} = x_B + L_R/2$.

For the subsequent simulation data show $V_{eT} > V_R$ (see Tables 1 and 2), we primarily discuss C_a and T_{sar} in the case of $k \in (1, +\infty)$. When $x_R = x_R^{(0)}$, $C_a = 0$, while $x_R = x_R^{(1)}$ and C_a achieve the maximum. Suppose that $l(x)$ represents the distance between the corresponding right edge points of the transmitter and the receiver in the Ox -axis. The change trend of $l(x)$ is $L_R \Rightarrow 0 \Rightarrow L_T$ with the relative movement of two platforms (see Figure 2). Thus, T_{sar} by (23) and (24) in the Appendix is calculated. Besides, the common irradiation time of two platforms is $T_v = C_a/V_R$.

Taking into account the difference value of k , we count C_a and T_{sar} , respectively (see the Appendix), when $k = 0$ and $C_a = L_T$. While in the case that V_{eT} , V_R , L_T , and L_R are constants, C_a is inversely proportional to $|V_{eT} - V_R|$ if

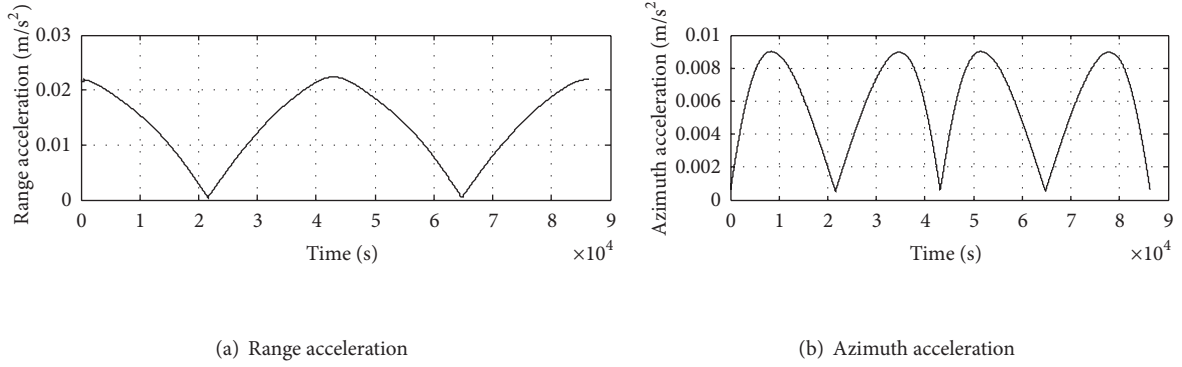


FIGURE 3: The range acceleration (a) and the azimuth acceleration (b) of GEOSAR ground track in local ground coordinate system.

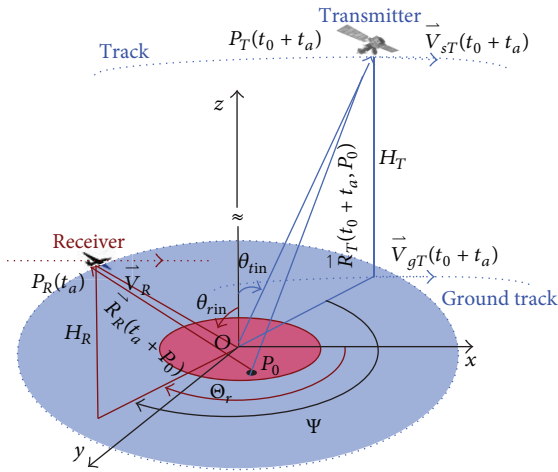


FIGURE 4: GEO-UAV BiSAR geometry.

TABLE 1: GEOSAR transmitter parameters.

GEOSAR parameters	Value
Orbit altitude	36000 km
Argument of perigee	90°
Right ascension of ascending node	30°
Orbit inclination	60°
Azimuth beam width	0.2°
Angle of elevation	0.6°

$k > 0$ ($|V_{eT} + V_R|$ if $k < 0$). And the maximum T_{sar} depends on the synthetic aperture time of receiver. If the coherent accumulated time is less than the maximum T_{sar} , the imaging quality is fuzzy in the zone which is known as “dead zone”. Conversely, it is called as “clear zone”.

4. Resolution of GEO-UAV BiSAR

GEO-UAV BiSAR geometry in local ground coordinate system is shown in Figure 4. The center of the scene is

TABLE 2: UAVSAR receiver parameters.

UAVSAR parameters	Value
Wavelength	0.03 m (X-band)
Bandwidth	150 MHz
Altitude	8 km
Incidence angle	1° ~ 80°
Angle between $R_T(t_0, O)$ and $R_R(t_0, O)$	0° ~ 360°
Antenna length	1 m

O point, GEOSAR locates $P_T(t_0 + t_a)$; UAVSAR locates $P_R(t_a)$. The time-domain matched filter is constructed by forming an instantaneous slant range to a point target $P_m = [x_m \ y_m \ z_m]^T$ referred to as the range equation

$$\vec{R}(t_a, P_m) = \vec{R}_T(t_0 + t_a, P_m) + \vec{R}_R(t_a, P_m), \quad (5)$$

where

$$\begin{aligned} \vec{R}_T(t_0 + t_a, P_m) &= P_T(t_0 + t_a) - P_m, \\ \vec{R}_R(t_a, P_m) &= P_R(t_a) - P_m = (P_R(0) - P_m) + \vec{V}_R t_a. \end{aligned} \quad (6)$$

Because GEOSAR shows a variable motion as $\vec{V}_{sT}(t_0 + t_a)$, the gradient of time delay $\vec{\nabla}t$ and the gradient of the Doppler shift $\vec{\nabla}f_a(t_a, P_m)$ are defined as (4.a) and (4.b):

$$\vec{\nabla}t = \frac{1}{c} \left(\frac{\vec{R}_T(t_0 + t_a, P_m)}{|\vec{R}_T(t_0 + t_a, P_m)|} + \frac{\vec{R}_R(t_a, P_m)}{|\vec{R}_R(t_a, P_m)|} \right). \quad (4.a)$$

Note that $\vec{\nabla}f_a(t_a, P_m)$ depends on the angular rate of two platforms. For $|\vec{V}_{sT}|/|\vec{R}_T(t_a, P_m)| = O(10^{-4})$ and $|\vec{V}_R|/|\vec{R}_R(t_a, P_m)| = (10^{-1})$, UAVSAR dominates $\vec{\nabla}f_a(t_a, P_m)$:

$$\begin{aligned} \vec{\nabla}f_a(t_a, P_m) &\approx \frac{1}{2\pi} \frac{\partial \nabla \Phi(t_a, P_m)}{\partial t_a} \\ &= -\frac{1}{\lambda} \left(\frac{1}{|\vec{R}_R(t_a, P_m)|} \left(\vec{V}_R - \left(\vec{V}_R \frac{\vec{R}_R(t_a, P_m)}{|\vec{R}_R(t_a, P_m)|} \right) \right. \right. \\ &\quad \left. \left. \times \frac{\vec{R}_R(t_a, P_m)}{|\vec{R}_R(t_a, P_m)|} \right) \right), \end{aligned} \quad (7)$$

$$\begin{aligned} \vec{\nabla}f_a(t_a, P_m) &= \frac{1}{2\pi} \frac{\partial \nabla \Phi(t_a, P_m)}{\partial t_a} \\ &= -\frac{1}{2\pi} \times \frac{2\pi}{\lambda} \frac{\partial}{\partial t_a} \left(\frac{\vec{R}_T(t_0+t_a, P_m)}{|\vec{R}_T(t_0+t_a, P_m)|} + \frac{\vec{R}_R(t_a, P_m)}{|\vec{R}_R(t_a, P_m)|} \right) \\ &= -\frac{1}{\lambda} \left(\frac{1}{|\vec{R}_T(t_0+t_a, P_m)|} \right. \\ &\quad \times \left(\vec{V}_{sT}(t_0+t_a) \right. \\ &\quad \left. - \left(\vec{V}_{sT}(t_0+t_a) \frac{\vec{R}_T(t_0+t_a, P_m)}{|\vec{R}_T(t_0+t_a, P_m)|} \right) \right. \\ &\quad \left. \times \frac{\vec{R}_T(t_0+t_a, P_m)}{|\vec{R}_T(t_0+t_a, P_m)|} \right) \\ &\quad \left. + \frac{1}{|\vec{R}_R(t_a, P_m)|} \right. \\ &\quad \left. \times \left(\vec{V}_R - \left(\vec{V}_R \frac{\vec{R}_R(t_a, P_m)}{|\vec{R}_R(t_a, P_m)|} \right) \frac{\vec{R}_R(t_a, P_m)}{|\vec{R}_R(t_a, P_m)|} \right) \right). \end{aligned} \quad (4.b)$$

The maximum delay time for movement in the ground plane is along the projection of $\vec{V}t$ into xOy plane, $\vec{\nabla}t_e$. Similarly, the maximum change in the Doppler frequency moves along the projection of $\vec{\nabla}f_a$ into xOy plane, $\vec{\nabla}f_e$. Thus,

the range resolution D_r and the azimuth resolution D_a are given by

$$\begin{aligned} D_r &= \frac{1}{B_r |\vec{\nabla}t_e|} \cdot \frac{|\vec{\nabla}t_e|}{|\vec{\nabla}t_e|}, \\ D_a &= \frac{1}{|\vec{\nabla}f_e| T_{sar}} \cdot \frac{|\vec{\nabla}f_g|}{|\vec{\nabla}f_e|}. \end{aligned} \quad (8)$$

BiSAR resolution has the properties of time varying and spatial varying. On the basis of the GEO-UAV BiSAR geometry, (8) is redescribed as

$$D_r = \frac{C}{2B_r \cos(\Psi/2)} \cdot \frac{|\vec{\nabla}t_e|}{|\vec{\nabla}t_e|},$$

$$D_a \approx \frac{H_R \lambda}{T_{sar}(t_0+t_a) V_R \cos \theta_{rin} \sqrt{1 - \sin^2 \theta_{rin} \cos^2(\Theta_r)}} \cdot \frac{|\vec{\nabla}f_e|}{|\vec{\nabla}f_e|}, \quad (9)$$

where Ψ is the illuminator out-of-plane angle (with respect to the receiver and centered in the origin), Θ_r is the angle between the Ox -axis and the projection of UAVSAR position into xOy plane, and Θ_r is determined by Ψ .

The range resolution mainly depends on Ψ through (9). It attains the maximum for $\Psi = 180^\circ$ and the minimum values for $\Psi = 0^\circ$. In other words, the gradient of time delay has no component onto xOy plane for $\Psi = 180^\circ$, GEO-UAV BiSAR construction has the worst range resolution.

The azimuth resolution is relative to coherent accumulated time and the attitude change of UAV. With the shorter coherent accumulated time $T_{sar}(t_0+t_a)$, the imaging quality of GEO-UAV BiSAR will decline gradually (dead zone1). Whereas, the azimuth resolution can further simplify as $D_a \approx D/\sqrt{1 - \sin^2 \theta_{rin} \cos^2 \Theta_r}$ in the clear zone. When θ_{rin} reaches an enough value, D_a is the maximum for $\Theta_r = 0^\circ, 180^\circ$, and 360° . And the gradient of the Doppler shift is the smallest component onto xOy plane.

For aforesaid reasons, the proper selection of original UAVSAR attitudes, θ_{rin} and Ψ , can make GEO-UAV BiSAR exhibit high resolution. To achieve this aim in clear zone, we will avoid the appearance of the worst construction in mutual movement process of transmitter and receiver. (Worst construction illuminates the area called dead zone2.)

In a periodical time of GEOSAR, the relative movement of GEOSAR and UAVSAR works in finite time $[t_0 - T_v/2, t_0 + T_v/2]$ (the local ground coordinate system is different for t_0 varying). Suppose that the original value of Ψ (corresponding t_0) is in CCI with regard to good imaging quality. For the sake of platform velocity differences, the variation range of Ψ , Ψ_{var} is still in CCI:

$$[\Psi - \max(\Psi_{var} - \Psi), \Psi + \max(\Psi_{var} - \Psi)] \in \text{CCI}, \quad (10)$$

where Ψ_{var} is related to the velocity ratio of the two platforms, k . Considering $k > 0$, Ψ_{var} is given by

$$\Psi_{\text{var}} = a \cos \left(\frac{\left(P_{s,LS}(t_0 + t_a) - \vec{V}_R \times t_a \right) \cdot \vec{R}_R(t_a, P_m)}{\left| P_{s,LS}(t_0 + t_a) - \vec{V}_R \times t_a \right| \cdot \left| \vec{R}_R(t_a, P_m) \right|} \right), \quad (11)$$

where $P_{s,LS}(t_0 + t_a)$ is the GEOSAR subpoint. And (11) can be further simplified as

$$\Psi_{\text{var}} \approx a \cos \left(\frac{\left(P_{s,LS}(t_0) + \left| \vec{V}_{eT} - \vec{V}_R \right| \times t_a \right) \cdot \vec{R}_R(t_a, P_m)}{\left| P_{s,LS}(t_0) + \left| \vec{V}_{eT} - \vec{V}_R \right| \times t_a \right| \cdot \left| \vec{R}_R(t_a, P_m) \right|} \right). \quad (12)$$

Since

$$\max(t_a) = \frac{T_v}{2} = \frac{V_R L_T - V_{eT} L_R}{2 V_R \left| \vec{V}_{eT} - \vec{V}_R \right|}, \quad (13)$$

where $\max(\Psi_{\text{var}})$ is expressed as

$$\begin{aligned} \max(\Psi_{\text{var}}) &= a \cos \left(\frac{\left(P_{s,LS}(t_0) + \left(\vec{V}_R L_T - \vec{V}_{eT} L_R \right) / 2 \right) \cdot \vec{R}_R(t_a, P_m)}{\left| P_{s,LS}(t_0) + \left(\vec{V}_R L_T - \vec{V}_{eT} L_R \right) / 2 \right| \cdot \left| \vec{R}_R(t_a, P_m) \right|} \right). \end{aligned} \quad (14)$$

To meet the condition of (10), $\max(\Psi_{\text{var}})$ will be in CCI also. Note from (14) that Ψ_{var} is related to \vec{V}_{eT} , L_R , \vec{V}_R , and L_T .

When $k < 0$, $\max(\Psi_{\text{var}})$ is the same to (14). However, GEOSAR runs on a circle orbit if $k = 0$. Under this circumstance, Ψ is meaningless for $\theta_{\text{rin}} = 0$. Hence, the range resolution is given by

$$D_r = \frac{C}{2B_r} \cdot \frac{\vec{V}t_e}{\left| \vec{V}t_e \right|}. \quad (15)$$

5. Simulation Analysis

In order to study the resolution of GEO-UAV BiSAR, we discuss the influence of coherent accumulated time and attitude change of UAV on the two-dimensional resolution. And the imaged results are disposed through using frequency domain RD method based on MSR.

5.1. Effect of Coherent Accumulated Time on Azimuth Resolution. Within a periodical time of GEOSAR, the velocity

TABLE 3: Azimuth coverage and coherent accumulated time of GEOSAR at different time instants.

Time t_0 (s)	$T_s/8$	$T_s/4$	$T_s/2$
V_{eT} (m/s)	366.54	464.15	232.08
Clear zone ($\times 10^4$ m)	[-2.09, 2.09]	[-1.49, 1.49]	[-3.95, 3.95]
Dead zone1 ($\times 10^4$ m)	[-2.12, 2.09] & [2.09, 2.12]	[-1.52, -1.49] & [1.49, 1.52]	[-3.98, -3.95] & [3.95, 3.98]
$\max(T_{\text{sar}})$ (s)	2.71	2.71	2.73

V_{eT} is a variable. The bistatic configuration changes with the different time instant t_0 selected (origin O is different with a function t_0 in local ground coordinate system). According to the parameters of GEOSAR and UAVSAR (see Tables 1 and 2), we can gain $k \in (1, +\infty)$. In the condition of $\theta_{\text{rin}} = 10^\circ$ and $\Psi = 311^\circ$, the azimuth coverage and the coherent accumulated time are calculated through (23) and (24) in the appendix. GEOSAR beam surface velocity, clear-zone, dead zone1, and coherent accumulated time for $t_0 = T_s/8$, $T_s/4$, and $T_s/2$ are shown in Table 3.

Simulations that demonstrate the azimuth coverage of GEO-UAV BiSAR are inversely proportional to $|V_{eT} - V_R|$. At a constant L_R , the size of dead zone shows a decrease with V_{eT} going up. The change of $\max(T_{\text{sar}})$ follows the squint angle of receiver that varies owing to the orbital movement of GEOSAR.

Taking $t_0 = T_s/8$ as an example, the influence of coherent accumulated time on azimuth resolution is drawn in Figure 5. In the clear zone, the azimuth resolution will achieve 0.99 m, while the azimuth resolution capability reduces with coherent accumulated time dropping gradually in the dead zone1.

5.2. Effect of the Initial Attitudes for Two Platforms on Resolution. Based on resolution analysis in Section 4, the appropriate attitude control of UAVSAR enables to avoid the appearance dead zone2 in the clear zone. As far as of range and the Doppler resolution are concerned, Figure 6 shows their variations as two functions of θ_{rin} and Ψ for GEO-UAV BiSAR ($t_0 = T_s/8$).

Ψ has a great effect on the range resolution, to which θ_{rin} is meaningless. If $\Psi \in [0^\circ, 90^\circ]$ and $\Psi \in [276^\circ, 360^\circ]$, BiSAR has higher resolution and $D_r \leq 1.4$ m. If $\Psi \in [91^\circ, 275^\circ]$, BiSAR resolution is much lower and $D_r > 1.4$ m. When $\Psi = 180^\circ$, it is the worst condition that gradient of time delay is equal to zero such that the range resolution reaches the maximum value (see Figure 6(a)).

For the azimuth resolution, both θ_{rin} and Ψ have certain amount of influences. If $\theta_{\text{rin}} \leq 45^\circ$, the azimuth resolution of GEO-UAV BiSAR is lower than 1.4 m (critical value of resolution). And if $\theta_{\text{rin}} > 45^\circ$, the azimuth resolution is still impacted by Ψ (see Figure 6(b)).

$$\Psi \in [0^\circ, 14^\circ] \& [44^\circ, 198^\circ] \& [230^\circ, 360^\circ] \implies D_a \leq 1.4 \text{ m},$$

$$\Psi \in [15^\circ, 43^\circ] \& [199^\circ, 229^\circ] \implies D_a > 1.4 \text{ m}.$$

(16)

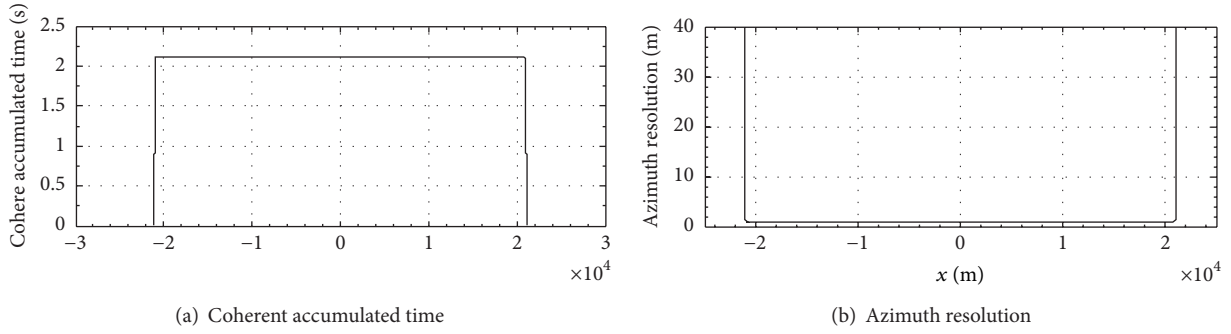


FIGURE 5: Coherent accumulated time (a) and azimuth resolution (b) ($t_0 = T_s/8$).

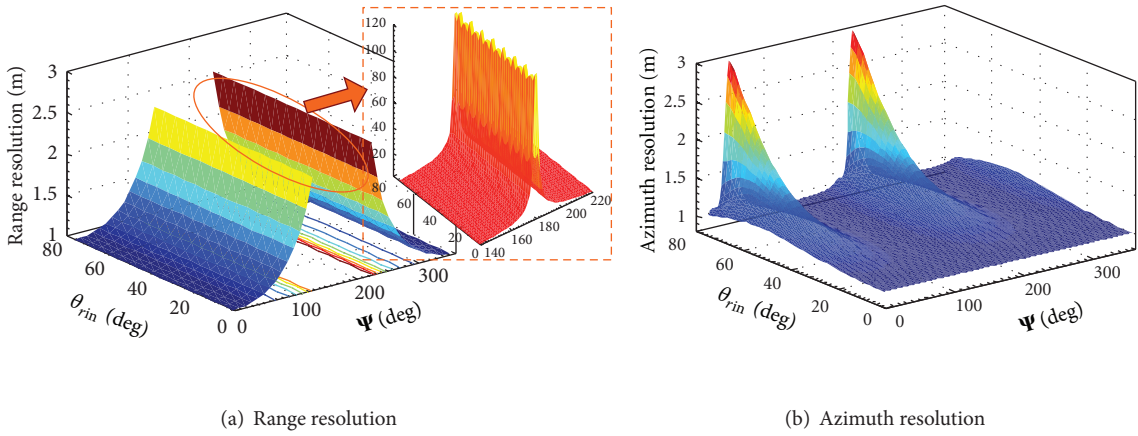


FIGURE 6: Range resolution (a) and azimuth resolution (b) as two functions of θ_{rin} and Ψ for GEO-UAV BiSAR.

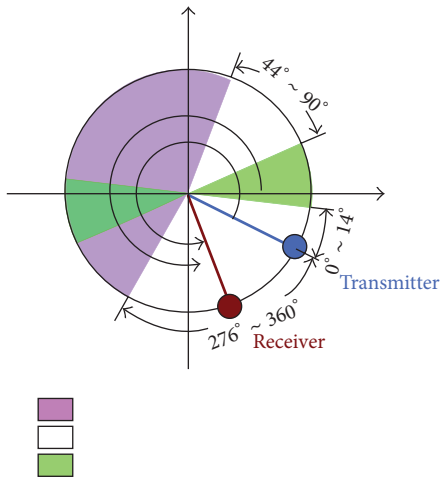


FIGURE 7: The unit location distribution of GEOSAR and UAVSAR.

To assure the high resolution of range and azimuth, the range value of Ψ is drawn in Figure 7. A unit circle represents the position projection of transmitter and receiver in xOy plane. If $\theta_{rin} \leq 45^\circ$, GEO-UAV BiSAR configuration can show high-resolution ability in the content of $\Psi \in$ area 2 and area

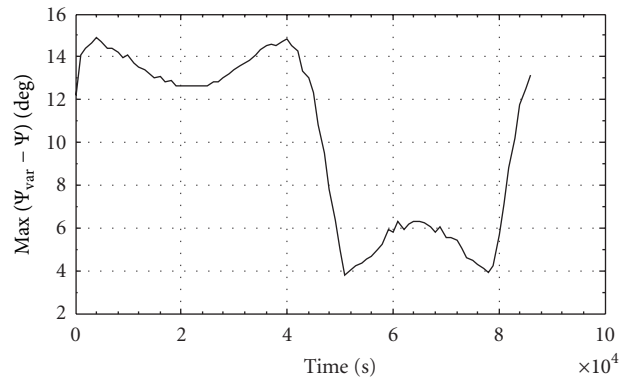


FIGURE 8: $\text{Max}(\Psi_{var} - \Psi)$ in an orbital period of GEOSAR.

3, whereas we need to avoid Ψ that appears in area 1 and area 3 if $\theta_{rin} > 45^\circ$.

With the mutual movement of two platforms ($\vec{V}_{eT}(t_0 + t_a) \neq \vec{V}_{eT}(t_0)$, and $\vec{V}_{eT}(t_0 + t_a)$ is time varying), the variational range of Ψ_{var} is different in the periodical time of GEOSAR. To avoid the appearance of the dead zone2 in the clear zone, we demand to meet (10). The variational range of $\text{max}(\Psi_{var} - \Psi)$ in the whole period of GEOSAR is shown in Figure 8. And

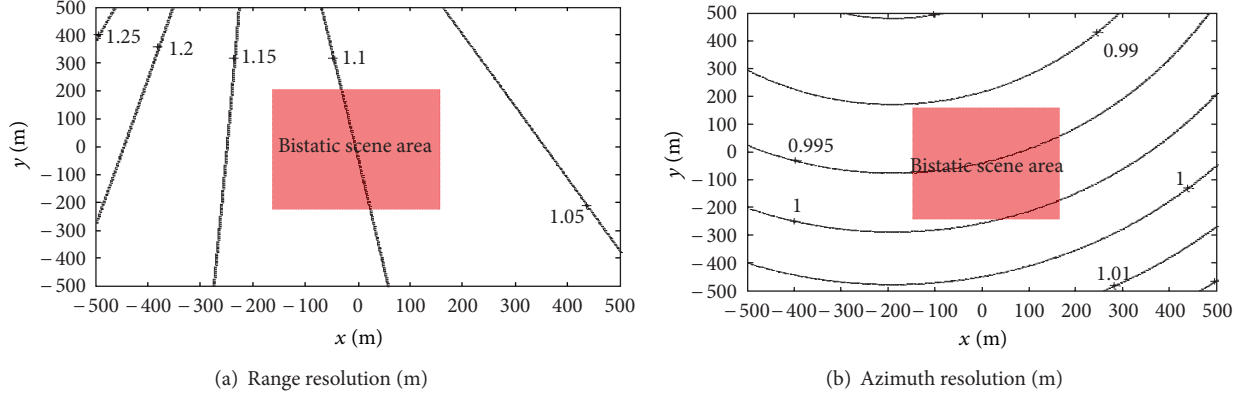


FIGURE 9: Range resolution in meters (a) and azimuth resolution in meters (b) of GEO-UAV BiSAR in xOy plane ($t_0 = T_s/8$). The red region represents the bistatic scene area.

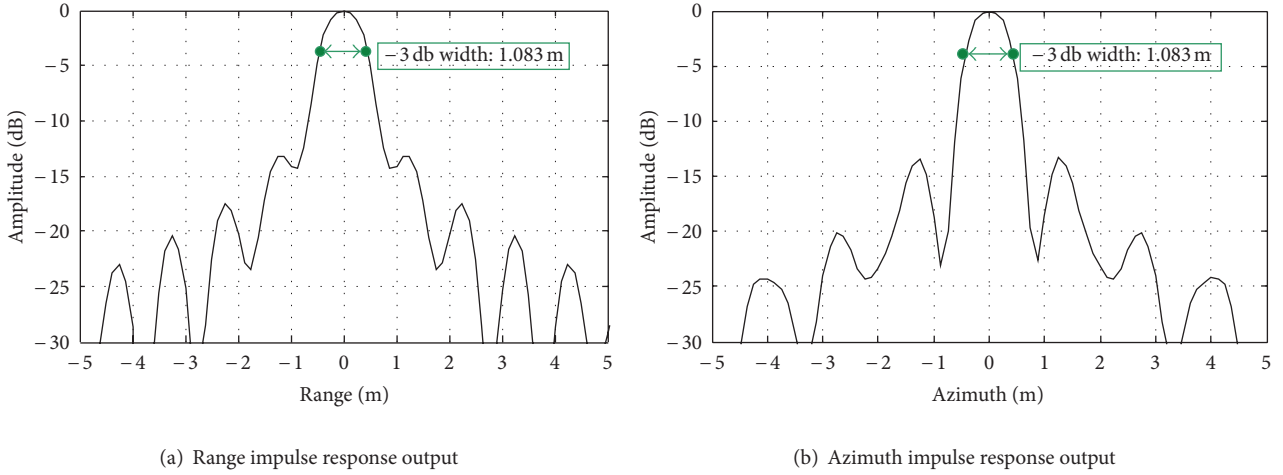


FIGURE 10: Range impulse response output (a) and azimuth impulse response output (b) for the point target ($t_0 = T_s/8$).

$\max(\Psi_{\text{var}} - \Psi)$ obtains the maximum 15° when $t_0 = T_s/20$. Hence, the proper extent of initial UAV attitude can be written as

$$\Psi \in [0^\circ, 75^\circ] \& [291^\circ, 360^\circ] (\theta_{\text{rin}} \leq 45^\circ), \quad (17)$$

$$\Psi \in [59^\circ, 75^\circ] \& [291^\circ, 358^\circ] (\theta_{\text{rin}} > 45^\circ).$$

Based on the aforementioned condition, we select $\theta_{\text{rin}} = 10^\circ$ and $\Psi = 311^\circ$. Figure 9 shows the range and azimuth resolution distributions of GEO-UAV BiSAR in xOy plane ($t_0 = T_s/8$). It is worth noting that the coherent accumulated time (2.71 s in Table 3) is considered for all point target in the bistatic scene area. The bistatic scene dimensions are 400 m in range and 244 m in azimuth. And the range resolutions from 1.07 m to 1.14 m are expected along with azimuth resolutions ranging from 0.99 m to 1.00 m. These values are deduced by (8) and (9). Thus, GEO-UAV BiSAR is suitable to the image in the local area.

5.3. Frequency Domain RD Based on MSR. To evaluate the resolution of GEO-UAV BiSAR, we will focus on an image with a frequency-domain SAR processor. The corresponding

processing approach has been developed based on MSR by means of the four-level Taylor expansion [18, 19]. RD method in frequency domain is performed by four steps, that is, range compression, secondary range compression, range cell migration, and azimuth compression.

If the attitude parameters of UAVSAR are $\theta_{\text{rin}} = 10^\circ$ and $\Psi = 311^\circ$, the impulse response output at the scene center target ($t_0 = T_s/8$) is drawn in Figure 10. The corresponding measured -3 dB resolutions are 1.08 m and 1.08 m, respectively, in comparison to the theoretical values of 1.08 m and 0.99 m (in Figure 9). It can be seen that the resolution has range and azimuth broadening of about 0.3% and 9%.

6. Conclusion

Bistatic geometrical configuration using GEOSAR as a transmitter and UAVSAR as a receiver is analyzed. From a theoretical level, firstly, the variation of bistatic geometrical configuration which has influence on azimuth common coverage and coherent accumulated time is studied according to the ellipse orbital movement of GEOSAR; then, the gradient method based on GEO-UAV SAR configuration (GEOSAR

TABLE 4: Space-time analysis of GEO-UAV BiSAR.

Velocity ratio	Azimuth maximum coverage (UAVSAR position in Ox axis)	Coherent accumulated time
$k = 0$	$C_a = L_T$ ($x_R = x_R^{(0)}$)	$T_{\text{sar}} = \frac{x - x_A}{V_R}, \quad x \in [x_A, L_R + x_A],$ $T_{\text{sar}} = \frac{L_R}{V_R}, \quad x \in [L_R + x_A, L_T - L_R + x_A],$ $T_{\text{sar}} = \frac{x - L_T + L_R - x_A}{V_R}, \quad x \in [L_T - L_R + x_A, L_T + x_A].$ (20)
$k \in (0, 1)$	$C_a = \frac{V_R L_T + V_{eT} L_R}{V_R - V_{eT}}$ ($x_R = x_R^{(0)}$)	$l(x) = L_T - \frac{V_R - V_{eT}}{V_R} (x - x_A),$ $T_{\text{sar}} = \min\left(\frac{L_R}{V_R}, \frac{L_T - l(x)}{V_{eT}}\right),$ $x \in \left[x_A, \frac{V_R L_T}{(V_R - V_{eT})} + x_A\right],$ (21)
		$l(x) = \frac{V_R - V_{eT}}{V_{gT}} (x - x_A) - \frac{V_R}{V_{eT}} L_T,$ $T_{\text{sar}} = \min\left(\frac{L_R}{V_R}, \frac{L_T - l(x)}{V_R}\right),$ $x \in \left[\frac{V_R L_T}{(V_R - V_{gT})} + x_A, \frac{V_R L_T + V_{eT} L_R}{(V_R - V_{eT})} + x_A\right].$ (22)
$k \in (1, +\infty)$	$C_a = \frac{V_R L_T + V_{eT} L_R}{V_{eT} - V_R}$ ($x_R = x_R^{(1)}$)	$l(x) = L_R - \frac{(V_{eT} - V_R)(x - x_B)}{V_{eT}},$ $T_{\text{sar}} = \frac{L_R - l(x)}{V_R},$ $x \in \left[x_B, \frac{V_{eT} L_R}{(V_{eT} - V_R)} + x_B\right],$ (23)
		$l(x) = \frac{(V_{eT} - V_R)(x - x_B)}{V_R} - L_R \frac{V_{eT}}{V_R},$ $T_{\text{sar}} = \min\left(\frac{L_R}{V_R}, \frac{L_T - l(x)}{V_{eT}}\right),$ $x \in \left[\frac{V_{eT} L_R}{(V_{eT} - V_R)} + x_B, \frac{V_R L_T + V_{eT} L_R}{(V_{eT} - V_R)} + x_B\right].$ (24)
$k < 0$	$C_a = \frac{V_R L_T + V_{eT} L_R}{V_R + V_{eT}}$ ($x_R = x_R^{(1)}$)	$l(x) = L_R - \frac{V_R + V_{eT}}{V_{eT}} (x - x_B),$ $T_{\text{sar}} = \min\left(\frac{L_R}{V_R}, \frac{L_T - l(x)}{V_R}\right),$ $x \in \left[x_B, \frac{V_{eT} L_R}{2(V_R + V_{eT})} + x_B\right],$ (25)
		$l(x) = \frac{V_R + V_{eT}}{V_R} (x - x_B) - \frac{V_{eT}}{V_R} L_R,$ $T_{\text{sar}} = \min\left(\frac{L_R}{V_R}, \frac{L_T - l(x)}{V_{eT}}\right),$ $x \in \left[\frac{V_{eT} L_R}{(V_R + V_{eT})} + x_B, \frac{V_{eT} L_R + V_R L_T}{(V_{eT} + V_R)} + x_B\right].$ (26)

exhibits the characteristics of high altitude and periodical motion) is proposed to deduce two-dimensional resolution.

Simulations illustrate that the resolution is accurately obtained from the geometrical simplification of gradient method which consists of two impact factors on the coherent accumulated time and the UAV attitude. The azimuth resolution capacity of GEO-UAV BiSAR shows a gradual decrease with coherent accumulated time reducing the relative motion of two platforms. Moreover, the proper initial selection of UAV attitude can avoid the appearance of dead zone in the swath. Such theoretical analysis, along with simulation results, further demonstrates the potential performance of GEO-UAV BiSAR that is mainly affected by the UAV attitude design when GEOSAR follows the orbital operation. Besides, the feasibility of GEO-UAV BiSAR configuration for high resolution imaging in the local field is verified.

The foregoing works in this paper inspire us to research on the existing bistatic particularities. However, the effect

of nonstationary movement related to phase center for GEOSAR and UAVSAR, which reduce the two-dimensional resolution, is ignored in this paper. In this case, the further experiments based on the nonstationary will be developed, and the resolution will be analyzed.

Appendix

See Table 4.

References

- [1] W. Edelstein, S. Madsen, A. Moussessian, and C. Chen, "Concepts and technologies for synthetic aperture radar from MEO and geosynchronous orbits," in *Enabling Sensor and Platform Technologies for Spaceborne Remote Sensing*, Processing of SPIE, pp. 195–203, Honolulu, Hawaii, USA, November 2004.

- [2] Z. Yu, J. Chen, C. Li, Z. Li, and Y. Zhang, "Concepts, properties and imaging technologies for GEOSAR," in *MIPPR 2009: Multispectral Image Acquisition and Processing*, vol. 7494 of *Processing of SPIE*, pp. 1–7, 2009.
- [3] M. Andraschko, J. Antol, R. Baize et al., "The potential for hosted payloads at NASA," in *IEEE Aerospace Conference*, pp. 1–12, Big Sky, Mt, USA, March 2012.
- [4] C. Prati, F. Rocca, D. Giancola, and A. M. Guarnieri, "Passive geosynchronous SAR system reusing backscattered digital audio broadcasting signals," *IEEE Transactions on Geoscience and Remote Sensing*, vol. 36, no. 6, pp. 1973–1976, 1998.
- [5] "Global Earthquake Satellite System, a 20 year plan to enable earthquake prediction, 2003," NASA, JPL, May 2005, <http://www.jpl.nasa.gov/>.
- [6] D. Bruno, S. E. Hobbs, and G. Ottavianelli, "Geosynchronous synthetic aperture radar: concept design, properties and possible applications," *Acta Astronautica*, vol. 59, no. 1–5, pp. 149–156, 2006.
- [7] G. Krieger and A. Moreira, "Spaceborne bi- and multistatic SAR: potential and challenges," *IEE Proceedings: Radar, Sonar and Navigation*, vol. 153, no. 3, pp. 184–186, 2006.
- [8] J. R. Rodon, A. Broquetas, A. M. Guarnieri, and F. Rocca, "Atmospheric phase screen retrieval from GEOSAR long term acquisition," in *Proceedings of the 9th European Conference on Synthetic Aperture Radar (EUSAR '12)*, pp. 79–82, Nuremberg, Germany, April 2012.
- [9] J. Ruiz, A. Broquetas, A. Monti, and F. Rocca, "A Ku-band geosynchronous synthetic aperture radar mission analysis with medium transmitted power and medium-sized antenna," in *IEEE International Geoscience and Remote Sensing Symposium (IGARSS '11)*, pp. 2456–2459, Vancouver, Canada, July 2011.
- [10] G. L. Guttrich, W. E. Sievers, and N. M. Tomljanovich, "Wide area surveillance concepts based on geosynchronous illumination and bistatic unmanned airborne vehicles or satellite reception," in *Proceedings of the IEEE National Radar Conference*, pp. 126–131, May 1997.
- [11] J. Palmer, S. Palumbo, A. Summers, D. Merrett, and S. Howard, "DSTO's experimental geosynchronous satellite based PBR," in *International Radar Conference on Surveillance for a Safer World (RADAR '09)*, pp. 1–6, December 2009.
- [12] L. Lei, Y. Zhou, J. Li, and B. Sun, "Synchronization of GEO spaceborne-airborne bistatic SAR," in *Proceedings of IEEE International Geoscience and Remote Sensing Symposium (IGARSS '08)*, vol. 3, pp. 1209–1211, July 2008.
- [13] J. Wang, Y. Wang, R. Chen, and J. Ge, "Research on the ground resolution of bistatic forward-looking SAR with geostationary illuminator and UAV receiver," in *Proceedings of the 9th European Conference on Synthetic Aperture Radar (EUSAR '12)*, pp. 567–570, Nuremberg, Germany, April 2012.
- [14] T. Zeng, M. Cherniakov, and T. Long, "Generalized approach to resolution analysis in BSAR," *IEEE Transactions on Aerospace and Electronic Systems*, vol. 41, no. 2, pp. 461–474, 2005.
- [15] A. Moccia and A. Renga, "Spatial resolution of bistatic synthetic aperture radar: impact of acquisition geometry on imaging performance," *IEEE Transactions on Geoscience and Remote Sensing*, vol. 49, no. 10, pp. 3487–3503, 2011.
- [16] R. Wang, O. Loffeld, Y. L. Neo et al., "Focusing bistatic SAR data in airborne/stationary configuration," *IEEE Transactions on Geoscience and Remote Sensing*, vol. 48, no. 1, pp. 452–465, 2010.
- [17] R. Wang, O. Loffeld, Q. Ul-Ann, H. Nies, A. M. Ortiz, and A. Samarah, "A bistatic point target reference spectrum for general bistatic SAR processing," *IEEE Geoscience and Remote Sensing Letters*, vol. 5, no. 3, pp. 517–521, 2008.
- [18] F. H. Wong, I. G. Cumming, and Y. L. Neo, "Focusing bistatic SAR data using the nonlinear chirp scaling algorithm," *IEEE Transactions on Geoscience and Remote Sensing*, vol. 46, no. 9, pp. 2493–2505, 2008.
- [19] F. H. Wong and T. S. Yeo, "New applications of nonlinear chirp scaling in SAR data processing," *IEEE Transactions on Geoscience and Remote Sensing*, vol. 39, no. 5, pp. 946–953, 2001.
- [20] D. Bruno and S. E. Hobbs, "Radar imaging from geosynchronous orbit: temporal decorrelation aspects," *IEEE Transactions on Geoscience and Remote Sensing*, vol. 48, no. 7, pp. 2924–2929, 2010.
- [21] I. Walterscheid, T. Espeter, A. R. Brenner et al., "Bistatic SAR experiments with PAMIR and TerraSAR-X-setup, processing, and image results," *IEEE Transactions on Geoscience and Remote Sensing*, vol. 48, no. 8, pp. 3268–3279, 2010.

Research Article

Rotating Parabolic-Reflector Antenna Target in SAR Data: Model, Characteristics, and Parameter Estimation

Bin Deng, Hong-Qiang Wang, Yu-Liang Qin, Sha Zhu, and Xiang Li

College of Electronic Science and Engineering, National University of Defense Technology, China

Correspondence should be addressed to Bin Deng; sagitdeng@163.com

Received 22 October 2012; Accepted 3 March 2013

Academic Editor: Gui Gao

Copyright © 2013 Bin Deng et al. This is an open access article distributed under the Creative Commons Attribution License, which permits unrestricted use, distribution, and reproduction in any medium, provided the original work is properly cited.

Parabolic-reflector antennas (PRAs), usually possessing rotation, are a particular type of targets of potential interest to the synthetic aperture radar (SAR) community. This paper is aimed to investigate PRA's scattering characteristics and then to extract PRA's parameters from SAR returns, for supporting image interpretation and target recognition. We at first obtain both closed-form and numeric solutions to PRA's backscattering by geometrical optics (GO), physical optics, and graphical electromagnetic computation, respectively. Based on the GO solution, a migratory scattering center model is at first presented for representing the movement of the specular point with aspect angle, and then a hybrid model, named the migratory/micromotion scattering center (MMSC) model, is proposed for characterizing a rotating PRA in the SAR geometry, which incorporates PRA's rotation into its migratory scattering center model. Additionally, we in detail analyze PRA's radar characteristics on radar cross-section, high-resolution range profiles, time-frequency distribution, and 2D images, which also confirm the models proposed. A maximal likelihood estimator is developed for jointly solving the MMSC model for PRA's multiple parameters by optimization. By exploiting the aforementioned characteristics, the coarse parameter estimation guarantees convergency upon global minima. The signatures recovered can be favorably utilized for SAR image interpretation and target recognition.

1. Introduction

Parabolic-reflector antennas (PRAs), due to their excellent beam directionality, are widely used in radar surveillance, navigation, microwave communication, and radio astronomy. Although they are antennas in themselves, PRAs are also present as a particular type of targets, gaining growing interest in some scenarios to the synthetic aperture radar (SAR) community [1]. Their scattering and rotation characteristics, which are obtainable with SAR, may be of valuable aid for target recognition. Therefore, it is desirable to detect and recognize them from SAR returns or imagery. However, this work is difficult because of two reasons. On one hand, the backscattering of PRAs is so complicated that they cannot be characterized by point scattering centers, and the directionality, favorable as it is for PRAs as antennas, results in aspect sensitivity and weak backscattering at most aspect angles when they are present as SAR targets. On the other hand, their rotation, due to mechanical scanning, changes the Doppler history and therefore makes their SAR images

blurred and enigmatic. And unfortunately, rotation cannot be processed by the mature technique, that is, SAR ground moving target indication (SAR/GMTI), though it is a valid tool for uniformly moving targets [2].

Conventionally, rotating PRAs (RPRAs) were investigated as micromotion targets. In 2009, the SAR/micromotion target indication concept was presented to generalize the SAR/GMTI technique and to intensively examine the detection and imaging problems for micromotion targets [3]. Actually, early in 2004, the picket fence shape was revealed to be representative of a rotating radar dish in the SAR azimuth image [4], but the dish (viz. PRA) was simplified as a combination of point scatterers, which are not qualified for characterizing PRA's complex scattering. In 2005 and 2010, wavelet decomposition and chirplet decomposition were used to successfully separate the return of an RPRAs from that of stationary parts. The returns were collected by the US Navy APY-6 radar [5, 6]. After separation, time-frequency distribution (TFD) was utilized to analyze the phase modulation and autocorrelation to estimate the rotating frequency.

The RPRA detected was annotated in the SAR image [1]. However, the RPRA's signature blurred in SAR imagery was not explained, and the aforementioned approaches are susceptible to range cell migration (RCM). TFD also usually suffers from cross-term interference. In 2007, RPRA data, collected by a microwave SAR system in University of Zurich, were analyzed [7]. A point-symmetrical image of the RPRA was obtained, and the time-frequency image showed a small fraction of a sinusoidal phase modulation. The conclusions, however, are only valid for slow rotating frequency and short coherent processing interval (CPI). PRA's radar characteristics have not been deeply studied either.

In this paper, we focus on characterization and non-TFD-based estimation of PRAs, both stationary and rotating, in spotlight SAR data. There are different types of PRAs, but we restrict our scope to a rotation-symmetrical PRA with a single reflector. Instead of processing returns in a single range cell, we use the phase history in the wavenumber domain, that is, the 2D Fourier transform (FT) of complex imagery, to extract PRAs and their parameters. We build for a PRA a new non-point-scattering center model able to describe the aspect sensitivity and the sliding of scatterers and then incorporate the motion model into it to obtain a hybrid scattering/motion model. Radar characteristics of PRAs are then analyzed. Afterwards, an estimation algorithm for this model is proposed. This idea fully exploits a priori information on target models, implements joint estimation of scattering and motion parameters, and circumvents TFD and other tough issues, such as clutter suppression, detection, RCM correction, and parameter estimation which have to be conducted separately and explicitly in SAR/GMTI.

This paper is organized as follows. In Section 2, geometrical optics (GO), physical optics (PO), and graphical electromagnetic computation (GRECO) are used to calculate the backscattering or complex radar cross-section (RCS) of a PRA. Then, based on the calculated results, we propose a new scattering center model and a hybrid scattering/motion model in Section 3. We then in Section 4 analyze the characteristics of PRAs. A few interesting signatures of PRAs are revealed, for example, periodicity of high-resolution range profile (HRRP) sequences, bowl- and bowknot-shaped images. Sections 5 and 6 provide a maximum likelihood estimator and a few results, and conclusions are reported in Section 7. The derivation throughout the paper may be a little difficult to follow, and we will try our best to clarify the problem.

2. Complex RCS Calculation for PRA

Backscattering of an antenna consists of two parts, that is, structured scattering, whose scattering principle is the same of as common objects, and pattern scattering, which is closely related to antenna's loads. Pattern scattering is weak for a PRA and, hence, not taken into account here. We will calculate PRA's complex RCS via GO, PO, and GRECO. GO is simple and is particularly suitable for smooth surface. PO has high accuracy near target's normal direction and can provide closed-form solutions in some particular aspects. And GRECO, as a tool and software, incorporates many

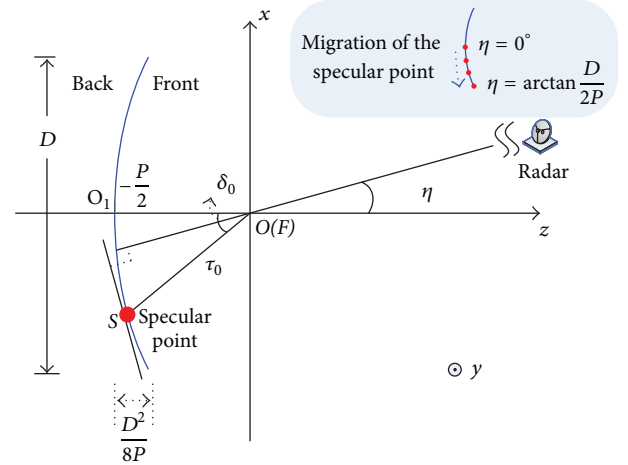


FIGURE 1: PRA geometry (x - z slice).

electromagnetic methods and can efficiently provide high-precision numerical solutions.

2.1. GO. As Figure 1 shows, let P denote the focus parameter of a PRA, τ , and δ denote the radius and angle (relative to $-z$ axis) of any point on a PRA. Other parameters encountered are defined in Figure 1 where the focus is located at the origin. O - z is the symmetrical axis. Then, the amplitude of the PRA's complex RCS, that is, the square root of RCS, can be obtained from the GO theory [8]

$$|\sqrt{\sigma_{\text{GO}}}| = \frac{\sqrt{\pi}P}{\cos^2\eta}. \quad (1)$$

Its phase can be easily derived from the position of the specular point S . Combining the amplitude and phase, we have the complex RCS

$$\sqrt{\sigma_{\text{GO}}} = \frac{\sqrt{\pi}P}{\cos^2\eta} \exp\left(-jK \frac{P}{2 \cos\eta}\right), \quad (2)$$

where $K = 4\pi f/c$ is the wavenumber, c is the speed of light, and f is the frequency. When choosing PRA's bottom center O_1 as the phase reference, we need to multiply (2) with $\exp(jK \cdot P/2 \cdot \cos\eta)$ and then have

$$\sqrt{\sigma_{\text{GO}}} = \frac{\sqrt{\pi}P}{\cos^2\eta} \exp\left(-jK \frac{P \sin^2\eta}{2 \cos\eta}\right). \quad (3)$$

Equations (2) and (3) hold only when η is chosen such that the specular point does not move outside the PRA. Specifically, when the incident field illuminates the PRA front side, η should be subjected to

$$|\eta| \leq \arctan \frac{D}{2P}. \quad (4)$$

2.2. PO. To facilitate application of PO, we use the Cartesian coordinate system and the cylinder coordinate system. Then in Figure 1, for any point Q in the PRA, suppose that its

position in the cylindrical coordinate system is $(\rho, \varphi, z) = (\rho, \varphi, \rho^2/(2P) - P/2)$. It can be vectorized in the Cartesian coordinate system as

$$\mathbf{r}' = (x, y, z)^T = \left(\rho \cos \varphi, \rho \sin \varphi, \frac{\rho^2}{2P} - \frac{P}{2} \right)^T. \quad (5)$$

The normal vector at Q is

$$\hat{\mathbf{n}} = \left(-\frac{\rho \cos \varphi}{P}, -\frac{\rho \sin \varphi}{P}, 1 \right)^T / \sqrt{1 + \frac{\rho^2}{P^2}}. \quad (6)$$

The backscattering direction can be expressed by

$$\hat{\mathbf{r}} = (\sin \eta, 0, \cos \eta)^T. \quad (7)$$

According to PO, the complex RCS of the PRA can be written as

$$\sqrt{\sigma_{\text{PO}}} = -j \frac{k}{\sqrt{\pi}} \int_0^{2\pi} \int_0^{D/2} \hat{\mathbf{r}} \cdot \hat{\mathbf{n}} \exp(jK\hat{\mathbf{r}} \cdot \mathbf{r}') \sqrt{1 + \frac{\rho^2}{P^2}} \rho d\rho d\varphi. \quad (8)$$

Generally, (8) can be calculated by using numerical methods, and its closed-form solution cannot be obtained due to its complexity. However, the closed-form solution exists for some particular incident angles. When $\eta = 0$, for example, the complex RCS we derive is

$$\begin{aligned} \sqrt{\sigma_{\text{PO}}}|_{\eta=0} &= -j2\sqrt{\pi}P \sin\left(K \frac{D^2}{16P}\right) \exp\left[-jK\left(\frac{P}{2} - \frac{D^2}{16P}\right)\right] \\ &= \sqrt{\pi}P \left[\exp\left(-jK \frac{D^2}{16P}\right) - \exp\left(jK \frac{D^2}{16P}\right) \right] \\ &\quad \times \exp\left[-jK\left(\frac{P}{2} - \frac{D^2}{16P}\right)\right]. \end{aligned} \quad (9)$$

2.3. GRECO. GRECO is an effective tool for calculating (complex) RCS of electrically large objects [9]. It is capable of calculating the reflected and diffracted fields with high precision and efficiency by using graphic hardware acceleration and can also perform well for a wide range of aspect angles. Therefore, we select it as a numeric method and benchmark for the GO and PO methods. The result will be given in Section 6.

3. Scattering Center Model and Hybrid Model

3.1. Migratory Scattering Model for a Stationary PRA. The scattering center models have developed from the point scattering model, damped exponential/Prony model [10], through the geometric theory of diffraction (GTD) model [11], localized scattering model [12], and attributed scattering model [13], to the polynomial model [14] and migratory

scattering model [15]. Their difference lies in that they use different models to characterize the dependency of complex RCS, including amplitude and/or phase, on frequency and/or aspect angle. We can find from (2) that, for a PRA, the complex RCS amplitude depends on aspect angle θ ($\theta = \eta$ when aspect angle is relative to PRA's axis of symmetry), resulting in aspect sensitivity, while the phase also depends on aspect angle but the dependency is not of the form of $\sin \theta$ or $\cos \theta$ as ideal point scattering is ($1/\cos \eta$ instead), which means that the scattering center will move when the aspect angle varies. By (2), we have in effect proven that a PRA can be approximated by the migratory scattering model containing a single scattering center, and the approximation has sound physical grounds. However, the amplitude term of complex RCS in (2), enough as it is for coarse analysis, is not an accurate model intended for parameter estimation, since GO does not take into account more scattering components, for example, edge diffraction. Therefore, we use a function, $s(\eta_\theta)$, to describe arbitrary aspect dependency. Then, from (3), we obtain the migratory scattering model for a stationary PRA

$$g(K, \theta) = s(\theta) \exp\left[-jK\left(x \cos \theta + y \sin \theta + \frac{P \sin^2 \eta_\theta}{2 \cos \eta_\theta}\right)\right], \quad (10)$$

where (x, y) are the coordinates of the PRA's bottom center O_1 , and η_θ is the θ -dependent incident angle.

For instance, When choosing PRA's geometrical center as the phase reference (in order for agreement with the GRECO geometry in Figure 3 and Section 4), we have

$$\begin{aligned} g(K, \theta') &= s(\theta') \exp\left[-jK\left(\frac{\sin \theta'}{4} + \frac{P \sin^2(\pi/2 - \theta')}{2 \cos(\pi/2 - \theta')}\right)\right] \\ &= s(\theta') \exp\left[-jK\left(\frac{\sin \theta'}{4} + \frac{P \cos^2 \theta'}{2 \sin \theta'}\right)\right]. \end{aligned} \quad (11)$$

When $\theta' = \omega t$ is around 90° (PRA's front against radar), where ω is the angular frequency and t is the slow time, the instantaneous Doppler can be obtained by taking the derivative of the phase in (11)

$$f_d \approx \frac{17.5}{\lambda} \cos(\omega t) \approx \frac{8.75\pi}{\lambda} - \frac{17.5\omega}{\lambda} t. \quad (12)$$

Equation (12) indicates that the PRA's return in azimuth is a sinusoidal frequency-modulated (SFM) signal or approximately a linear frequency-modulated (LFM) signal when the PRA is illuminated broadside.

3.2. Hybrid Model for a RPRA in the SAR Geometry. It is well known that a PRA usually possesses rotation in operation. Thus, we need to establish its motion model by finding the range from SAR to the specular point S. For the SAR geometry shown in Figure 2, O is the center of the scenario

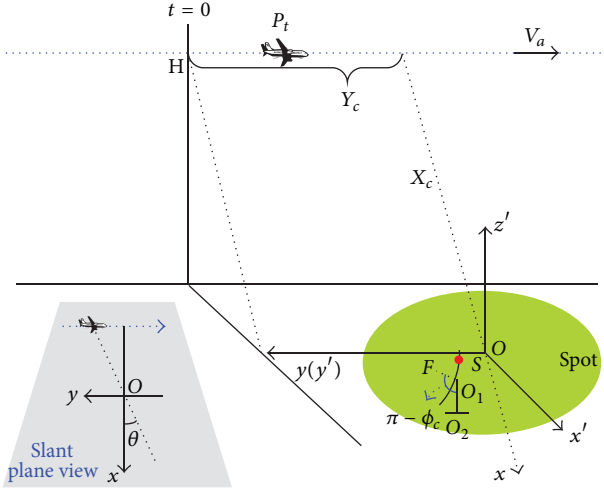


FIGURE 2: SAR geometry with a RPRA.

illuminated by SAR. Assume that a PRA is rotating around its vertical axis, and the pivot is the top of the vertical axis, identical to O_1 . The angle between the O - z' axis and the PRA's axis of symmetry, ϕ_c , remains constant during the rotation around O_1O_2 . $\theta_c = -\arctan(Y_c/X_c)$ is the slant angle. When $Y_c = 0$, SAR is side-looking, and otherwise it operates in squint-looking mode. θ is the angle of light of sight (LOS) in O - xy (i.e., slant plane). The relationship between θ and t is

$$X_c \tan \theta = V_a t - Y_c. \quad (13)$$

When $\theta_c = 0$ and the extent of aspect angle θ is small, $\tan \theta \approx \theta$, and then (13) reduces to

$$\theta = \frac{V_a}{X_c} t. \quad (14)$$

Clearly, θ also has the meaning of slow time.

For deriving the range model, we at first make the following definitions.

In O - xy at slow time t ,

P_t is at $(-X_c, Y_c - V_a t)$ (SAR's position),

O_1 is at (x, y) (bottom center of the PRA).

In O - $x'y'z'$ at slow time t , the normalized vectors of $\overline{O_1F}$ and \overline{OH} are

$$\mathbf{n}_{O_1F} = (\cos \gamma \sin \phi_c, \sin \gamma \sin \phi_c, \cos \phi_c),$$

$$\mathbf{n}_{OH} = (\cos \alpha_0 \sin \beta_0, \sin \alpha_0 \sin \beta_0, \cos \beta_0),$$

where $\gamma = \omega t + \gamma_0$, $\omega = 2\pi f_m$ is the rotating angular frequency and γ_0 is the initial phase, both unknown, and α_0 as well as β_0 are known for parameter estimation in Section 5.

Then, we can easily have

$$\begin{aligned} \cos \eta_\theta &= \mathbf{n}_{O_1F} \cdot \mathbf{n}_{O_1P_t} \approx \mathbf{n}_{O_1F} \cdot \mathbf{n}_{OP_t} \approx \mathbf{n}_{O_1F} \cdot \mathbf{n}_{OH} \\ &= \sin \phi_c \sin \beta_0 \cos(\gamma - \alpha_0) + \cos \phi_c \cos \beta_0, \end{aligned} \quad (15)$$

where the approximation is because O_1P_t is approximately parallel to OP_t and even to OH when the extent of θ is not large.

We can also easily have

$$|P_t O_1| = \sqrt{(V_a t - Y_c + y)^2 + (X_c + x)^2}. \quad (16)$$

From (3) or (10), we have

$$\overline{O_1S} \cdot \mathbf{n}_{P_t O_1} = \frac{P \sin^2 \eta_\theta}{2 \cos \eta_\theta}. \quad (17)$$

Then using the far-field plane wave assumption and (16) as well as (17), we can obtain the range from P_t to S at slow time t

$$\begin{aligned} R(t) &\stackrel{\text{def}}{=} R_\theta = |P_t O_1| + \overline{O_1S} \cdot \mathbf{n}_{P_t O_1} \\ &= \sqrt{(V_a t - Y_c + y)^2 + (X_c + x)^2} + \frac{P \sin^2 \eta_\theta}{2 \cos \eta_\theta} \\ &\approx \sqrt{(V_a t - Y_c)^2 + X_c^2} + x \cos \theta + y \sin \theta + \frac{P \sin^2 \eta_\theta}{2 \cos \eta_\theta}, \end{aligned} \quad (18)$$

where η_θ can be calculated by (15).

After range compression and discarding insignificant factors representing the beam pattern and window functions, SAR returns can be written in the frequency slow time domain as

$$G(K, \theta) = s(\theta) \exp[-jKR(t)]. \quad (19)$$

When processing spotlight SAR data with algorithms such as the polar format algorithm (PFA), one usually compensates the returns with the scenario center's phase, that is, to multiply (19) with $\exp(jK\sqrt{(V_a t - Y_c)^2 + X_c^2})$. Hence, we obtain the resulting returns

$$\begin{aligned} g(K, \theta) &= s(\theta) \exp\left[-jK\left(x \cos \theta + y \sin \theta + \frac{P \sin^2 \eta_\theta}{2 \cos \eta_\theta}\right)\right] \\ &= s(\theta) \exp\left[-jK\left(x \cos \theta + y \sin \theta + \frac{P}{2}\left(\frac{1}{\cos \eta_\theta} - \cos \eta_\theta\right)\right)\right] \\ &= \sum_{i=0}^I b(i) \lambda_i(\theta) \\ &\quad \times \exp\left[-jK\left(x \cos \theta + y \sin \theta + \frac{P}{2}\left(\frac{1}{\cos \eta_\theta} - \cos \eta_\theta\right)\right)\right], \end{aligned} \quad (20)$$

which is named the hybrid scattering/motion model, or migratory/micromotion scattering center (MMSC) model,

where $\lambda_i(\theta)$ are orthogonal basis functions. It is of the same form as (10) derived based on a turntable, but herein it is derived from the SAR geometry and its η_θ is determined by (15). This model has incorporated motion parameters into the scattering center model, providing the rationale for joint estimation of scattering-motion parameters. It will be seen in next section that the model provides a very good representation of a PRA. By the way, the 2D inverse FT of (20), interpolation probably needed, will produce an SAR complex image.

Assume that θ is minor and near 0° , $\theta_c = 0^\circ$, and η_θ is around 0° or 180° . Then, we have

$$\frac{1}{\cos \eta_\theta} \approx \begin{cases} 2 - \cos \eta_\theta, & \text{when } \eta_\theta \text{ is around } 0^\circ, \\ -2 - \cos \eta_\theta, & \text{when } \eta_\theta \text{ is around } 180^\circ. \end{cases} \quad (21)$$

Applying (14), (15), and (21) to (20) leads to

$$\begin{aligned} g(K, \theta) &\approx s(\theta) \exp \left[-jK(x \cos \theta + y \sin \theta - P \cos \eta_\theta \right. \\ &\quad \left. + P \operatorname{sign}(\cos(\eta_\theta))) \right] \\ &\approx C \cdot s(\theta) \\ &\quad \times \exp \left[-jK \right. \\ &\quad \left. \times \left(\frac{V_a y t}{X_c} - P \sin \phi_c \sin \beta_0 \cos(\omega t + \gamma_0 - \alpha_0) \right) \right], \end{aligned} \quad (22)$$

where C is an insignificant unknown constant factor. The instantaneous Doppler, or micro-Doppler, can be obtained by taking the derivative of the phase

$$f_d \approx -\frac{2\omega P \sin \phi_c \sin \beta_0}{\lambda} \sin(\omega t + \gamma_0 - \alpha_0) - \frac{2V_a y}{\lambda X_c}. \quad (23)$$

Both (22) and (23) indicate that the RPRAs azimuth return is an SFM signal, but in effect, it can be approximated by an LFM signal due to broadside flash.

4. Radar Characteristics of a PRA and Validation of the MMSC Model

The analysis proceeds with radar characteristics of a PRA, both stationary and rotating, in terms of RCS, HRRPs, TFD, and SAR images. The results from GO, PO, and GRECO are all based on the following geometry and parameters.

As shown in Figure 3, the origin is now set at its geometrical center O_2 according to our GRECO software's definition. $O_1 O_2 = O_2 O_3 = 0.25$ m. The PRA's depth $O_1 O_3 = 0.5$ m, $P = 9$ m, and $D = 6$ m. The frequencies are from 9.8 GHz to 10.2 GHz stepped by 0.01 GHz with central frequency $f_c = 10$ GHz (therefore the bandwidth is 400 MHz and the range resolution is 0.375 m), and the aspect angles are from -180° to 180° stepped by 0.1° . Then, we use GRECO to calculate the complex RCS of a PRA on a turntable (equivalent to radar's circling a stationary PRA, at an angular frequency $\omega = \theta'/t$). We now analyze the calculated results.

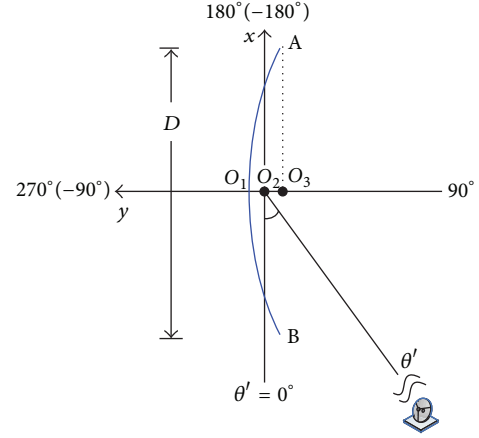


FIGURE 3: PRA geometry for GO, PO and GRECO.

4.1. Stationary PRA

4.1.1. RCS Characteristics. As shown by Figures 4(a) and 4(b), the PRA's RCS exhibits strong dependency on aspect angle θ' . Its scattering is intense (about 250 m^2 or $24 \text{ dB} \cdot \text{m}^2$, far larger than the PRA's aperture area $\pi(D/2)^2 \approx 28 \text{ m}^2$) when the LOS deviates from its axis of symmetry by no more than about 18° . Otherwise its RCS abruptly declines to zero. This phenomenon is generally called broadside flash [16]. From (4), $|\eta| \leq \arctan[6/(2 \times 9)] \approx 18.4^\circ$, which agrees with GRECO results (solid line) and means that GO has correctly predicted the aspect supporting interval. Figure 4(c) shows that GO can also give a coarse prediction for the RCS- θ' function by frequency-free (1). For more accurate description, $s(\theta)$ is therefore used in (10).

From Figure 4(b), we can also find that the RCS- θ' curves are almost identical for different frequencies, except when $\theta' = \pm 90^\circ$, indicating weak frequency dependency of RCS. This is confirmed by Figure 5(a), which shows the RCS-frequency functions are valued between 22 and 26 in dBm^2 , a small range, regardless of aspects (except $\theta' = \pm 90^\circ$). Therefore, our MMSC model, though not considering RCS's dependency on frequency, that is, $s(\theta)$ does not contain f in (20), is judged reasonable from this viewpoint. However, when the LOS is perpendicular to the PRA's bottom, RCS takes on obvious oscillation for PO and GRECO (Figure 5(b)). The reason may be stated in terms of multiple scatterers; that is, there may be additional scattering centers besides the specular point predicted by GO at this aspect.

4.1.2. HRRP Characteristics. Figure 6 depicts the HRRP sequence of the PRA, derived from GRECO data. Since HRRPs at some aspects are too weak to display in Figure 6(a), we modify their amplitudes for every aspect into a normalized value, as shown in Figure 6(b). We will analyze its HRRP characteristics from the following points.

- (1) Overall, strong HRRPs occur periodically when $\theta' \in [-108^\circ, -72^\circ] \cup [72^\circ, 108^\circ]$, which is consistent with our analysis of RCS. The HRRPs' intensity is almost identical for front and back illumination.

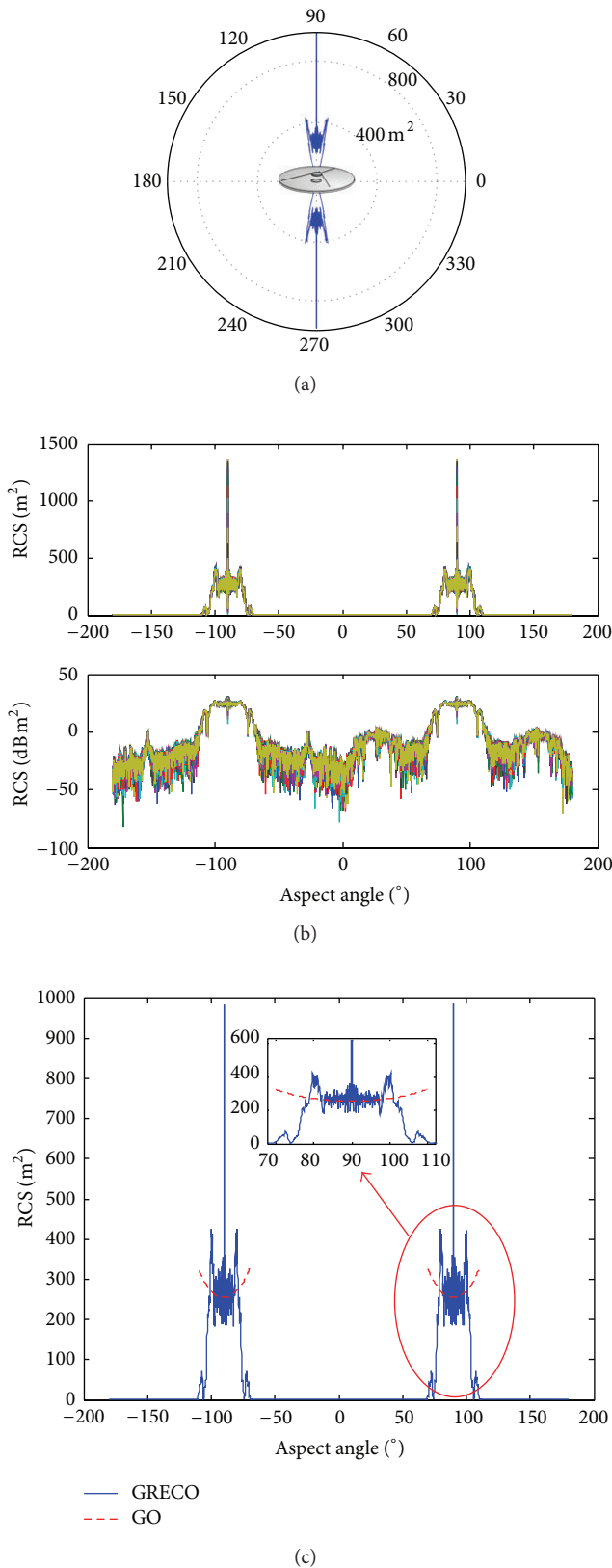


FIGURE 4: PRA RCS's aspect dependency. (a) GRECO, at carrier frequency 10 GHz; (b) GRECO, at different frequencies; (c) GRECO and GO, at carrier frequency 10 GHz.

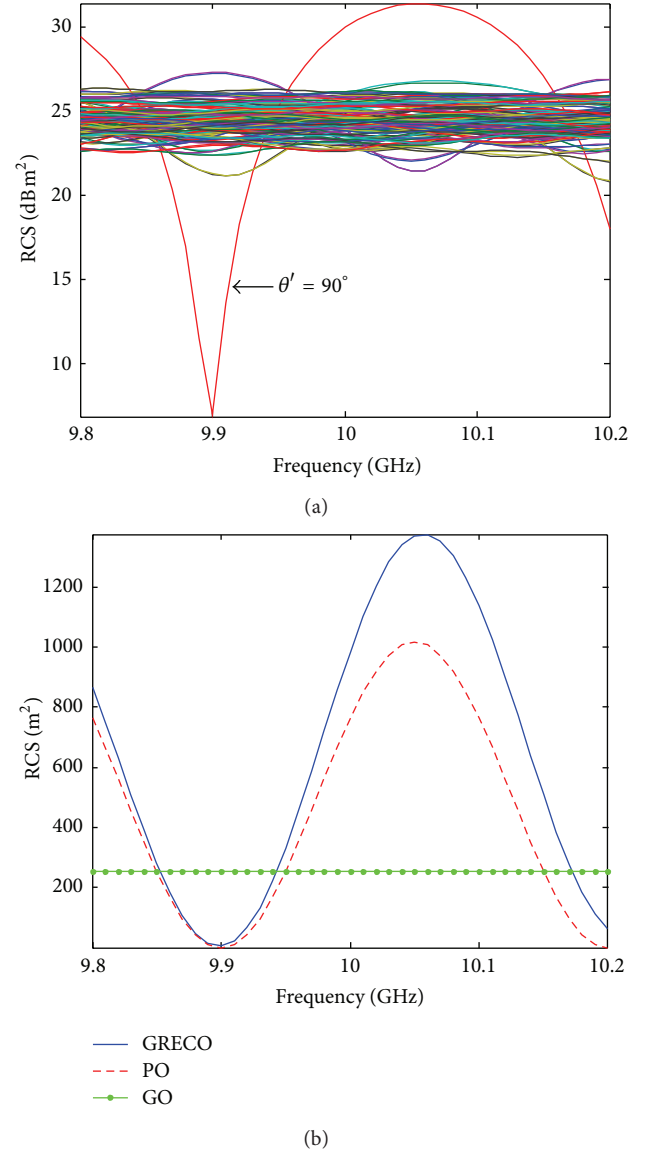


FIGURE 5: RCS's frequency dependency. (a) GRECO, at different aspects; (b) GRECO, PO, and GO, $\theta' = 90^\circ$.

- (2) When illuminated broadside ($\theta' = \pm 90^\circ$), the PRA has two scattering centers at ± 0.25 m with the same amplitude (two peaks in Figure 6(a); only for this aspect, the bandwidth is 2 GHz as opposed to 400 MHz to resolve them). This can be interpreted by (9) given by PO, the second square-bracketed term of which clearly shows that the positions of the two scattering centers are $\pm D^2/(16P) = \pm 0.25$ m. And the conclusion also confirms our conjecture on the reason of RCS oscillation in Figure 5(b). In effect, the two centers correspond to the PRA's bottom center and edge.
- (3) When $\theta' \in [-108^\circ, -72^\circ] \cup [72^\circ, 108^\circ]$ and $\theta' \neq \pm 90^\circ$, the PRA assumes a single scattering center. When the PRA's front side is illuminated, the center moves

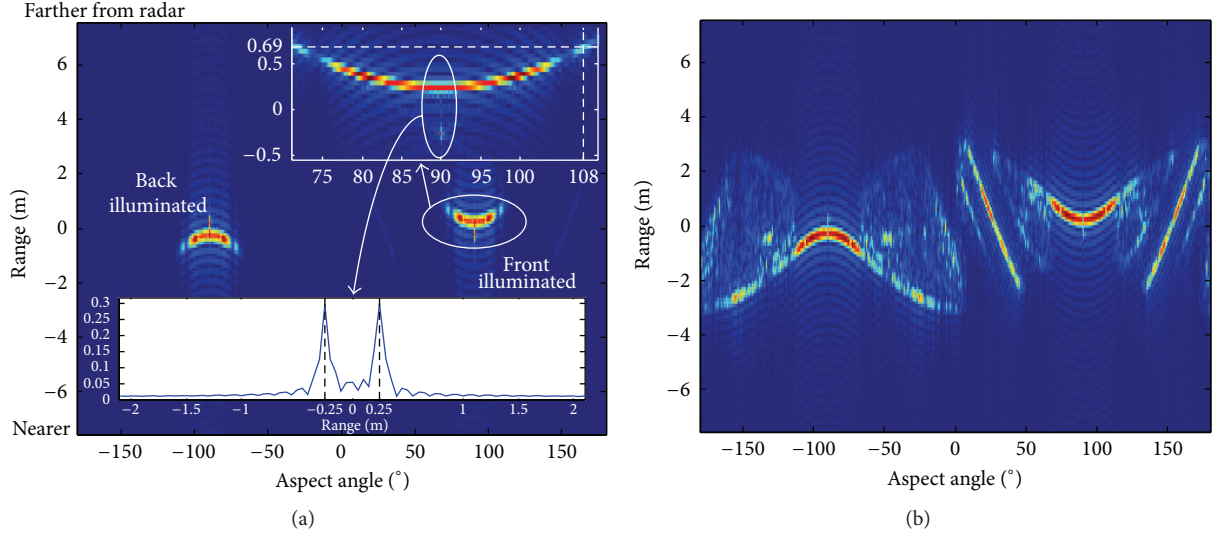


FIGURE 6: HRRP sequences of the PRA with (a) original and (b) normalized amplitude. GRECO data are used.

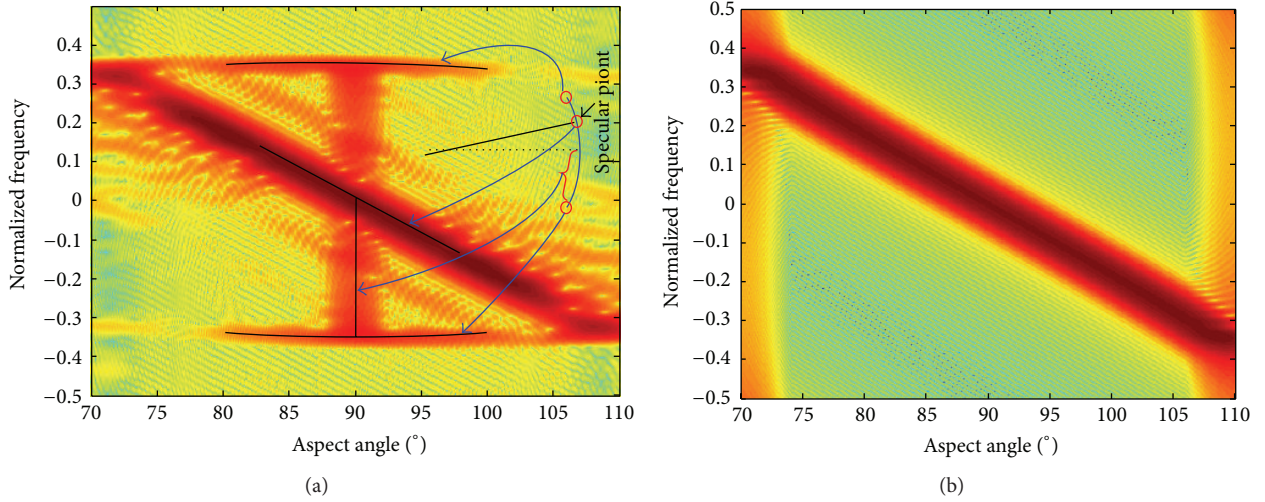


FIGURE 7: TFD of the PRA with data from (a) GRECO and (b) our PRA scattering center model.

further with deviation of the LOS from the PRA's symmetry axis. The case is just the opposite when the back side is illuminated. This conclusion also agrees with our model's prediction (see (10) and (11)). More specifically, in Figure 3, when $\theta' = 108^\circ$, the scattering center should move to $\sin \theta' / 4 + P \cos^2 \theta' / (2 \sin \theta') \approx 0.69$ m, which is in good agreement with the reality in the top-right corner of Figure 6(a). Beyond this range, the center will move outside the PRA and therefore disappear.

- (4) When $\theta' \notin [-108^\circ, -72^\circ] \cup [72^\circ, 108^\circ]$, the HRRPs are too weak and we have to resort to Figure 6(b). Clearly, for these aspects, the scattering is rather complicated due to disappearing of the specular point, and more scattering centers are present beyond the prediction of GO and our models. Fortunately, these HRRPs are so weak that they can be safely ignored.

4.1.3. TFD Characteristics. We also plot the TFD according to the PRA's complex RCS at the central frequency, only for aspects at which the PRA's RCS is strong. The PRA is placed on a "rotatable" turntable, and thus the aspect angle has the sense of slow time. Figure 7(a) shows the TFD based on GRECO-derived data. It is clear that the PRA contains three main scattering centers. One is the specular point, related to the slant line in Figure 7(a). The slant line agrees well with (12) and its graphical presentation in Figure 7(b). Two is at the PRA's edge, that is, points A and B in Figure 3, related to the top and bottom curves in Figure 7(a). Each curve is effectively a small fraction of a sine wave. We now try to explain the vertical line in the middle of Figure 7(a). When $\theta' = 90^\circ$, different parts of the PRA have wide-range relative velocities, from 0 corresponding to O_1 to the maximum and minimum corresponding to point A and B in Figure 3. Therefore the instantaneous Doppler at $\theta' =$

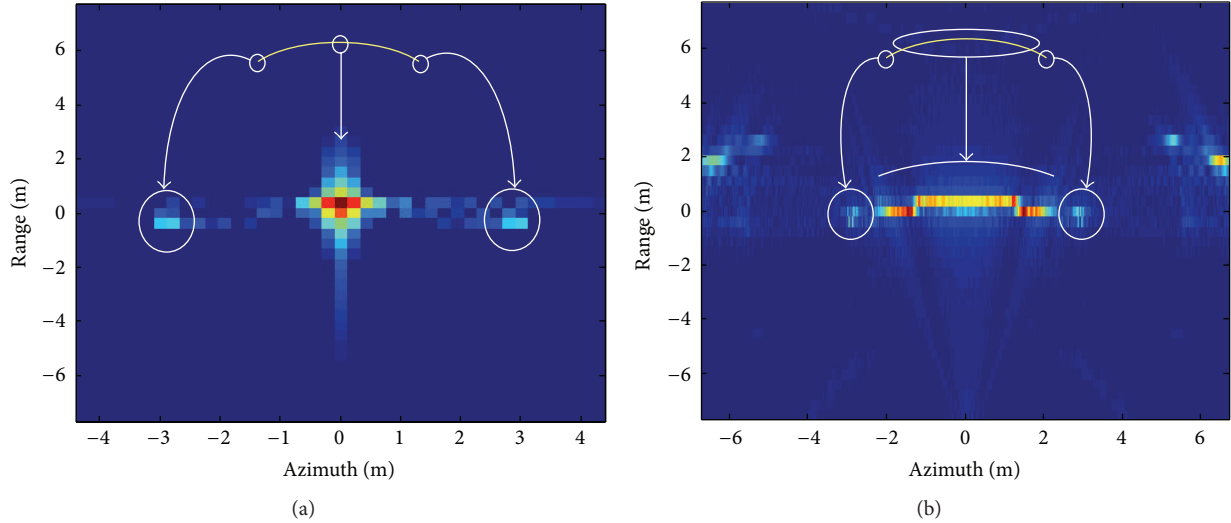


FIGURE 8: 2D images of the PRA in a turntable, by CBP, using GRECO data. (a) $\theta^l \in [88^\circ, 92^\circ]$; (b) $\theta^l \in [0^\circ, 180^\circ]$.

TABLE 1: SAR and RPRA's parameters.

Bandwidth	400 MHz	Reference range X_c	10000 m
Central frequency f_c	10 GHz	PRA's focus parameter P	9 m
Slant angle θ_c	0	Diameter of the PRA's aperture D	6 m
CPI	8.7 s	PRA rotating frequency f_m	0.1~0.3 Hz
Airplane velocity V_a	200 m/s	ϕ_c	$\pi/4$
Angular extent	10°	γ_0	π

90° contains all the components throughout between the maximal, and minimal Doppler, leading to a vertical line in Figure 7(a). In addition, it is clear that, though there are several components in Figure 7(a), the slant line has the strongest intensity. Thereby it is reasonable for our scattering center models to contain only the specular scattering component.

4.1.4. 2D Image Characteristics. The 2D images of the PRA are formulated by the convolution back-projection (CBP) algorithm, displayed in Figure 8 for narrow and wide angles, respectively. From Figure 8(a), three scattering centers are present, with the middle bright one at the PRA's bottom center and the other darker two at its edge. This is in accordance with Figure 7(a). However, in the wide-angle case (Figure 8(b)), the PRA exhibits a bowl-shaped signature, and the bowl's size is equal to the true size of the PRA. The two points corresponding to the PRA's edge are still visible at the bowl's edge. The bowl shape is due to the migration of the specular point within such a wide angle. From Figure 6 it is well known at different aspects, that the specular point is located at different positions, and therefore they cannot be coherently integrated into a single strong point in the resulting image. Instead, the energy is spread over the bowl shape. Moreover, there is an other weak energy distributed at the left and right edges of Figure 8(b). This energy results from other types of scattering from the PRA, for example, creeping wave. Again, the PRA, when its back side faces radar, will assume similar

signatures to Figure 8, but the bowl's direction is the opposite. To summarize, 2D images provide a very good representation of PRA's structure, and the specular scattering contributes to PRA's dominant energy.

4.2. Rotating PRA. When a PRA is rotating in the SAR geometry, its radar characteristics will considerably vary due to the rotation. In what follows, we proceed with the analysis of an RPRA based on the MMSC model since the real SAR data of an RPRA are unavailable for the moment. Simulation parameters are shown in Table 1.

4.2.1. RCS, HRRP, and TFD Characteristics. Suppose $f_m = 0.3$ Hz, which is also a typical value for real RPRA's. In Figure 9(a), as is expected, the RPRA's RCS sequence takes on periodicity due to the rotation and the period is about 3.3 s, in good agreement with the true value $1/f_m$. Its TFD also shows the periodicity (Figure 9(b)). In any segment, the slantline-shaped TFD represents an LFM signal, or a fraction of a SFM signal, as expected by (23). In effect, a sine wave is impossible to be displayed in the TF image owing to broadside flash. Note also that the slant lines may be blurry due to short time and the TF-resolution limit. This kind of periodicity is also characteristic of the HRRP sequence in Figure 9(c). However, a curve similar to the left one in Figure 6(a) is not present. This is because that the back of the PRA has no chance to be illuminated by SAR for the parameters in Table 1.

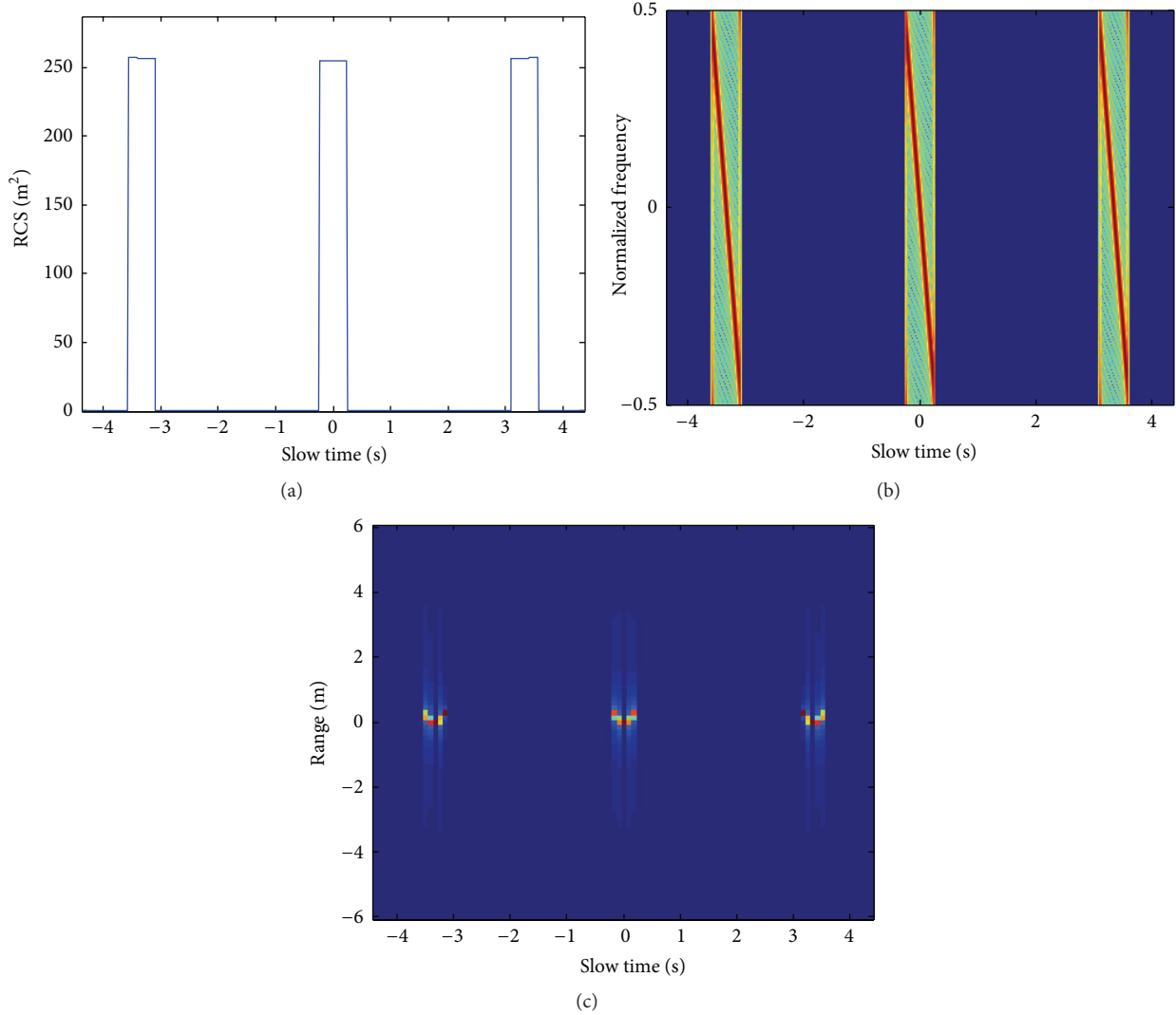


FIGURE 9: RPRAs characteristics. (a) RCS sequence; (b) TFD; (c) HRRP sequence.

4.2.2. SAR Image Characteristics. The presence of rotation changes the Doppler history of the PRA's returns, thus bringing out new signatures distinct from of the stationary PRA. When the PRA rotates at a small frequency, it takes on blurred lines in the SAR image (Figure 10(a)). When it rotates more rapidly, the image takes on a bowknot shape with several intersectant lines (Figure 10(b)). The faster the PRA rotates, the more lines there are. When $f_m = 2$ Hz, we cannot distinguish these lines from each other. As a result, the image exhibits another kind of bowknots as shown in Figure 10(c). We also find that the angular extent of the bowknots is approximately equal to that of SAR, that is, 10° , in Figures 10(b) and 10(c), after the units of the two axes are equalized. These interesting signatures can provide new features for target recognition, notwithstanding that the underlying reason is enigmatic and remains to be explored in the future.

4.2.3. Effective Illumination Condition. In Figure 9(c), we have found that the back of the PRA is not illuminated

by SAR. In effect, even if it is illuminated, there is not backscattering strong enough if the incident angle is too large. In such a case, the illumination is not effective. Then, what is the condition of effective illumination? Clearly, $|\eta_\theta| \leq \Delta$ or $\pi - \Delta \leq |\eta_\theta| \leq \pi + \Delta$ needs and only needs to be satisfied where Δ is half the aspect supporting interval (e.g., 18°). Substituting it into (15) and after some simple manipulations, we find that the sufficient and necessary conditions for effective front or back illumination are, respectively,

$$|\beta_0 - \phi_c| \leq \Delta \quad (24)$$

$$\beta_0 + \phi_c \geq \pi - \Delta. \quad (25)$$

If (24) and (25) are combined, we readily obtain a necessary condition of both sides being illuminated

$$\Delta \geq \frac{\pi}{3}. \quad (26)$$

However, in general, $\Delta < \pi/4$ for PRAs. Therefore, it is impossible for both sides of a PRA to be effectively illuminated.

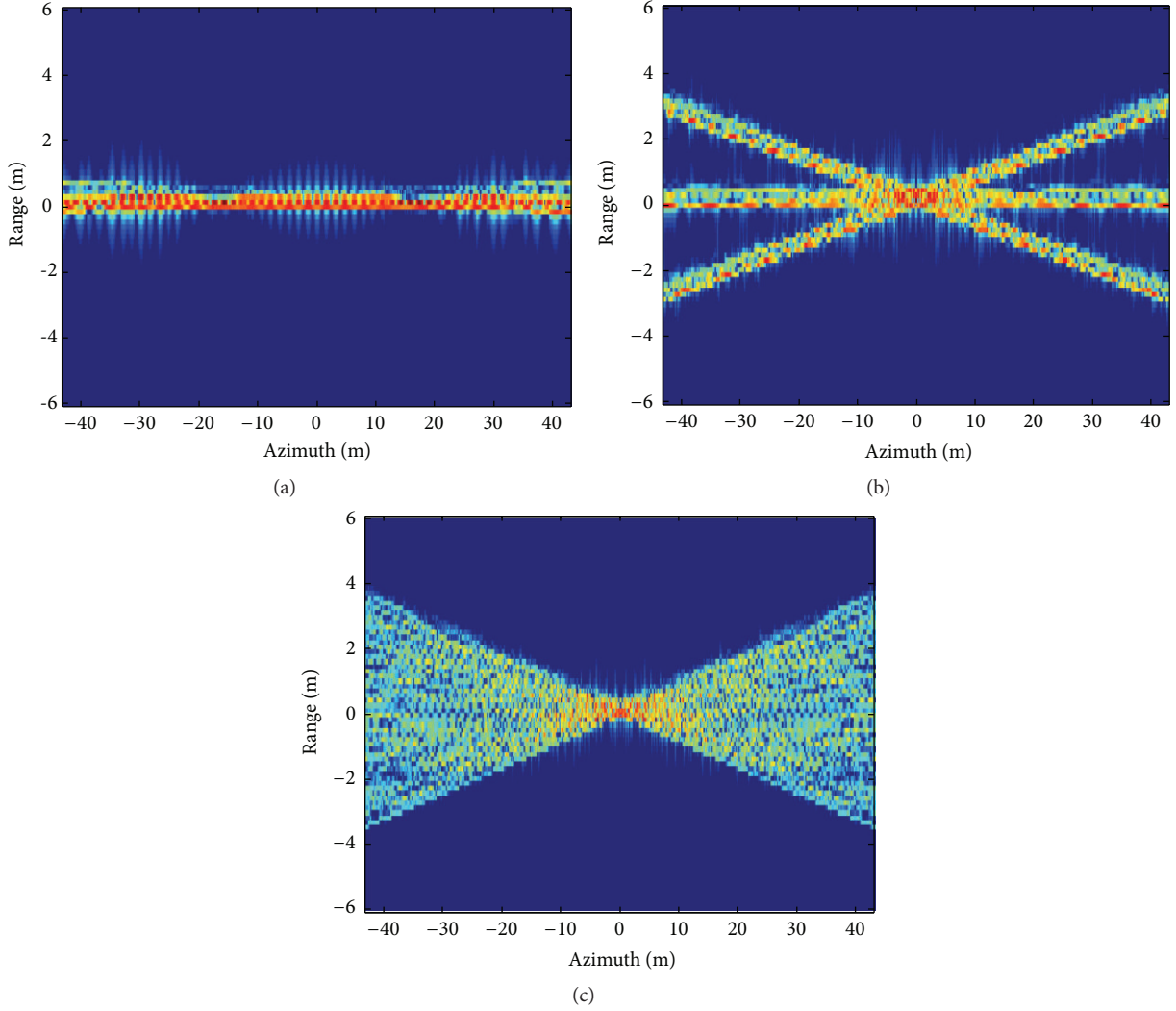


FIGURE 10: SAR images of an RPRA, formulated by CBP, when (a) $f_m = 0.2$ Hz, (b) $f_m = 0.3$ Hz, and (c) $f_m = 2$ Hz.

The analyses made earlier have fully supported our scattering center models and provided deep insight into PRA's characteristics. These characteristics can be used as feature for SAR image interpretation and target detection or recognition. They can also be used for parameter's coarse estimation as shown in Section 5.

5. MLE of Parameters in the MMSC Model

Once the MMSC model is built, the estimation for parameters in this model can be performed from measured data, and there are various ways available, for example, MLE [14], the regularization method [17], and the sparse representation method [15], though they were not intended for our problem herein. Actually, from a unified viewpoint, all of them belong to optimization algorithms for solving inverse problems. In this paper, we develop an MLE method for the MMSC model, which is equivalent to the nonlinear least squares estimation [14]. Note that only one PRA target is assumed for simplicity, but it can be generalized for multiple targets by introducing RELAX or CLEAN techniques, thereby circumventing the estimation of the model order.

5.1. Maximal Likelihood Estimator. In (20), $s(\theta)$ has been parameterized in basis functions. For notational expediency, (20) can be further vectorized as

$$\mathbf{g} = \Phi(\vartheta) \mathbf{b} + \mathbf{v}, \quad (27)$$

where \mathbf{g} is the measured echo vector, \mathbf{v} is the noise vector, $\vartheta \stackrel{\text{def}}{=} (x, y, f_m, \gamma_0, \phi_c, P)$ is unknown, $\mathbf{b} \stackrel{\text{def}}{=} [b(0), \dots, b(I)]^T$ is unknown, and

$$e_{K\theta} \stackrel{\text{def}}{=} \exp \left[-jK \left(x \cos \theta + y \sin \theta + \frac{P \sin^2 \eta_\theta}{2 \cos \eta_\theta} \right) \right],$$

$$\Phi \stackrel{\text{def}}{=} \begin{bmatrix} e_{K_1 \theta_1} & 0 \\ \vdots & \vdots \\ 0 & e_{K_1 \theta_M} \\ \vdots & \vdots \\ e_{K_N \theta_1} & 0 \\ \vdots & \vdots \\ 0 & e_{K_N \theta_M} \end{bmatrix} \begin{bmatrix} \lambda_0(\theta_1) & \dots & \lambda_O(\theta_1) \\ \vdots & \vdots & \vdots \\ \lambda_0(\theta_M) & \dots & \lambda_O(\theta_M) \end{bmatrix}, \quad (28)$$

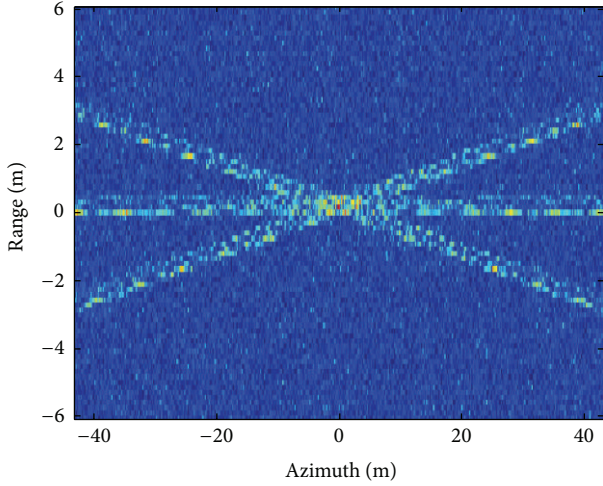


FIGURE 11: PRA's image under SNR = -3 dB, by CBP.

TABLE 2: Final estimated results.

	x (m)	y (m)	f_m (Hz)
True value	0	0	0.3
Coarse estimate	0.12	-0.10	0.32
Estimate	0.0013	0.0108	0.2995
	γ_0 (rad)	ϕ_c (rad)	P (m)
True value	$\pi/2$	$\pi/4$	9
Coarse estimate	$0 : \pi/4 : 7\pi/4$	0.68	10
Estimate	1.5715	0.7841	9.0179

where the derivation of Φ is not difficult but tedious, therefore not given here.

We try to solve for ϑ and \mathbf{b} from (27). Clearly, this is an inverse problem. Using MLE, we at first obtain ϑ 's estimate

$$\hat{\vartheta} = \arg \min_{\vartheta} \left\| \mathbf{g} - \Phi(\Phi^H \Phi)^{-1} \Phi^H \mathbf{g} \right\|_2^2. \quad (29)$$

Afterwards, by substituting $\hat{\vartheta}$ into Φ , we have the least-squares estimate of \mathbf{b}

$$\hat{\mathbf{b}} = (\Phi^H \Phi)^{-1} \Phi^H \mathbf{g}. \quad (30)$$

Finally, by use of $\hat{\mathbf{b}}$, the reflectivity function can be found as

$$\hat{s}(\theta) = \sum_{i=0}^I \hat{b}(i) \lambda_i(\theta). \quad (31)$$

5.2. Determination of the Initial Value of ϑ . Equation (29) is an optimization function, and it is easy to cause local minima. One may either try to find efficient global optimization algorithms, which have not been found to date, or to determine initial values with higher precision. The latter line of thought entails a thorough understanding of the target characteristics, which, fortunately, has been analyzed in detail in Section 4. Therefore, we give the coarse estimation method for ϑ .

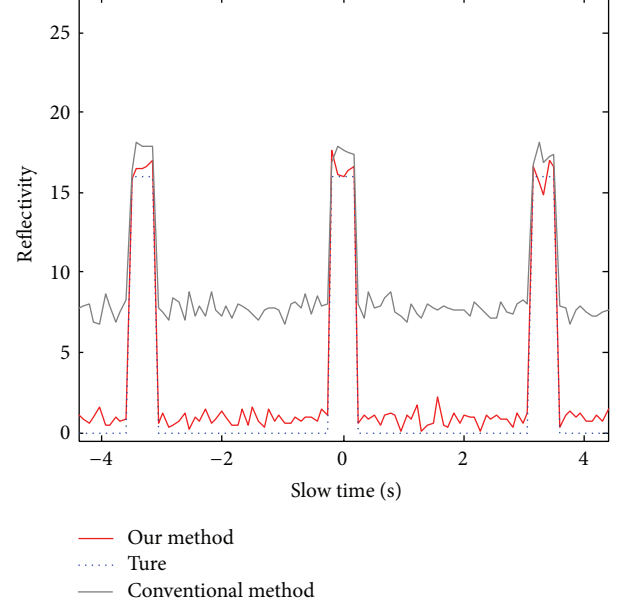


FIGURE 12: Recovered reflectivity with respect to slow time.

(x, y) : From Figure 10, the center of an RPRAs blurred image indicates the position of the scattering center. So, (x, y) can be estimated, respectively, by

$$x = \frac{\iint x' \cdot I(x', y') dx' dy'}{\iint I(x', y') dx' dy'} \quad (32)$$

$$y = \frac{\iint y' \cdot I(x', y') dx' dy'}{\iint I(x', y') dx' dy'}$$

where $I(x', y')$ is the gray-level image.

f_m : It can be estimated by finding the rotating period from an HRRP sequence (see Figure 10) and then taking its reciprocal.

ϕ_c and P : We have not found any effective method for estimating them separately. However, from (23), after obtaining f_m and ω , we can find $P \sin \phi_c$ as a whole by estimating the Doppler slope. P can be set as a mean value from a priori knowledge, at the order of meters. ϕ_c can then be determined accordingly.

γ_0 : It is hard to be estimated. We just take a set of values of it as the coarse estimates; so, the objective function will be optimized with different initial values, resulting in multiple local minima, the minimum of which is finally taken as the global minimum. We find through simulation that the optimization is not sensitive to the choice of γ_0 's initial values.

6. Simulation Results

In this section, we present some estimation results by the proposed method in Section 5. $f_m = 0.3$ Hz, $\alpha_0 = \pi$, $\beta_0 = \pi/4$, the signal-to-noise ratio (SNR) is -3 dB, and other parameters are shown in Table 1. The Dirac function is chosen as the basis function. The optimization algorithm we use is

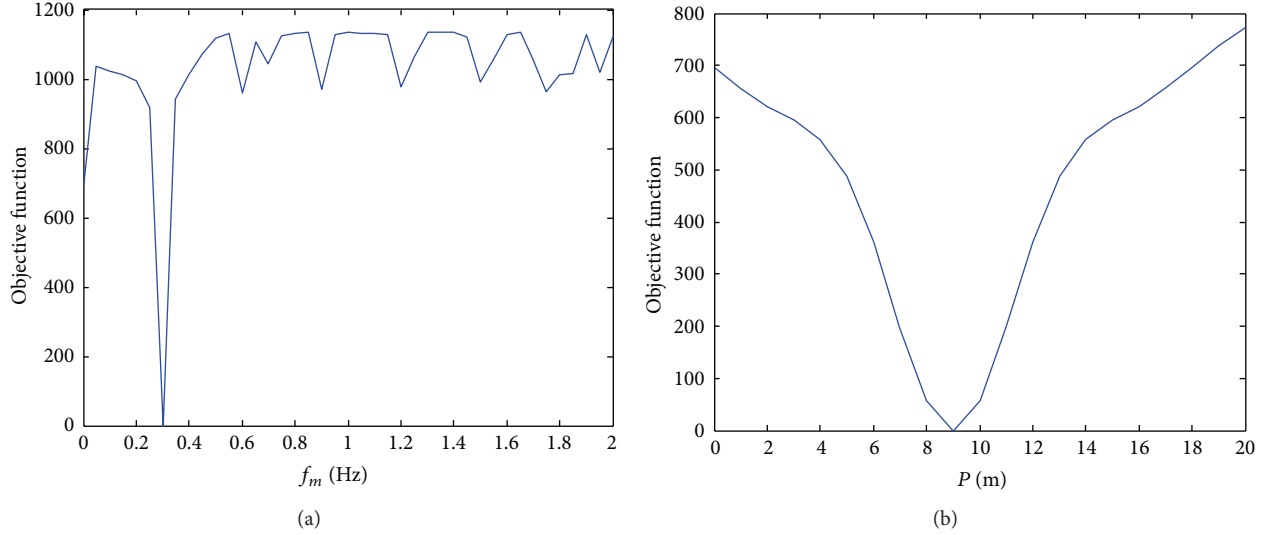


FIGURE 13: Objective function slices along (a) the rotating frequency and (b) the focus parameter.

sequential quadratic programming (SQP), which has proven successful in solving our problem.

The RPRA's SAR image is shown in Figure 11, which is similar to Figure 10(b) except for being contaminated by noise. The coarse estimates for initial values are shown in Table 2. Using the estimator proposed, we finally obtain the estimates of the PRA's parameters, which, obviously, agree well with their true values. To our best knowledge, there is not any published work on extracting the overall information of an RPRA in SAR and so, overall comparison cannot be performed. Once the six parameters are obtained, the coefficients of the basis functions can be found and therefore the reflectivity function $\hat{s}(\theta)$ results (Figure 12). Note that θ is proportional to slow time by (14). Figure 12 indicates that the reflectivity is successfully recovered, and the periodicity implies the broadside flash signature which can be favorably used in target recognition. Also, the square of the reflectivity is accordant with the RCS sequence in Figure 9(a). Although the conventional method also gives estimates the reflectivity by evaluating the mean of the returns' amplitude sequence, it has poorer agreement with the reality, and more problematically, this method needs finding range cells containing micromotion targets at first, which is in itself a tough job but is now circumvented by our approach through building the MMSC model in the phase domain.

Again, we can see through the slices of the objective function shown by Figure 13 that improper initial values of f_m will lead to local minima, but the coarsely estimating precision for it is able to guarantee the convexity of the objective function within a necessary interval. It is similar to other parameters except P which tolerates larger error of initial estimates (Figure 13(b)).

7. Conclusion

As a special type of targets in SAR, RPRA's have a few interesting characteristics which can be exploited for understanding SAR images. In this paper, we have at first obtained the

closed-form and numeric solutions for PRA's backscattering, via GO, PO, and GRECO, respectively. From its GO solution, a new scattering center model has been proposed for characterizing the migration of the specular point on the PRA, and then the rotating parameters have been incorporated into the model to obtain a hybrid model or MMSC model in SAR geometry. Using the models and the scattering data calculated, we have in detailed investigated the radar characteristics of a PRA and RPRA alike. Their RCS, HRRP sequences, and TFD all show that a PRA exhibits broadside flash as well as periodicity and contains a single migratory scattering center for limited aspects, whose energy is dominant. The bowl-shaped image of a stationary PRA reflects its structure perfectly, while the SAR image of an RPRA assumes distinct signatures. All these characteristics have confirmed the MMSC model, and they also provide novel information on targets' structures and motions. Then, using this information for coarse estimation of PRA's parameters, we have developed a maximal likelihood estimator to solve the MMSC model. Simulation results at -3 dB of SNR demonstrate the estimator's performance. The parameters estimated, for example, the rotating frequency and focus parameter, can faithfully record the information on PRA's motion and size and therefore can be used advantageously as features for target recognition. However, we have concentrated only on a PRA in a homogeneous scenario which can be characterized by white Gaussian noise and lacked consideration of clutters stronger and more complex. Additionally, selection of basis functions has not been discussed, either. Notwithstanding its limitation, this study provides a basis for interpretation of SAR images containing PRAs, and the idea of hybrid modeling is also instrumental for other fields such as SAR/GMTI.

Acknowledgment

The authors acknowledge the support from Provincial Science Foundation for Distinguished Young Scholars in Hunan

(no. 11JJ1010) and National Science Fund of China (no. 61171133, no. 61101182, and no. 61025006).

References

- [1] W. J. Miceli and L. A. Gross, "Test results from the AN/APY-6 SAR/GMTI surveillance, tracking and targeting radar," in *Proceedings of the IEEE Radar Conference*, pp. 13–17, Atlanta, Ga, USA, May 2001.
- [2] X. Li, B. Deng, Y. Qin, H. Wang, and Y. Li, "The influence of target micromotion on SAR and GMTI," *IEEE Transactions on Geoscience and Remote Sensing*, vol. 49, no. 7, pp. 2738–2751, 2011.
- [3] B. Deng, G. Wu, Y. Qin, H. Wang, and X. Li, "SAR/MMTI: an extension to conventional SAR/GMTI and a combination of SAR and micromotion techniques," in *Proceedings of the IET International Radar Conference*, Guilin, China, April 2009.
- [4] S. D. Silverstein and C. E. Hawkins, "Synthetic aperture radar image signatures of rotating objects," in *Proceedings of the Conference Record of the Thirty-Eighth Asilomar Conference on Signals, Systems and Computers*, pp. 1663–1667, November 2004.
- [5] T. Thayaparan, S. Abrol, and S. Qian, "Micro-doppler analysis of rotating target in SAR," Tech. Rep. TM-2005, DRDC, Ottawa, Canada, 2005.
- [6] T. Thayaparan, K. Suresh, S. Qian, K. Venkataramaniah, S. SivaSankaraSai, and K. S. Sridharan, "Micro-Doppler analysis of a rotating target in synthetic aperture radar," *IET Signal Processing*, vol. 4, no. 3, pp. 245–255, 2010.
- [7] M. Rüegg, E. Meier, and D. Nüesch, "Vibration and rotation in millimeter-wave SAR," *IEEE Transactions on Geoscience and Remote Sensing*, vol. 45, no. 2, pp. 293–304, 2007.
- [8] D. C. Jenn, *Radar and Laser Cross Section Engineering*, American Institute of Aeronautics and Astronautics, 2005.
- [9] J. M. Rius, M. Ferrando, and L. Jofre, "High-frequency RCS of complex radar targets in real-time," *IEEE Transactions on Antennas and Propagation*, vol. 41, no. 9, pp. 1308–1319, 1993.
- [10] M. Hurst and R. Mittra, "Scattering center analysis via prony's method," *IEEE Transactions on Antennas and Propagation*, vol. 35, no. 8, pp. 986–988, 1987.
- [11] L. C. Potter, D. M. Chiang, R. Carriere, and M. J. Gerry, "GTD-based parametric model for radar scattering," *IEEE Transactions on Antennas and Propagation*, vol. 43, no. 10, pp. 1058–1067, 1995.
- [12] L. C. Potter and R. L. Moses, "Attributed scattering centers for SAR ATR," *IEEE Transactions on Image Processing*, vol. 6, no. 1, pp. 79–91, 1997.
- [13] M. J. Gerry, L. C. Potter, I. J. Gupta, and A. D. Van Merwe, "A parametric model for synthetic aperture radar measurements," *IEEE Transactions on Antennas and Propagation*, vol. 47, no. 7, pp. 1179–1188, 1999.
- [14] R. Jonsson, A. Genell, D. Lösaus, and F. Dicander, "Scattering center parameter estimation using a polynomial model for the amplitude aspect dependence," in *Proceedings of the Algorithms for Synthetic Aperture Radar Imagery IX*, pp. 46–57, Orlando, Fla, USA, April 2002.
- [15] K. R. Varshney, M. Çetin, J. W. Fisher, and A. S. Willsky, "Sparse representation in structured dictionaries with application to synthetic aperture radar," *IEEE Transactions on Signal Processing*, vol. 56, no. 8, pp. 3548–3561, 2008.
- [16] R. D. Chaney, A. S. Willsky, and L. M. Novak, "Coherent aspect-dependent SAR image formation," in *Proceedings of the SPIE Algorithms for Synthetic Aperture Radar Imagery*, vol. 2230, pp. 256–274, 1994.
- [17] B. D. Rigling, "Use of nonquadratic regularization in fourier imaging," *IEEE Transactions on Aerospace and Electronic Systems*, vol. 45, no. 1, pp. 250–265, 2009.

Research Article

Junction Point Detection Algorithm for SAR Image

Jun Zhang, Tingjin Luo, Gui Gao, and Lin Lian

Department of Information System and Management, National University of Defense Technology, Changsha 410073, China

Correspondence should be addressed to Jun Zhang; aiya0215@263.net

Received 19 December 2012; Revised 4 February 2013; Accepted 21 February 2013

Academic Editor: Deren Li

Copyright © 2013 Jun Zhang et al. This is an open access article distributed under the Creative Commons Attribution License, which permits unrestricted use, distribution, and reproduction in any medium, provided the original work is properly cited.

In this paper, we propose a novel junction point detector based on an azimuth consensus for remote sensing images. To eliminate the impact of noise and some noncorrelated edges of SAR image, an azimuth consensus constraint is developed. In addition to detecting the locations of junctions at the subpixel level, this operator recognizes their structures as well. A new formula that includes a minimization criterion for the total weighted distance is proposed to compute the locations of junction points accurately. Compared with other well-known detectors, including Forstner, JUDOCA, and CPDA, the experimental results indicate that our operator outperforms them both in location accuracy of junction points and in angle accuracy of branch edges. Moreover, our method possesses satisfying robustness to the impact of noise and changes of the SAR images. Our operator can be potentially used to solve a number of problems in computer vision, such as SAR image registration, wide-baseline matching, and UAV navigation system.

1. Introduction

Synthetic Aperture Radar is able to provide high resolution ground data or images even under heavy weather conditions, and it is widely used in areas of military reconnoiter, topographical mapping, resource exploration and vegetation analysis, and so on. Therefore, it is very important for understanding and analyzing SAR images. Nevertheless, due to the impact of image-forming mechanism and wide dynamic range, SAR images consist of massive coherent macula noises and make the accurate extractions of corners very difficult at the same time, they also hinder the development of SAR image application systems. Therefore, it is crucial to detect and extract the identifiable, invariant, and information-intensive features for SAR image application systems.

Corner feature detection in images is a fundamental problem in computer vision and has been successfully used in visual tracking, panoramic image stitching, and motion estimation [1–3] among other applications. In these systems, detecting corner features is the first critical step toward many more complicated processes. Over the past decades, there

have been many corner and junction detectors proposed in published literatures. These detectors compete with each other in terms of localization accuracy, speed, and information they provide. Common corner detection algorithms can be divided into three categories: (1) algorithms based on gray level statistics, which detect the pattern of the center point by calculating the numbers of similar approximation (or different) points between the local neighborhood (or boundary) and the center of the gray scale, such as SUSAN [4] and FAST [5]; (2) algorithms based on the second-order structure tensor, which builds the autocorrelation matrix of the corner around its local neighborhood region and determines whether the point is the corner by eigenvalue analysis of the matrix, such as the typical algorithms of Förstner and Gülch [6], Harris and Stephens [7], and KLT [8] and some other methods based on improved structure tensors [9, 10]; (3) algorithms based on curvature analysis, that is, the detection of the large curvature points on the edge at the corners, such as CSS [11], ECSS [12], and CPDA [13].

Although corner detectors have been found to perform very well in many areas, a number of inherent weaknesses

have been exposed in practical application. Most often, the criterion on which the detection is based is neglected (e.g., local structural information). In particular for SAR images, because they include massive coherent noises, the traditional corner detectors will extract pseudopoints and affect the efficiency and results of SAR image matching and application. By contrast, junction detectors are concerned with both the locations and structures. Due to multibranches topology stability, during matching detectors can effectively filter out the external interference by using richer information and thereby ensure better matching results.

Although McDermott [14] observes that junction point detection is very difficult, even a well-developed human visual system is not an exception. However, due to the above-mentioned advantages of junction detectors, there are many junction detectors proposed in published literatures. The approach described in [15] detects junctions using a piecewise constant function that partitions a circular template into wedge-shaped regions and introduces a minimum description length principle and dynamic programming algorithm to compute the optimal parameters of a model. Chabat et al. [16] introduce a junction detector based on the analysis of local anisotropy and identifying corners as points with a strong gradient but not oriented in a single dominant direction. Cazorla et al. [17, 18] propose two Bayesian methods for junction classification that evolved from the Kona method: a region-based method and an edge-based method. Bergevin and Bubel [19] propose a junction characterization and a validation method where junction branches of volumetric objects are extracted at points of interest in a 2D image using a topologically constrained grouping process and a binary split tree. Perwass [20] proposes a method to extract the intersections between the conic curves and to determine all possible linear support domains, then to determine the edges from the image gradients and to determine the type of extracted junction points by the local geometry structural analysis of edges.

Recently, Elias and Laganière [21] propose Junction Detection Operator based on Circumferential Anchors (JUDOCA), which represents the latest research result on junction point detection algorithms. JUDOCA has been successfully used to solve many problems, such as 3-D reconstruction, camera parameter enhancing, and indoor and obstacle localization [22–24]. However, JUDOCA also has some drawbacks; for example, it only computes integer-valued junction points and cannot achieve subpixel position precision and uses the path directions instead of the dip angles of junction branches, which brings extra errors, and its algorithm is sensitive to fractured edges.

In this paper, we present a novel branch-point detection algorithm based on azimuth consensus. At the same time, compared with previous methods, our proposed algorithm can extract junction points at the level of sub-pixel accuracy and low contrast change and build a set of characteristic descriptions for recognition. In addition, experimental results indicate that our proposed algorithm provides improved positioning accuracy for junction points and angle accuracy for branch edges, and it has improved the robustness to noises especially for SAR images.

The contribution of this paper is summarized as follows. Section 2 provides the definition of the azimuth consensus and groups the edge points that satisfy the azimuth consensus constraints. Section 3 describes the accurate calculation of junction point locations and the characteristic description for a junction point and its branch edge structure. Experimental results are present in Section 4, where proposed algorithm is compared with previous algorithms with respect to accuracy, contrast change, noise, and SAR images. Section 5 concludes the paper and discusses future work.

2. Junction Point Detection and Branch Edge Grouping

2.1. Subpixel Location of Edge Points. For a given SAR image $f(\mathbf{x})$, where $\mathbf{x} = [x, y]^T$ is the coordinate vector, which is corresponding to a pixel in the image, the gradient of $f(\mathbf{x})$ in the location \mathbf{x} is defined as

$$\vec{f}(\mathbf{x}) = [f_x(\mathbf{x}), f_y(\mathbf{x})]^T, \quad (1)$$

where $f_x(\mathbf{x})$ and $f_y(\mathbf{x})$ are the first-order partial derivatives of $f(\mathbf{x})$ with respect to the x - and y -directions, respectively.

The gradient magnitude and orientation in \mathbf{x} are given by

$$\begin{aligned} \|\vec{f}(\mathbf{x})\| &= \sqrt{f_x^2(\mathbf{x}) + f_y^2(\mathbf{x})}, \\ o(\mathbf{x}) &= \tan^{-1} \left(\frac{f_y(\mathbf{x})}{f_x(\mathbf{x})} \right) // 180^\circ, \end{aligned} \quad (2)$$

where $//$ is the modular operation which limits the range of gradient orientation to $[0^\circ, 180^\circ)$, and the vertical direction of gradient orientation is defined as $o^\perp(\mathbf{x}) = (o(\mathbf{x}) + 90^\circ) // 180^\circ$.

To find the edge points of an image, our method utilizes non-maxima suppression [25] to determine the gradient magnitude image in the direction of the gradient orientation (see Figure 1(a)). Let \mathbf{p}_1 and \mathbf{p}_2 be two solutions of the following equation (6) in the local neighborhood circle region that has \mathbf{x} as its center and has a radius of r :

$$\begin{aligned} \vec{f}(\mathbf{x})^T (\mathbf{p} - \mathbf{x}) &= 0, \\ \|\mathbf{p} - \mathbf{x}\| &= r. \end{aligned} \quad (3)$$

Because it is possible that coordinate values of \mathbf{p}_1 and \mathbf{p}_2 are nonintegers, their gradient magnitude values of $v(\mathbf{p}_1)$ and $v(\mathbf{p}_2)$ are calculated by the bilinear interpolation method. Let $\|\vec{f}(\mathbf{x})\|_{\text{NMS}}$ be the gradient magnitude image after performing non-maximal suppression. If $\|\vec{f}(\mathbf{x})\| < \max(v(\mathbf{p}_1), v(\mathbf{p}_2))$, then $\|\vec{f}(\mathbf{x})\|_{\text{NMS}} = 0$. If $\|\vec{f}(\mathbf{x})\| \geq \max(v(\mathbf{p}_1), v(\mathbf{p}_2))$, then $\|\vec{f}(\mathbf{x})\|_{\text{NMS}} = \|\vec{f}(\mathbf{x})\|$. In the direction $o(\mathbf{x})$, using the points $(\mathbf{x}, \|\vec{f}(\mathbf{x})\|)$, $(\mathbf{p}_1, v(\mathbf{p}_1))$ and $(\mathbf{p}_2, v(\mathbf{p}_2))$ fitting a parabolic curve, \mathbf{x}' —the real-valued sub-pixel location of \mathbf{x} —is the peak

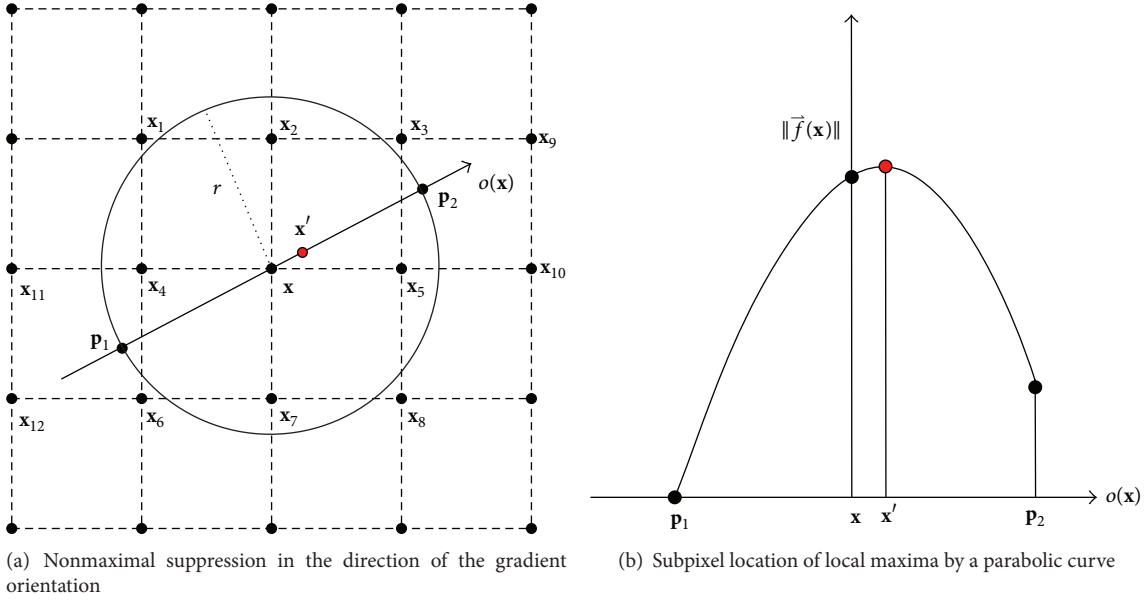


FIGURE 1: Non-maximal suppression and sub-pixel location of an edge point.

of the constructed parabolic curve (as shown in Figure 1(b)). The formula of the sub-pixel location \mathbf{x}' is

$$\mathbf{x}' = \mathbf{x} + r \cdot \frac{v(\mathbf{p}_1) - v(\mathbf{p}_2)}{2(v(\mathbf{p}_1) + v(\mathbf{p}_2) - 2\|\vec{f}'(\mathbf{x})\|)} \begin{bmatrix} \cos(o(\mathbf{x})) \\ -\sin(o(\mathbf{x})) \end{bmatrix}. \quad (4)$$

2.2. Azimuth Consensus. Let Ω be the local circular region for which $\mathbf{x}_0 = [x_0, y_0]^T$ is its center and its radius is λ in the image $\|\vec{f}(\mathbf{x})\|_{\text{NMS}}$ and define N that is an assembly consisting of nonzero intensity value, that is,

$$N = \left\{ \mathbf{x} \mid \|\vec{f}(\mathbf{x})\|_{\text{NMS}} > 0, \mathbf{x} \in \Omega, \mathbf{x} \neq \mathbf{x}_0 \right\}. \quad (5)$$

The set N' is defined as the sub-pixel position of all points in N . For each point, let $\mathbf{x} = [x, y]^T \in N$, and then compute the angle $s_{x_0}(\mathbf{x})$ of its corresponding center point \mathbf{x}_0 , that is,

$$s_{x_0}(\mathbf{x}) = \begin{cases} \tan^{-1}\left(\frac{y' - y_0}{x' - x_0}\right), & x' > x_0, y' > y_0 \\ \tan^{-1}\left(\frac{y' - y_0}{x' - x_0}\right) + 360^\circ, & x' > x_0, y' < y_0 \\ \tan^{-1}\left(\frac{y' - y_0}{x' - x_0}\right) + 180^\circ, & x' < x_0 \\ 90^\circ, & x' = x_0, y' > y_0 \\ 270^\circ, & x' = x_0, y' < y_0 \end{cases} \quad (6)$$

where x' and y' are the coordinates of sub-pixel position $\mathbf{x}' = [x', y']^T (\mathbf{x}' \in N')$. $\Delta_{x_0}(\mathbf{x})$ is defined as the angle between $s_{x_0}(\mathbf{x})$ and $o^\perp(\mathbf{x})$:

$$\Delta_{x_0}(\mathbf{x}) = \sin^{-1}\left(\left|\sin(s_{x_0}(\mathbf{x}) - o^\perp(\mathbf{x}))\right|\right). \quad (7)$$

Formula (7) ensures that the range of the angle $\Delta_{x_0}(\mathbf{x})$ belongs to $[0^\circ, 90^\circ]$. If a certain point $\mathbf{x} = [x, y]^T$, which belongs to the set N defined by the formula (9), satisfies the formula (12) condition, and then \mathbf{x} has azimuth consensus for \mathbf{x}_0 (ε is a choosing angle threshold):

$$\Delta_{x_0}(\mathbf{x}) < \varepsilon. \quad (8)$$

From the geometrical presentation of azimuth consensus, we find that if point \mathbf{x} is located in one of the straight lines that cross over the center \mathbf{x}_0 , then $\Delta_{x_0}(\mathbf{x}) = 0$; otherwise $\Delta_{x_0}(\mathbf{x}) > 0$. Azimuth consensus consists of the relative position and the edge orientation information, so it is able to filter out the distortion of noise and unrelated edge points effectively.

2.3. Junction Point Classification and Branch Edge Grouping.

The set $M = \{\mathbf{x} \mid \Delta_{x_0}(\mathbf{x}) < \varepsilon, \mathbf{x} \in N\}$ consists of all points in N that satisfy the azimuth consensus constraints, and the set M' is a set of sub-pixel locations corresponding to M . From (6), the range of angles $s_{x_0}(\mathbf{x})$, which is relative to the center \mathbf{x}_0 , of the points in M belongs to $[0^\circ, 360^\circ)$. The points in M are classified based on the distribution of angles to determine all the junction branches of \mathbf{x}_0 . Simultaneously, based on the classified results of the junction point classification algorithm, which is shown in Algorithm 1, the algorithm decides whether \mathbf{x}_0 is a junction point or not.

In Algorithm 1, to eliminate the wrap-around effect of the angles and ensure that the junction points corresponding to the angles close to 0° and 360° are divided into the same

Input: $M = \{x_1, x_2, \dots, x_m\}$, the dip angle set $\{\varphi_1, \varphi_2, \dots, \varphi_m\}$ corresponding to M , and the threshold angle τ

Output: The classification result set E of branch edges' points

Initialize: Set the set $E = \text{NULL}$

Main steps of algorithm:

- (1) Define a $m \times m$ matrix H and initialize $H = \text{null}$; and then compute all the elements of the matrix according to the equation

$$H(i, j) = \begin{cases} \cos(\phi_i - \phi_j), & \text{if } \cos(\phi_i - \phi_j) \geq \cos(\tau), \\ \text{null}, & \text{otherwise,} \end{cases} \quad 1 \leq i < j \leq m$$
- (2) Calculate the position of the maximal value of H ; assuming the maximum is at (i, j) , set $H(i, j) = \text{null}$, $v_1 = \sin(\varphi_i) + \sin(\varphi_j)$ and $v_2 = \cos(\varphi_i) + \cos(\varphi_j)$, and then, compute the classification center ϕ

$$\phi = \begin{cases} \tan^{-1}\left(\frac{v_1}{v_2}\right), & v_1 > 0, v_2 > 0 \\ \tan^{-1}\left(\frac{v_1}{v_2}\right) + 360^\circ, & v_1 > 0, v_2 < 0 \\ \tan^{-1}\left(\frac{v_1}{v_2}\right) + 180^\circ, & v_2 < 0 \\ 90^\circ, & v_1 > 0, v_2 = 0 \\ 270^\circ, & v_1 < 0, v_2 = 0 \end{cases}$$
- (3) Update v_1, v_2 and ϕ by all angles that satisfy the condition $\cos(\varphi_k - \phi) \geq \cos(\tau)$ ($k = 1, 2, \dots, m$) searched from the set $\{\varphi_1, \varphi_2, \dots, \varphi_m\}$;
- (4) Repeat step (3) until the angle set that satisfies the condition $\cos(\varphi_k - \phi) \geq \cos(\tau)$ never change and place the junction points corresponding to the angle set into E ;
- (5) Repeat steps (2), (3) and (4) until all the elements of H are null, and then return E .

ALGORITHM 1: Junction point classification algorithm.

branch edge, we construct the matrix H by the cosine value of the D value between the two angles. By executing the algorithm in Algorithm 1, all junction edge points E of the current point \mathbf{x}_0 are computed. If \mathbf{x}_0 is a valid junction point, then E must satisfy the following conditions.

- (i) The size of set E , that is, the number of branch edges, is larger than 2.
- (ii) If the size of E is equal to two, the intersection angle must be larger than a fixed threshold to avoid *Colinearity*.
- (iii) The junction and edge points in its local neighborhood area often violate the azimuth consensus constraints. So for every junction edge point, the gradient magnitude of all pixels that are in the Bresenham path [26] between \mathbf{x}_0 and its closest point is nonzero.

Using the above-described detection algorithm, many junction points are often detected in the neighborhood of the actual junction points. A response function as (13) is to determine the actual location of the junction points:

$$c(\mathbf{x}_0) = \sum_i \left(\prod_{\mathbf{x} \in \mathbf{X}_i} \frac{1}{\sqrt{2\pi}\sigma} \exp\left(-\frac{(\Delta_{\mathbf{x}_0}(\mathbf{x}))^2}{2\sigma^2}\right) \cdot \left\| \vec{f}(\mathbf{x}) \right\|_{\text{NMS}} \right), \quad (9)$$

where \mathbf{X}_i is a set composed of the i th branch points and σ is the standard deviation of the Gaussian function.

3. Accurate Junction Point Localization and Characterization

3.1. Accurate Junction Point Localization. To improve the accuracy of the location of junction points, we compute the accurate location of junction points based on the minimal distance criterion [6, 27]. Assume that \mathbf{x}_0 is the integer-valued location of a junction point, that \mathbf{x}_e is its related junction edges' point, and that \mathbf{x}'_e is the sub-pixel location corresponding to \mathbf{x}_e . From (1), the gradient of \mathbf{x}_e is $\vec{f}(\mathbf{x}_e)$, so the equation of line crossover \mathbf{x}'_e is represented by

$$\vec{f}(\mathbf{x}_e)^\top (\mathbf{x} - \mathbf{x}'_e) = 0. \quad (10)$$

The optimal locations of the junction points satisfy the condition that the total weighted distance from all line segments is the shortest, that is,

$$\begin{aligned} \mathbf{x}^* &= \arg \min_{\mathbf{x}} \sum_{\mathbf{x}_e \in E} (D_{\mathbf{x}_e}(\mathbf{x}))^2 \\ &= \arg \min_{\mathbf{x}} \sum_{\mathbf{x}_e \in E} \left| \vec{f}(\mathbf{x}_e)^\top (\mathbf{x} - \mathbf{x}'_e) \right|^2 \\ &= \arg \min_{\mathbf{x}} \sum_{\mathbf{x}_e \in E} (\mathbf{x} - \mathbf{x}'_e)^\top \vec{f}(\mathbf{x}_e) \vec{f}(\mathbf{x}_e)^\top (\mathbf{x} - \mathbf{x}'_e) \\ &= \arg \min_{\mathbf{x}} (\mathbf{x}^\top \mathbf{A} \mathbf{x} - 2\mathbf{x}^\top \mathbf{b} + \mathbf{c}), \end{aligned} \quad (11)$$

where \mathbf{A} , \mathbf{b} , and \mathbf{c} are shown as the following equation (12), respectively:

$$\begin{aligned}\mathbf{A} &= \sum_{\mathbf{x}_e \in E} \vec{f}(\mathbf{x}_e) \vec{f}(\mathbf{x}_e)^T, \\ \mathbf{b} &= \sum_{\mathbf{x}_e \in E} \vec{f}(\mathbf{x}_e) \vec{f}(\mathbf{x}_e)^T \mathbf{x}'_e, \\ \mathbf{c} &= \sum_{\mathbf{x}_e \in E} \mathbf{x}'_e{}^T \vec{f}(\mathbf{x}_e) \vec{f}(\mathbf{x}_e)^T \mathbf{x}'_e.\end{aligned}\quad (12)$$

To minimize formula (11), the optimal location of junction point \mathbf{x}^* is determined by taking the derivative of the right-side function with respect to \mathbf{x} and setting it to zero, yielding $\mathbf{x}^* = \mathbf{A}^{-1}\mathbf{b}$.

3.2. Accurate Branch Edge Orientation and Characterization. After calculating the accurate location of junction point \mathbf{x}^* , update the current center location \mathbf{x}_0 as \mathbf{x}^* , and then, use (6), and compute the dip angles of branch edges points that fulfill the azimuth consensus constraints. With the dip angle set of a certain junction point labeled as $\{\theta_1, \theta_2, \dots, \theta_u\}$, the optimal orientation of this branch edge is described as

$$\theta^* = \arg \max_{\theta} \sum_{i=1}^u \cos(\theta - \theta_i). \quad (13)$$

In (13), $\sum_i \cos(\theta - \theta_i)$ is considered to be the object function for the following reasons: first, the distribution of the edge angles is relatively centered on a small area, so it decreases the search range of the optimal solution for the best angle; second, the cosine function is not susceptible to the sign of the D -value between two angles; third, the cosine function can eliminate the warp-around effect and map the angles close to 0° and 360° into the same value.

Next, calculate the value of $\sum_i \cos(\theta - \theta_i)$ according to every value θ , find the maxima from a series of $\sum_i \cos(\theta - \theta_i)$, and set the maxima to θ^* . After executing the above steps for the branch edges corresponding to all the junction points, the characterization description set for all junction points is created as

$$J = \{J_i \mid J_i = \langle x_i, y_i, \theta_{i1}^*, \theta_{i2}^*, \dots, \theta_{im_i}^* \rangle, i = 1, 2, \dots, n\}, \quad (14)$$

where n is the number of junction points detected, m_i is the number of branch edges corresponding to a junction point, and every element J_i , which is represented as $m_i + 2$ tuple, describes the i th junction point location and branch edges angle information corresponding to the i th junction point.

4. Experimental Results Comparison and Analysis

4.1. Experiment Design and Parameter Setting. The experiments included four parts: comparisons with the Forstner, CPDA, and JUDOCA algorithms in terms of the location accuracy, junction edge orientation accuracy, contrast

TABLE 1: Other experimental parameters setting.

Public parameter	Value
Standard deviation of Gaussian partial derivatives	1.5
Radius of nonmaxima suppression	3
Range of branch edges' angle (JUDOCA and our proposed method)	($30^\circ, 150^\circ$)

changes, and the impact of noise. We chose these algorithms to be compared with our proposed method because of the error control and local optimization mechanism of these algorithms.

Note that in the accuracy experiment, because CPDA is unable to detect all the junction points using the default parameter values, during the edge extraction step, the high and low thresholds are modified to be 0.2 and 0.05, respectively, and the gap connection length is set to two, while the other three algorithms maintain their default values. In addition, in the following experiments, the parameters shown in Table 1 are equal, the other parameters use default values.

4.2. Accuracy of the Location of the Junction Points and the Orientation of the Branch Edges. To quantify the precision of our chosen methods, the ground truth data are required for all the locations of the junction points and the orientations of the branch edges. Therefore, we construct two artificial images for testing (as shown in Figures 2(a) and 2(c), where the digits in the images number represent the junction points in consecutive order).

The First Test Image: quadrate image [28] of size $500 * 500$, including $25 * 51 * 51$ square boxes, as shown in Figure 2(a). These 25 squares have the following characteristics: (1) the four edges of the 1st square (the square in the upper left corner) are parallel with the corresponding horizontal and vertical lines; (2) the n th square is rotated $3.6(n - 1)$ degrees ($n = 1, 2, \dots, 25$) along the 1st square in a clockwise direction; (3) the distance between two centers of adjacent squares is 100 pixels; (4) the center coordinates of the 1st square are (51, 51). The other test image: polygon image [28] of size $256 * 256$, including nine regular polygons as shown in Figure 2(c). These 9 polygons have the following characteristics: (1) the height of all regular polygons is 50 pixels; (2) the adjacent polygons form the public edges and vertices; (3) the coordinates of the junction points labeled as 1, 14, and 24 are (55, 76), (190, 65), and (130, 190), respectively.

Forstner, CPDA, JUDOCA, and our proposed algorithm are used to determine the junction points from the two images described above and compared with the known baseline data; the smaller the error of the result, the higher the detection accuracy. The formula of the location error of the junction points is defined as

$$LE = \sqrt{(x - x_g)^2 + (y - y_g)^2}, \quad (15)$$

where (x, y) and (x_g, y_g) are the location of junction points extracted by the above-mentioned algorithms and the actual location of junction points, respectively.

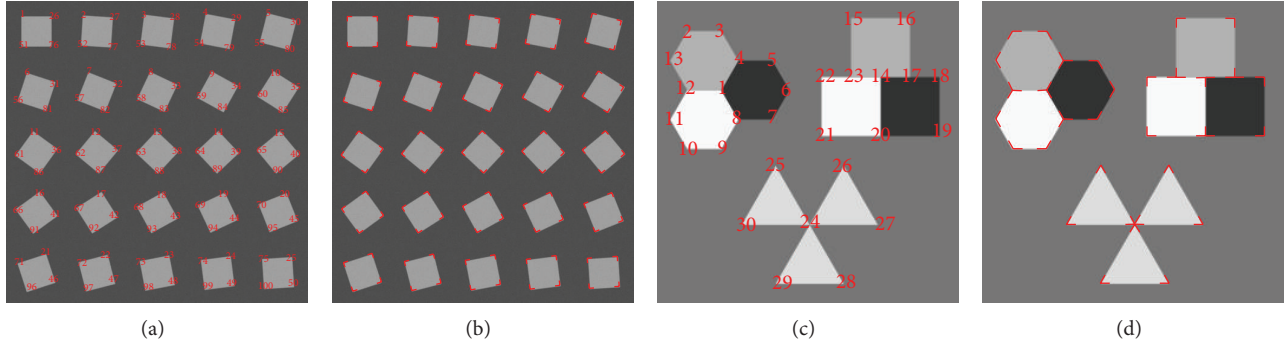


FIGURE 2: The results of junction points and junction branches detection for two images: quadrate image and polygon image. (a) Quadrate image. (b) The junction detection result of our proposed method. (c) Polygon image. (d) The junction detection result of our proposed method.

TABLE 2: The mean error of the junction points' position among the Forstner algorithm, CPDA, JUDOCA, and our proposed method for the quadrate image and polygon image (unit: pixel).

	Forstner	CPDA	JUDOCA	Proposed method
Quadrate	0.2437	1.3270	0.6525	0.2876
Polygon	0.4046	1.4206	1.4222	0.3475

The location error curves for the above two test images determined by using the four detection operators are shown in Figure 3, where the horizontal axes represent the labeled junction points and the vertical axes describe the location error of the junction points determined by formula (15). The mean location error of all the junction points is listed in Table 2. The performance of the Forstner algorithm is the best option; for location accuracy, our proposed method can maintain the error to under-one pixel, just as the Forstner algorithm does, and achieve sub-pixel location accuracy (as shown in Figures 2(b) and 2(d)). The error of CPDA and JUDOCA are both larger than that of the Forstner algorithm and the mean error is greater than one pixel. For some junction points in Figure 2(c), the error of CPDA is even over 3 pixels. This is why our proposed algorithm introduces the same accurate location method to detect junction points and extract their accurate locations, while CPDA and JUDOCA only extract integer-valued junction point locations and cannot achieve sub-pixel location accuracy because the edge orientation information is unused to optimize junction point location.

4.3. Noise Impact. In this section, we test the impact of noise on our proposed algorithm. Random noises are added to the original image, and all operations are applied to this noisy version. Figure 4 from row 1 to row 2 shows the images combined with 1% and 1.2% noise, respectively, and each noisy image includes 26 junction points. When the test image includes the noise, the detection result often contains both the correct junction points and a certain number of pseudopoints (i.e., false alarms).

Assuming the number of the real junction points in the test image is N_g and the number of the detected junction

points is N_t , which includes N_c correct junction points, we can compute the recall rate ($RR = N_c/N_g$) and precision rate ($PR = N_c/N_t$) to examine the operator performance. In the experiment, we chose contrast measure criterion combined with RR and PR [29]:

$$ACU = \frac{RR + PR}{2} \times 100\%. \quad (16)$$

The results of the four algorithms for the two noisy test images are shown in Figure 4 columns from (a) to (d). The results for N_t , N_c , RR, and ACU determined from these test images are listed in Table 3. The experimental results indicate that RR of Forstner operator is the highest. However, the Forstner operator ignores the more stable edge information in the local area, thereby leading to the extraction of more pseudojunction points; therefore, PR is the lowest, and ACU only is approximately 50%. CPDA exhibits strong robustness to the impact of noise and results in a higher PR and a value of ACU that is able to reach 70%. This result is mainly because CPDA extracts junction points by using discrete curvature estimates and by using fracture-edge connectivity technology.

However, the noises can lead to parted branch edges and thereby cause RR to decrease. The robustness of JUDOCA to noise is weaker than that of CPDA, especially its ACU, which is under high noise conditions and reduced by half, compared to the value of ACU under low noise conditions. PR and ACU of our method are the highest among the four methods; that is, it has the best robustness to the impact of noise. This excellent performance using our method is due to the introduction of azimuth consensus constraints to filter out the noise and the lack of a strict requirement for a connective path of branch edges.

4.4. Experiment Results for SAR Images. This experiment is different from the first four experiments on artificial test images, as it is usually very difficult to extract the ground truth data from the natural images. This difficulty is primarily because junction point detection for SAR images is not only relative to the local structural pattern but is also often related to the observation view and the observer's subjective judgment [14]. Therefore, in this section, we adopt

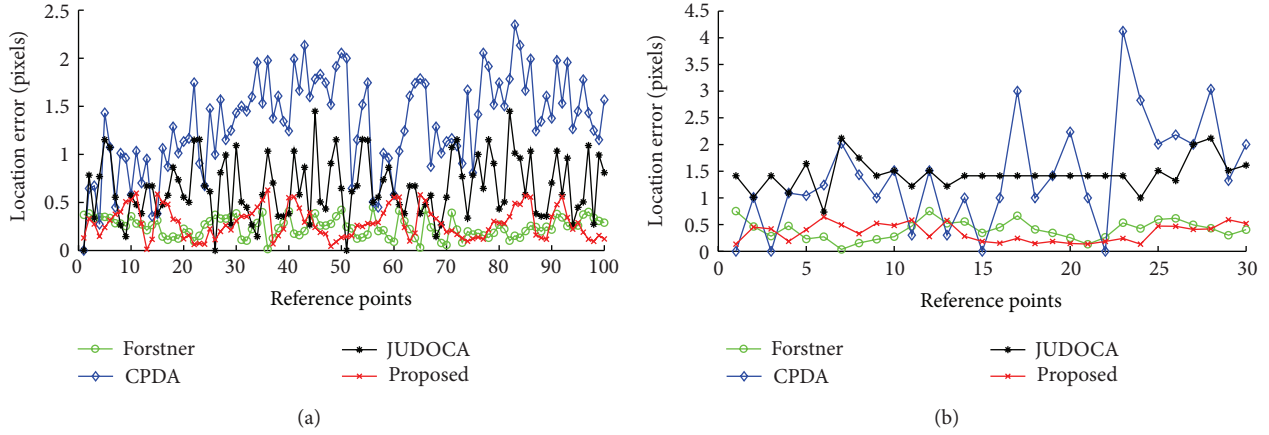


FIGURE 3: Location accuracy contrast among the Forstner algorithm, CPDA, JUDOCA, and our proposed method for detected junction points. (a) The horizontal axis represents the labeled number of 1 ~ 100 junction points in Figure 2(a) and the vertical axis describes the location error of the junction points detected by the Forstner algorithm, CPDA, JUDOCA, and our proposed method. (b) The horizontal axis represents the labeled number of 1 ~ 30 junction points in Figure 2(c) and the vertical axis describes the location error of the junction points detected by the Forstner algorithm, CPDA, JUDOCA, and our proposed method.

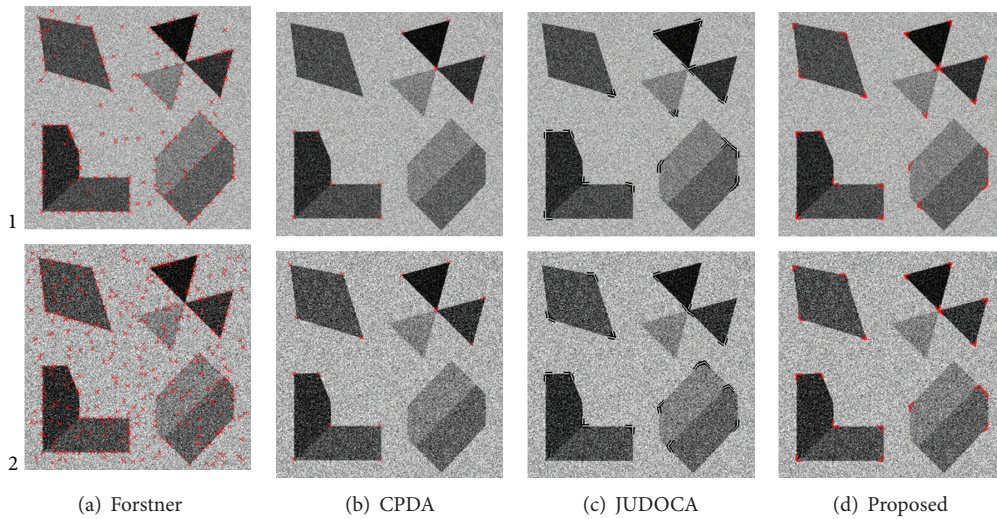


FIGURE 4: Junction points detection results under different noise conditions. From row 1 to row 2, the random noises added is 1% and 1.2%, respectively. The results of the four methods are shown as the images from column (a) to column (d).

the qualitative evaluation criterion and choose two SAR images, which have different revolutions (as shown in Figure 5). The results of the two images are shown in Figures 5(a) and 5(b), respectively. The results in Figure 5(a) indicate that, for some obvious junction points, JUDOCA missed more points than our proposed method and it lost a part of the branch edges; the results for the SAR image in the City of Maoming are shown in Figure 5(b) and indicate that the two algorithms achieve comparable detection results.

Note that under the situation consisting of massive noises, JUDOCA extracts more pseudojunction points around the circumference region than our method (especially in Figure 5(a)), but the points in the circle easily introduce significant location error because they are inappropriately detected as junction points. Thus, during the detection of a

junction point, JUDOCA chooses and filters out the branch edges and noise impact only by the connective paths. By contrast, our proposed algorithm can effectively filter out the noise impact and the circumference points by using azimuth consensus and extract more useful structural information.

5. Conclusion

This paper presents a novel method for junction point detection to detect junctions accurately in SAR images. The proposed algorithm uses an azimuth consensus to filter out the impact of noise and pseudo-junction points, such as those from a homogeneous region and 1D-edge points. The experimental results demonstrate that our proposed algorithm

TABLE 3: Performance of four methods with different levels of noise.

	Forstner					CPDA					JUDOCA					Proposed				
	N_t	N_c	RR	PR	ACU	N_t	N_c	RR	PR	ACU	N_t	N_c	RR	PR	ACU	N_t	N_c	RR	PR	ACU
Image 1	173	24	0.92	0.14	53%	12	11	0.42	0.92	67%	15	14	0.54	0.93	74%	21	20	0.77	0.95	86%
Image 2	363	21	0.81	0.06	44%	16	14	0.54	0.88	71%	16	15	0.58	0.94	76%	19	19	0.73	1.00	87%

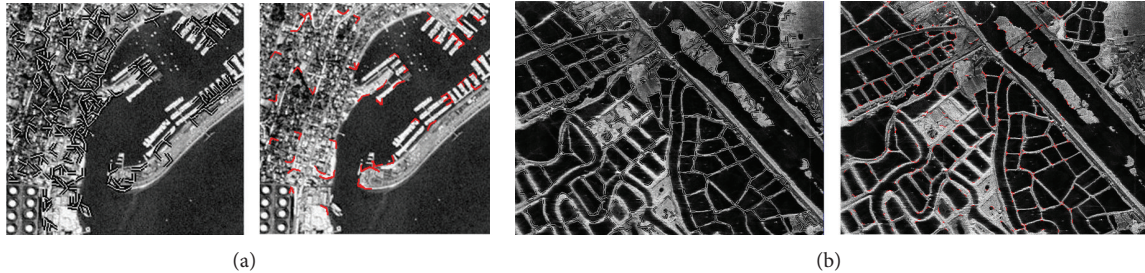


FIGURE 5: Comparison of the detection results for four SAR images [29]. (a) The detection results of the SAR image (size: 256 * 256). Left: JUDOCA; right: proposed algorithm. (b) The detection results of the SAR image in the City of Maoming (size: 1358 * 1036). Left: JUDOCA; right: proposed algorithm.

exhibits improved performance in the detection accuracy and is less susceptible to contrast change and noise impact than JUDOCA and CPDA. One area of our future work is to apply the junction detector to computer vision. Possible applications include content-based image registration, SAR image stitching, and multisensory image matching.

Acknowledgment

This research was partially supported by the National Natural Science Foundation of China under Grants 61170159 and 60902093.

References

- [1] I. Golightly and D. Jones, "Corner detection and matching for visual tracking during power line inspection," *Image and Vision Computing*, vol. 21, no. 9, pp. 827–840, 2003.
- [2] I. Zoghlami, O. Faugeras, and R. Deriche, "Using geometric corners to build a 2D mosaic from a set of images," in *Proceedings of the IEEE Computer Society Conference on Computer Vision and Pattern Recognition*, pp. 420–425, June 1997.
- [3] Y. Liu, X. Zhang, and T. S. Huang, "Estimation of 3D structure and motion from image corners," *Pattern Recognition*, vol. 36, no. 6, pp. 1269–1277, 2003.
- [4] S. M. Smith and J. M. Brady, "SUSAN—a new approach to low level image processing," *International Journal of Computer Vision*, vol. 23, no. 1, pp. 45–78, 1997.
- [5] E. Rosten, R. Porter, and T. Drummond, "Faster and better: a machine learning approach to corner detection," *IEEE Transactions on Pattern Analysis and Machine Intelligence*, vol. 32, no. 1, pp. 105–119, 2009.
- [6] W. F. Förstner and E. Gülch, "A fast operator for detection and precise location of distinct point, corners and centres of circular features," in *Proceedings of the ISPRS Conference on Fast Processing of Photogrammetric Data*, pp. 281–305, 1987.
- [7] C. Harris and M. Stephens, "A combined corner and edge detection," in *Proceedings of the 4th Alvey Vision Conference*, pp. 147–151, 1988.
- [8] C. Tomasi and T. Kanade, "Detection and tracking of point features," Tech. Rep. CMU-CS-91-132, Computer Science Department, Carnegie Mellon University, Pittsburgh, Pa, USA, 1991.
- [9] U. Köthe, "Edge and junction detection with an improved structure tensor," in *Proceedings of the DAGM-Symposium (DAGM '03)*, vol. 2781 of *Lecture Notes in Computer Science*, pp. 25–32, 2003.
- [10] T. Brox, J. Weickert, B. Burgeth, and P. Mrázek, "Nonlinear structure tensors," *Image and Vision Computing*, vol. 24, no. 1, pp. 41–55, 2006.
- [11] F. Mokhtarian and R. Suomela, "Robust image corner detection through curvature scale space," *IEEE Transactions on Pattern Analysis and Machine Intelligence*, vol. 20, no. 12, pp. 1376–1381, 1998.
- [12] F. Mokhtarian and F. Mohanna, "Enhancing the curvature scale space corner detector," in *Proceedings of the 8th Scandinavian Conference on Image Analysis*, pp. 145–152, Bergen, Norway, 2001.
- [13] J. H. Han and T. Poston, "Chord-to-point distance accumulation and planar curvature: a new approach to discrete curvature," *Pattern Recognition Letters*, vol. 22, no. 10, pp. 1133–1144, 2001.
- [14] J. McDermott, "Psychophysics with junctions in real images," *Perception*, vol. 33, no. 9, pp. 1101–1127, 2004.
- [15] L. Parida, D. Geiger, and R. Hummel, "Junctions: detection, classification, and reconstruction," *IEEE Transactions on Pattern Analysis and Machine Intelligence*, vol. 20, no. 7, pp. 687–698, 1998.
- [16] F. Chabat, G. Z. Yang, and D. M. Hansell, "Corner orientation detector," *Image and Vision Computing*, vol. 17, no. 10, pp. 761–769, 1999.
- [17] M. Cazorla, F. Escolano, D. Gallardo, and R. Rizo, "Junction detection and grouping with probabilistic edge models and Bayesian A," *Pattern Recognition*, vol. 35, no. 9, pp. 1869–1881, 2002.

- [18] M. A. Cazorla and F. Escolano, "Two Bayesian methods for junction classification," *IEEE Transactions on Image Processing*, vol. 12, no. 3, pp. 317–327, 2003.
- [19] R. Bergevin and A. Bube, "Detection and characterization of junctions in a 2D image," *Computer Vision and Image Understanding*, vol. 93, no. 3, pp. 288–309, 2004.
- [20] C. Perwass, "Junction and corner detection through the extraction and analysis of line segments," in *Proceedings of the 10th International Workshop Combinatorial Image Analysis (IWCIA '04)*, vol. 3322 of *Lecture Notes in Computer Science*, pp. 568–582, 2004.
- [21] R. Elias and R. Laganière, "JUDOCA: junction detection operator based on circumferential anchors," *IEEE Transactions on Image Processing*, vol. 21, no. 4, pp. 2109–2118, 2012.
- [22] R. Elias, "Sparse view stereo matching," *Pattern Recognition Letters*, vol. 28, no. 13, pp. 1667–1678, 2007.
- [23] R. Elias, "Enhancing sensor measurements through wide baseline stereo," *ELCVIA*, vol. 7, no. 3, pp. 36–53, 2008.
- [24] H. Hajjdiab, R. Elias, and R. Laganière, "Wide baseline obstacle detection and localization," in *Proceedings of the International Symposium on Signal Processing and Its Applications (ISSPA '03)*, vol. 1, pp. 21–24, 2003.
- [25] P. Kovesi, *Invariant measures of image features from phase information [Ph.D. thesis]*, The University of Western Australia, 1996.
- [26] J. Bresenham, "Algorithm for computer control of a digital plotter," *IBM Systems Journal*, vol. 4, no. 1, pp. 25–30, 1965.
- [27] T. Lindeberg, "Junction detection with automatic selection of detection scales and localization scales," in *Proceedings of the 1st International Conference on Image Processing (ICIP '94)*, vol. 1, pp. 924–928, Austin, Tex, USA, November 1994.
- [28] <http://www.ipb.uni-bonn.de/software/foerstneroperator/>.
- [29] http://www.crisp.nus.edu.sg/~research/tutorial/opt_int.htm#multispectral.

Research Article

Using Open-Source Components to Process Interferometric TerraSAR-X Spotlight Data

Michael Jendryke,^{1,2} Timo Balz,¹ Houjun Jiang,¹ Mingsheng Liao,¹ and Uwe Stilla²

¹ State Key Laboratory of Information Engineering in Surveying, Mapping and Remote Sensing, Wuhan University, Wuhan, Hubei 430079, China

² Photogrammetry and Remote Sensing, Technische Universitaet Muenchen, 80333 Munich, Germany

Correspondence should be addressed to Michael Jendryke; michael.jendryke@rub.de

Received 21 November 2012; Accepted 20 January 2013

Academic Editor: Gui Gao

Copyright © 2013 Michael Jendryke et al. This is an open access article distributed under the Creative Commons Attribution License, which permits unrestricted use, distribution, and reproduction in any medium, provided the original work is properly cited.

We address the processing of interferometric TerraSAR-X and TanDEM-X spotlight data. Processing steps necessary to derive interferograms at high spatial resolution from bi- and monostatic satellite images will be explained. The spotlight image mode is a beam steering technique focusing the antenna on a specific ground area. This results in a linear Doppler shift frequency in azimuth direction, which has to be matched to the master image. While shifting the interpolation kernel in azimuth during resampling, the frequency spectrum of the slave image is aligned to the master image. We show how to process bistatic TanDEM-X images and propose an integrated processing option for monostatic TerraSAR-X data in the Delft Object-oriented Radar Interferometric Software (DORIS). The paper focuses on the implementation of this algorithm for high-resolution spotlight InSAR in a public domain tool; hence, it becomes available to a larger research community. The results are presented for three test areas: Uluru in Australia, Las Vegas in the USA, and Lüneburg in Germany.

1. Introduction

Radar remote sensing with SAR (Synthetic Aperture Radar) satellites is used to observe the Earth from space (~500 km away) [1]. It is a space-borne image acquisition technique that is able to penetrate cloud coverage and that is not dependent on sunlight. The Earth's surface is illuminated with electromagnetic waves sent by the satellite antenna [2, 3]. The backscattered signal is received by the same antenna (monostatic) or other antennas (bi- or multistatic) and is stored as a complex image with amplitude and phase information [4]. SAR images have a broad range of applications such as urban surveillance [5, 6], damage assessment [7–9], glacier monitoring [10], and deformation mapping [11, 12].

New generation satellites as TerraSAR-X or COSMO-SkyMed provide images in single polarization with a resolution of approximately 1 m (with 300 MHz bandwidth) [13]. The highest-resolution image mode is called spotlight mode and covers—compared to other image modes—a relatively small ground area [13]. TerraSAR-X and COSMO-SkyMed

operate in the X-band spectrum, which is particularly useful for observing man-made structures. High resolution is of interest when monitoring small parts of urban areas and single building structures [5]. In order to achieve resolution in the meter or submeter region, the antenna beam is steered backwards, while the satellite passes the area of observation [14]. One limitation is that continuous acquisition along the ground track is not possible. A full spotlight scene with two subsets is shown in Figure 1.

A consequence of beam steering is the linear Doppler shift, that causes mismatched image spectra, which have to be aligned in order to create spotlight interferograms [14]. The ground area has to be sampled more often to achieve high spatial resolution, which is only possible by increasing the illumination time. Therefore, the beam is directed forward (from the perspective of the satellite) and gradually motioned backwards as the antenna passes the area of interest [13]. This means a positive Doppler frequency at the first image line, which is linearly declining line by line, reaching a single line with zero Doppler in the image center and negative

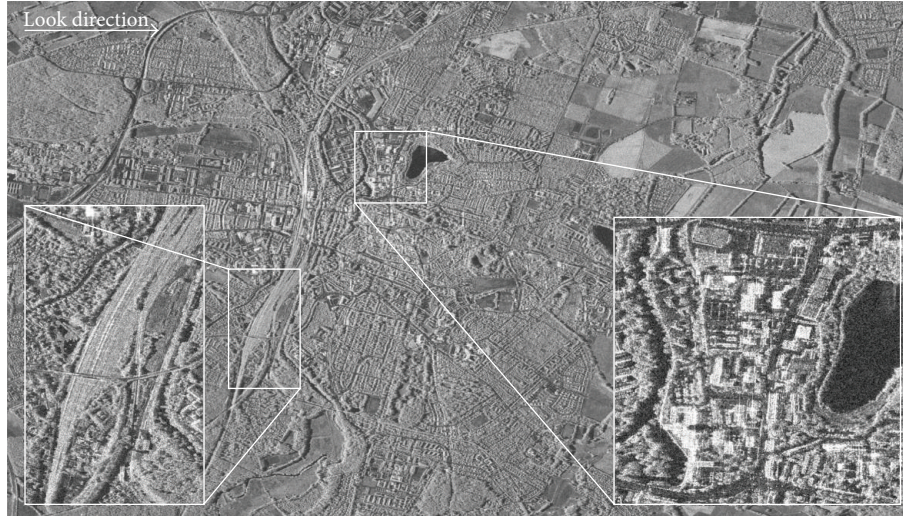


FIGURE 1: TerraSAR-X Spotlight image (full scene) of Lüneburg, Germany. Left subset shows a railway station, right subset shows building structures and a pond, © DLR 2010.

frequencies towards the last line. Matching the two image spectra is the challenge in interferometric processing of spotlight data.

The purpose of this paper is (i) to explain high-resolution spotlight interferogram generation for bi- and monostatic acquisitions, (ii) the implementation of a resampling algorithm described in detail in Eineder et al. [14], and (iii) making it available to the research community by incorporating the source code into DORIS [15]. This will enable researchers to generate coherent high-resolution interferograms with an open software solution. The key point of this paper lies in the instruction to process bi- and monostatic acquisitions.

In this paper, we show TanDEM-X single pass interferometry (bistatic) and TerraSAR-X (TSX) repeat pass interferometry (monostatic). We abbreviate the TerraSAR-X satellite as TSX, TanDEM-X as TDX, and the bistatic product, generated by the satellite constellation, as TDM. In the first (bistatic) case, one satellite serves as a sender to illuminate the ground. Both antennas on satellite 1 (TSX) and 2 (TDX) are used for receiving [16]. In order to form images in this mode, the spacecrafts have to orbit in close formation and must be linked together to acquire two images at almost the same time from slightly different positions [4]. In the second case, one satellite serves as a sending and receiving antenna during one image acquisition. Images are recorded every time the satellite passes the area of interest.

This article is divided into four parts starting from simple to more complex operations. It will first discuss TDM spotlight products (TanDEM-X bistatic) and the additional processing steps required to generate a bistatic interferogram. The second part illustrates how proper spotlight interferograms are derived by describing how spotlight images are acquired and subsequently treated during the resampling process. The last two parts show examples and discuss the results, which are achieved with the presented implementation.

2. TanDEM-X Spotlight Interferometry

TanDEM-X (TDX) is the twin satellite of TerraSAR-X (TSX), and the mission purpose of this constellation is to acquire a global homogeneous DEM [4]. Using InSAR to generate a DEM (digital elevation model) is well known since NASA's SRTM (Shuttle Radar Topography Mission). However, there are certain aspects that have to be considered to maximize the quality of the interferogram and therefore the resulting DEM. In order to minimize phase decorrelation (due to temporal changes or surface deformation), both satellites have to record the images within a very short time delay. Another aspect in DEM generation is the height ambiguity, which is determined by choosing an appropriate baseline. Both satellites orbit consistently in very close formation, recording images at almost the same time with a defined baseline. Images taken in this setup show very high coherence and are therefore particularly suitable for interferogram generation, as shown in Figure 15.

2.1. Mission Design for Bistatic Image Acquisition. The primary mission goal of TanDEM-X is the generation of a DEM of unprecedented accuracy with a spatial resolution of 12 m and a relative vertical accuracy of 2 m [16]. The global coverage will be larger towards the poles compared to the SRTM [16].

The mission design is a constellation of TSX and TDX as a twin concept. It is based on two almost identical SAR systems orbiting in close formation. When TSX was launched, it already incorporated all necessary equipment and procedures to operate with a second satellite. Both satellites need to be able to synchronize the phase; therefore, X-band horn antennas are installed on both satellites. The dual frequency GPS receiver estimates the orbit parameters precisely. The pulse repetition frequency (PRF) is synchronized by GPS measurements. An additional cold gas propulsion system

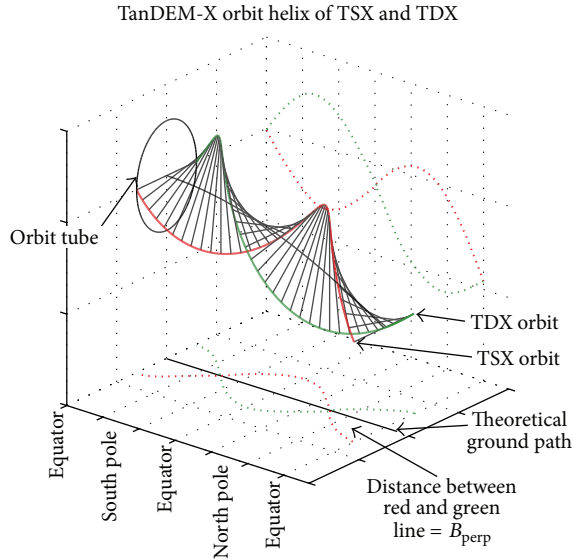


FIGURE 2: TerraSAR-X (red) and TanDEM-X (green) orbit constellation—close formation helix-like orbit. X-axis is one revolution around the globe.

allows TDX to keep the right orbit attitude. Both satellites can operate separately in the image mode spotlight (see image formation in Section 3.1), stripmap, or ScanSAR. Operating as a twin system brings up three different data acquisition modes these include, bistatic—which will be discussed below—pursuit monostatic, and alternating bistatic [17].

In bistatic imaging, one satellite is serving as transmitter, and both satellites receive the backscattered signal. Temporal decorrelation is minimized, and the atmospheric effects are equal in both images [4]. Ground objects that move within this velocity range, for example, water or trees affected by wind, are still incoherent. Coherent results are achieved by synchronizing the PRF between the two receiving antennas. The desired difference between both images is a slightly different view angle. That is expressed by the effective baseline, which is half the perpendicular baseline [4]. The modeling and determination of the orbital baseline for bistatic are discussed in [18].

To ensure a constant baseline, both satellites orbit in a helix-like fashion, with a short distance along the flight pass. One satellite rotates around the orbit tube of the second satellite. This is necessary to keep an effective baseline of around 200 m [4]. Schematic sketches are shown in Figures 2 and 3. One can imagine two circular orbits with a cross track distance of ~ 360 m at the Equator and $\sim \pm 400$ m radial distance at the poles [4]. With two orbits as described above, one satellite (e.g., TSX) is considered as the reference. The second spacecraft (e.g., TDX) is then revolving around the orbit of the reference. One whole circle is performed during one revolution around the Earth. Having a controlled orbit gives a predictable perpendicular baseline and height ambiguity.

The differences between repeat pass and single pass interferometry are visualized in Figure 3. Repeat pass interferometry refers to a single satellite system (M) acquiring one image at a time. To observe the Earth two times in a row with similar image geometry—a prerequisite for interferometry [2]—the satellite has to pass the same location/orbit again. However, this is only possible after a certain amount of time, expressed by the temporal baseline, for example, ~ 11 days for TSX. Single pass interferometry refers to an image pair generation within the same overpass. The temporal baseline between both images is then nearly zero. The advantages of two satellites (M and S) being just several hundred meter apart is that the temporal phase decorrelation is very low. A coherent image pair will produce an interferogram of high accuracy and quality with minimized temporal decorrelation due to vegetation or varying weather conditions. Atmospheric effects on two different dates can be neglected [4].

2.2. Processing Considerations. In this part, we will discuss the actual processing steps for TDM images necessary to generate an interferogram and subsequently flatten it. A bistatic complex image pair is the recorded backscatter signal of two identical satellite antennas with a defined baseline. The delivered TDM spotlight product is an already coregistered pair of standard SSC images and named CoSSC. Obligatory processing steps before interferogram formation are already done. This information is mentioned in the auxiliary XML file of a TDM CoSSC image pair. During the processing with DORIS, three issues occurred: (i) the changes in the data format to 16-bit floating point, (ii) extracting the right baseline, and (iii) the different range (travel) times for the reference phase.

TDM data are delivered in the CoSSC file format with complex half-precision float values (float16). Float16 is defined by the IEEE 754 standard and explained in [19]. SSC data is delivered as complex integer with 16-bit precision. As a result, one complex number consists of two 16-bit floating-point values. A conversion from float16 to float32 was performed with a library developed by [20]. Correct values are maintained, and the data can be used in non-float16 compatible software.

The metadata states that both images are cropped to the same extent, corrected for bistatic mode, spectral filtered in range and azimuth, coregistered, and resampled. Therefore, interferogram generation can be started directly. Depending on the setup, either one of the satellites is used as the master (TSX or TDX). By taking the complex phase information of the master and slave, an interferogram can be derived with

$$I = M \cdot S^* \cdot R^* \quad (1)$$

M is the complex signal of the master, S^* is the complex conjugate of the slave, R^* the conjugate of the reference phase, and I is the resulting interferogram [21].

DORIS extracts the orbital parameters slightly different for TDM. By default, it reads the data as if both images were acquired independently in the monostatic mode. Bistatic image processing with TDM data is not considered [15]. The

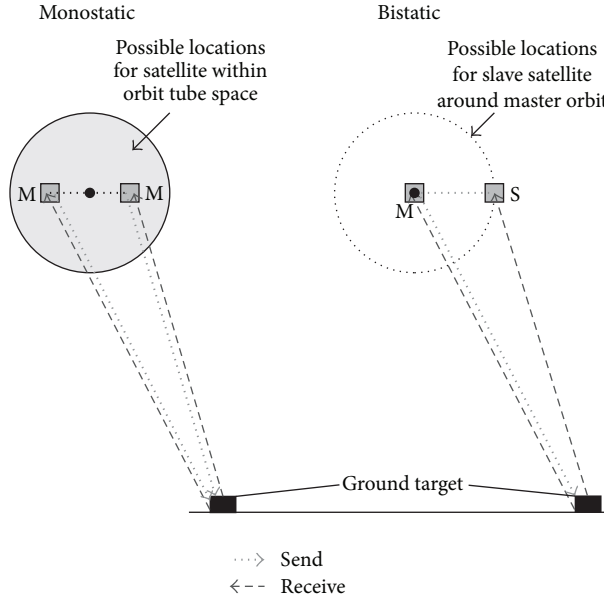


FIGURE 3: Monostatic (left side) image acquisition on two dates: the satellite (M) sends a signal (dotted line) and receives the echo (dashed line) during each overpass. Bistatic image acquisition generates two images in a single overpass with almost no time difference. One satellite serves as transmitter, and both serve as receiving antennas. The baseline of the slave satellite is desired to be on a circle around the master, see Figure 2.

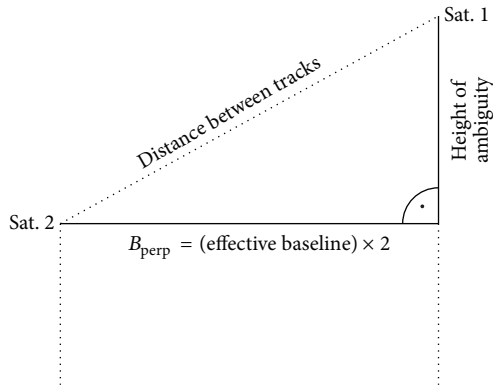


FIGURE 4: Relation of baseline annotations and orbit geometry for TanDEM-X.

orbit information is retrieved based on the annotation files of TSX and TDX separately. Both files are treated as if they were two separate acquisitions with a temporal baseline of 0 days. This is sufficient at the initial reading step. When estimating the baseline in DORIS, a mismatch between the perpendicular baseline and the effective baseline occurred. According to Krieger and Moreira [4], the effective baseline is half the length of the perpendicular baseline which is due to the bistatic acquisition mode (see Figure 4). The DORIS result file has to be modified accordingly.

Due to the bistatic acquisition, one has to take care of the range times by taking half the travel time instead of the full range, distance from and to the antenna. The reference

phase $\Phi_{\text{reference}}$ as mentioned and annotated with R in (1) for a mono- or bistatic image pair is calculated by

$$\Phi_{\text{reference}} = \Phi_{\text{Master_const}} \cdot \mathbf{t}_{\text{range_Master}} - \Phi_{\text{Slave_const}} \cdot \mathbf{t}_{\text{range_Slave}}. \quad (2)$$

$\Phi_{\text{Master_const}}$ is a constant value, based on the wavelength of the master image and derived with either option in

$$\begin{aligned} \text{Monostatic} : & \left\{ \Phi_{\text{Master_const}} = \frac{-4.0 \cdot \pi \cdot c}{\lambda_{\text{Master}}} \right\}, \\ \text{Bistatic} : & \left\{ \Phi_{\text{Master_const}} = \frac{-2.0 \cdot \pi \cdot c}{\lambda_{\text{Master}}} \right\}, \end{aligned} \quad (3)$$

where c is the speed of light and λ_{Master} is the wavelength of the master image. For a signal traveling to the ground and back to the satellite (monostatic), the factor would be -4.0 , for two full phase circles, instead of -2.0 . This comes from the radar range equation and has to be changed for the bistatic mode. $\mathbf{t}_{\text{range_Master}}$ is the range time based on the pixel location as stated as follows:

$$\mathbf{t}_{\text{range_Master}} = \mathbf{t}_{\text{range}_0} + \frac{(\text{pixel} - 1.0)}{\text{RSR}}. \quad (4)$$

Pixel is the pixel number (column as integer) of that particular line, and RSR is the range sampling rate as annotated in the metadata. The interferometric phase can now be processed correctly.

3. TerraSAR-X Spotlight Interferometry

Very high-resolution spaceborne SAR images generated with current satellites are only possible by sweeping the

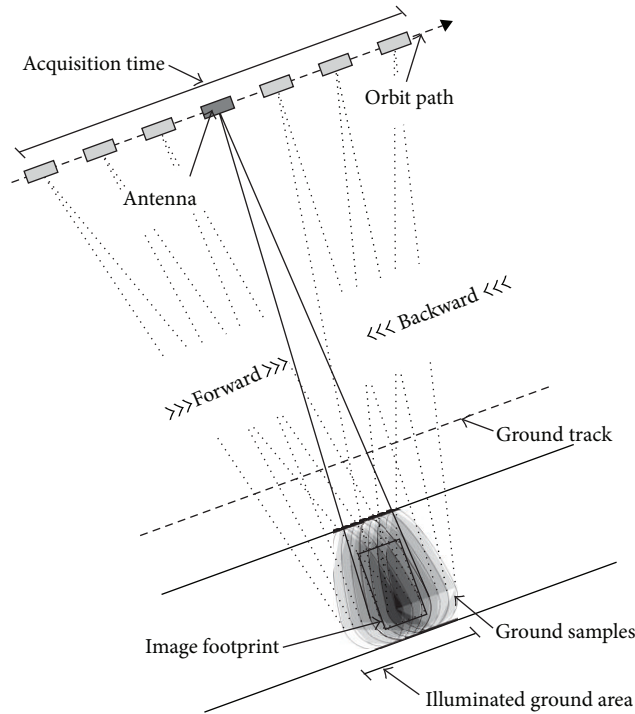


FIGURE 5: Image acquisition geometry for spotlight mode. The beam is steered backwards when the satellite passes the area of interest [4].

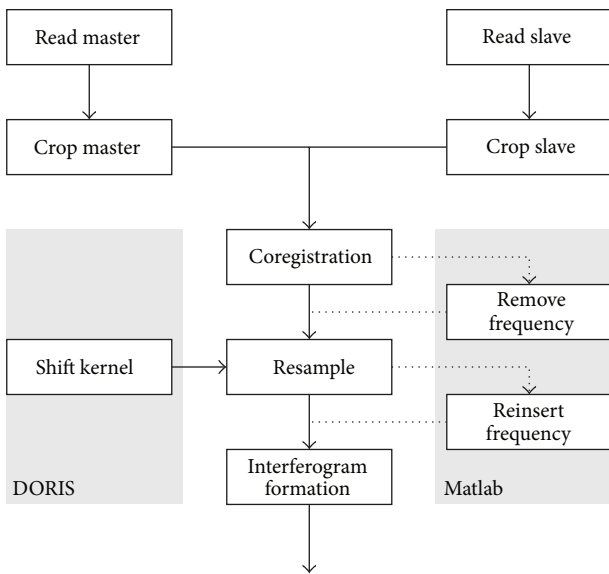


FIGURE 6: General processing flow chart. Two options: implementation in DORIS shifting the kernel (left); external scripts in MATLAB to set the image spectrum to zero (right).

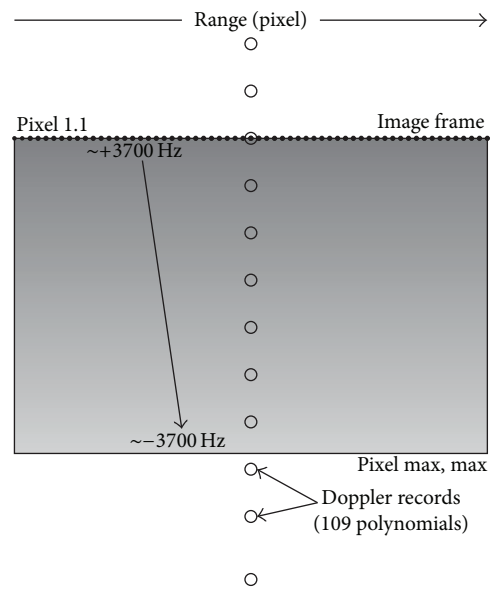


FIGURE 7: Schematic sketch of interpolation values derived from XML data. The x -axis represents the range time calculated from the pixel number, and the y -axis is interpolated from the annotated Doppler polynomial records. The recording of them starts and ends before and after the actual image footprint.

antenna beam in spotlight mode. The occurring problems are mentioned above. We argue that especially high-resolution interferograms would be explored more frequently, if the processing could be done with more ease.

3.1. Spotlight Image Formation in Repeat Pass. Spotlight image mode of TSX and TDX is a sliding azimuth beam

steering technique [14]. As shown in Figure 5, the satellite passes the area of interest in a certain time. The observation time is increased by steering the antenna beam in azimuth. See Figure 5 for a diagram of this process. The drift rate of

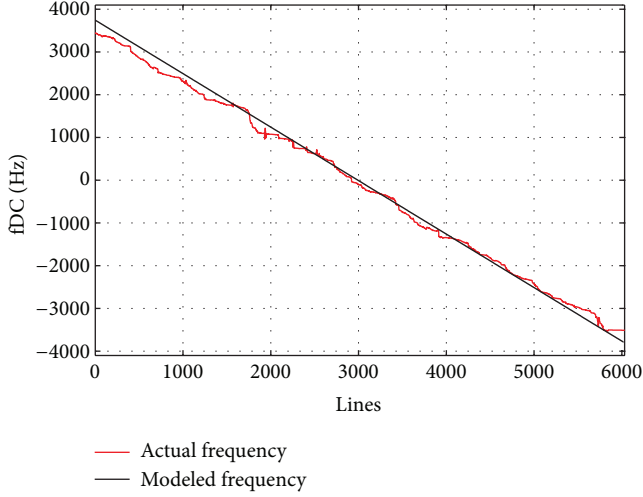


FIGURE 8: Modeled and actual Doppler frequency at pixel 4000 (range) from the first to the last line.

the sweeping motion is slower than the overpass velocity. Consequently, the beam is sliding over an area and not starting at a single location. This results in more ground samples and an increased ground resolution. One shortcoming is the limited image frame length. A longer illumination time is achieved in azimuth, but not in range. High-range resolution is accomplished with a bandwidth of 300 MHz [13].

The Doppler frequency decreases over the whole image length in azimuth. This behavior is different compared to the standard stripmap mode. The Doppler spectrum of a spotlight image follows a linear trend from positive Doppler frequencies around 3700 Hz, to negative values around -3700 Hz, as visualized in Figure 7. Theoretically, only one zero Doppler line exists in the center of the image. This is the case when the beam is steered exactly perpendicular to the orbit and the Earth. Stripmap images do not have this linear trend—all lines are centered around the Doppler frequency. Proper treatment of the Doppler frequency is necessary for InSAR processing. The amplitude information is not affected.

3.2. Implementation of Processing Method. As discussed in [14] and mentioned in [15, 22], there are two options to deal with the different image spectra of master and slave. Correct phase information is kept when the spectrum of the slave is set to zero before resampling or the interpolation kernel is shifted during the resampling step. We implemented the first option in MATLAB. Both options are shown as a flow chart in Figure 6. Shifting the interpolation kernel is the second option and is described in detail in [14]. The according Doppler frequency, to multiply the kernel with, is retrieved by exploiting the annotated Doppler polynomials (see Figure 7). Eineder et al. [14] propose a low-pass azimuth bandpass filter after resampling. We will focus solely on the generation of the frequency matrix for the pixel-by-pixel calculation of the interpolation kernel.

The chosen interpolation kernel is a six-point cubic convolution kernel as described in [22], implemented in DORIS

and shown in (5). Hanssen and Bamler [22] recommend a six-point cubic convolution kernel for high-resolution applications that is also recommended by Eineder et al. [14] and used in our implementation:

$$i(x) = \begin{cases} (\alpha - \beta + 2)|x|^3 - (\alpha - \beta + 3)|x|^2 + 1 & 0 \leq |x| < 1 \\ \alpha|x|^3 - (5\alpha - \beta)|x|^2 + (8\alpha - 3\beta)|x| - (4\alpha - 2\beta) & 1 \leq |x| < 2 \\ \beta|x|^3 - (8\beta)|x|^2 + (21\beta)|x| - (18\beta) & 2 \leq |x| < 3 \\ 0 & 3 \leq |x|, \end{cases} \quad (5)$$

where α and β are two parameters ($\alpha = -1/2$ and $\beta = 1/2$) as defined by [22]. The resulting interpolation kernel $i(x)$ is then multiplied with the modeled Doppler frequency during resampling.

To calculate the frequency matrix, the timing and Doppler rate metadata are evaluated for each product specifically. See appendix of [14, 23] for a more elaborate description. Figure 7 helps to visualize the pixel-by-pixel calculation for the frequency matrix. The number of Doppler polynomial records is variable and not fixed. The recording of these discrete measurements starts and ends before and after the actual image footprint.

Each annotated Doppler polynomial is evaluated along the range time as described in [16] and shown as follows:

$$\begin{aligned} \text{fDC}(\text{pixel}) = & (\text{fDC}_{\text{coef}0} * (P(\text{pixel}) - \text{Refpoint})^0) \\ & + (\text{fDC}_{\text{coef}1} * (P(\text{pixel}) - \text{Refpoint})^1) \\ & + (\text{fDC}_{\text{coef}2} * (P(\text{pixel}) - \text{Refpoint})^2). \end{aligned} \quad (6)$$

$P(\text{pixel})$ is the function $\text{pixel}2t_{\text{range}}(\text{pixel})$ which calculates the range time based on the pixel number (integer value), the range sampling frequency RSF, and the start range time $t_{\text{range}0}$. The corresponding calculation is shown as follows:

$$\text{pixel}2t_{\text{range}}(\text{pixel}) = t_{\text{range}0} + \frac{(\text{pixel} - 1.0)}{\text{RSF}}. \quad (7)$$

The timing information gathered from the metadata are in the system receive time (the actual uptime of the satellite) and has to be converted to zero-Doppler time system by

$$t_{\text{SSC}} = \left(t_{\text{RAW}} - \left(\frac{f_{\text{DC}}(t_{\text{RAW}})}{FM_{\text{rate}}} \right) \right) - t_{\text{zero-Doppler Start}}. \quad (8)$$

t_{RAW} is the time UTC annotation in seconds, and $t_{\text{zero-Doppler Start}}$ is the actual first zero Doppler time. The mentioned FM_{rate} is calculated according to the following function

$$FM_{\text{rate}} = \frac{\text{fDC}_{\text{coef}0} - \text{fDC}_{\text{coef}1}}{2}. \quad (9)$$

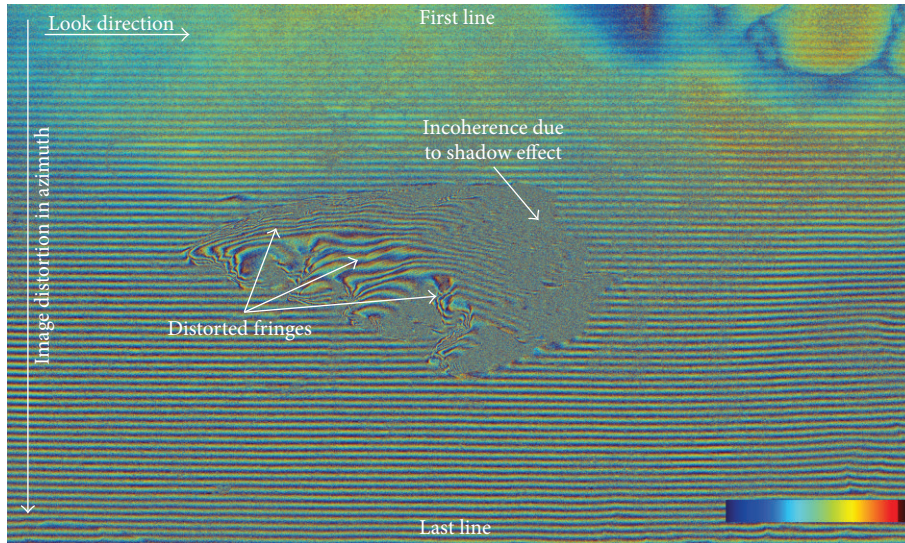


FIGURE 9: TerraSAR-X image pair (Uluru) with default frequency shift in DORIS. The image is not corrected and gets distorted towards the last line.

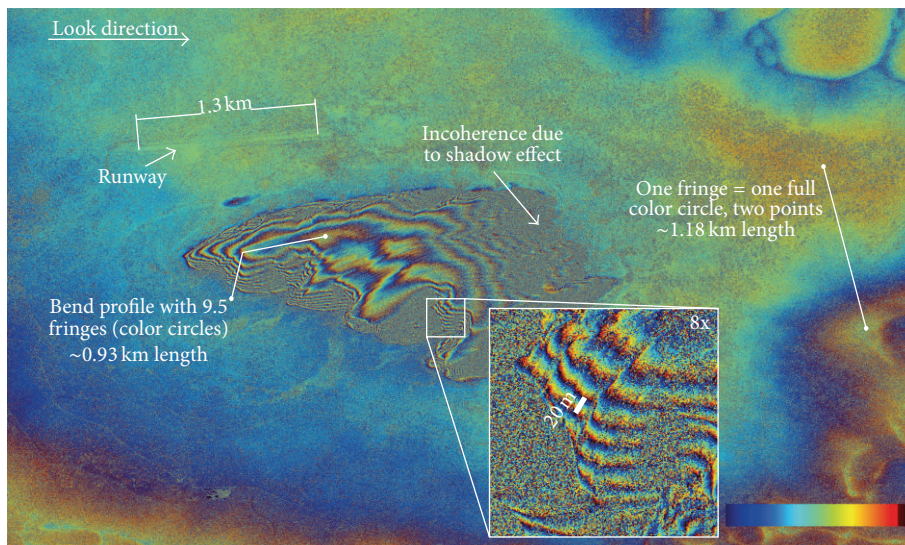


FIGURE 10: Interferogram generated with DORIS using the cc6p_SP interpolation kernel. Temporal baseline is 11 days and perpendicular baseline is 233.7 m with a height ambiguity of 34 m. Master acquired on 2009-02-12 and slave on 2009-02-23.

$\hat{f}_{DC_{coef}f_0}$ marks the Doppler rate at the start of the scene and $\hat{f}_{DC_{coef}f_1}$ at the end of the scene. The FM_{rate} is the average of these values. To interpolate along azimuth, the \hat{f}_{DC} and t_{SSC} values are used.

Comparing the actual frequency and the interpolated modeled frequency derived from the metadata is shown in Figure 8. The spectrum for a single line in azimuth is colored in red and follows an almost linear trend from approx. 3500 Hz in the first line to around -3500 Hz in the last line

of the image. To shift the kernel, the modeled frequency was used (black line).

4. Results and Discussion

Results for one bistatic TDM product and several monostatic image pairs from TSX and TDX have been produced. A TDM pair from Las Vegas in high-resolution spotlight mode was used to test the bistatic configuration of DORIS, and



FIGURE 11: Time series of TerraSAR-X ascending stack, showing flattened interferograms. Area: Convention Center in Las Vegas, USA. Temperature annotations indicate the relative temperature difference to the master image (2010-03-24), source [18].

the result is shown in Figure 13. Our implementation of the `cc6p_SP` processing option in the resampling stage of DORIS (version 4.06 beta) was tested with the following TerraSAR-X HS source images: ascending and descending data stacks from Las Vegas (20 images each) and one data stack from Lüneburg (16 images). In addition, a sample dataset from Uluru, Australia, provided by Infoterra Germany [24] was used. All scenes were acquired in high-resolution spotlight mode. The process chain includes all steps listed in DORIS manual [21] until coherence estimation. We present flattened interferograms, flattened and filtered interferograms, and coherence images.

The implementation of bistatic image processing was done in DORIS, and the results are shown in Figures 13 and 15. By taking care of the float16-bit data format, the reference phase, and the effective baseline, a coherent interferogram was generated.

To demonstrate the effect of running DORIS with the default parameters in the input card “resample”, that is, frequency shift in azimuth as described in [21] during

interpolation leads to the results shown in Figure 9. Applying the default frequency shift, results in an interferogram where the phase seems to be correct in the first lines, getting more and more distorted and corrupted towards the last line. This is due to the not applied linear kernel shift in azimuth. Using a six-point cubic convolution kernel with a linear frequency shift, as described above and in [21], yields a flattened interferogram as shown in Figure 10.

There are a few things to pay attention to in Figure 10, for example, fringes along steep slopes and distorted fringes due to low coherence caused by shadow effects. The results are not DEM corrected. The phase follows the topography. Along the bend profile (bottom to top of the rock), 9.5 fringes can be counted. Evidence for a relatively flat surrounding area is given by the distance between two points (~ 1.18 Km, annotation on the right) with one phase circle.

Stacking images is a commonly used technique for time series analysis. A TSX ascending image stack over Las Vegas was used to generate interferograms, flattened the phase, and then cropped to the extend of the Convention Center

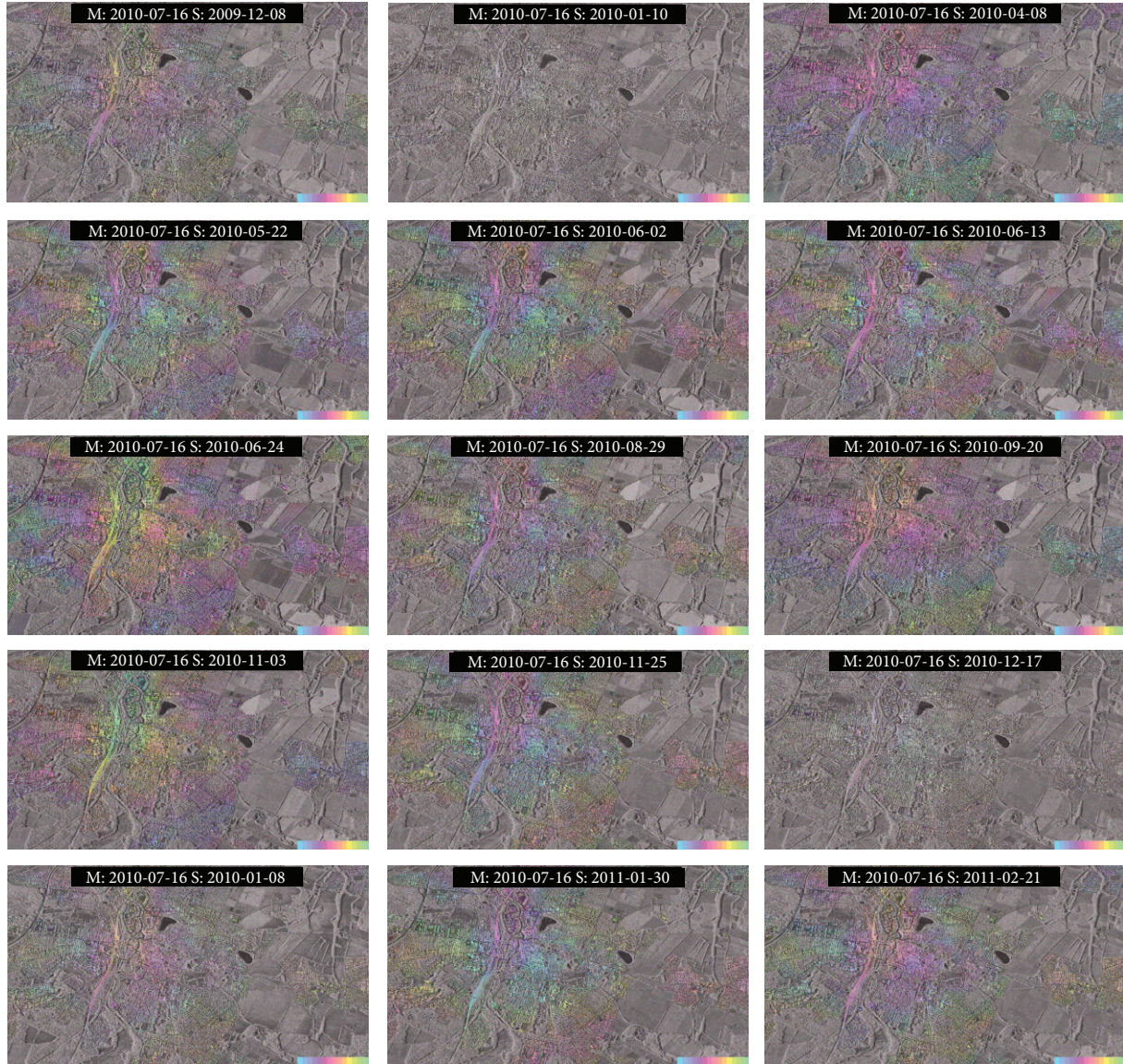


FIGURE 12: Time series of 15 full scene TerraSAR-X spotlight interferograms over Lüneburg, Germany. The color intensity has been increased extremely.

($36^{\circ}07'52.44''$ North, $115^{\circ}09'04.85''$ West), see Figure 11. Each pair was processed with exactly the same parameter set. The master image was chosen based on minimizing B_{perp} . The subsets are still in radar coordinates and not reprojected, the illumination direction is from the left. We show this result, because (a) the roof is a relatively flat surface with high backscatter, and (b) it is from the center of the image where the Doppler shift between both acquisitions is rather low. Relating the visualized phase to the temperature information (relative to the master), one can see that the roof gets more deformed the greater the absolute temperature difference.

The data stack of Lüneburg with 16 images shows less coherence. The interferograms for a full scene are depicted in Figure 12. Coherent areas are found in the urban area where ground is covered with solid structures like buildings and roads. The surrounding fields are mostly

incoherent, and therefore homogeneous phase information cannot be derived for these areas. The master image was selected based on minimizing temporal and perpendicular baselines.

A comparison of bi- and monostatic images is illustrated in Figures 13 and 14. The higher brilliance of the TDM image pair, compared to the TSX/TDX image pair, is due to the small temporal decorrelation for bistatic image acquisitions.

Looking at the hotels and the Convention Center in Figures 13 and 14 demonstrates two things. First, the phase or fringes following along the front of the hotels are similar in both scenes. Second, the phase on the Convention Center is very smooth in the TDM image pair. On the other hand, the TSX image pair shows more fringes on the roof, indicating a motion of the roof in LOS (line of sight) between both acquisitions.

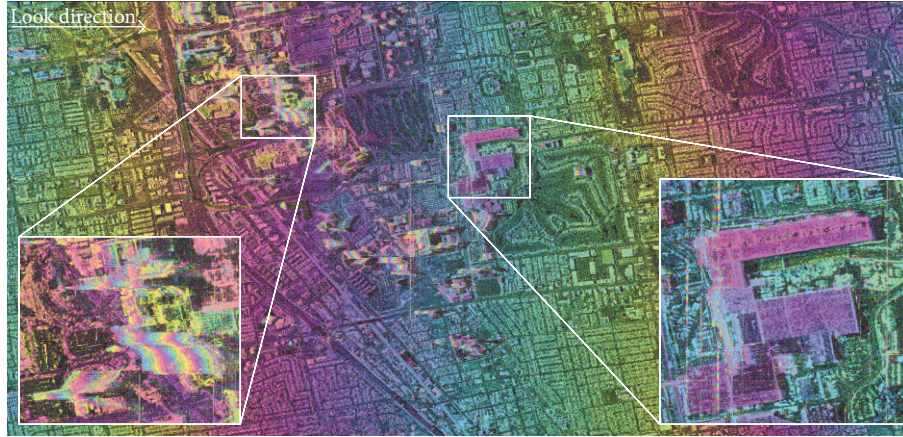


FIGURE 13: TanDEM-X flattened interferogram in radar coordinates with amplitude image in background. Subsets show hotels and the Las Vegas Convention Center. Temporal baseline 0 days, effective baseline: ~ 87 m.

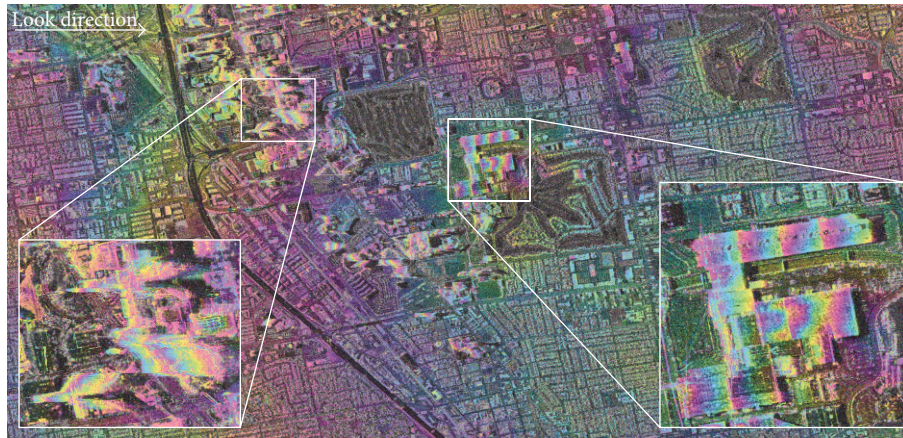


FIGURE 14: TerraSAR-X flattened interferogram in radar coordinates with amplitude image in background. Subsets show hotels and the Las Vegas Convention Center. Temporal baseline 110 days, perpendicular baseline: 48.1 m.

On the subject of coherence—which is a strong indicator for the quality of an interferogram—the effect of bistatic acquisitions compared to repeat pass interferometry becomes apparent. In the bistatic TDM image pair over Las Vegas, we observe a mean coherence for the whole scene of about 0.7048, see Figure 15. However comparing this with a pair of TerraSAR-X acquisitions with a temporal baseline of 11 days gives a mean coherence of 0.6486, see Figure 16. The mentioned pair was taken on 2010-09-19 for the master and 2010-09-08 for the slave. Picking two images with a longer temporal baseline of 110 days for 2010-03-24 (master) and 2010-07-12 (slave) gives a mean coherence of 0.5206, see Figure 17 for a histogram as well.

Comparing the relatively dense urbanized scene of Las Vegas with a relatively rural setting in Lüneburg illustrates the following. The coherence for any scene in Lüneburg is rather low, for example, a temporal baseline of 22 days in summer between the images taken on the 2010-07-16 and 2010-06-24 gives a mean coherence of 0.4029. There are two special cases: one in Las Vegas and one in Lüneburg where very low

coherence was noticeable by visual interpretation. The image pairs in question are 2010-03-24 with 2010-08-03 (Las Vegas) and 2010-07-16 with 2010-01-10 (Lüneburg) which show a mean coherence value of 0.4071 and 0.3506, respectively. In the case of Lüneburg we were able to retrace the possible cause by checking the weather data, that was snowfall [25] on that particular day.

5. Conclusion

In this paper, we explained the steps necessary to process bistatic and monostatic TanDEM-X and TerraSAR-X image acquisitions utilizing a public domain tool: DORIS. DORIS was modified and extended for this purpose. We have also clarified the basic concepts of bistatic acquisitions and illustrated linear Doppler drift, which occurs during the beam steering technique used in spotlight image creation. We specifically focused on the generation of a Doppler frequency matrix that is used to shift the interpolation kernel during



FIGURE 15: TanDEM-X coherence image. The brighter the more coherent. Parks and water become visible due to the effects of wind.



FIGURE 16: TerraSAR-X repeat pass coherence image. Master 2010-07-12 slave: 2010-03-24.

resampling. Furthermore experimental results based on several input datasets, demonstrated that our implementation gives consistently good output. A comparison of bistatic TDM and monostatic TSX/TDX interferograms shows the difference in phase and general coherence.

The character of the paper is rather instructional with a focus on the explanation of bi- and monostatic very high-resolution SAR images. The key point lies within the guidance to understand and produce TSX spotlight interferograms. We also show that advanced image acquisition techniques like spotlight and or bistatic spotlight can be processed with already available open-source software solutions. Additionally, it demonstrates the quality and consistency of the data which has been used in the experiments. This paper can serve as a basis for future papers by illustrating the potential of the very high-resolution repeat or single pass SAR interferometry.

A TanDEM-X interferogram can be retrieved by just a few modifications in the source code of DORIS. The overall

coherence of the image is relatively high, given the very short temporal baseline in bistatic acquisitions. Experimental results showed that the roof of the Las Vegas Convention Center or other buildings can exhibit thermal deformation. This is observable due to the phase information. In the case of TDM, the phase is very homogenous because of the contemporaneous image acquisition. That indicates no motion, at least not detectable with SAR within the acquisition period.

Particularly interesting is the comparison of the bistatic and monostatic images. The overall coherence of a TDM is, as expected, very high. Even water does not show up with the significant dark signature. The TSX image pair with 110 days temporal baseline is less coherent, and objects in quick motion like trees/leaves and water show very low coherence.

Spotlight InSAR in DORIS requires some modifications to calculate consistent interferograms. The annotated Doppler information in the XML metafile have to be evaluated, and a Doppler frequency matrix was created. It was then used to shift the six-point cubic convolution kernel

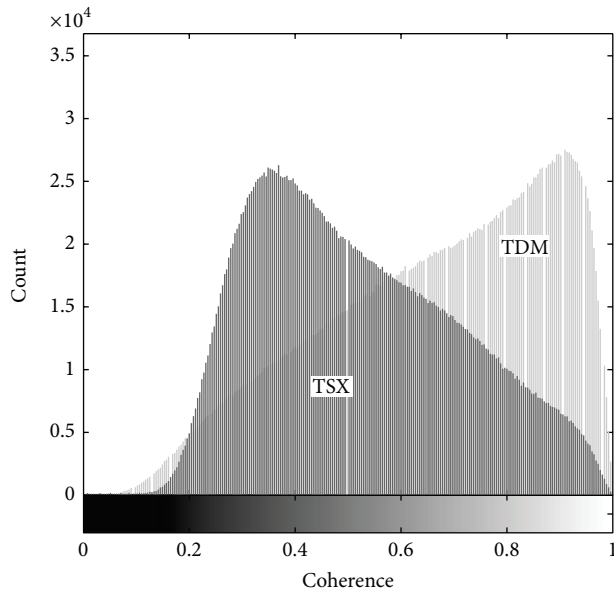


FIGURE 17: Coherence histogram comparison between TerraSAR-X (TSX) with 110 days B_{temp} and a TanDEM-X product (TDM).

during the resampling stage to match both image spectra. A new “cc6p_SP” option in the processing input card “RS_METHOD” in DORIS has been added to accomplish this. We have compared the result to a calculation that used the default kernel shift in DORIS. The result was expectantly distorted. Additionally, we compared to a result made by a commercially available software, with very high agreement to our result.

Interpreting the phase information on the roof of the Las Vegas Convention Center gave evidence of correlation between temperature and number of fringes or distance between fringes, respectively. The higher the temperature differences to the master image the greater the deformation. This was qualitatively assessed by looking at the fringes appearing for separate roof sections.

The initial goal was to provide an implementation of an already known algorithm to process TerraSAR-X spotlight images in freely available software, DORIS. As seen from the results, the integrated processing option to shift the interpolation kernel according to the Doppler frequency works seamlessly and effectively. It enables researchers to process high-resolution spotlight interferograms.

The code is directly available upon request from the corresponding author and will probably be included in the next release of DORIS.

Acknowledgments

This work is financially supported by the National Key Basic Research Program of China (Grant no. 2013CB733205), the National Natural Science Foundation of China (Grant no. 41174120), and the German Academic Exchange Service (DAAD). The authors would like to thank the German

Aerospace Center (DLR) for providing the test datasets via the DLR AO LAN1301 and LAN0634.

References

- [1] M. Eineder, H. Runge, E. Börner et al., “SAR interferometry with TerraSAR-X,” in *Proceedings of FRINGE Workshop*, Frascati, Italy, December 2003.
- [2] R. Hanssen, *Radar Interferometry: Data Interpretation and Error Analysis*, 2001.
- [3] I. Woodhouse, *Introduction to Microwave Remote Sensing*, 2005.
- [4] G. Krieger and A. Moreira, “TanDEM-X: a satellite formation for high-resolution SAR interferometry,” *IEEE Transactions on Geoscience and Remote Sensing*, vol. 45, no. 11, pp. 3317–3341, 2007.
- [5] U. Soergel, U. Thoennessen, A. Brenner, and U. Stilla, “High-resolution SAR data: new opportunities and challenges for the analysis of urban areas,” *IEE Proceedings: Radar, Sonar and Navigation*, vol. 153, no. 3, pp. 294–300, 2006.
- [6] P. Gamba, B. Houshmand, and M. Sacconi, “Detection and extraction of buildings from interferometric SAR data,” *IEEE Transactions on Geoscience and Remote Sensing*, vol. 38, no. 1, pp. 611–618, 2000.
- [7] T. Balz and M. Liao, “Building-damage detection using postseismic high-resolution SAR satellite data,” *International Journal of Remote Sensing*, vol. 31, no. 13, pp. 3369–3391, 2010.
- [8] Y. Dong, Q. Li, A. Dou, and X. Wang, “Extracting damages caused by the 2008 Ms 8.0 Wenchuan earthquake from SAR remote sensing data,” *Journal of Asian Earth Sciences*, vol. 40, no. 4, pp. 907–914, 2011.
- [9] D. Ehrlich, H. D. Guo, K. Molch, J. W. Ma, and M. Pesaresi, “Identifying damage caused by the 2008 Wenchuan earthquake from VHR remote sensing data,” *International Journal of Digital Earth*, vol. 2, no. 4, pp. 309–326, 2009.
- [10] T. Moon, I. Joughin, B. Smith, and I. Howat, “21st-century evolution of greenland outlet glacier velocities,” *Science*, vol. 336, no. 6081, pp. 576–578, 2012.
- [11] D. Perissin, Z. Wang, and H. Lin, “Shanghai subway tunnels and highways monitoring through Cosmo-SkyMed Persistent Scatterers,” *ISPRS Journal of Photogrammetry and Remote Sensing*, vol. 73, pp. 58–67, 2012.
- [12] T. Wang and D. Perissin, “Deformation monitoring by long term D-InSAR analysis in Three Gorges area, China,” *IEEE Geoscience and Remote Sensing Letters*, vol. 4, pp. 7–10, 2008.
- [13] German Aerospace Agency, DLR, “TerraSAR-X ground segment basic product specification document,” in *Working Paper TX-GS-DD-3*, no. 1.7, 2010.
- [14] M. Eineder, N. Adam, R. Bamler, N. Yague-Martinez, and H. Breit, “Spaceborne spotlight SAR interferometry with TerraSAR-X,” *IEEE Transactions on Geoscience and Remote Sensing*, vol. 47, no. 5, pp. 1524–1535, 2009.
- [15] B. Kampes, R. Hanssen, and Z. Perski, “Radar interferometry with public domain tools,” in *Proceedings of FRINGE Workshop*, Frascati, Italy, December 2003.
- [16] H. Fiedler, G. Krieger, M. Werner, and K. Reiniger, “The TanDEM-X mission design and data acquisition plan,” in *Proceedings of the European Conference on Synthetic Aperture Radar (EUSAR '06)*, Dresden, Germany, May 2006.
- [17] German Aerospace Agency, DLR, “TanDEM-X ground segment experimental product description,” in *Working Paper TD-GS-PS-3028*, no. 1.2, 2007.

- [18] J. Tu, D. Gu, Y. Wu, and D. Yi, "Error modeling and analysis for InSAR spatial baseline determination of satellite formation flying," *Mathematical Problems in Engineering*, vol. 2012, pp. 1–23, 2012.
- [19] J. van der Zijp, "Fast half float conversions," Working paper, 2012, [ftp://www.fox-toolkit.org/pub/fasthalffloatconversion.pdf](http://www.fox-toolkit.org/pub/fasthalffloatconversion.pdf).
- [20] C. Rau, "Half-precision floating point library," sourceforge.net, 2012, <http://half.sourceforge.net/>.
- [21] Technical University Delft, "Delft Object-oriented Radar Interferometric Software User's manual and technical documentation," Tech. Rep., Delft, The Netherlands, 2008.
- [22] R. Hanssen and R. Bamler, "Evaluation of interpolation kernels for SAR interferometry," *IEEE Transactions on Geoscience and Remote Sensing*, vol. 37, no. 1, pp. 318–321, 1999.
- [23] German Aerospace Agency, DLR, "TerraSAR-X ground segment level 1b product format specification," in *Working Paper TX-GS-DD-3307*, no. 1.3, 2007.
- [24] ASTRIUM, "Sample Imagery, Australia, Urulu—InSAR," 2009, <http://www.astrium-geo.com/en/23-sample-imagery>.
- [25] The Weather Channel Companies, "Weather Underground," 2010, <http://www.wunderground.com/>.

Research Article

Modeling Multilook Magnitude and Phase in Extremely Heterogeneous Clutter

Gui Gao, Gongtao Shi, and Shilin Zhou

College of Electronic Science and Engineering, National University of Defense Technology, Changsha, Hunan 410073, China

Correspondence should be addressed to Gui Gao; dellar@126.com

Received 30 December 2012; Accepted 18 January 2013

Academic Editor: Deren Li

Copyright © 2013 Gui Gao et al. This is an open access article distributed under the Creative Commons Attribution License, which permits unrestricted use, distribution, and reproduction in any medium, provided the original work is properly cited.

This paper proposes a joint distribution of magnitude and phase for multilook SAR interferogram in extremely heterogeneous clutter. The presented theoretical distribution, called simply here \mathcal{F}^2 distribution and derived from the multiplicative model and the known joint distribution of the homogeneous clutter, is shown to be able to model the extremely heterogeneous clutter areas. Moreover, we estimate distribution parameters by means of the well-known method-of-log-cumulants (MoLC). The experimental results applied on actual dual-channel SAR images prove the good performance of the proposed distribution.

1. Introduction

Ground moving target identification (GMTI) using synthetic aperture radar (SAR) has been a growing interest over the last couple of decades in many applications, such as military surveillance and reconnaissance of ground vehicles and civilian ship monitoring of harbor [1–3]. The recent works [3, 4] reported in this field show that the multilook interferogram, defined as the product of the first channel and the complex conjugate of the second, is an important tool for detecting moving targets. However, precise knowledge of the interferogram's phase and magnitude statistics, that is, the joint probability density function (PDF), is a major issue currently under study in the development of statistically based detector tests for distinguishing the moving targets from clutter [3–5].

Some investigations for statistical modeling of multilook SAR interferogram have been presented in the past, for example, [3–5]. Lee et al. [5] firstly proposed the joint distribution of interferometric magnitude and phase with the condition of a constant radar cross section (RCS) background based on the complex Wishart distribution, presented by Goodman

[6]. The analytical expression of this joint distribution is given as [5]

$$p_{\xi, \psi}(\xi, \psi) = \frac{2n^{n+1}\xi^n}{\pi\Gamma(n)(1-\rho^2)} \exp\left(\frac{2n\rho\xi\cos\psi}{1-\rho^2}\right) K_{n-1}\left(\frac{2n\xi}{1-\rho^2}\right), \quad (1)$$

where ξ and ψ are the normalized interferogram's magnitude and the multilook phase. n represents number of looks, and ρ indicates the magnitude of the complex correlation coefficient. $K_{n-1}(\cdot)$ is the second type modified Bessel function with order $(n-1)$. $\Gamma(\cdot)$ indicates the Gamma function. In the analysis of lot of literatures, it is shown [3–5] that the PDF shown in (1) is valid for modeling homogeneous areas, whereas it also tends to deviate strongly in most cases whose scenes contain heterogeneous or extremely heterogeneous regions.

Additionally, as the phase statistic is highly invariant against changes of the clutter type [3], the marginal PDFs of interferometric magnitude for heterogeneous and extremely heterogeneous regions are derived by Gierull [4]. Meanwhile,

an original joint PDF of interferometric magnitude and phase for heterogeneous clutter is also given in afore-mentioned literature. Unfortunately, the joint PDFs of interferometric magnitude and phase for extremely heterogeneous regions are still a hard task by means of combining the marginal PDFs of magnitude and the ones of phase owing to that ξ and ψ are not statistically independent [3].

In this paper, our objective is to present a novel joint distribution of interferometric magnitude and phase for extremely heterogeneous clutter. We test the performance of the proposed distribution utilizing a representative dual-channel SAR image of urban area described as an extremely heterogeneous region.

2. The Joint Distribution

2.1. The Known Joint Distribution for Heterogeneous Regions. Considering an n -look interferogram I_n , it is the average of n single-look interferograms. Assuming the energy of two channels is identical, it is well known that I_n can be modeled by the multiplicative model as [4]

$$I_n = A^2 \xi e^{j\psi}, \quad (2)$$

where A represents the backscattering RCS magnitude of each channel.

As analyzed by Frery et al. [7], the random variable A obeys a reciprocal of the square root of a Gamma distribution to characterize highly heterogeneous situation, that is, $A \sim \Gamma^{-1/2}(-\alpha, \gamma)$. Supposing $W = A^2$, the PDF of W is given by

$$p_W(w) = \frac{\gamma^{-\alpha}}{\Gamma(-\alpha)} w^{\alpha-1} \exp\left(-\frac{\gamma}{w}\right), \quad -\alpha, \gamma > 0, \quad (3)$$

where α ($-\alpha \in (0, \infty)$) is a shape parameter, which essentially reflects the degrees of homogeneity for processed areas. γ is a scale parameter related to the mean energy of processed areas.

Therefore, the modified interferometric magnitude η of heterogeneous clutter is given as $\eta = A^2 \xi := W\xi$ and the joint distribution of η and ψ can be expressed by

$$p_{\eta, \psi}(\eta, \psi) = \int_0^\infty p_W(w) p(\eta | w, \psi) dw. \quad (4)$$

Applying (1), we get the right hand-side of the integral shown in (4) as

$$\begin{aligned} p(\eta | w, \psi) &= \frac{1}{w} P\left(\frac{\eta}{w}, \psi\right) \\ &= \frac{2n^{n+1} \eta^n}{\pi \Gamma(n) (1-\rho^2)} \left(\frac{1}{w}\right)^{n+1} \\ &\quad \times \exp\left(\frac{2n\eta\rho \cos \psi}{1-\rho^2} \times \frac{1}{w}\right) K_{n-1}\left(\frac{2n\eta}{1-\rho^2} \times \frac{1}{w}\right). \end{aligned} \quad (5)$$

Combining (3) and (5) by (4), and utilizing the integral formula $\int_0^\infty x^{\mu-1} e^{-ax} K_\nu(bx) dx = (\sqrt{\pi}(2b)^\nu / (a+b)^{\mu+\nu}) \cdot$

$((\Gamma(\mu+\nu)\Gamma(\mu-\nu))/\Gamma(\mu+1/2)) {}_2F_1(\mu+\nu, \nu+1/2; \mu+1/2; (a-b)/(a+b))$ [8], the joint distribution of magnitude and phase in the heterogeneous clutter is finally derived as [4]

$$\begin{aligned} p_{\eta, \psi}(\eta, \psi) &= \frac{(2n)^{2n} \gamma^{-\alpha}}{2\sqrt{\pi}(1-\rho^2)^{-(n-\alpha)}} \cdot \frac{\Gamma(2n-\alpha)\Gamma(-\alpha+2)}{\Gamma(n)\Gamma(-\alpha)\Gamma(n-\alpha+3/2)} \cdot \eta^{2n-1} \\ &\quad \cdot [f_1(\eta, \psi)]^{-(2n-\alpha)} \\ &\quad \cdot {}_2F_1\left(2n-\alpha, n-\frac{1}{2}; n-\alpha+\frac{3}{2}; f_2(\eta, \psi)\right), \end{aligned} \quad (6)$$

where ${}_2F_1$ is the Gauss hypergeometric function and

$$\begin{aligned} f_1(\eta, \psi) &= (1-\rho^2)\gamma + 2n\eta(1-\rho \cos \psi), \\ f_2(\eta, \psi) &= \frac{(1-\rho^2)\gamma - 2n\eta(1+\rho \cos \psi)}{(1-\rho^2)\gamma + 2n\eta(1-\rho \cos \psi)}. \end{aligned} \quad (7)$$

2.2. The New Joint Distribution for Extremely Heterogeneous Regions. For extremely heterogeneous clutter like the urban areas, the histograms show the heavy trail. To solve this problem, Gierull [4] proposed a transformation of η into $\varsigma = \eta^\delta$, $\delta \in \mathbb{R}^+$, where the interferometric magnitude ς and phase of extremely heterogeneous clutter can be derived by (6) with Jacobian $\det |J| = (1/\delta)\eta^{1/\delta-1}$ to

$$\begin{aligned} p_{\varsigma, \psi}(\varsigma, \psi) &= \frac{(2n)^{2n} \gamma^{-\alpha}}{2\sqrt{\pi}\delta(1-\rho^2)^{-(n-\alpha)}} \cdot \frac{\Gamma(2n-\alpha)\Gamma(-\alpha+2)}{\Gamma(n)\Gamma(-\alpha)\Gamma(n-\alpha+3/2)} \\ &\quad \cdot \varsigma^{(2n/\delta)-1} [f'_1(\varsigma, \psi)]^{-(2n-\alpha)} \end{aligned} \quad (8)$$

$$\times {}_2F_1\left(2n-\alpha, n-\frac{1}{2}; n-\alpha+\frac{3}{2}; f'_2(\varsigma, \psi)\right),$$

where $f'_1(\varsigma, \psi)$ and $f'_2(\varsigma, \psi)$ are the following functions:

$$\begin{aligned} f'_1(\varsigma, \psi) &= (1-\rho^2)\gamma + 2n\varsigma^{1/\delta}(1-\rho \cos \psi), \\ f'_2(\varsigma, \psi) &= \frac{(1-\rho^2)\gamma - 2n\varsigma^{1/\delta}(1+\rho \cos \psi)}{(1-\rho^2)\gamma + 2n\varsigma^{1/\delta}(1-\rho \cos \psi)}. \end{aligned} \quad (9)$$

Hereafter (8) is denoted simply by \mathcal{F}^2 . The marginal PDF of interferometric magnitude ς is further given by integrating (8) with respect to the phase ψ as

$$\begin{aligned} p_\varsigma(\varsigma) &= \left(\frac{2n}{\gamma(1+\rho)}\right)^n \cdot \frac{\Gamma(n-\alpha)}{\delta \Gamma(n)\Gamma(-\alpha)} \\ &\quad \cdot \frac{\varsigma^{(n/\delta)-1}}{(1+(2n/\gamma(1+\rho))\varsigma^{1/\delta})^{n-\alpha}}, \quad \rho, -\alpha, \gamma, n, \delta, \varsigma > 0. \end{aligned} \quad (10)$$

$$p_{\xi,\psi}(\xi, \psi) \xrightarrow[\bar{D}]{\substack{\delta \rightarrow 1, \\ -\alpha, \gamma > 0}} p_{\eta,\psi}(\eta, \psi) \xrightarrow[\bar{D}]{\substack{-\alpha, \gamma \rightarrow \infty, \\ (-\alpha/\gamma) \rightarrow 1}} p_{\xi,\psi}(\xi, \psi)$$

FIGURE 1: The relationship of the joint distributions.

2.3. Relationship between Distributions. The relations of the aforementioned joint distributions are summarized in Figure 1, where the symbol \bar{D} denotes the convergence in distribution. It is clear from the derivations of (5) and (8) that the \mathcal{F}^2 distribution converges to the $p_{\eta,\psi}(\eta, \psi)$ when $-\alpha, \gamma > 0$, $\delta \rightarrow 1$. Similarly, $p_{\eta,\psi}(\eta, \psi)$ also converges to $p_{\xi,\psi}(\xi, \psi)$ under the condition that $-\alpha, \gamma \rightarrow \infty$, $(-\alpha/\gamma) \rightarrow 1$. The properties stated in Figure 1 show that either homogeneous, heterogeneous, or extremely heterogeneous interferogram's magnitude and phase statistics can be treated as the outcome of the proposed \mathcal{F}^2 distribution.

3. Parameter Estimations

The MoLC, which relies on the Mellin transform [9], is a more feasible parametric PDF estimation technique for distributions defined on $[0, +\infty)$. Given p as a function defined over \mathbb{R}^+ , the Mellin transform of p is defined as

$$\mathcal{M}[p(x)](s) = \int_0^{\infty} x^{s-1} p(x) dx. \quad (11)$$

Thus, the second-kind first characteristic function and the second-kind second characteristic function are given, respectively, by

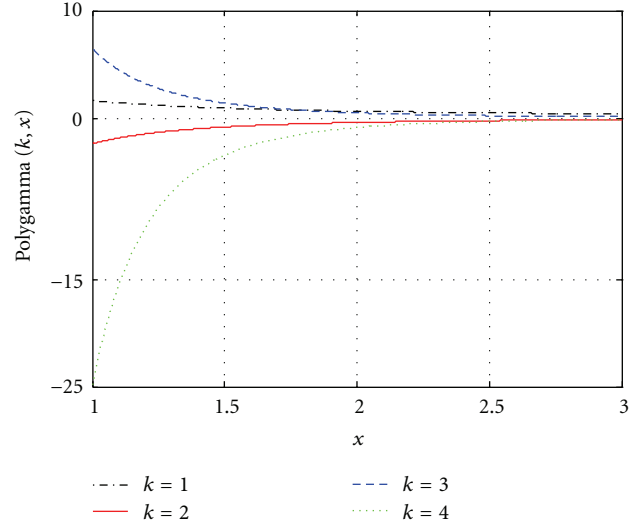
$$\begin{aligned} \phi(s) &= \mathcal{M}[p(x)](s) = \int_0^{\infty} x^{s-1} p(x) dx, \\ \Phi(s) &= \ln \phi(s). \end{aligned} \quad (12)$$

The estimate $\hat{\rho}$ of parameter ρ has been obtained by Abdelfattah and Nicolas; the details can be found in [10]. However, here, we are interested in estimates of the parameters α , γ , n , and δ in the \mathcal{F}^2 distribution. To make the deriving process be simplified, we notice that the parameters of the \mathcal{F}^2 distribution and the corresponding marginal PDF of magnitude given by (10) are identical. Motivated by this property, by plugging (10) into (12), one gets

$$\begin{aligned} \phi(s) &= \left(\frac{\gamma(1+\rho)}{2n} \right)^{\delta(s-1)} \\ &\cdot \frac{\Gamma(n+\delta(s-1)) \Gamma(-\alpha-\delta(s-1))}{\Gamma(n) \Gamma(-\alpha)}, \end{aligned} \quad (13)$$

$$\begin{aligned} \Phi(s) &= \delta(s-1) \ln \left(\frac{\gamma(1+\rho)}{2n} \right) + \ln \Gamma(n+\delta(s-1)) \\ &+ \ln \Gamma(-\alpha-\delta(s-1)) - \ln \left(\frac{\Gamma(n)}{\Gamma(-\alpha)} \right). \end{aligned}$$

The k th-order derivative of $\Phi(s)$ at $s = 1$ is the k th-order second-kind cumulant also named "log-cumulant."


 FIGURE 2: The $\Psi(k, \cdot)$ function.

Consequently, the k th-order log-cumulants corresponding to the \mathcal{F}^2 distribution are

$$\tilde{c}_1 = \delta \left[\ln \left(\frac{\gamma(1+\hat{\rho})}{2n} \right) + \Psi(n) - \Psi(-\alpha) \right], \quad (14)$$

$$\tilde{c}_k = \delta^k \left[\Psi(k-1, n) + (-1)^k \Psi(k-1, -\alpha) \right], \quad k \geq 2, \quad (15)$$

where $\Psi(\cdot)$ represents the digamma function and $\Psi(k, \cdot)$ is the k th-order polygamma function. Additionally, the log-cumulants \tilde{c}_k can be directly estimated by N samples x_i as follows:

$$\hat{\tilde{c}}_1 = \frac{1}{N} \sum_{i=1}^N [\ln(x_i)], \quad (16)$$

$$\hat{\tilde{c}}_k = \frac{1}{N} \sum_{i=1}^N \left[(\ln(x_i) - \hat{\tilde{c}}_1)^k \right], \quad k \geq 2.$$

The $\Psi(k, \cdot)$ functions with varying k are shown in Figure 2. Thus (15) is continuous and strictly monotonically for each parameter of δ , n , and α . To obtain the numerical solution quickly and simply, we set k as an even (i.e., letting $k = 2$, $k = 4$ and $k = 6$ in (15), resp.). On the other hand, we stress that (15) does not contain γ , thus allowing us to split the nonlinear solution procedure into two distinct stages. First, the estimates $\hat{\delta}$, \hat{n} , and $\hat{\alpha}$ of the parameters δ , n , and α are acquired by solving (15) and (16), that is,

$$\hat{\delta}^2 [\Psi(1, \hat{n}) + \Psi(1, -\hat{\alpha})] = \frac{1}{N} \sum_{i=1}^N \left[(\ln(x_i) - \hat{\tilde{c}}_1)^2 \right],$$

$$\hat{\delta}^4 [\Psi(3, \hat{n}) + \Psi(3, -\hat{\alpha})] = \frac{1}{N} \sum_{i=1}^N \left[(\ln(x_i) - \hat{\tilde{c}}_1)^4 \right], \quad (17)$$

$$\hat{\delta}^6 [\Psi(5, \hat{n}) + \Psi(5, -\hat{\alpha})] = \frac{1}{N} \sum_{i=1}^N \left[(\ln(x_i) - \hat{\tilde{c}}_1)^6 \right].$$



FIGURE 3: The tested SAR data of urban.

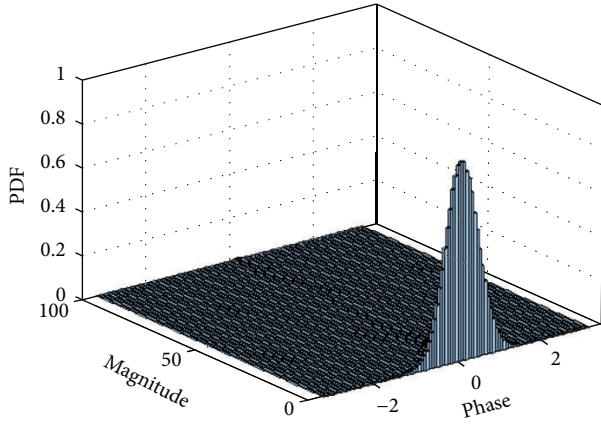


FIGURE 4: The three-dimension histogram of the tested urban area.

Second, via (14) and (16), the estimate $\hat{\gamma}$ of the parameter γ is

$$\hat{\gamma} = 2\hat{n} \exp \frac{\left(\left(\frac{1}{N\hat{\delta}} \right) \sum_{i=1}^N [\ln(x_i)] - \Psi(\hat{n}) + \Psi(-\hat{\alpha}) \right)}{(1 + \hat{\rho})}. \quad (18)$$

4. Experimental Analysis

In this section, we present simulation results obtained by measured SAR data using the proposed \mathcal{F}^2 distribution. Especially, we provide the fitting performance of urban area indicated as extremely heterogeneous clutter to support the prior theoretical analysis that the \mathcal{F}^2 distribution is able to model the clutter areas with widely varying degrees of homogeneity.

As a representative example, the test dual-channel SAR data of urban used in this study were acquired by an airborne SAR system of China in Beijing operated in X band and HH polarization, with the spatial resolution 10 m \times 2 m (azimuth

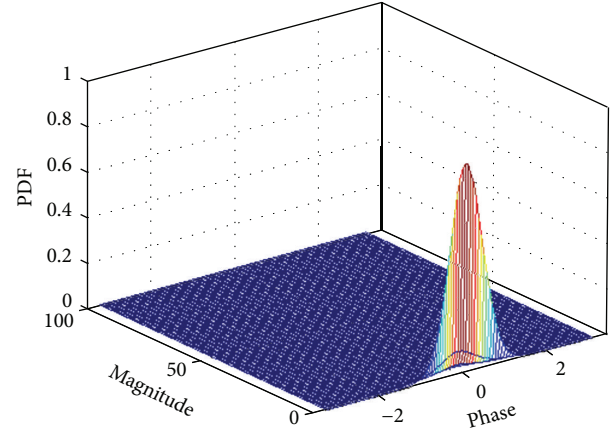
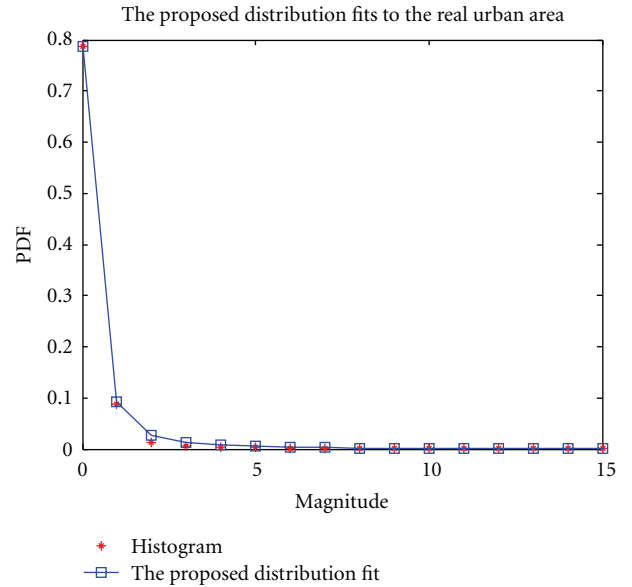


FIGURE 5: The estimated PDF of the previous area.

FIGURE 6: Plots of fitting results by limiting $\psi = 0$

\times range); see Figure 3. The three-dimension histogram of the urban interferogram is shown in Figure 4.

We apply the proposed parametric estimation algorithm in Section 3 to the above-mentioned urban area. The results of parametric estimation of the corresponding \mathcal{F}^2 distribution are listed in Table 1. Based on these estimated parameters, the fitting histogram is given in Figure 5. It is clearly seen that the \mathcal{F}^2 distribution performs very well in fitting the histogram of the urban area from the viewpoint of the visual comparison between the histogram and the estimated PDF.

Furthermore, in order to assess the effectiveness of the presented \mathcal{F}^2 distribution, we test the developed model on the previous urban area by limiting various phase ψ values. Figure 6 yields the fitting result with the condition of $\psi = 0$. It is easy to observe that the \mathcal{F}^2 distribution agrees well with the given urban area which implies the wide modeling ability of the proposed distribution, as expected.

TABLE 1: Parameter estimations of noted clutter areas in Figure 3.

\mathcal{F}^2	$\hat{\rho}$	0.7659
	\hat{n}	0.9107
	$\hat{\alpha}$	-0.9108
	$\hat{\gamma}$	0.1404
	$\hat{\delta}$	0.9897

5. Conclusion

In this paper, we have developed a joint distribution of magnitude and phase for multilook SAR interferogram in extremely heterogeneous clutter. We also provide the corresponding parameter estimation technique based on the MoLC. The theoretical analysis and experimental results of measured multilook SAR data both have shown the good performance modeling extremely heterogeneous clutter. Since either homogeneous, heterogeneous, or extremely heterogeneous interferogram's magnitude and phase statistics can be treated as the outcome of the proposed \mathcal{F}^2 distribution (as Figure 1 stated), the presented distribution turns out to be suitable for the clutter with widely varying degrees of homogeneity.

Acknowledgment

The author would like to acknowledge the National Natural Science Foundation of China for the support under Grant 41171316.

References

- [1] D. Cerutti-Maori, J. Klare, A. R. Brenner, and J. H. G. Ender, "Wide-area traffic monitoring with the SAR/GMTI system PAMIR," *IEEE Transactions on Geoscience and Remote Sensing*, vol. 46, no. 10, pp. 3019–3030, 2008.
- [2] E. Chapin and C. W. Chen, "Along-track interferometry for ground moving target indication," *IEEE Aerospace and Electronic Systems Magazine*, vol. 23, no. 6, pp. 19–24, 2008.
- [3] I. C. Sikaneta, *Detection of ground moving objects with synthetic aperture radar [Ph.D. thesis]*, University of Ottawa, 2002.
- [4] C. H. Gierull, "Statistical analysis of multilook SAR interferograms for CFAR detection of ground moving targets," *IEEE Transactions on Geoscience and Remote Sensing*, vol. 42, no. 4, pp. 691–701, 2004.
- [5] J. S. Lee, K. W. Hoppel, S. A. Mango, and A. R. Miller, "Intensity and phase statistics of multilook polarimetric and interferometric SAR imagery," *IEEE Transactions on Geoscience and Remote Sensing*, vol. 32, no. 5, pp. 1017–1028, 1994.
- [6] N. R. Goodman, "Statistical analysis based on a certain multivariate complex gaussian distribution (an introduction)," *The Annals of Mathematical Statistics*, vol. 34, no. 1, pp. 152–177, 1963.
- [7] A. C. Frery, H. J. Muller, C. C. F. Yanasse, and S. J. S. Sant'Anna, "A model for extremely heterogeneous clutter," *IEEE Transactions on Geoscience and Remote Sensing*, vol. 35, no. 3, pp. 648–659, 1997.
- [8] S. I. Gradshteyn and I. M. Ryzhik, *Table of Integrals, Series, and Products*, Academic Press, San Diego, Calif, USA, 7th edition, 2007.

- [9] J. M. Nicolas, "Introduction to second kind statistic: application of log-moments and log-cumulants to SAR image law analysis," *Traitement du Signal*, vol. 19, no. 3, pp. 139–167, 2002.
- [10] R. Abdelfattah and J. M. Nicolas, "Interferometric SAR coherence magnitude estimation using second kind statistics," *IEEE Transactions on Geoscience and Remote Sensing*, vol. 44, no. 7, pp. 1942–1953, 2006.

Research Article

Ship Detection in High-Resolution Dual-Polarization SAR Amplitude Images

Gui Gao, Gongtao Shi, and Shilin Zhou

School of Electronics Science and Engineering, National University of Defense Technology, Changsha, Hunan 410073, China

Correspondence should be addressed to Gui Gao; dellar@126.com

Received 31 October 2012; Accepted 8 January 2013

Academic Editor: Deren Li

Copyright © 2013 Gui Gao et al. This is an open access article distributed under the Creative Commons Attribution License, which permits unrestricted use, distribution, and reproduction in any medium, provided the original work is properly cited.

A constant false alarm rate (CFAR) detecting method for ships in high-resolution dual-polarization synthetic aperture radar (SAR) amplitude images has been proposed in this paper. First, by the production of amplitude images from two polarimetric channels, a novel detector simply called the PMA detector has been constructed. We testified that the PMA detector could improve the signal-to-clutter ratio (SCR) and make the discrimination of a ship from clutter more easily. Second, the PMA detector's statistical model has been described by the well-known \mathcal{G}^0 distribution when facing complex sea background. The experiments performed on measured dual-polarization TerraSAR-X images demonstrate the good performance of the proposed CFAR detecting method.

1. Introduction

Ship detection in high-resolution synthetic aperture radar (SAR) images has become an increasing interest during the past several years [1]. It plays an important role for various potential applications like marine surveillance, vessel traffic control, military service, and so forth [1–3]. Additionally, with the development of sensor techniques, the advanced polarimetric SAR systems have also been validated that more completed description of target-scattering behavior could be provided than traditional single-channel SAR systems, such as HH, HV, and VV SAR, which is not sufficient for ship detection [2, 4]. Since better discriminating target signal from the surrounding clutter can be obtained by polarimetric SAR systems, ship detection in multipolarimetric or dual-polarimetric SAR images is receiving intensive attentions in present.

Nowadays, some famous contemporary satellite SAR systems, for example, TerraSAR-X, COSMO-SkyMed, and RadarSat-2, support dual-polarization acquisition mode [5]. However, the available data is, mostly, the amplitude data and not the complex-valued data [6]. It is an important data modality because of the image products provided by many satellite SAR systems, for instance, ERS. Thus, we mainly

focus on ship detection using only dual-pol SAR amplitude images in this paper.

A wide variety of methods have been proposed for detecting ships in polarimetric SAR images. The basic idea is to reduce three channels of polarimetric SAR data to a single decision criterion [7]. Some popular detectors [7], including the optimal polarimetric detector (OPD), the polarimetric whitening filter (PWF), the span detector, the power maximization synthesis (PMS) detector, and, more recently, the identity likelihood ratio test (ILRT), have been developed and shown that they can perform in a way that targets are more easily discriminated from clutter. Unfortunately, other detectors mentioned earlier except for the span detector are very difficult to implement due to the missing of phase information when the only amplitude is considered [7].

The span detector is a widely used processor which is a noncoherent sum of all polarimetric channels and only makes use of image intensities or amplitudes. It has also been proven that this detector can acquire a better detection performance than HH, HV, or VV individually. Nevertheless, the expected adaptive detection threshold is impossible when facing complex clutter background by this detector, which limits the applications of this detector.

Our goal is to present a powerful detector for ship detection in high-resolution dual-polarization SAR amplitude images. On one hand, this detector can improve the signal-to-clutter ratio (SCR) to enhance the moving targets or restrain the clutter. Meanwhile, we wish that a flexible and adaptive constant false alarm rate (CFAR) threshold could be derived from this detector. Under this consideration, this paper proposed a novel detector similarly with the span detector, simply called the product of multilook amplitudes (PMAs) detector.

2. Dual-Polarization SAR Data Description

The fundamental quantities measured by a polarimetric SAR are the complex scattering matrix with four elements, which, in complete form, can be expressed by [8]

$$\mathbf{S} = \begin{bmatrix} S_{hh} & S_{hv} \\ S_{vh} & S_{vv} \end{bmatrix}, \quad (1)$$

where S_{pq} is the scattering element with p transmit and q receive polarizations; p and q denote either horizontal (h) or vertical (v) polarization. In a reciprocal medium, the cross-polar elements of the scattering are identical; that is, $S_{hv} = S_{vh}$. In this matter, the scattering matrix shown in (1) can be organized into a column vector

$$\mathbf{X} = [S_{hh} \ S_{hv} \ S_{vv}]^T, \quad (2)$$

where the superscript “T” represents transpose. The equation (2) is called single-look complex scattering vector. Based on the coherent nature of SAR, \mathbf{X} follows a zero mean multivariate complex Gaussian distribution. The detailed discussion about this distribution can be found in [8] and [10].

2.1. Polarimetric Covariance Matrix for Dual-Polarization Case. For dual-polarization case, the single look scattering vector shown in (2) can be simplified to

$$\mathbf{u} = [S_1 \ S_2]^T. \quad (3)$$

Herein, for convenience, we use S_1 or S_2 to indicate one of the scattering elements S_{hh} , S_{hv} , and S_{vv} in any order, as well as $S_1 \neq S_2$. Additionally, to reduce the influence of speckle, SAR data are often multi-look averaged. As the polarimetric information can also be represented by a covariance matrix, the n -look sample covariance matrix is defined as [8, 9]

$$\mathbf{R} = \frac{1}{n} \sum_{k=1}^n \mathbf{u}(k) \mathbf{u}(k)^H = \frac{1}{n} \sum_{k=1}^n \begin{bmatrix} |S_1(k)|^2 & S_1(k) S_2(k)^* \\ S_1(k)^* S_2(k) & |S_2(k)|^2 \end{bmatrix}, \quad (4)$$

where the superscript * means complex conjugate and H represents conjugate complex transpose, n is the number of looks, and $\mathbf{u}(k) = [S_1(k), S_2(k)]^T$ is the k th single-look image. Assuming statistical ergodicity and constant RCS

background, the random matrix \mathbf{R} , known as the complex Wishart distribution [10], is with probability density

$$p_{\mathbf{R}}(\mathbf{R}) = \frac{n^{2n} \det(\mathbf{R})^{n-2} \exp[-n \text{Tr}(\mathbf{C}^{-1} \mathbf{R})]}{\pi \Gamma(n) \Gamma(n-1) \det(\mathbf{C})^n}, \quad (5)$$

where $\Gamma(\cdot)$ is the gamma function, and $\text{Tr}(\cdot)$ indicates the matrix trace. The symbol $\det(\cdot)$ denotes the determinant operator, and the covariance matrix is 2×2 complex, Hermitian, written as

$$\mathbf{C} = E[\mathbf{u} \mathbf{u}^H] = \begin{bmatrix} E(|S_1|^2) & \sqrt{E(|S_1|^2) E(|S_2|^2)} \rho e^{j\theta} \\ \sqrt{E(|S_1|^2) E(|S_2|^2)} \rho e^{-j\theta} & E(|S_2|^2) \end{bmatrix}, \quad (6)$$

where $\rho e^{j\theta}$ is the complex correlation coefficient of two components in (3).

2.2. The Joint Distribution of Two Multilook Intensities from Different Polarimetric Channels. When only incomplete polarimetric data are available, for instance, the amplitude or intensity of copolarized components (i.e., HH and VV), the joint distribution of intensity, or amplitude from two correlated polarimetric channels is of importance for constructing signal processing algorithms such as detection and classification in this case. Lee et al. [8] have derived the PDF of joint normalized multilook intensities by integrating (5) with respect to the two off-diagonal elements, which is modeled as

$$p_{R_1, R_2}(R_1, R_2) = \frac{n^{n+1} (R_1 R_2)^{(n-1)/2} \exp(-n(R_1 + R_2)/(1 - \rho^2))}{\Gamma(n) (1 - \rho^2) \rho^{n-1}} \times I_{n-1} \left(2n \sqrt{R_1 R_2} \frac{\rho}{1 - \rho^2} \right), \quad R_1, R_2, n > 0, 0 < \rho < 1, \quad (7)$$

where $I_{n-1}(\cdot)$ is the first type modified Bessel function of order $n - 1$, R_i , $i = 1, 2$, represents normalized multi-look intensity of i th polarimetric channel with the expression $R_i = (1/n) \sum_{k=1}^n (|S_i(k)|^2 / E(|S_i|^2))$.

Furthermore, to facilitate the posterior derivation, by the transforms with the following forms:

$$\begin{aligned} B_1 &= nR_1, \\ B_2 &= nR_2, \end{aligned} \quad (8)$$

one can obtain the joint density of B_1 and B_2 as (see [8] for details)

$$p_{B_1, B_2}(B_1, B_2) = \frac{(B_1 B_2)^{(n-1)/2} \exp(-(B_1 + B_2)/(1 - \rho^2))}{\Gamma(n) (1 - \rho^2) \rho^{n-1}} \times I_{n-1} \left(2 \sqrt{B_1 B_2} \frac{\rho}{1 - \rho^2} \right), \quad B_1, B_2, n > 0, 0 < \rho < 1. \quad (9)$$

3. The PMA Detector

3.1. PMA Detector. In a single-channel SAR image, it is usually assumed that strong backscattering comes from targets. A target point will be lost when the backscattering amplitude or intensity from the target is not large enough compared with the clutter background, generally, due to low signal-to-clutter ratio (SCR). In other words, SCR is an essential factor influencing the detection performance when only amplitude or intensity data are available. Thus, the principle designing a good detector should naturally enable SCR to be improved, that is, enhancing target and restraining clutter.

As we know, the span detector is a widely used processor which is a noncoherent sum of all polarimetric channels and only makes use of image intensities. For dual-polarization multilook case, the span is given by [7]

$$\text{span} = \frac{1}{n} \sum_{k=1}^n |S_1(k)|^2 + \frac{1}{n} \sum_{k=1}^n |S_2(k)|^2. \quad (10)$$

This detector can be regarded as the synthetic power of all channels. Consequently, some investigations have shown that a lower noise level and a higher SCR can be obtained by this detector than HH, HV, or VV individually. This conclusion implies that the way of synthetic power can arrive at the purpose of improving SCR, so that the targets can be more easily discriminated from the clutter, compared with that only arbitrary single-channel information is used. Meanwhile, it is also very hard to adaptively give a proper detection threshold by the span detector due to the unknown knowledge of the corresponding statistics. Motivated by these considerations, we construct a detector in this paper by means of another synthetic power, that is, the product of multilook amplitudes from two polarimetric channels, for convenience, called PMA detector which can be defined as

$$\xi = \sigma_1 \sigma_2 \sqrt{R_1 R_2} = \sigma_1 \sigma_2 \frac{\sqrt{B_1 B_2}}{n}, \quad (11)$$

where $\sigma_i = E(|S_i|^2)$. From an intuitive understanding, in the variable ξ domain, for the targets, their amplitudes of two polarimetric channels are both larger than the surrounding clutter, which results in a much faster cumulative speed of power for targets verse clutter by multiplying the first image amplitude by the second image one, and, hence, targets' values of ξ are much more prominent and target signal can be enhanced.

3.2. The CFAR Algorithm of PMA Detector. For dual-pol SAR amplitude data, based on the multiplicative model and the assumption that the energy of two channels is balanced, the product of multilook amplitudes from two polarimetric channels can be denoted as

$$\begin{aligned} \zeta &= \sqrt{\frac{1}{n} \sum_{k=1}^n |A_1 X_1(k)|^2 \frac{1}{n} \sum_{k=1}^n |A_2 X_2(k)|^2} \\ &= \sqrt{A_1^2 A_2^2 \frac{1}{n} \sum_{k=1}^n |X_1(k)|^2 \frac{1}{n} \sum_{k=1}^n |X_2(k)|^2} = A_1 A_2 \xi, \end{aligned} \quad (12)$$

where A_i represents the backscattering RCS amplitude component of i th receiving polarimetric channel, and $X_i(k) = |S_i(k)|^2 / E(|S_i|^2)$. Recently, Frery et al. [11] have proposed a well-known \mathcal{G}^0 distribution to model the clutter regions in SAR images, and the product of multilook amplitudes from two polarimetric channels, that is, the proposed detector in this paper, employs an intensity expression of this distribution with three distinct parameters σ , n , and α , when applying to the modeling of sea background. That is,

$$p_\zeta(\zeta) = \frac{\sigma^n}{B(n, -\alpha)} \frac{\zeta^{n-1}}{(1 + \sigma\zeta)^{n-\alpha}}, \quad \sigma, n, -\alpha, \zeta > 0, \quad (13)$$

where $B(\cdot, \cdot)$ is the beta function. The estimates $\hat{\alpha}$, $\hat{\sigma}$, and \hat{n} corresponded, respectively, to the parameters α , σ , and n can be easily obtained with the help of numerical calculation based on the method of log-cumulants (MoLC) [12] as

$$\begin{aligned} \Psi(\hat{n}) - \Psi(-\hat{\alpha}) - \ln(\hat{\sigma}) &= \frac{1}{N} \sum_{i=1}^N [\ln(x_i)] = \hat{\zeta}_1, \\ \Psi(1, \hat{n}) + \Psi(1, -\hat{\alpha}) &= \frac{1}{N} \sum_{i=1}^N [(\ln(x_i) - \hat{\zeta}_1)^2], \\ \Psi(2, \hat{n}) - \Psi(2, -\hat{\alpha}) &= \frac{1}{N} \sum_{i=1}^N [(\ln(x_i) - \hat{\zeta}_1)^3], \end{aligned} \quad (14)$$

where $\Psi(\cdot)$ represents the digamma function (i.e., the logarithmic derivative of the gamma function), $\Psi(r, \cdot)$ is the r th order polygamma function (i.e., the k th order derivative of the digamma function), and $\{x_i\}$, $i \in [1, N]$, is a given sample set.

Given the density shown in (13), its cumulative distribution function (CDF) is written as [11]

$$F_\zeta(x) = \frac{\sigma^n x^n}{nB(n, -\alpha)} {}_2F_1(n - \alpha, n; n + 1; -\sigma x), \quad (15)$$

where ${}_2F_1(\cdot, \cdot; \cdot; \cdot)$ is the Gauss hypergeometric function. For a given value of the false alarm probability, denoted by P_{fa} , the corresponding CFAR threshold T for the distribution shown in (13) can be obtained from

$$1 - P_{fa} = F_\zeta(T) = \frac{\sigma^n T^n}{nB(n, -\alpha)} {}_2F_1(n - \alpha, n; n + 1; -\sigma T). \quad (16)$$

Considering that $F_\zeta(T)$ is strictly monotonously increasing, the threshold T can be accurately calculated via the numerical solution or a simple bisection method.

4. Experimental Results and Analysis

The test dual-pol SAR amplitude data used in this study are a large TerraSAR-X StripMap mode geocoded scene over Nanjing, China, acquired with high-resolution 6 m \times 6 m (azimuth \times range) and HH-polarization and VV-polarization. Figure 1(a) provides a fake-color image of

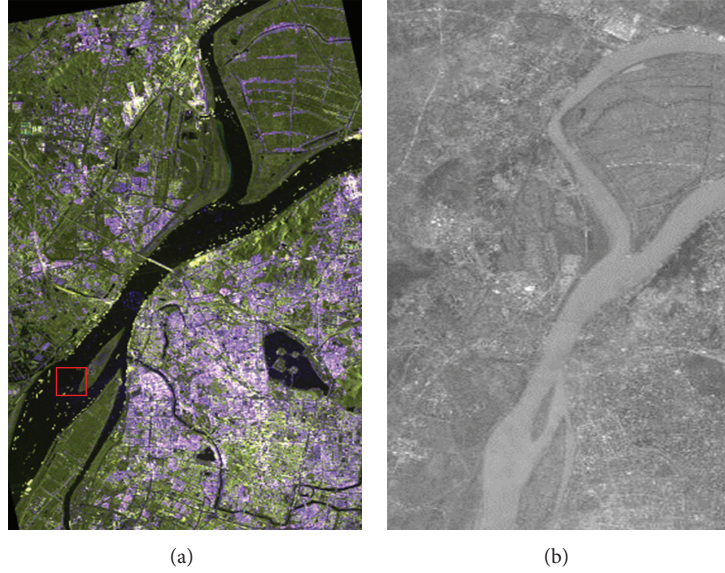


FIGURE 1: The image of Nanjing: (a) TerraSAR-X image; (b) SPOT5 optical image.

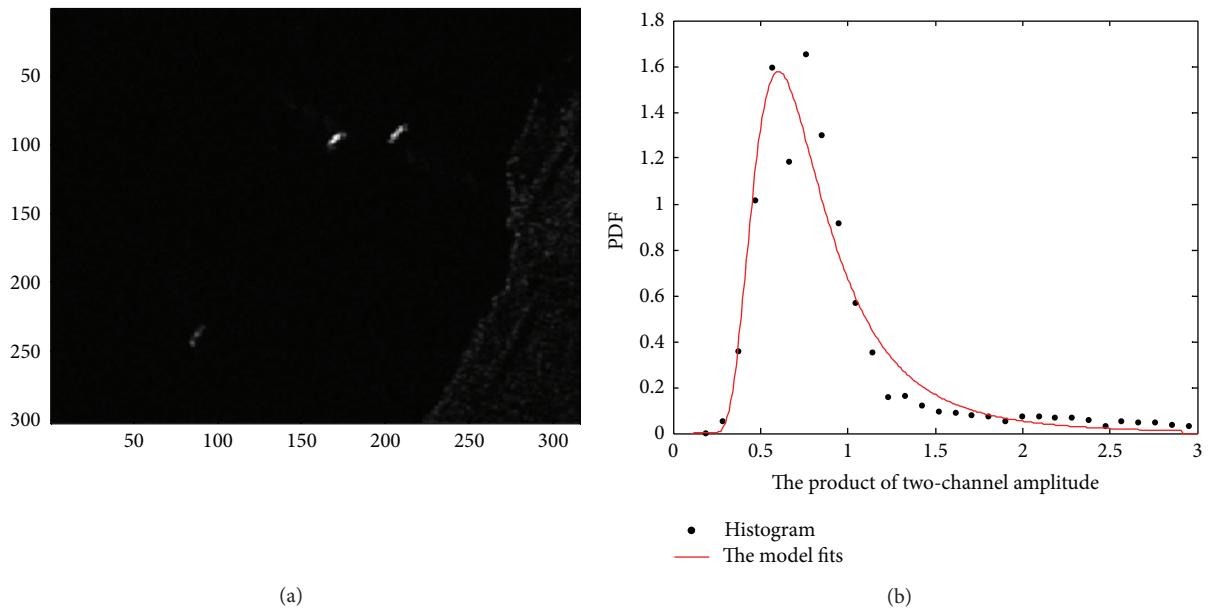


FIGURE 2: The ship chip: (a) the product image; (b) the fitting result.

this scene. The horizontal and vertical axes are the directions of azimuth and range, respectively. Meanwhile, in order to make a visible comparison, Figure 1(b) gives an optical (ground truth) remote sensing photograph of the test site from SPOT5 satellite.

The red rectangle box region shown in Figure 1(a) consisting of several ships and sea clutter is our investigating area. The product image of multilook amplitudes from two polarimetric channels is shown in Figure 2(a). Figure 2(b) shows the fitting results of the distribution in (13) for the product image of the area indicated in the rectangle box in Figure 2(a). The parameters n , α , and σ are estimated to $\hat{n} = 100.5744$, $\hat{\alpha} = -1.7851$, and $\hat{\sigma} = 120.7748$, respectively. As

shown in Figure 2(b), it is clear that the fitting result agrees well with the theoretical distribution.

Furthermore, giving the theoretical false alarm probability $P_{fa} = 10^{-8}$, the detection results are shown in Figure 3. It is easy to observe that all ships are detected, whilst a false alarm occurs, which proves the effectiveness of CFAR detection method based on PMA detector for ships.

5. Conclusion

Aiming at the adaptive detection of a ship when only high-resolution dual-polarization SAR amplitude data are

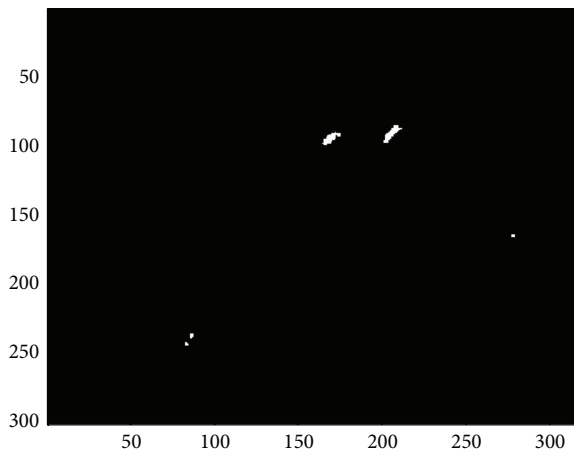


FIGURE 3: The ship detecting result.

available, a CFAR detecting method has been proposed in this paper. We first design a novel PMA detector, which can improve the signal-to-clutter ratio (SCR) and make the discrimination of a ship from clutter more easily. Meanwhile, the PMA detector's statistical model has been described by the well-known \mathcal{G}^0 distribution when facing complex sea background. The experiments performed on measured dual-polarization TerraSAR-X images demonstrate the good performance of the proposed CFAR detecting method.

Acknowledgment

The author would like to appreciate the National Natural Science Foundation of China for the support under Grant no. 41171316.

References

- [1] D. J. Crisp, *The State-of-the-Art in Ship Detection in Synthetic Aperture Radar Imagery*, DSTO, Departement Defence, Australian Government, Canberra, Australia, Public Release Document DSTO-RR-0272, 2004.
- [2] C. J. Oliver and S. Quegan, *Understanding Synthetic Aperture Radar Images*, Artech House, Norwood, Mass, USA, 1998.
- [3] I. C. Sikaneta, *Detection of ground moving objects with synthetic aperture radar [Ph.D. thesis]*, University of Ottawa, 2002.
- [4] F. T. Ulaby and C. Elachi, *Radar Polarimetric for Geoscience Application*, Artech House, Boston, Mass, USA, 1990.
- [5] C. E. Livingstone and A. A. Thompson, "The moving object detection experiment on RADARSAT-2," *Canadian Journal of Remote Sensing*, vol. 30, no. 3, pp. 355–368, 2004.
- [6] V. A. Krylov, G. Moser, S. B. Serpico, and J. Zerubia, "Supervised high-resolution dual-polarization SAR image classification by finite mixtures and copulas," *IEEE Journal on Selected Topics in Signal Processing*, vol. 5, no. 3, pp. 554–566, 2011.
- [7] R. D. Chaney, M. C. Bud, and L. M. Novak, "On the performance of polarimetric target detection algorithms," *IEEE Aerospace and Electronic Systems Magazine*, vol. 5, no. 11, pp. 10–15, 1990.
- [8] J. S. Lee, K. W. Hoppel, S. A. Mango, and A. R. Miller, "Interferometric SAR imagery," *IEEE Transactions on Geoscience and Remote Sensing*, vol. 32, no. 5, pp. 1017–1028, 1994.
- [9] C. H. Gierull, "Statistics of SAR interferograms with application to moving target detection," Tech. Rep. 2001-045, Defense Research Establishment Ottawa, Department of National Defense, Ottawa, Canada, 2001.
- [10] N. R. Goodman, "Statistical analysis based on a certain multivariate complex gaussian distribution (an introduction)," *Annals of Mathematical Statistics*, vol. 34, no. 152, pp. 152–180, 1963.
- [11] A. C. Frery, J. Jacobo-Berlles, J. Gambini, and M. E. Mejail, "Polarimetric SAR image segmentation with B-splines and a new statistical model," *Multidimensional Systems and Signal Processing*, vol. 21, no. 4, pp. 319–342, 2010.
- [12] J. M. Nicolas, "Introduction to second kind statistic: application of log-moments and log-cumulants to SAR image law analysis," *Traitement du Signal*, vol. 19, no. 3, pp. 139–167, 2002.

Research Article

The Design and Experiments on Corner Reflectors for Urban Ground Deformation Monitoring in Hong Kong

Yuxiao Qin, Daniele Perissin, and Ling Lei

Institute of Space and Earth Information Science, The Chinese University of Hong Kong, Hong Kong

Correspondence should be addressed to Yuxiao Qin; yuxiao@cuhk.edu.hk

Received 2 November 2012; Revised 23 December 2012; Accepted 5 January 2013

Academic Editor: Deren Li

Copyright © 2013 Yuxiao Qin et al. This is an open access article distributed under the Creative Commons Attribution License, which permits unrestricted use, distribution, and reproduction in any medium, provided the original work is properly cited.

PSInSAR technology has been proved to be a powerful tool for monitoring urban ground displacement information to a millimetric accuracy. When it comes to the validation of PS-derived ground deformation, artificial corner reflector (CR) can be very useful due to its relative stability and high signal-to-noise ratio (SNR). In this paper, we will evaluate some general criteria for designing and setting up corner reflectors, including the shape, size, material, location, and others. An ideal prototype known as the rectangular trihedral with special designs is brought up in this paper, and validation experiments were conducted in Hong Kong to demonstrate the ability of the proposed prototype. The field data agreed with theoretical analysis, bringing up an economical and applicable approach for CR application in urban ground deformation monitoring.

1. Introduction

In recent years, Interferometry Synthetic Aperture Radar (InSAR) [1, 2] technology has been proved to be a powerful tool that can provide high-resolution information on topography and ground displacement [3]. Furthermore, in order to overcome the limitations of InSAR technology, namely, the spatiotemporal decorrelation and atmospheric disturbance displacement [4–6], Permanent Scatterers (PSInSAR) technology [5, 6] was proposed. The technique can effectively identify, estimate, and remove atmospheric distortions, leaving the PS displacement as the only contribution to the signal phase shift, and it has been proved that 1 mm accuracy for deformation monitoring can be achieved [7]. Since then, the technology has been applied widely in ground displacement monitoring [8–10].

However, in practice, sometimes artificial scatterers are needed for PSInSAR measurement for various reasons. In the first place, PSInSAR-derived displacement is the relative movement to a reference point that usually possesses a high coherence and known displacement. Assuming that the entire region of monitoring area is descending, thus an artificial scatterer can be used as the reference point, and the

deformation of scatterer can be usually precisely measured by other instruments. In the second place, when it comes to the validation of PSInSAR measurements, an artificial scatterer should be a preferred option to retrieve deformation trend, making them very useful for validation purpose. In general, artificial scatterers were manually lifted or lowered with millimetric precision and compared with the PSInSAR-derived results. As a consequence, corner reflector is brought up as one of the most commonly applied artificial scatterers. Corner reflectors are objects that exhibit a high radar cross-section (RCS) and a high signal-to-noise ratio (SNR). These typical characteristics of CR qualify it InSAR analysis.

In this paper, we will discuss the general principle for building a “user-friendly” corner reflector for InSAR analysis. A common rectangular trihedral reflector with a relative small size of 0.5 m wide basement and 0.75 m height, holed plate, and adjustable basement is proposed. The small size guarantees the mobility and stability of the reflector, while the adjustable basement makes it adjustable and more precise. In addition, under the premise of a reasonable RCS or at least a high SNR, the plates of CR are holed to withdraw the power of wind and filter the precipitation. The RCS and SNR are calculated to demonstrate the applicability of the proposed

CR. In the end, the performance of this kind of reflector is evaluated, and the result demonstrates that for regional subsidence validation, the proposed CR can achieve 1 mm stability.

2. Corner Reflector

2.1. General Criteria for Designing a Corner Reflector. In general, a corner reflector should be built regarding the following principles: it should be easy to point, light to carry, easy to mount, difficult to be reached by unauthorized people, well fixed, and resistant to all weather conditions. Additionally, in particular for a validation experiment, the height must be adjustable. To meet the above requirements, a prototype shown in Figures 1 and 2 is designed and assembled. This prototype possesses the following characteristics: first of all, it is in cubic shape and made of aluminum and the side panels are holed to reduce the weight. Secondly, the reflector is fixed onto a concrete basement on the ground with four anchors and screws to fix and adjust its height. The advantage of this type of corners is that it does not require any complicated pointing procedure and can be mounted easily. When deploying the CR, one simply turns the mouth to the satellite viewing direction. More detailed discussion of the reflector will be carried out in the following section.

2.2. The Material of Corner Reflector. For the reason of keeping the mechanical stability and accuracy of artificial shifts to a millimetric level, both the size and the weight of the structure should be kept limited. In this regard, the corner reflector in this case is made of aluminum, which is remarkable for its low density and ability to resist corrosion due to the phenomenon of passivation. The density of common aluminum alloy varies from 2.6 g/cm^3 to 2.9 g/cm^3 , while the density of common iron and steel can vary from 7.75 to 8.05 g/cm^3 . For example, a small trihedral corner reflector made of aluminum with a size of $50 \text{ cm} * 50 \text{ cm} * 75 \text{ cm}$ and 2 mm width weighs approximately 5.6 kg (take density as 2.8 g/cm^3), but if the same corner is made of steel, it will weigh 16 kg (8 g/cm^3) in total, which is a remarkable increasing in weight.

2.3. The Shape of Corner Reflector. In principle, the reflector should be characterized by a reflectivity much higher than that of the surrounding scatterers [7]; that is to say, the reflector should have a high RCS for a relative small size. Some of the most common corner reflectors being used are flat plate, dihedral, triangular trihedral, and cubic trihedral, and their featured RCSs [11] are listed in Table 1. From the table, we can see that the circular trihedral offers the greatest RCS. However, considering the fact that the square trihedral offers a maximum RCS very close to that of circular ones, yet making square trihedral is easier than making circular ones, it is considered better to use rectangle trihedral in this case. In addition, although dihedral is favored for its lightness and simply design [12–15], we choose cubic trihedral for the following reasons. In the first place, the aluminum and holed plate can effectively reduce the weight of corners, overcoming

the disadvantage of cumbersome compared with dihedral; in the second place, compared with the dihedral, the trihedral is more tolerant to the deviation of incident angles from the maximum angle, which suggests that trihedral would produce relatively large RCS even when the incident signal is not at the most ideal angle [16]. From these analyses, it seems that cubic trihedral corner reflector would serve as the best choice due to its robust geometric construction, relatively high tolerance of the incident signal's deviation from the optimal angle, and relatively high RCS value.

For TerraSAR-X satellite with wavelength $\lambda = 3.1 \text{ cm}$ and a small corner reflector with an edge of 0.5 m and height of 0.75 m , the maximum theoretical RCS $\sigma \approx 38.7 \text{ dB}$; for a bigger reflector with edge of 1 m , the maximum theoretical RCS $\sigma \approx 48.6 \text{ dB}$, both making it very easy to be identified from a low RCS background.

2.4. The Holed Plate. As stated above, the reflectors are exposed in open air and should be resistant to all weather conditions, mostly precipitation and wind. To solve the problem, the holed plates are introduced to the design of reflectors. With the holes on the plate, the wind forces will be lower, water can be filtered through the base, and the weight of the object can be reduced. For example, for the holed plate designed in Figure 3, for each plate, the holes can significantly reduce the weight by 35%.

However, the holed designation will result in a loss of RCS reflectance, and the transmittivity through holes can be calculated by the following formula [17]:

$$T_{db} = 20 \lg \left(\frac{3ab\lambda_0}{2\pi d^3 \cos \theta} \right) + \frac{32t}{d}, \quad (1)$$

where θ is the incidence angle and t is the plate thickness. a , b , and d are shown in Figure 3.

Typically, the dimension of the hole should be less than $\lambda/8$. However, considering that the incidence on the plates is never 0° and the different scattering properties at different frequencies, it can be demonstrated that in the case of C-band and X-band the holes on the plates can reach a diameter of 1 cm , with a respective filled/vacuum ratio of the plates of 60%, preserving a good RCS [18]. In this case, according to the diameter of holes, distance between holes, the wavelength of X-band (we will be using the reflector for TerraSAR-X calibrations), and the incidence angle (37° in this case) of TerraSAR-X satellite, we can calculate that the RCS loses $T_{dB} \approx 21 \text{ dB}$. For the smaller reflector, the maximum RCS is 38.7 dB ; after the losses from holes are considered, the RCS of reflector will still be around 17.7 dB , equivalent to 60 m^2 ; for the bigger one, the attenuated RCS will be around 27.6 dB , equivalent to nearly 600 m^2 . If the background RCS is low enough, the reflector can still be identified easily for its significant RCS value.

2.5. The Signal-to-Clutter Ratio of Corner Reflector. The corner reflector to be used in the experiment should maximize the RCS or at least the signal-to-clutter ratio (SCR) of the target to allow accurate phase measurements, while keeping the weight and the size as small as possible. SCR is the ratio

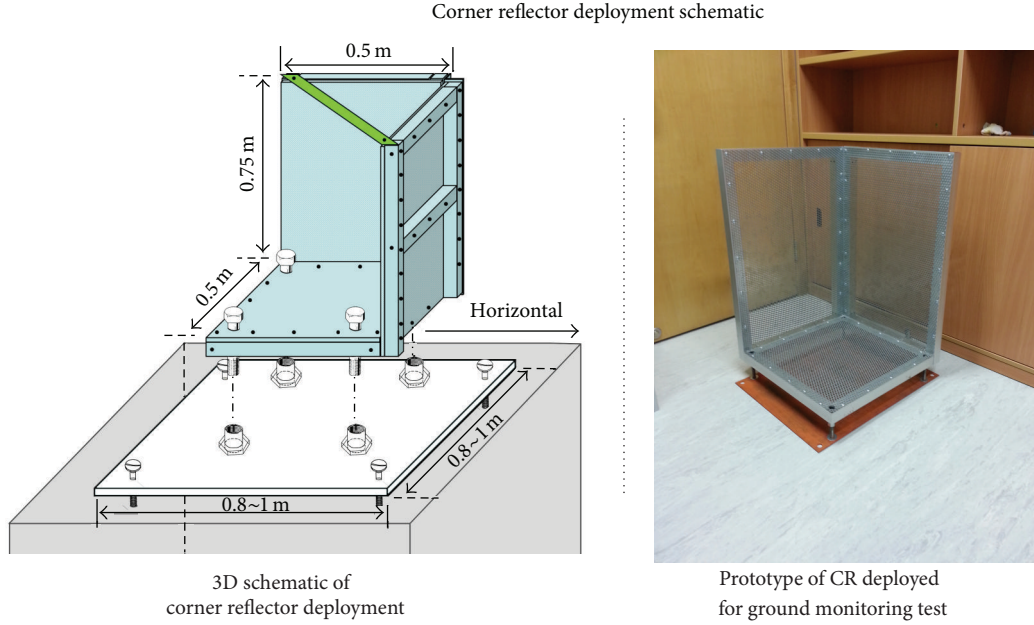


FIGURE 1: Schematic of corner reflector deployment.

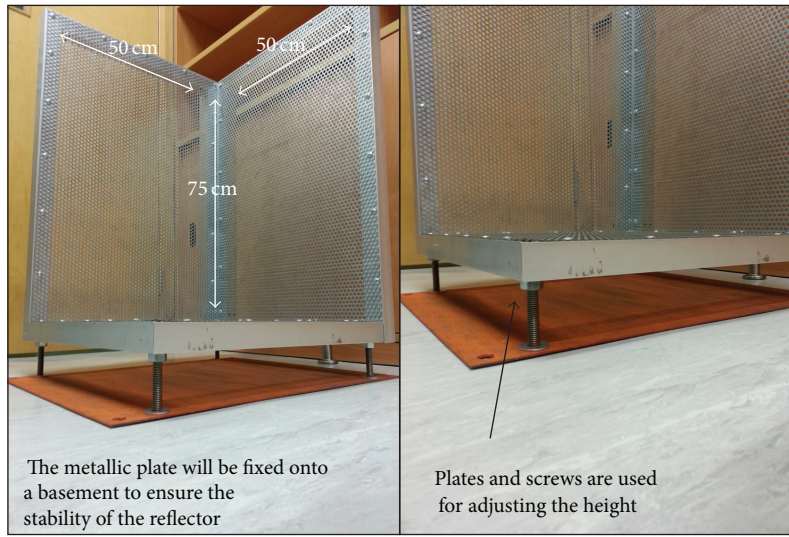


FIGURE 2: The picture of the reflector.

TABLE 1: RCSs of the most common reflectors (where a is the side length, and λ is the wavelength).

Types of canonical reflectors	Maximum RCS (m^2)
Triangular trihedral	$4\pi a^4/3\lambda^2$
Rectangular dihedral	$8\pi a^4/\lambda^2$
Square trihedral	$12\pi a^4/\lambda^2$
Circular (quarter disc) trihedral	$15.6\pi a^4/\lambda^2$

between the RCS of the reflector and that of the background scenario and is directly related to the dispersion of the phase values. For high SCR values, the relationship between

SCR, phase noise, and the dispersion of the displacement measurements along the satellite line of sight (LOS) can be approximated as follows [19]:

$$\sigma_{LOS} = \frac{\lambda}{4\pi} \cdot \sigma_{\phi} \approx \frac{\lambda}{4\pi} \cdot \sqrt{\frac{1}{2 \cdot SCR}}, \quad (2)$$

$$SCR = \frac{RCS_{corner}}{RCS_{background}} = \frac{A_{corner}^2}{A_{background}^2},$$

where A is the amplitude of the targets. For example, a design requirement on the SCR of 100 (20 dB) corresponds to a dispersion of the displacement measurements in LOS direction of about 0.17 mm at X-band, guaranteeing a theoretical

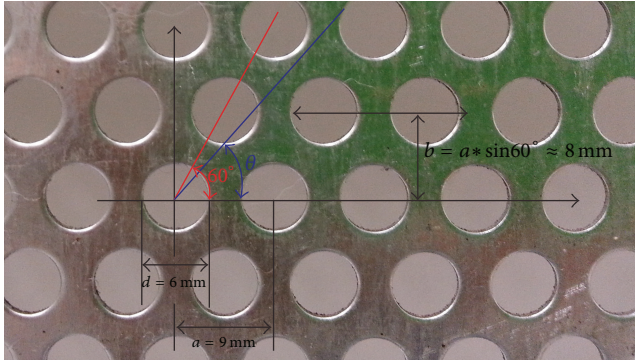


FIGURE 3: The prototype of the holed plate and the parameters of holes and relative positions.

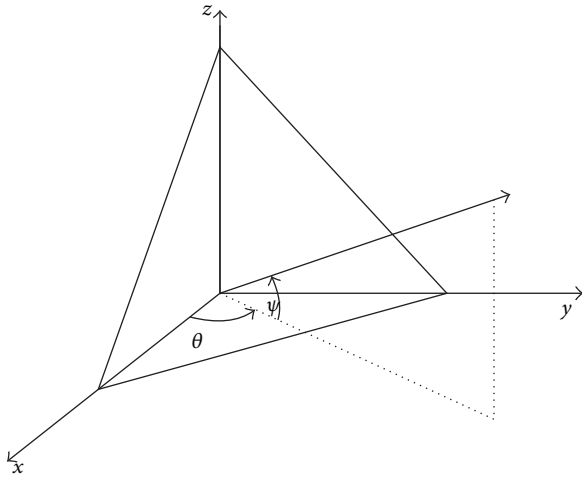


FIGURE 4: The azimuth angle (θ) and off-nadir angle (Ψ) defined for a corner reflector.

submillimetric dispersion. Naturally, in order to gain a high SCR value and thus a submillimetric dispersion, the CRs should be deployed and placed with low noise value.

2.6. The Installation of Corner Reflector. In order to gain a maximum RCS, the corner reflector should be installed on a horizontal plate and the direction of the reflectors should be set along LOS in order to gain the maximum RCS. If the direction deviates from the LOS direction or tilts slightly, the RCS value would decrease considering the different shape and size of the corners.

Figure 5 plots contours of constant RCS as a function of azimuth and off-nadir angles for a rectangular trihedral reflector with sizes of $0.5 \text{ m} * 0.5 \text{ m} * 1 \text{ m}$. The azimuth and off-nadir angle for x -axis and y -axis correspond to θ and Ψ in Figure 4. It is noted that the -3 dB width of the trihedral response spans nearly 20 degrees in azimuth and 20 degrees in off-nadir. This means that the reflector can tolerate a rather high angle excursion without losing much RCS.

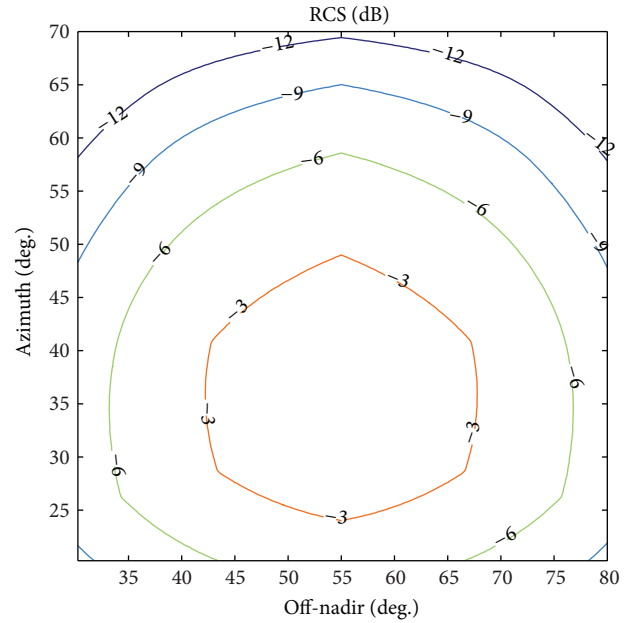


FIGURE 5: Contours of constant relative RCS for rectangular trihedral corner reflector.

2.7. The Bending of Corner's Plate. The most possible influencing factors that could bias the result are precipitation and bending plates. The former one can be excluded since the holed plate is applied to the test, but still we should consider the curved surfaces that would generate possible delays.

A possible phenomenon that may bend metallic plates is the thermal expansion. However, the calculation reveals that considering the trihedral with mentioned size, the thermal expansion is only able to result in an expansion of 0.1 mm level, thus not very likely to introduce significant bias to our monitoring experiments.

3. On-Site Test for Corner Reflectors

3.1. The Comparison between Two Cubic Trihedrals of Different Sizes. As part of the test, two different sizes of rectangular trihedral corner reflectors, the bigger one being exactly twice the size of the small one, were designed and tested for the experiment to evaluate which one is more applicable. The two prototypes of holed-plated reflectors with sizes of $0.5 \text{ m} * 0.5 \text{ m} * 1 \text{ m}$ and $1 \text{ m} * 1 \text{ m} * 1.5 \text{ m}$ have been tested in a football pitch in Hong Kong, and the SAR images are shown in Figure 6. From the images, we can see that with a relative low noise background, the reflectors can be easily identified on SAR images despite the holes. For the bigger reflector, the amplitude is even large enough to generate a star-like graph on SAR image.

The amplitude of two reflectors is compared and shown in Figures 7 and 8. According to Table 1, RCS of the bigger reflector should be 16 times bigger than the smaller one. Meanwhile, in correspondence to the pointwise target k , by means of the calibration constant K_{cal} , we can evaluate the

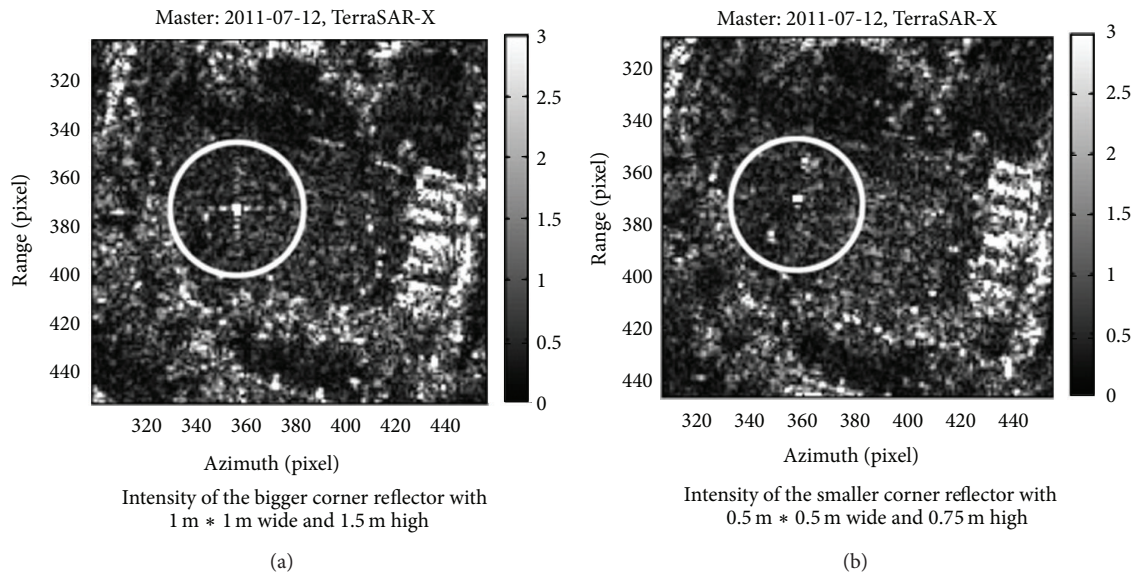


FIGURE 6: The intensity of two different sizes of reflectors with the same size of holes on the plate. The reflectors are deployed in a football pitch that has a very low noise background, and the signal of the reflector is evident.

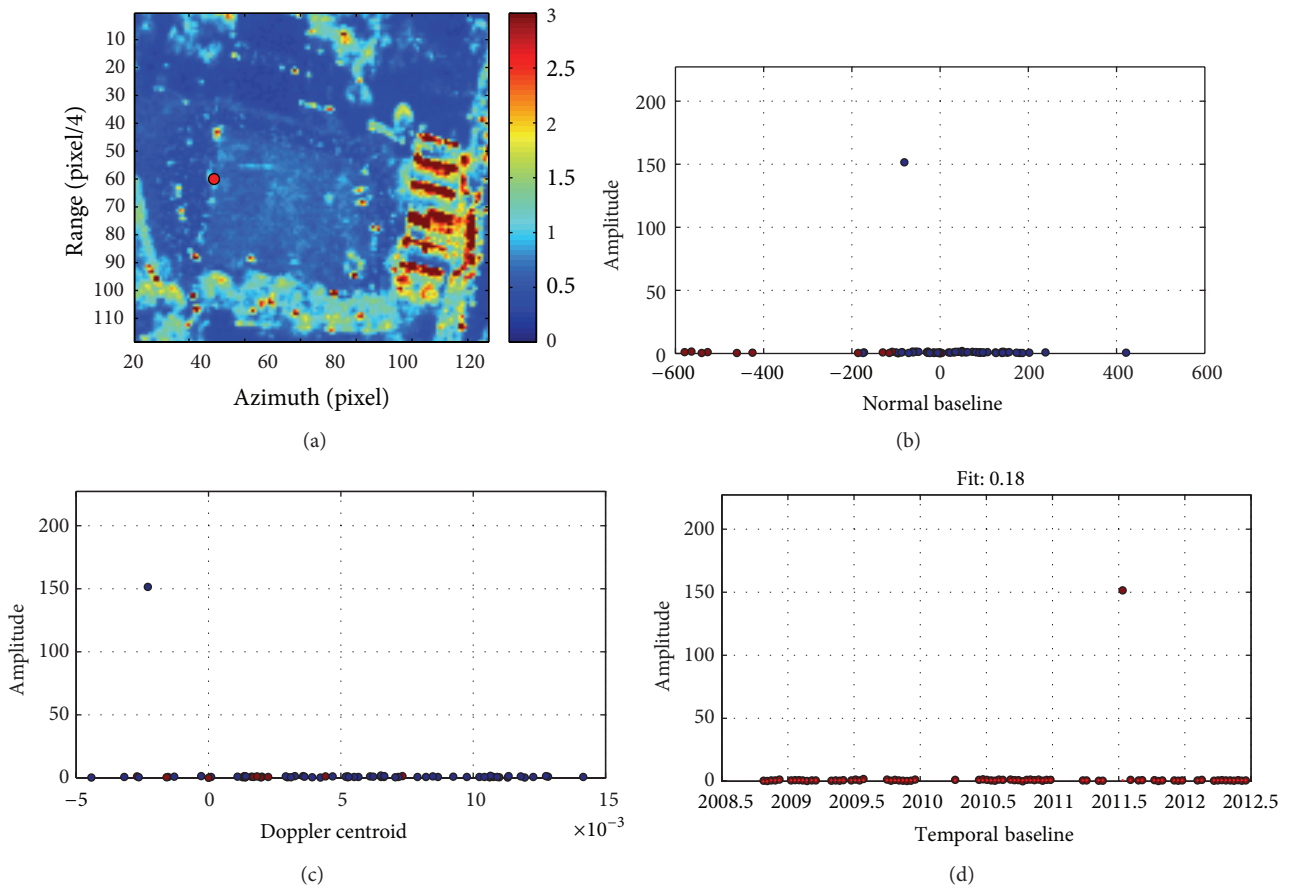


FIGURE 7: Amplitude Analysis of the bigger corner reflector. (a) shows the location of the reflector; (d) shows the amplitude time series of the location. The one outlined in the amplitude time series indicates the deployment and test of the reflector.

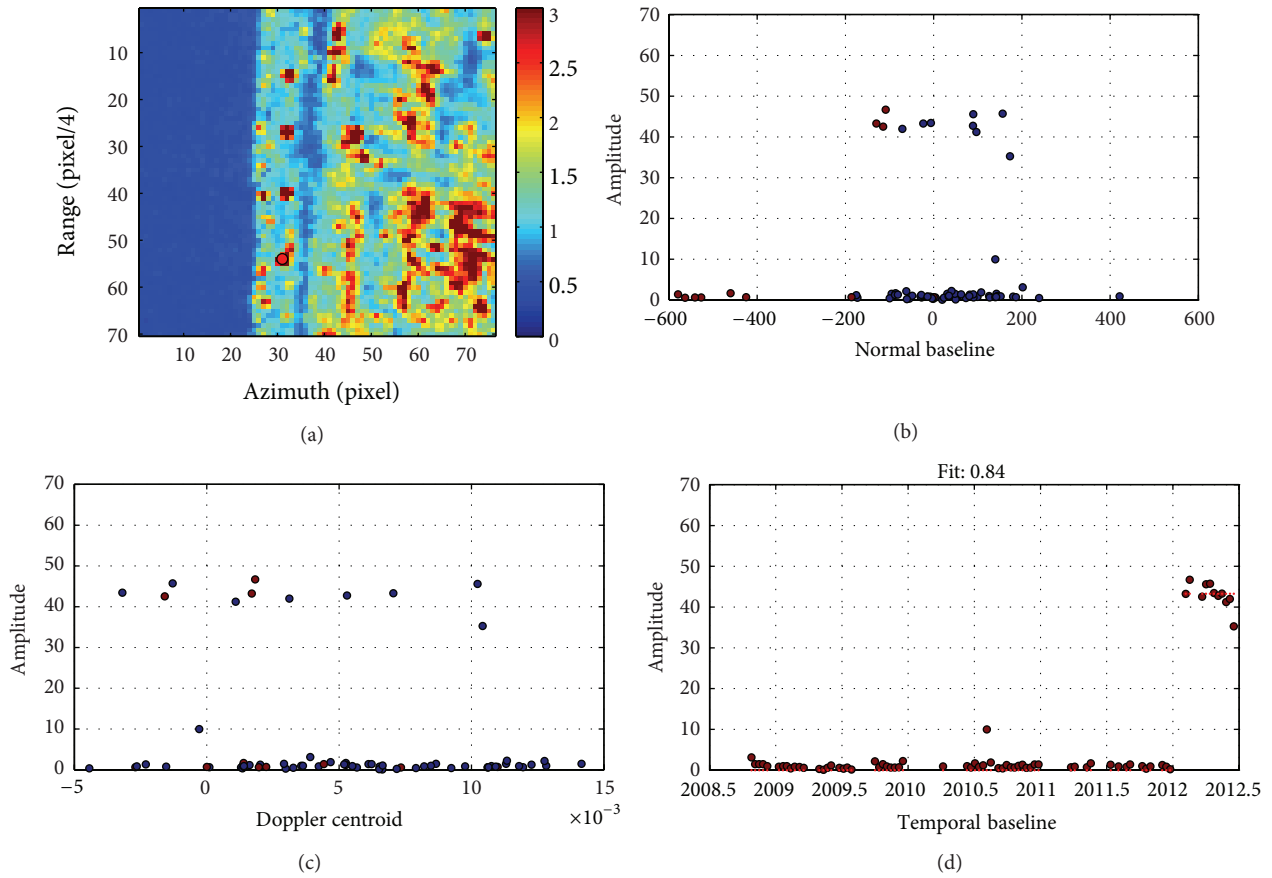


FIGURE 8: Amplitude analysis of the smaller corner reflector. (a) shows the location of the reflector; (d) shows the amplitude time series of the location. The amplitude leap indicates the deployment of reflectors.

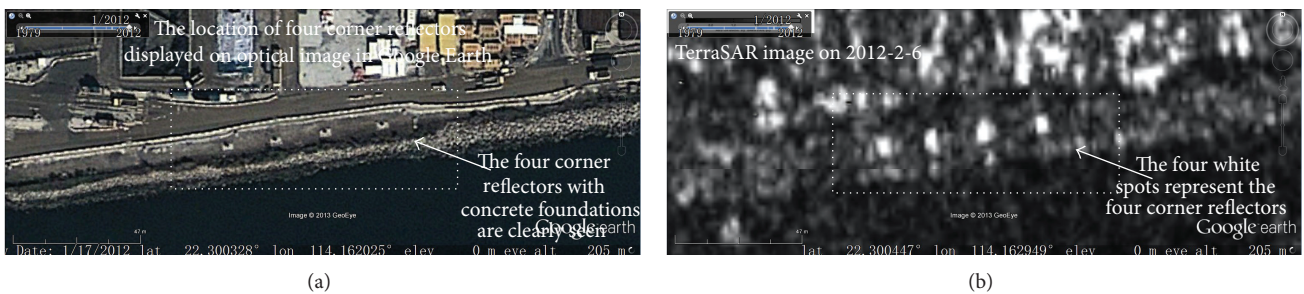


FIGURE 9: (a) The location of CRs in optical image displayed in Google Earth. The location is near the sea that is identical for its low intensity in RADAR images. (b) The location and intensity of the four CRs on TSX images. From the images, we can see that the background radiation in that area is very low, and the intensity of CRs is considerably high.

relationship between amplitude and RCS by the following equation:

$$\text{RCS}_k = \text{Amplitude}_k^2 \times K_{\text{cal}}, \quad (3)$$

where K_{cal} is the calibration constant [20]; thus the amplitude of the bigger RCS should be theoretically 4 times the amplitude of the smaller one. In this experiment, as shown in Figures 7 and 8, the amplitude of the bigger one is around 3.5 times the smaller one, which is rather close to the theoretical value a rough estimation.

Generally speaking, since the mechanical stability and accuracy of the shifts to the reflector must be precisely controlled to millimetric level, both the size and weight of the reflector should be kept to a certain limit. In other words, the shape and size of reflector must seek thier balance between a good RCS value and an applicable size. By looking into the amplitude time series of the reflectors in Figures 7 and 8, we can see that both reflectors are showing a very good SNR and identifiable amplitude change. However when considering the size and weight of the reflectors, the smaller one should be preferred for its convenience in carrying and deployment.

3.2. The Deployment of Corner Reflector. An ideal place for placing the reflectors is an area that presents a low background radiation to facilitate identifying the CR and to guarantee good phase stability. In addition, in order to demonstrate the PSInSAR capability of detecting millimetric changes with CR, it is suggested to place all the CRs within a certain distance, in order to avoid possible unexpected relative motions and to keep the atmospheric noise as limited as possible. In general, this distance should not exceed 200 meters [21]. For example, as shown in Figure 9, we deployed four CRs in an area where the background radiation is considerably low. The four CRs are within a range of 200 meters so that the atmospheric noise is kept to a low level. One of them is selected as the reference target for the process, which means that it will stay stable in all the time.

3.3. The Validation Test of Corner Reflector. In order to evaluate the performance of this type of CR, a validation test is carried out in urban area in Hong Kong. As shown in Figure 9, four CRs are deployed in an area with low background scattering. The reflector toward far west is set to be the reference scatterer and was kept stable, while the others are being manually lifted. For the estimation of corresponding PSInSAR movement of each CR, totally 11 scenes from January 2012 to June 2012 of TerraSAR-X and TanDEM-X data have been applied for analysis. The TSX and TDX satellites for generating the images process an active-phases array X-band SAR antenna with a wavelength of 31 mm and frequency of 9.6 GHz, with a resolution of up to 1 meter. The minimum interval between the two consequent acquisitions is 11 days. The TSX sensor acquires images over Hong Kong at about 6:25 PM, along an ascending orbit (from north to south, edging slightly westward) and it is right-looking, with an incidence angle of approximately 37 degrees.

To analyze the performance of PSInSAR technique, the estimated PSInSAR-derived displacements and values measured by ground survey were being compared, and a linear regression is conducted for the purpose of analyzing the deviation between the two measurements. The linear correlation coefficient of the regression is higher than 0.99, stating univocally the linear correlation between the displacements detected by InSAR and by the leveling survey. The root mean square error (RMSE) is around 0.85 mm, lower than 1 mm. In other words, the outcome of the analysis is slightly better than the best result that could be expected from such an analysis, revealing that InSAR can definitely reach the same accuracy of optical leveling and may overtake it.

4. Conclusion

In this paper, we discussed the design and experiments on different types and sizes of corner reflectors and brought up a small-size rectangular trihedral reflector. We concluded the great superiority of this type for deploying and estimating the difference between InSAR and ground truth data, by which the PSInSAR estimated deformation results can be easily validated and applied. The type of corner reflector has demonstrated its ability and potential in PSInSAR analysis, perfectly balancing the mobility, stability, and precision, showing an accuracy of less than 1 mm and thus making a good reference as a corner reflector prototype.

Acknowledgments

The TerraSAR-X data used in this project have been provided by Infoterra Germany, through the cooperation with Ralf Duering, Beijing. This work was partially supported by the Research Grants Council (RGC), General Research Fund (GRF) (Project Reference no. 415911) of HKSAR, and Direct Grant Funded Project (Reference no. 2021130).

References

- [1] J. C. Curlander and R. N. McDonough, *Synthetic Aperture Radar: Systems and Signal Processing*, John Wiley & Sons, New York, NY, USA, 1991.
- [2] R. Gens and J. L. van Genderen, "SAR interferometry—issues, techniques, applications," *International Journal of Remote Sensing*, vol. 17, no. 10, pp. 1803–1835, 1996.
- [3] F. Amelung, D. L. Galloway, J. W. Bell, H. A. Zebker, and R. J. Laczniak, "Sensing the ups and downs of Las Vegas: InSAR reveals structural control of land subsidence and aquifer-system deformation," *Geology*, vol. 27, no. 6, pp. 483–486, 1999.
- [4] H. A. Zebker and J. Villasenor, "Decorrelation in interferometric radar echoes," *IEEE Transactions on Geoscience and Remote Sensing*, vol. 30, no. 5, pp. 950–959, 1992.
- [5] H. A. Zebker, P. A. Rosen, and S. Hensley, "Atmospheric effects in interferometric synthetic aperture radar surface deformation and topographic maps," *Journal of Geophysical Research: Solid Earth*, vol. 102, no. 4, pp. 7547–7563, 1997.
- [6] A. Ferretti, C. Prati, and F. Rocca, "Permanent scatterers in SAR interferometry," *IEEE TGARS*, vol. 39, no. 1, 2001.

- [7] A. Ferretti, G. Savio, R. Barzaghi et al., "Submillimeter accuracy of InSAR time series: experimental validation," *IEEE Transactions on Geoscience and Remote Sensing*, vol. 45, no. 5, pp. 1142–1153, 2007.
- [8] A. H.-M. Ng, L. Ge, X. Li, and K. Zhang, "Monitoring ground deformation in Beijing, China with persistent scatterer SAR interferometry," *Journal of Geodesy*, vol. 86, no. 6, pp. 375–392, 2012.
- [9] Q. Zhao, H. Lin, W. Gao, H. A. Zebker, A. Chen, and K. Yeung, "InSAR detection of residual settlement of an ocean reclamation engineering project: a case study of Hong Kong International Airport," *Journal of Oceanography*, vol. 67, no. 4, pp. 415–426, 2011.
- [10] G. Herreraa, R. Tomás, J. M. Lopez-Sanchez et al., "Validation and comparison of Advanced Differential Interferometry Techniques: murcia metropolitan area case study," *ISPRS Journal of Photogrammetry and Remote Sensing*, vol. 64, no. 5, pp. 501–512, 2009.
- [11] B. C. Brock and A. W. Doerry, "Radar cross section of triangular trihedral reflector with extended bottom plate," 2009.
- [12] E. F. Knott, "RCS reduction of dihedral corners," *IEEE Transactions on Antennas and Propagation*, vol. 25, no. 3, pp. 406–409, 1977.
- [13] S. Y. Wang and S. K. Jeng, "Compact RCS formula for a dihedral corner reflector at arbitrary aspect angles," *IEEE Transactions on Antennas and Propagation*, vol. 46, no. 7, pp. 1112–1113, 1998.
- [14] K. Hayashi, R. Sato, Y. Yamaguchi, and H. Yamada, "Polarimetric scattering analysis for a finite dihedral corner reflector," *IEICE Transactions on Communications*, vol. E89-B, no. 1, pp. 191–195, 2006.
- [15] P. Corona, A. de Bonitatibus, G. Ferrara, and C. Gennarelli, "A very accurate model for backscattering by right angled dihedral corners," in *Proceedings of the IEEE Antennas and Propagation Society International Symposium*, vol. 4, pp. 1734–1737, May 1990.
- [16] X.-J. Shan, J.-Y. Yin, D.-L. Yu, C.-F. Li, J.-J. Zhao, and G.-F. Zhang, "Analysis of artificial corner reflector's radar cross section: a physical optics perspective," *Arabian Journal of Geosciences*, 2012.
- [17] T. Y. Otoshi, "Study of microwave leakage through perforated flat plates," *IEEE Transactions on Microwave Theory and Techniques*, vol. 20, no. 3, pp. 235–236, 1972.
- [18] A. Parizzi, D. Perissin, C. Prati, and F. Rocca, "Artificial scatterers in SAR interferometry," in *Proceedings of Dragon Symposium*, Santorini, Greece, June-July 2005.
- [19] G. Ketelaar, P. Marinkovic, and R. Hanssen, "Validation of point scatterer phase statistics in multi-pass InSAR," in *Proceedings of CEOS SAR Workshop*, Ulm, Germany, May 2004.
- [20] D. Perissin and A. Ferretti, "Urban-target recognition by means of repeated spaceborne SAR images," *IEEE Transactions on Geoscience and Remote Sensing*, vol. 45, no. 12, pp. 4043–4058, 2007.
- [21] P. Marinkovic, G. Ketelaar, F. van Leijen, and R. Hanssen, "InSAR quality control—analysis of five years of corner reflector time series," in *Proceedings of the 5th International Workshop on ERS/Envisat SAR Interferometry (FRINGE '07)*, Frascati, Italy, November 2007.

Research Article

Characterizing the Statistical Properties of SAR Clutter by Using an Empirical Distribution

Gui Gao, Gongtao Shi, Huanxin Zou, and Shilin Zhou

School of Electronics Science and Engineering, National University of Defense Technology, Changsha, Hunan 410073, China

Correspondence should be addressed to Gui Gao; dellar@126.com

Received 3 November 2012; Accepted 30 November 2012

Academic Editor: Deren Li

Copyright © 2013 Gui Gao et al. This is an open access article distributed under the Creative Commons Attribution License, which permits unrestricted use, distribution, and reproduction in any medium, provided the original work is properly cited.

The performances on the applications of synthetic aperture radar (SAR) data strongly depend on the statistical characteristics of the pixel amplitudes or intensities. In this paper, a new empirical model, called simply \mathcal{HG}^0 , has been proposed to characterize the statistical properties of SAR clutter data over the wide range of homogeneous, heterogeneous, and extremely heterogeneous returns of terrain classes. A particular case of the \mathcal{HG}^0 distribution is the well-known \mathcal{G}^0 distributions. We also derived analytically the estimators of the presented \mathcal{HG}^0 model by applying the “method of log cumulants” (MoLCs). The performance of the proposed model is verified by using some measured SAR images.

1. Introduction

Nowadays, synthetic aperture radar (SAR) has become an advanced tool as compared to optical sensors for monitoring land or sea surfaces because of its advantages regardless of weather conditions [1, 2]. The interpretation of statistical properties of SAR clutter with various terrain classes is a crucial task for designing filtering [3], detection [4], segmentation [5], and classification [6–8] of algorithms to optimally exploit the contents of the processed SAR images. These analyses result in a growing interest in developing precise models for the statistics of the pixel amplitudes or intensities.

It is known that SAR images are strongly affected by speckle noise due to its coherent imaging mechanism [1, 2, 9, 10]. This noise effect degrades the information of SAR images and limits the surveillance performances. To overcome this drawback, much work has been done to match amplitude or intensity statistics [3, 5, 6, 8, 11]. Among the existing statistical models, the parametric distributions have been intensively investigated because of their high accuracy and flexibility, which are usually obtained by two approaches.

The first is to consider the physical mechanism of the backscattering from the land surfaces. The multiplicative model [1, 2] by combining the speckle noise and the terrain backscatter is commonly used in this class. Generally, multi-look SAR speckle noise intensity is assumed to obey a gamma

distribution. Therefore, a central task for establishing this type of statistical models is to aim at the backscatter modeling of different terrain classes [1, 2, 11]. Two important distributions, consisting of \mathcal{H} as well as \mathcal{G}^0 , which, in turn, in relation to the Gamma and inverse Gamma distribution for the intensity backscatter, have received a great deal of attention [2, 5–7, 9, 11, 12]. As compared to \mathcal{H} , \mathcal{G}^0 agrees reasonably better with the heavy tail behavior coming from the extremely heterogeneous clutter like the cases of urban areas or other man-made structures [11].

The second is to conduct the distributions from a purely mathematics view irrespective with physical property of radar clutter backscatter. Some known examples are the lognormal, weibull, and more recently the Fisher [6] (completely identical to the \mathcal{G}^0) distributions. The lognormal and weibull fit sometimes well with the SAR histogram of some heterogeneous and ocean regions [9]. However, they tend to occur a large deviation estimating the histograms with the heavy tail behavior.

This paper is devoted to report an empirical model (denoted simply as \mathcal{HG}^0) for characterizing the statistical properties of SAR clutter data to obtain the modeling ability of more heterogeneous clutter. The proposed model has the \mathcal{G}^0 distribution as a special case. Furthermore, using the second-kind statistics theory developed by Nicolas [13],

which relies on the Mellin transform [14], that is, “method-of-log-cumulants” (MoLC), we derive the parameter estimators of the new distribution model.

In the rest of this paper, the proposed distribution is first given in Section 2. Section 3 derives the corresponding parameter estimators based on the MoLC. We provide the experimental results of the $\mathcal{H}\mathcal{G}^0$ model using measured SAR data in Section 4, the comparisons with that \mathcal{G}^0 fits are also discussed in this section. The last section concludes this paper and give a perspective in the future work.

2. The Proposed Distribution

The proposed amplitude distribution is defined as

$$p_{Z_A}(z) = -\frac{2\sigma\lambda^{v\alpha}n^n\Gamma((\alpha-n)/v)}{v\Gamma(v\alpha)\Gamma(n)} \times z^{2n-1}(\lambda+nz^{-2v})^{(n-\alpha)/v}, \quad -\alpha, -v, \lambda, \sigma, n, z > 0, \quad (1)$$

where σ , α , and λ are the power, shape, scale parameters, respectively. v indicates the stretching parameter. $\Gamma(\cdot)$ represents the Gamma function. n is the number of looks. The corresponding intensity expression of (1) is further given by

$$p_{Z_I}(z) = -\frac{\sigma\lambda^{v\alpha}n^n\Gamma((\alpha-n)/v)}{v\Gamma(v\alpha)\Gamma(n)} \times z^{n-1}(\lambda+nz^{-v})^{(n-\alpha)/v}, \quad -\alpha, -v, \lambda, \sigma, n, z > 0. \quad (2)$$

We refer to this distribution characterized by (1) or (2) as the $\mathcal{H}\mathcal{G}^0$ distribution. Specifically, we call the $\mathcal{H}\mathcal{G}_I^0$ distribution and the $\mathcal{H}\mathcal{G}_A^0$ distribution, correspond to (2) and (1), respectively, to distinct the intensity statistic as well as the amplitude statistic. Figure 1 gives some examples of the $\mathcal{H}\mathcal{G}_A^0$ distribution with respect to the various parameters. From this figure, it can be seen clearly that the parameter α reflects the degree of homogeneity for the tested returns, which implies that the smaller value of $|\alpha|$ obtains, the more in-homogeneous (i.e., larger tails) they are. Meanwhile, v corresponds to a stretching of the SAR image amplitude or intensity, showing a strong effect for low values of the return. Moreover, as an independent parameter, σ indicates the whole fluctuation (contains magnifying or shrinking) of power of densities along the vertical axis. The parameter λ controls the peak value of the density.

Although the probability density functions (PDFs) characterized by (1) or (2) are shown as the empirical models, the $\mathcal{H}\mathcal{G}^0$ model also can be derived within the structure of the multiplicative model [1, 2, 11]. Herein, we account for the intensity distribution as an example, the following theorem is established.

Theorem 1. *Letting X_I and Y_I indicates the backscattering RCS component and speckle noise one, respectively, Z_I denotes the observed intensity of SAR data. Therefore, the relationship*

of this three variables is expressed by the multiplicative model as

$$Z_I = X_I \cdot Y_I. \quad (3)$$

If X_I obeys

$$p_{X_I}(x) = \frac{\sigma\lambda^{v\alpha}}{\Gamma(v\alpha)}x^{\alpha-1}\exp(-\lambda x^v), \quad -\alpha, -v, \lambda, \sigma, x > 0 \quad (4)$$

and the PDF of Y_I is

$$p_{Y_I}(y) = \frac{n^n}{\Gamma(n)}y^{n-1}\exp(-ny^{-v}), \quad y, n, -v > 0. \quad (5)$$

Then the distribution of the intensity return is characterized by the density shown in (2), that is, $Z_I \sim \mathcal{H}\mathcal{G}_I^0(\alpha, v, \lambda, \sigma, n)$.

Proof. Combining (4) and (5) via (3), the PDF of Z_I can be easily derived as

$$p_{Z_I}(z) = \int_0^\infty \frac{1}{x} \cdot p_{X_I}(x) \cdot p_{Y_I}\left(\frac{z}{x}\right) dx = \frac{\sigma\lambda^{v\alpha}n^n}{\Gamma(v\alpha)\Gamma(n)}z^{n-1} \int_0^\infty x^{\alpha-n-1}\exp\{(-\lambda-nz^{-v})x^v\} dx. \quad (6)$$

A variable change of $t = 1/x$ leads to $x = 1/t$ and $dx = -t^{-2}dt$, (6) turns out be

$$p_{Z_I}(z) = \frac{\sigma\lambda^{v\alpha}n^n}{\Gamma(v\alpha)\Gamma(n)}z^{n-1} \int_0^\infty t^{-\alpha+n-1}\exp\{(-\lambda-nz^{-v})t^{-v}\} dt. \quad (7)$$

Applying the integral formula $\int_0^\infty x^{a-1}\exp(-\mu x^p)dx = (1/p)\mu^{-a/p}\Gamma(a/p)$, $\text{Re } \mu > 0$, $\text{Re } a > 0$, $p > 0$ [15, 3.478, Equation 1], one can easily obtain the result that (7) is equal to (2).

Furthermore, $\mathcal{H}\mathcal{G}^0$ has the charming property that the well-known \mathcal{G}^0 , presented by Frery et al. [11] to model homogeneous, heterogeneous, and extremely heterogeneous terrains, is a special case of this proposed model when $\sigma = 1$ and $v = -1$. Thus, the proposed model exhibits higher fitting ability as compared to \mathcal{G}^0 .

As derived in Appendix A, the m th order moments of the $\mathcal{H}\mathcal{G}_I^0$ are given by

$$E(z_I^m) = \frac{\sigma\lambda^{v\alpha-(m+\alpha)/v}n^{n+(m+n)/v}\Gamma(-(m+n)/v)\Gamma((\alpha+m)/v)}{v^2\Gamma(v\alpha)\Gamma(n)}. \quad (8)$$

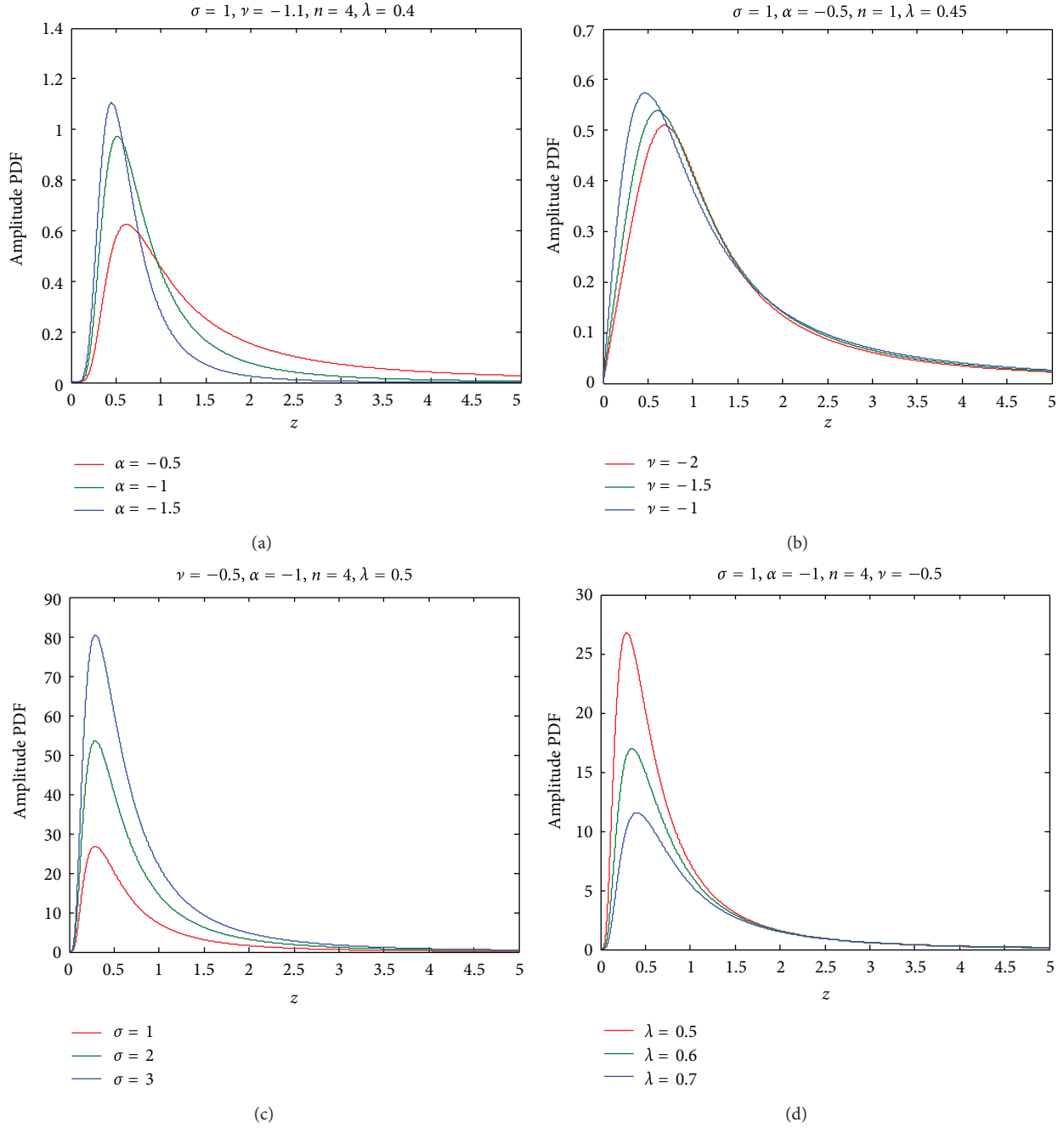


FIGURE 1: Plots of $\mathcal{H}\mathcal{G}_A^o$ versus different parameters.

The m th order moments of the corresponding amplitude random variable can easily be given by $E(z_A^m) = E(z_1^{m/2})$. \boxtimes

3. The Parameter Estimators of the Proposed Distribution

3.1. *The Log-Cumulants of $\mathcal{H}\mathcal{G}^o$* . Nicolas [13] has proposed a parametric PDF estimation technique based on the MoLC for a function defined over \mathbb{R}^+ . Given a positive-valued random variable X with the PDF $p_X(x)$, the second-kind first and

second characteristic functions are, respectively, defined as [13]

$$\begin{aligned} \phi_X(s) &= \mathcal{M}[p_X(x)](s) = \int_0^\infty x^{s-1} p_X(x) dx, \\ \varphi_X(s) &= \log(\phi_X(s)), \end{aligned} \tag{9}$$

where \mathcal{M} is the Mellin transform operator. The r th order derivative of $\varphi_X(s)$ at $s = 1$ is the log-cumulants of order r ,

that is,

$$k_r = \left. \frac{d^r \varphi_X(s)}{ds^r} \right|_{s=1}. \quad (10)$$

Hereafter, we take the intensity distribution $\mathcal{H}\mathcal{G}_1^0$ as an example to estimate its parameters v , α , and λ . The processing of the amplitude one is similar. Owing to $\phi_X(s) = E(X^{s-1})$, consequently, via (8) and (9), the second-kind second characteristic functions of the $\mathcal{H}\mathcal{G}_1^0$ distribution yields

$$\begin{aligned} \varphi_{\mathcal{H}\mathcal{G}_1^0}(s) &= \log(\sigma) + \log(\lambda^{v\alpha - (\alpha/v)}) \\ &+ \frac{1-s}{v} \log(\lambda) + \log(n^{n+(n/v)}) + \frac{s-1}{v} \log(n) \\ &+ \log\left(\Gamma\left(-\frac{s-1+n}{v}\right)\right) + \log\left(\Gamma\left(\frac{\alpha+s-1}{v}\right)\right) \\ &- \log(v^2 \Gamma(v\alpha) \Gamma(n)) \end{aligned} \quad (11)$$

which leads to that the log-cumulants of the $\mathcal{H}\mathcal{G}_1^0$ are expressed as

$$\begin{aligned} k_1 &= \frac{\log(n/\lambda) - \Psi(-n/v) + \Psi(\alpha/v)}{v}, \\ k_r &= \frac{\Psi(r-1, -n/v)}{(-v)^r} + \frac{\Psi(r-1, \alpha/v)}{v^r}, \quad r \geq 2, \end{aligned} \quad (12)$$

where $\Psi(\cdot)$ represents the digamma function, and $\Psi(r, \cdot)$ is the r th order polygamma function.

Given a sample set $\{z_i\}$, $i \in [1, N]$, the log-cumulants can be estimated directly by

$$\begin{aligned} \hat{k}_1 &= \frac{1}{N} \sum_{i=1}^N [\ln(z_i)], \\ \hat{k}_r &= \frac{1}{N} \sum_{i=1}^N [(\ln(z_i) - \hat{k}_1)^r], \quad r \geq 2. \end{aligned} \quad (13)$$

3.2. The Parameter Estimators of $\mathcal{H}\mathcal{G}^0$. We notice that (12) is independent of the parameter σ and the r th log-cumulants shown in (12) are irrespective with the parameter λ on the condition that $r \geq 2$. In addition, we regard the parameter n as a known constant, which can be replaced by the equivalent number of looks (ENLs) [4, 11] or obtained from some prior knowledge about processed SAR images, hence, allowing us to divide the parameter estimates to three stages.

First, the estimates \hat{v} and $\hat{\alpha}$ of the parameters v as well as α are obtained by solving the following equations resorting to the numerical computation:

$$\begin{aligned} \hat{k}_2 &= \frac{\Psi(1, -n/\hat{v}) + \Psi(1, \hat{\alpha}/\hat{v})}{\hat{v}^2}, \\ \hat{k}_3 &= \frac{\Psi(2, \hat{\alpha}/\hat{v}) - \Psi(2, -n/\hat{v})}{\hat{v}^3}. \end{aligned} \quad (14)$$

Second, according to the first equation of (12), the estimate $\hat{\lambda}$ of the parameter λ is

$$\hat{\lambda} = \frac{n}{\exp(\hat{v}\hat{k}_1 + \Psi(-n/\hat{v}) - \Psi(\hat{\alpha}/\hat{v}))}. \quad (15)$$

We assume the observed amplitude PDF is $\hat{p}_{Z_A}(z)$ from the actual data, which corresponds to the histogram of tested data. The theoretical amplitude PDF denotes as $p_{Z_A}(z)$. As the previous analysis, since σ indicates the whole proportion fluctuation of $p_{Z_A}(z)$, $p_{Z_A}(z)/\sigma$ can be calculated by using \hat{v} , $\hat{\alpha}$, and $\hat{\lambda}$. Given a sample amplitude set $\{z_i \mid i = 1 \cdots N\}$, let the symbol $q_{Z_A}(z)$ be equal to $p_{Z_A}(z)/\sigma$, then the estimate $\hat{\sigma}$ of the parameter σ is simply given by

$$\hat{\sigma} = E\left(\frac{\hat{p}_{Z_A}(z_i)}{q_{Z_A}(z_i)}\right), \quad z_i \in \mathcal{Z}, \quad (16)$$

where \mathcal{Z} is a subset of $\{z_i \mid i = 1 \cdots N\}$. Here, in order to facilitate the stable fitting, we choose empirically all points of histogram within 3 dB bandwidth to calculate σ , such that $\mathcal{Z} = \{z_i \mid \hat{p}_{Z_A}(z_i) > \hat{p}_{\max}/2, \hat{p}_{\max} = \max(\hat{p}_{Z_A}(z_i)), i \in [1, N]\}$.

4. Experimental Results

In this section, we aim at verifying the performance of the proposed $\mathcal{H}\mathcal{G}^0$. In order to assess how the $\mathcal{H}\mathcal{G}^0$ performs, several space-borne TerraSAR-X geocoded scenes with various land-over typologies as examples are reported. Figures 2(a)–2(d) show four selected typical patches from a large ‘‘Sanchagang’’ TerraSAR-X image with low resolution, which are the portions of water body, drying riverbed, mountain, and a town returns, respectively. The four types of scenes are related to the homogeneous and heterogeneous terrains. For simplicity, we denote them as ‘‘water-body’’, ‘‘drying riverbed’’, ‘‘mountain’’, and ‘‘town.’’ Additionally, two urban areas shown in Figures 2(e)–2(f), extracted from a large ‘‘Beijing’’ TerraSAR-X scene with high resolution, are further carried out to demonstrate the effectiveness of the proposed model on the extremely heterogeneous terrains. Likewise, the two urban images are denoted by ‘‘urban1’’ and ‘‘urban2.’’ The main parameters of TerraSAR-X systems for ‘‘Sanchagang’’ and ‘‘Beijing’’ data are listed in Table 1.

The estimated PDFs of the proposed $\mathcal{H}\mathcal{G}^0$ model for the histograms of six selected areas indicated in Figure 2 are shown in Figure 3. As the corresponding comparisons, the fitting results with the intensively used \mathcal{G}^0 distribution are also provided, where parameter estimates of this distribution are derived by Tison et al. [6] based on the MoLC. Herein, the estimate n in $\mathcal{H}\mathcal{G}^0$ is first replaced by the ENL, that is, [4]

$$\hat{n} = ENL = n_a + n_r, \quad (17)$$

where n_a and n_r are the effective number of looks in the azimuth and range. For the previous ‘‘Sanchagang’’ and ‘‘Beijing’’ TerraSAR-X images used in this investigation, n_a and n_r are listed in the last two columns of Table 1 according

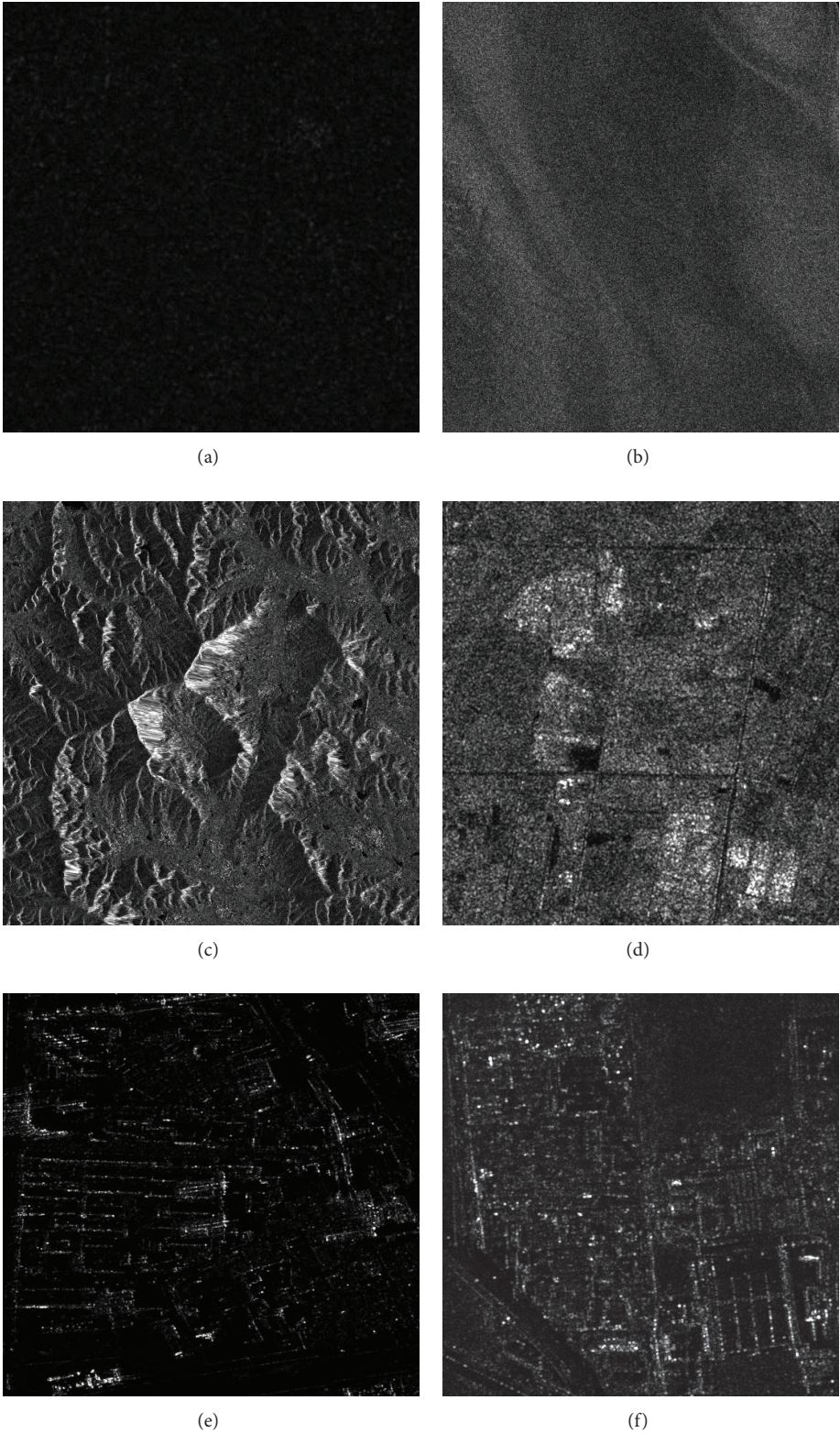


FIGURE 2: The Tested TerraSAR-X SAR image. (a) “Water body” patch with a size of 332 px × 322 px, (b) “drying riverbed” image (size: 1597 × 1734 pixels), (c) “mountain” image (size: 1996 × 2034 pixels), (d) “town” image (size: 525 × 560 pixels), (e) “urban1” image (size: 1198 × 1342 pixels), and (f) “urban2” image (size: 705 × 728 pixels).

TABLE 1: The main parameters of TerraSAR-X space-borne systems for the data in this study.

Testing site	Acquisition mode	Polarization	Resolution (az × rg)	Date	Size	Azimuth looks	Range looks
Beijing, China	SpotLight	HH	1.92 m × 2.26 m	2008-01-31T10:03 UTC	21333 px × 20000 px	1.19	1.02
Sanchagang, China	StripMap	VV	6.11 m × 5.98 m	2008-01-01T22:20 UTC	11909 px × 22363 px	1.02	2.67

TABLE 2: Parameter estimations of noted areas in Figure 2.

Area	$\mathcal{HG}_A^o(\alpha, \nu, \lambda, \sigma, n)$
“Water body”	(−6.6029, −1.1001, 6.3048, 1.0709, 3.683)
“Drying riverbed”	(−6.0382, −1.0555, 5.6813, 1.1897, 3.683)
“Mountain”	(−2.9788, −0.5779, 2.4694, 0.1426, 3.683)
“Town”	(−5.062, −0.7271, 4.5872, 0.4861, 3.683)
“Urban1”	(−1.1774, −0.4895, 0.6905, 11.1945, 2.22)
“Urban2”	(−0.8641, −0.7065, 0.3227, 2.3517, 2.22)

to reading their metadata files. Next, the estimates of all other parameters in \mathcal{HG} are accomplished by the estimators derived in Section 3, which are shown at Table 2.

Furthermore, in order to quantitatively assess the performances that different distributions fit, we define an error ratio factor (ERF) as

$$\delta = \frac{\sum_{i=1}^N \|p_c(z_i) - q(z_i)\|^2}{\sum_{i=1}^N \|p_b(z_i) - q(z_i)\|^2}, \quad (18)$$

where $\{z_i \mid i = 1 \dots N\}$ is a sample set, $p_c(\cdot)$ represents the compared theoretical PDF, $p_b(\cdot)$ is the basic theoretical PDF, and $q(\cdot)$ indicates the actual PDF from the observed data. The symbol $\|\cdot\|$ denotes 2-norm. It is obvious that the numerator and denominator in (18) separately imply the total fitting errors with the p_c and p_b to approximate q . The better the performances of p_c related to p_b fit, the smaller δ is, and vice versa. Specifically, $\delta = 1$, if both p_c and p_b have the identical capability for fitting the measured data.

Let \mathcal{HG}_A^o represent the basic amplitude PDF, and let \mathcal{G}_A^o be the compared amplitude one. The δ values of the previous six areas in this study are given in Figure 3 (see the yellow textbox). It can be clearly seen that the proposed \mathcal{HG}_A^o better agrees with the amplitude histograms of all six terrains than the \mathcal{G}_A^o , as expected, because the δ values are larger than 1 for all six areas. The same conclusion can be confirmed from a visual point of view and implies the higher fitting precision, using \mathcal{HG} than using \mathcal{G}^o , over homogeneous, heterogeneous, and extremely heterogeneous regions.

5. Conclusion and Perspective

We have developed an empirical model, \mathcal{HG}^o , to exploit the knowledge of statistical characteristics of SAR amplitude or intensity images over the wide terrain classes with homogeneous, heterogeneous, and extremely heterogeneous backscattering properties. The parameter estimators of this

model based on the MoLC are also provided. Consequently, we report the performances of different land-over typologies with \mathcal{HG}^o distribution fits. The experimental results show that the \mathcal{HG}^o distribution is a more advanced model compared with the known \mathcal{G}^o distribution to characterize the multilook processed SAR data.

As we know, a preliminary statistical analysis of SAR clutter data is important for designing signal processing algorithms, such as speckle filtering, target detection, building extraction, image segmentation, and classification. In future, it is worth expecting to use the \mathcal{HG}^o distribution in these fields. Herein, we firstly attempt to give an analytical derivation for constructing a constant false alarm rate (CFAR) detector to promote the upcoming studies of target detection in SAR images.

Given the propose amplitude model \mathcal{HG}_A^o shown in (1), its cumulative distribution function (CDF) is written as (see Appendix B)

$$F_{\mathcal{HG}_A^o}(x) = -\frac{\sigma \lambda^{\nu\alpha+(n-\alpha)/\nu} n^{n-1} \Gamma((\alpha-n)/\nu)}{\nu \Gamma(\nu\alpha) \Gamma(n)} x^{2n} \times {}_2F_1\left(\frac{\alpha-n}{\nu}, -\frac{n}{\nu}; 1 - \frac{n}{\nu}; -\frac{n}{\lambda} x^{-2\nu}\right), \quad (19)$$

$-\alpha, -\nu, \lambda, \sigma, n, x > 0,$

where ${}_2F_1(\cdot, \cdot; \cdot; \cdot)$ is the Gauss hypergeometric function. For a given value of the false alarm probability, denoted by P_{fa} , the corresponding CFAR threshold T for the \mathcal{HG}_A^o distribution can be obtained from

$$1 - P_{fa} = F_{\mathcal{HG}_A^o}(T) = -\frac{\sigma \lambda^{\nu\alpha+(n-\alpha)/\nu} n^{n-1} \Gamma((\alpha-n)/\nu)}{\nu \Gamma(\nu\alpha) \Gamma(n)} T^{2n} \times {}_2F_1\left(\frac{\alpha-n}{\nu}, -\frac{n}{\nu}; 1 - \frac{n}{\nu}; -\frac{n}{\lambda} T^{-2\nu}\right). \quad (20)$$

Considering $F_{\mathcal{HG}_A^o}(T)$ is strictly monotonously increasing, the threshold T can be accurately calculated with the help of the numerical solution or a simple bisection method [16].

Our future work will focus on demonstrating the performances of the proposed CFAR detector using some measured SAR data and investigating how the \mathcal{HG}^o distribution performs when extending it to other application fields.

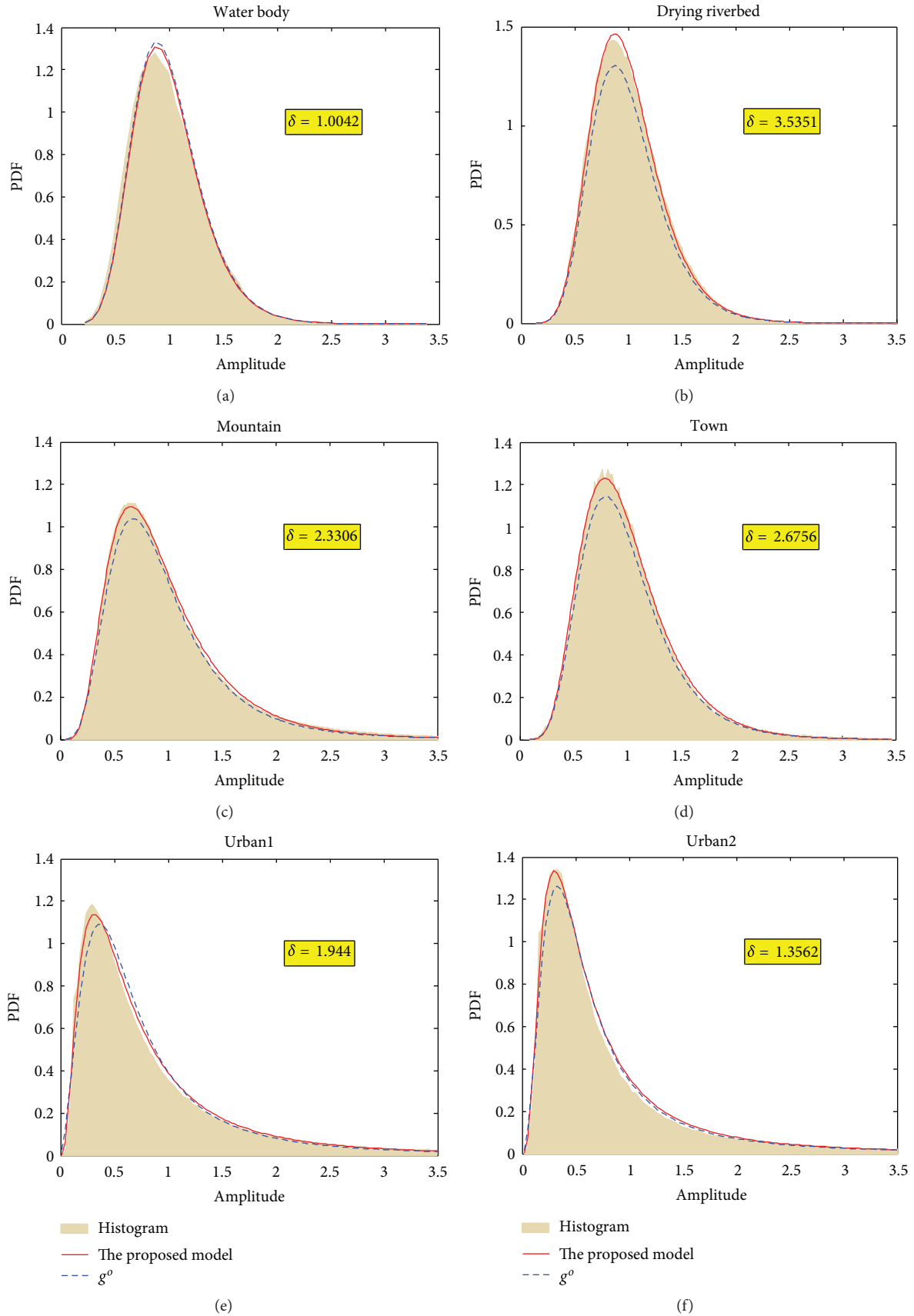


FIGURE 3: Plots of amplitude histograms and of the estimated PDFs: (a)–(f) are corresponded to the fitting results for the scenes shown in Figures 2(a)–2(f), respectively.

Appendices

A. The Derivation of m th Order Moments of the $\mathcal{H}\mathcal{G}_I^o$ Distribution

Via (2), the m th order moments of the $\mathcal{H}\mathcal{G}_I^o$ are expressed as

$$\begin{aligned} E(z_I^m) &= \int_0^\infty z^m p_{Z_I}(z) dz \\ &= -\frac{\sigma \lambda^{v\alpha} n^n \Gamma((\alpha - n)/v)}{v \Gamma(v\alpha) \Gamma(n)} \\ &\quad \times \lambda^{(n-\alpha)/v} \int_0^\infty z^{m+n-1} \left(1 + \frac{n}{\lambda} z^{-v}\right)^{(n-\alpha)/v} dz. \end{aligned} \quad (\text{A.1})$$

A variable replacement $x = z^{-v}$ leads to $z = x^{-1/v}$ and $dz = -(1/v)x^{-(1/v)-1} dx$; thus (A.1) can be rewritten as

$$\begin{aligned} E(z_I^m) &= -\frac{\sigma \lambda^{v\alpha} n^n \Gamma((\alpha - n)/v)}{v^2 \Gamma(v\alpha) \Gamma(n)} \\ &\quad \times \lambda^{(n-\alpha)/v} \int_0^\infty x^{((m+n)/v)-1} \left(1 + \frac{n}{\lambda} x\right)^{(n-\alpha)/v} dx. \end{aligned} \quad (\text{A.2})$$

According to the integral formula $\int_0^\infty x^{\mu-1} dx / (1 + \beta x)^v = \beta^{-\mu} \Gamma(\mu) \Gamma(v - \mu) / \Gamma(v)$, $|\arg \beta| < \pi$, $\text{Re } v > \text{Re } \mu > 0$ [15, 3.194, Equation 3], one can obtain (8).

B. The Derivation of the Cumulative Distribution Function of $\mathcal{H}\mathcal{G}_A^o$

Based on the definition of the CDF, the CDF of $\mathcal{H}\mathcal{G}_A^o$ is

$$\begin{aligned} F_{\mathcal{H}\mathcal{G}_A^o}(x) &= \int_{-\infty}^x p_{Z_A}(z) dz = \int_0^x p_{Z_A}(z) dz \\ &= -\frac{2\sigma \lambda^{v\alpha} n^n \Gamma((\alpha - n)/v)}{v \Gamma(v\alpha) \Gamma(n)} \\ &\quad \times \lambda^{(n-\alpha)/v} \int_0^x z^{2n-1} \left(1 + \frac{n}{\lambda} z^{-2v}\right)^{(n-\alpha)/v} dz. \end{aligned} \quad (\text{B.1})$$

Similarly, utilizing a symbol change $t = z^{-2v}$, (B.1) turns out to be

$$\begin{aligned} F_{\mathcal{H}\mathcal{G}_A^o}(x) &= \frac{\sigma \lambda^{v\alpha} n^n \Gamma((\alpha - n)/v)}{v^2 \Gamma(v\alpha) \Gamma(n)} \\ &\quad \times \lambda^{(n-\alpha)/v} \int_0^{x^{-2v}} t^{(-n/v)-1} \left(1 + \frac{n}{\lambda} t\right)^{(n-\alpha)/v} dt. \end{aligned} \quad (\text{B.2})$$

Likewise, applying the integral formula $\int_0^\mu x^{\mu-1} dx / (1 + \beta x)^v = (\mu^\mu / \mu)_2 F_1(v, \mu; 1 + \mu; -\beta \mu)$, $|\arg(1 + \beta \mu)| < \pi$, $\text{Re } \mu > 0$ [15, 3.194, Equation 1], we arrive at (19) by simplifying (B.2).

References

- [1] C. J. Oliver and S. Quegan, *Understanding Synthetic Aperture Radar Images*, Artech House, Norwood, Mass, USA, 1998.
- [2] G. Gao, "Statistical modeling of SAR images: a survey," *Sensors*, vol. 10, no. 1, pp. 775–795, 2010.
- [3] A. Achim, E. E. Kuruoğlu, and J. Zerubia, "SAR image filtering based on the heavy-tailed rayleigh model," *IEEE Transactions on Image Processing*, vol. 15, no. 9, pp. 2686–2693, 2006.
- [4] T. Esch, M. Thiel, A. Schenk, A. Roth, A. Müller, and S. Dech, "Delineation of Urban footprints from TerraSAR-X data by analyzing speckle characteristics and intensity information," *IEEE Transactions on Geoscience and Remote Sensing*, vol. 48, no. 2, pp. 905–916, 2010.
- [5] A. C. Frery, J. Jacobo-Berlles, J. Gambini, and M. E. Mejail, "Polarimetric SAR image segmentation with B-splines and a new statistical model," *Multidimensional Systems and Signal Processing*, vol. 21, no. 4, pp. 319–342, 2010.
- [6] C. Tison, J. M. Nicolas, F. Tupin, and H. Maitre, "A new statistical model for Markovian classification of Urban areas in high-Resolution SAR images," *IEEE Transactions on Geoscience and Remote Sensing*, vol. 42, no. 10, pp. 2046–2057, 2004.
- [7] A. C. Frery, A. H. Correia, and C. D. C. Freitas, "Classifying multifrequency fully polarimetric imagery with multiple sources of statistical evidence and contextual information," *IEEE Transactions on Geoscience and Remote Sensing*, vol. 45, no. 10, pp. 3098–3109, 2007.
- [8] V. A. Krylov, G. Moser, S. B. Serpico, and J. Zerubia, "Supervised high-resolution dual-polarization SAR image classification by finite mixtures and copulas," *IEEE Journal on Selected Topics in Signal Processing*, vol. 5, no. 3, pp. 554–566, 2011.
- [9] Y. Delignon, R. Garello, and A. Hillion, "Statistical modeling of ocean SAR image," *IEE Proceedings Radar, Sonar and Navigation*, vol. 144, no. 6, pp. 348–354, 1997.
- [10] Y. Delignon and W. Pieczynski, "Modeling non-Rayleigh speckle distribution in SAR images," *IEEE Transactions on Geoscience and Remote Sensing*, vol. 40, no. 6, pp. 1430–1435, 2002.
- [11] A. C. Frery, H.-J. Müller, C. D. C. F. Yanasse, and S. J. S. Sant'Anna, "A model for extremely heterogeneous clutter," *IEEE Transactions on Geoscience and Remote Sensing*, vol. 35, no. 3, pp. 648–659, 1997.
- [12] K. L. P. Vasconcellos, A. C. Frery, and L. B. Silva, "Improving estimation in speckled imagery," *Computational Statistics*, vol. 20, no. 3, pp. 503–519, 2005.
- [13] J. M. Nicolas, "Introduction to second kind statistic: application of log-moments and log-cumulants to SAR image law analysis," *Traitement du Signal*, vol. 19, no. 3, pp. 139–167, 2002.
- [14] S. N. Anfinsen and T. Eltoft, "Application of the Matrix-variate mellin transform to analysis of polarimetric radar images," *IEEE Transactions on Geoscience and Remote Sensing*, vol. 49, no. 6, pp. 2281–2295, 2011.
- [15] S. I. Gradshteyn and I. M. Ryzhik, *Table of Integrals, Series, and Products*, Academic Press, San Diego, Calif, USA, 7th edition, 2007.
- [16] G. Moser, J. Zerubia, and S. B. Serpico, "SAR amplitude probability density function estimation based on a generalized Gaussian model," *IEEE Transactions on Image Processing*, vol. 15, no. 6, pp. 1429–1442, 2006.

Research Article

A Wide-Beam Scanning Mode for Near-Space Passive SARs

Peng Zhou, Peng Ren, and Yongshou Dai

College of Information and Control Engineering, China University of Petroleum, Qingdao 266580, China

Correspondence should be addressed to Peng Zhou, hdpuzp@163.com

Received 13 September 2012; Accepted 20 November 2012

Academic Editor: Gui Gao

Copyright © 2012 Peng Zhou et al. This is an open access article distributed under the Creative Commons Attribution License, which permits unrestricted use, distribution, and reproduction in any medium, provided the original work is properly cited.

A near-space passive SAR consists of a passive radar receiver placed on a near-space vehicle and another existing radar on a satellite serving as an illuminator. In this paper, we present a wide-beam scanning mode for near-space passive SARs for the purpose of increasing the azimuth scene extension. The receiving distance of a near-space SAR is much shorter than that of a satellite-based SAR, and the synthetic aperture time for a near-space passive SAR is not longer than the time interval during which a target transverses the azimuth beam of a transmitter. We design our novel mode by spreading the azimuth beam of a receiver to match the azimuth footprint of the transmitter. We also synchronize the azimuth beam of the receiver with that of the satellite within seconds during the beam scanning to further increase the scene extension. Furthermore, we formulate the azimuth scene extension and the footprint overlapping time for near-space passive SARs in terms of the possible locations of the involved satellites and receivers. Experimental simulations demonstrate the effectiveness of our proposed mode, especially revealing that the wide-beam scanning mode improves the azimuth scene extension and footprint overlapping time over the wide-beam mode, without decreasing azimuth resolution.

1. Introduction

In the study of astronautics and aeronautics, the space between the traditional realms of satellites and typical airplanes is commonly referred to as the near-space, which is quantitatively defined as the atmospheric region from about 20 kilometers to 100 kilometers above the Earth's surface [1]. Since the near-space is above the troposphere, there are no atmospheric obstacles (e.g., clouds, thunderstorms, and precipitation) against remote detections or long-term communications. Therefore, the near-space exhibits great potentials for extensive applications to space attack and defense systems.

Near-space passive SARs [2] are a new type of synthetic aperture radar (SAR). The receiver of a near-space passive SAR is placed on a near-space vehicle. On the other hand, it employs another existing radar on a satellite as the illuminator. Near-space passive SARs are considered as a typical unit with asymmetric structure in the future sensor web [3] because the altitude and velocity of a near-space vehicle is very different from those of a satellite.

Spaceborne/airborne hybrid bistatic SAR [4–7], whose transmitter is spaceborne and receiver is placed on an aircraft, has a resemblance to a near-space passive SAR. However, the latter has two advantages over the former, that is, (1) wider imaging swaths introduced by the greater flying altitude of a receiver platform and (2) greater flexibility induced by the variability of the velocity of a receiver platform, ranging from approximately 5 to 3000 meters per second.

On the other hand, one common feature for near-space passive SARs and spaceborne/airborne hybrid bistatic SARs is that there is a great difference between the velocity of the transmitter platform and that of the receiver platform with regard to a point target. As a result, neither of the two classes of SARs can work on the classic strip-map mode [8]. In the research literature of spaceborne/airborne hybrid bistatic SARs, a double sliding spotlight mode has been proposed to increase the azimuth scene extension, depending on the beam steering on both sides [9]. However, this mode is not applicable to systems using sources of opportunity. To address this shortcoming, a wide-beam mode has been

studied [10] for noncooperative systems, in accordance with the fact that the receiving distance of a hybrid bistatic SAR is far shorter than that of a monostatic spaceborne SAR. In this paper, we present a wide-beam scanning mode, which enables a hybrid bistatic SAR to further increase the azimuth scene extension. The proposed mode can be used for bistatic SARs with asymmetric structure. In our work, simulations and evaluations will be made for testing the mode for near-space passive SARs.

2. Wide-Beam Scanning Mode

2.1. Overview. The receiving distance of a near-space SAR is much shorter than that of a satellite-based SAR. Furthermore, its synthetic aperture time is shorter or equal to the time interval during which a target traverses the azimuth beam of the transmitter. Based on these two properties of near-space passive SARs, we design a novel mode by spreading the azimuth beam of a near-space SAR to increase the azimuth scene extension. Furthermore, we synchronize the azimuth beam of the receiver with that of the satellite within seconds during the beam scanning to further increase the scene extension. Note that here we assume the receivers are equipped with phased array antennas to perform the beam scanning. We refer to the proposed mode as the wide-beam scanning mode. This mode allows the footprint velocity of a receiver in azimuth to be increased to that of a satellite footprint, provided that the azimuth footprint of the receiver is spread to the same width as that of the azimuth footprint of the transmitter. Under this condition, the synthetic aperture time achieves its maximum value.

Figure 1 illustrates the spatial layout of the proposed wide-beam scanning mode. At the time $t = t_{\text{start}}$, the receiver's beam starts scanning. The angle Λ_{max} is the maximum steering angle of the beam of the receiver. When $t = 0$, the satellite and the near-space vehicle pass by the scene center simultaneously and the receiver is side looking. At the time $t = t_{\text{end}}$, the scanning of the beam of the receiver comes to an end. The length L_{scene} is the achieved azimuth scene extension.

2.2. SNR for a Near-Space Passive SAR. The radar equation for a bistatic SAR [11] is

$$P_r = \frac{P_t \lambda^2 G_t G_r \sigma_b^0 A_{\text{res},b}}{(4\pi)^3 R_t^2 R_r^2}. \quad (1)$$

Here P_t and P_r are the transmitted and received powers, respectively. G_t and G_r are the transmitting and receiving gains, respectively. R_t and R_r are the distances from the transmitter and the receiver to the target, respectively. λ is the signal wavelength, σ_b^0 is the bistatic normalized radar cross section, and $A_{\text{res},b}$ is the area of the resolution cell.

For simplicity, we assume that the satellite and the near-space vehicle move in parallel flight paths and towards the

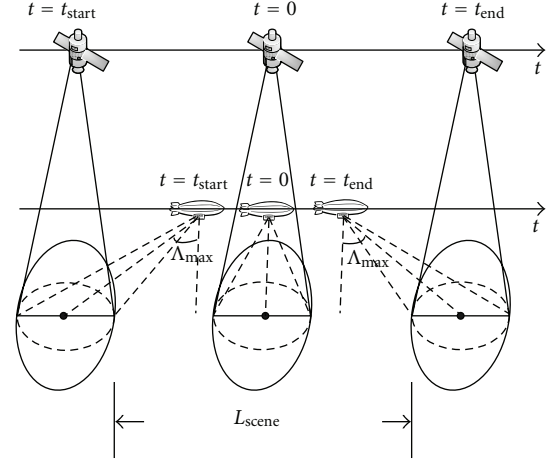


FIGURE 1: Spatial layout for the wide-beam scanning mode.

same direction. In this scenario, the ground-range and the azimuth resolution can be computed as [11, 12]

$$\rho_{\text{gr},b} = \frac{C}{2B \cos(\beta/2) \sin \eta_b}, \quad (2)$$

$$\rho_{\text{az},b} = \frac{\lambda}{V_t/R_t + V_r/R_r} \cdot \frac{1}{\xi_{\text{int},b}}.$$

Here $\rho_{\text{gr},b}$ and $\rho_{\text{az},b}$ are the ground-range and the azimuth resolution, respectively. V_t and V_r are the flying speeds of the transmitter and the receiver platform respectively, C is the speed of light, B is the bandwidth of the transmitted signal, β is the bistatic angle, η_b is the incidence angle of the bistatic bisector direction, and $\xi_{\text{int},b}$ is the synthetic aperture time. The area of the resolution cell is the product of the ground-range and the azimuth resolution.

Substituting (2) into (1) and taking the range and azimuth compression gains into consideration, we have

$$\text{SNR}_b = \frac{P_t \lambda^3 G_t G_r \sigma_b^0 \eta}{(4\pi)^3 R_t^2 R_r^2 k T_r F_r L_b} \cdot \left(\frac{1}{V_t/R_t + V_r/R_r} \cdot \frac{C}{2B \cos(\beta/2) \sin \eta_b} \right), \quad (3)$$

where SNR_b is the signal-to-noise ratio after range and azimuth compression, η is the duty cycle, k is the Boltzmann constant, T_r is the receiver noise temperature, F_r is the receiver noise figure, and L_b is the system loss factor.

To make the beam coverage in azimuth identical, we set the azimuth antenna length of the near-space vehicle to

$$l_{\text{az},r} = \frac{R_r}{R_t} \cdot \frac{l_{\text{az},t}}{\cos \Lambda_r}. \quad (4)$$

Here $l_{\text{az},t}$ and $l_{\text{az},r}$ are the azimuth antenna length of the satellite and the near-space vehicle, respectively. Λ_r is the azimuth scanning angle of the receiving antenna, which is varying in the scanning process. The presence of Λ_r is caused

by the beam spread effect during the beam scanning process. The SNR under this condition is given by

$$\text{SNR}_b = \frac{P_t \rho_t \rho_r l_{az,t}^2 l_{el,t} l_{el,r} \sigma_b^0 \eta}{4\pi \lambda R_t^3 R_r k T_r F_r L_b} \cdot \left(\frac{1}{V_t/R_t + V_r/R_r} \cdot \frac{C}{2B \cos(\beta/2) \sin \eta_b} \right). \quad (5)$$

Here ρ_t and ρ_r are the aperture efficiencies of the transmitting and receiving antennas, respectively. $l_{el,t}$ and $l_{el,r}$ are the elevational antenna lengths of the satellite and the near-space vehicle, respectively. Note that there is no parameter Λ_r in (5) due to the SNR loss caused by the azimuth scanning of the receiving antenna. For a monostatic spaceborne SAR, we reformulate (5) as follows:

$$\text{SNR}_t = \frac{P_t \rho_t^2 l_{az,t}^2 l_{el,t}^2 \sigma^0 \eta}{4\pi \lambda R_t^4 k T_r F_r L_t} \cdot \left(\frac{R_t}{2V_t} \cdot \frac{C}{2B \sin \eta_t} \right), \quad (6)$$

where SNR_t is the SNR after compression for a monostatic spaceborne SAR, σ^0 is the monostatic normalized radar cross section, and η_t is the incidence angle in a monostatic spaceborne SAR. Additionally, T_r , F_r , L_t are the receiver noise temperature, the receiver noise figure, and the system loss factor in a monostatic spaceborne SAR, respectively. Dividing (5) by (6), we have

$$\begin{aligned} \frac{\text{SNR}_b}{\text{SNR}_t} &= \frac{\rho_r \sigma_b^0 T_r F_r L_t \sin \eta_t}{\rho_t \sigma^0 T_r F_r L_b \cos(\beta/2) \sin \eta_b} \cdot \frac{l_{el,r}}{l_{el,t}} \cdot \frac{2}{R_r/R_t + V_r/V_t} \\ &= K \cdot \frac{l_{el,r}}{l_{el,t}} \cdot \frac{2}{R_r/R_t + V_r/V_t}, \end{aligned} \quad (7)$$

where K is a variable for brevity, whose value is around 1.

We then make an estimate of the SNR ratio. We assume that an X-band transmitter is placed on a LEO satellite flying at approximately 515 km altitude with $R_t = 700$ km and a near space receiver is flying at an altitude of 20 km with $R_r = 35$ km, and $V_r = 5$ m/s, $V_t = 7600$ m/s, $l_{el,t} = 0.7$ m, $l_{el,r} = 0.08$ m, $K \approx 1$, and the calculated SNR ratio is about 4.5. This ratio that is greater than 1 results from the much shorter receiving distance compared to the transmitting distance and assures the feasibility of the proposed mode. In particular, the receiving beam can be spread by weighting the amplitude and phase of the phased array elements, and thus the ratio can be significantly increased.

2.3. PRF for a Near-Space Passive SAR. For a monostatic spaceborne SAR, the employed PRF satisfies [13]

$$\left(B_{az,t} \approx \frac{2V_t}{l_{az,t}} \right) < \text{PRF}_t < \frac{1}{T_{dur,t} + \tau_p}, \quad (8)$$

where $B_{az,t}$, PRF_t , $T_{dur,t}$, τ_p are the Doppler bandwidth, the employed PRF, the echo duration time, and the pulse width of the transmitted signal in a monostatic spaceborne SAR, respectively.

For a near-space passive SAR the Doppler bandwidth is given by

$$B_{az,b} \approx \frac{V_t}{l_{az,t}} + \frac{V_r^2}{V_t^2} \cdot \frac{R_r R_t}{R_r^2 + (1 - (V_r/V_t))^2 y^2} \cdot \frac{V_t}{l_{az,t}}, \quad (9)$$

where y is the coordinate in the azimuth direction and centered at the scene center. The derivation is omitted for the simplicity. According to (9), the Doppler bandwidth achieves its maximum value at the scene center. In this case, the Doppler bandwidth is given as

$$B_{az,b,\max} \approx \left(1 + \frac{V_r^2}{V_t^2} \frac{R_t}{R_r} \right) \cdot \frac{V_t}{l_{az,t}}. \quad (10)$$

It is clear that if the ratio $(V_r^2/V_t^2) \cdot (R_t/R_r)$ is not greater than 1, the employed PRF for the spaceborne illuminator will not cause the Doppler ambiguity to a near-space passive SAR. In most cases, the above constraint can be satisfied except when the receiver platform moves rapidly, for example, faster than 1500 m/s when R_t is more than 25 times of R_r . In this case, some procedures to remove the azimuth spectral folding phenomenon must be taken when designing the imaging algorithm for a near-space passive SAR, and the study of such procedures is another research topic, which is beyond the scope of this work.

Spaceborne/airborne hybrid bistatic SARs and near-space passive SARs show resemblance in geometric layout of involved elements, because for the SAR systems it is common that the altitude and velocity of a satellite are far greater than those of the corresponding receiver platform. Therefore, in most cases, the echo duration time in a monostatic spaceborne SAR is longer than that in a near-space passive SAR since the swath is much longer in a monostatic spaceborne SAR, which is essentially similar to the case for a spaceborne/airborne hybrid bistatic SAR. Thus the employed PRF for the spaceborne illuminator will not cause the range ambiguity to a near-space passive SAR. We refer the readers to [10] for a detailed explanation of a spaceborne/airborne hybrid bistatic SAR.

In Summary, if the ratio $(V_r^2/V_t^2) \cdot (R_t/R_r)$ is not greater than 1, the PRF of the illuminator satisfies

$$B_{az,b,\max} < \text{PRF}_t < \frac{1}{T_{dur,b} + \tau_p}, \quad (11)$$

where $T_{dur,b}$ is the echo duration time for a near-space passive SAR. On the other hand, when the ratio $(V_r^2/V_t^2) \cdot (R_t/R_r)$ is greater than 1, the azimuth spectral folding phenomenon should be removed. The study of how to remove the spectral folding phenomenon is a whole new nontrivial problem, which will be addressed in our future research.

2.4. Formulation of the Azimuth Scene Extension and the Footprint Overlapping Time. The azimuth scene extension

TABLE 1: Parameters employed in the simulation.

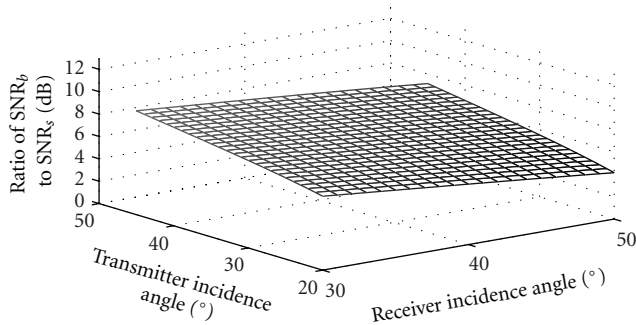
Parameters	TerraSAR-X	An X-band receiver	Envisat	A C-band receiver	TerraSAR-L	A L-band receiver
Altitude (km)	515	20	800	20	645	20
Velocity (km/s)	7.6	0.005	7.45	0.005	7.53	0.005
Incidence angle ($^{\circ}$)	20–45	30–50	15–45	30–55	20–45	40–50
Carrier frequency (GHz)	9.65	9.65	5.331	5.331	1.2575	1.2575
Peak power (kw)	2.26	—	2.3	—	4	—
Loss ¹ (dB)	2/5	3	2/5	3	2/5	3
Aperture efficiency	0.7	0.7	0.7	0.7	0.7	0.7
normalized radar cross section (dB)	−20	−20	−20	−20	−30	−30
Pulse width (μ s)	45	—	25	—	35	—
Noise figure (dB)	5	5	5	5	5	5
Noise temperature (K)	300	300	300	300	300	300
Bandwidth (MHz)	150	150	16	16	85	85
Beamwidth ELV ($^{\circ}$)	2.3	18.6	2.2	12.7	4.2	21.2
Beamwidth Az ² ($^{\circ}$)	0.33	—	0.29	—	1.1	—
Maximum steering angle ($^{\circ}$)	—	30	—	30	—	40
PRF (KHz)	4	4	2	2	2	2
Operational PRF range (KHz)	3–6.5	—	1.6–2.5	—	1.5–3	—

¹The left of the slash sign is the transmit loss for the near-space passive SAR; the right is the total loss for the monostatic spaceborne SAR.

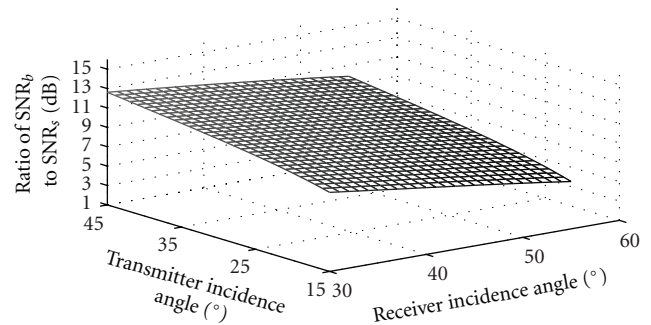
²The azimuth beamwidth of the receiver is calculated by (4).

TABLE 2: Ratio of azimuth scene extension and footprint overlapping time in wide-beam scanning mode to wide-beam mode.

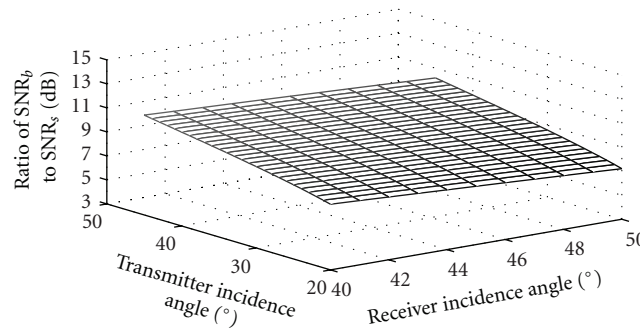
Ratio	X-band simulation	C-band simulation	L-band simulation
Azimuth scene extension	5.2–10	3.5–8.3	1.2–2.9
footprint overlapping time	3.1–5.5	2.3–4.6	1.1–1.9



(a) simulation result of X band



(b) simulation result of C band



(c) simulation result of L band

FIGURE 2: Simulation results of SNR ratio.

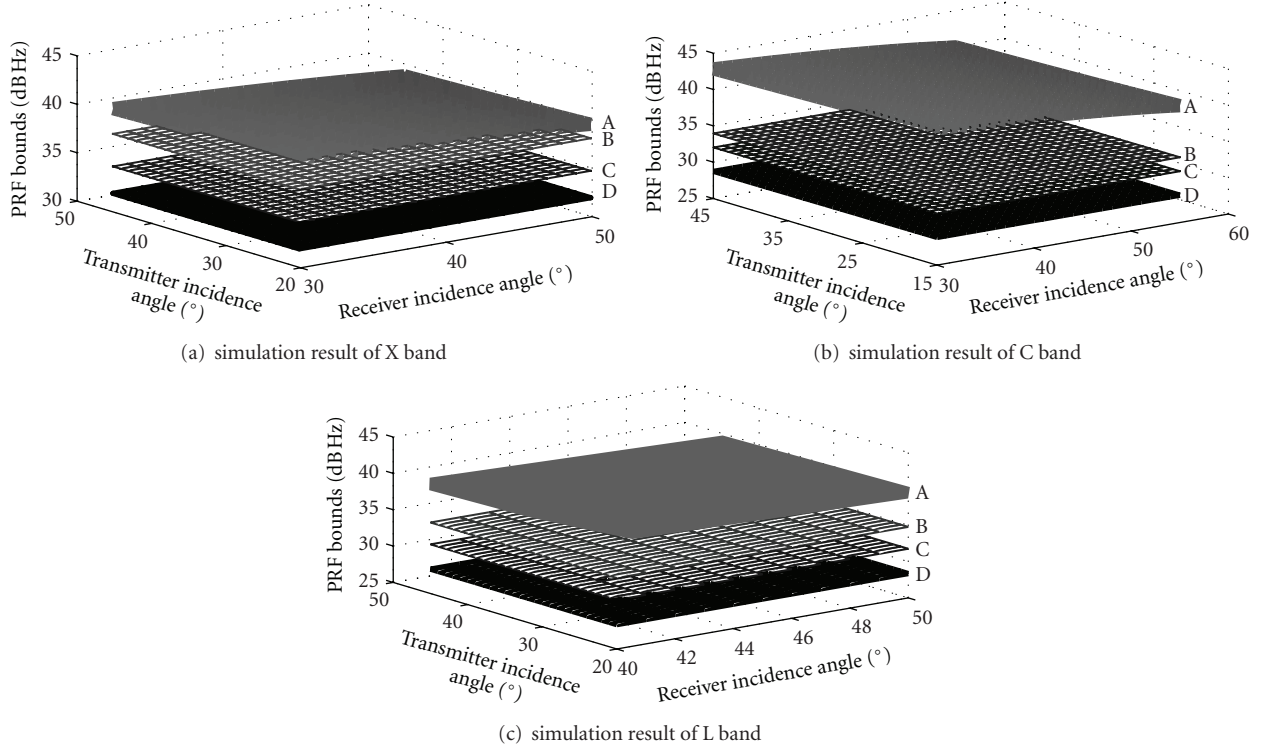


FIGURE 3: Simulation results of PRF bound with $V_r = 5\text{m/s}$. Curved surface A: the upper bound of the PRF for near-space passive SAR. Curved surface B: the upper bound of the operational PRF range for the corresponding spaceborne illuminator. Curved surface C: the lower bound of the operational PRF range for the corresponding spaceborne illuminator. Curved surface D: the lower bound of the PRF for near-space passive SAR.

L_{scene} and the footprint overlapping time t_{overlap} are separately formulated as follows:

$$L_{\text{scene}} = \frac{V_r D_{\text{az},t} + 2V_t R_r \cdot \tan(\Lambda_{\text{max}} - (\theta_{\text{az},r}/2))}{V_t - V_r}, \quad (12)$$

$$t_{\text{overlap}} = \frac{L_{\text{scene}} + D_{\text{az},t}}{V_t}.$$

Here $\theta_{\text{az},r}$ is the 3-dB beam width of the receiver's beam at the start or end of the scan. $D_{\text{az},t}$ is the azimuth footprint dimension of the transmitter. The deduction is omitted for brevity.

In our framework, the azimuth resolution discussed in [10] is reformulated as

$$\rho_{\text{az},b} = \frac{l_{\text{az},t}}{1 + (R_t/R_r) \cdot (V_r/V_t)}. \quad (13)$$

We then make an estimate of their magnitudes using the same parameter values as described in Section 2.2. Λ_{max} is set to 30° , $l_{\text{az},t}$ is set to 4 m, and λ is set to 0.031 m. The value of $\theta_{\text{az},r}$ can be computed using (4). In this study, L_{scene} and t_{overlap} are approximately 34 km and 5 s, respectively. In contrast, their values are 4 km and 1.1 s under the wide-beam mode presented in [10]. It is clear that with our assumed parameter values, the proposed mode greatly improves L_{scene} and t_{overlap} over the wide-beam mode [10]. Nevertheless, the

azimuth resolutions for the two modes are the same because of their identical synthetic aperture time.

3. Simulations

We conduct simulations to demonstrate the effectiveness of the wide-beam scanning mode. We use the parameters of TerraSAR-X, Envisat, and TerraSAR-L as those of X-, C-, and L-band radar satellites, and these parameters are employed in our simulations. All possible incidence angles, both for the illuminator and for the receiver, are examined. Table 1 lists the parameters used in the simulations. Additionally, the velocity of the receiver is set to 1000, 1500, and 2000 m/s separately in the simulations of PRF bounds for different receiver speeds.

We use the parameters in Table 1 to compute the SNR ratio by (7) and show the results in Figure 2. It can be seen that the lowest ratio is greater than 4 dB. This SNR in a near-space passive SAR guarantees acceptable image qualities. We compute the lowest allowable PRF using (10) with relevant parameters. The greatest acceptable values of PRF are also computed according to the geometric properties of the spatial layout of the modes. The results of PRF bounds are depicted in Figure 3, in which the curved surfaces A and D are the upper and lower bounds of the PRF for the near-space passive SAR, respectively, and the curved surfaces B

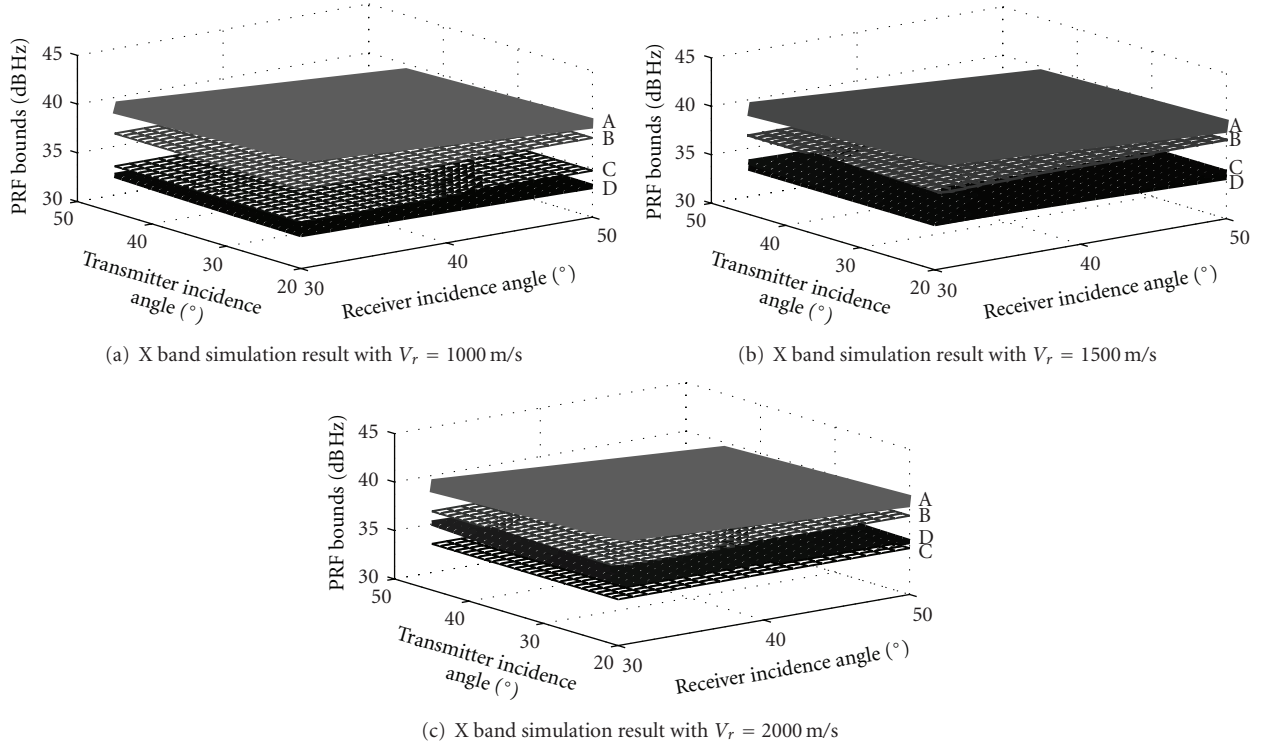


FIGURE 4: Simulation results of PRF bound with different receiver speed. Curved surface A: the upper bound of the PRF for near-space passive SAR. Curved surface B: the upper bound of the operational PRF range for the corresponding spaceborne illuminator. Curved surface C: the lower bound of the operational PRF range for the corresponding spaceborne illuminator. Curved surface D: the lower bound of the PRF for near-space passive SAR.

and C are the upper and lower bounds of the operational PRF ranges for the corresponding spaceborne illuminator, respectively. It is clear that the operational PRF ranges for the spaceborne illuminator are between the acceptable upper and lower bounds for the near-space passive SAR. Note that the receiver velocity is set to 5m/s, which is a typical speed of a floater in the near-space. In Section 2, we have observed that the lower bound of the acceptable PRF may be greater than the PRF employed by the spaceborne illuminator when the receiver platform moves rapidly. The third simulation verifies this observation. Figure 4 illustrates the acceptable PRF bound when the receiver's velocity is set to 1000, 1500, and 2000 m/s separately. We note that the curved surfaces C and D nearly overlap when the receiver's velocity is set to 1500 m/s and that the curved surface D is above the surface C when the velocity reaches 2000 m/s.

Another simulation is performed to compute the ratio of the azimuth scene extension and the footprint overlapping time for the wide-beam scanning mode and the wide-beam mode. The results are listed in Table 2, and it can be seen that the values of the azimuth scene extension and the footprint overlapping time are remarkably improved by using the proposed mode, especially for the X and C bands. The reason why the improvement in L band is relatively small is that the beam width of a receiver at this band is relatively wide due to its relatively long wavelength (see (12)).

4. Conclusions and Future Work

We have presented a wide-beam scanning mode for near-space passive SARs. Theoretical analysis and simulations have shown that the SNR resulting from our method is greater than that for a monostatic spaceborne SAR. This promising result provides the possibility for enabling near-space passive SARs to image with acceptable qualities. Experimental simulations validate that the azimuth scene extension and the footprint overlapping time in wide-beam scanning mode are greater than the values in wide-beam mode. This improvement from the presented mode does not degrade the azimuth resolution.

In our future work, we will investigate more complicated beam expansion algorithms to further increase the SNR. In other words, we will spread the beam by weighting amplitudes and phases on each array element. We will also study the performance of our new algorithms in improving SNR.

Acknowledgments

This work is supported by National Natural Science Foundation of China (no. 61105005) and by the Fundamental Research Funds for the Central Universities (no. 27R0905024A).

References

- [1] W. Q. Wang, "Near-space vehicles: supply a gap between satellites and airplanes for remote sensing," *IEEE Aerospace and Electronic Systems Magazine*, vol. 26, no. 4, pp. 4–9, 2011.
- [2] W.-Q. Wang, J. Cai, and Q. Peng, "Near-space microwave radar remote sensing: potentials and challenge analysis," *Remote Sensing*, vol. 2, no. 3, pp. 717–739, 2010.
- [3] W. Keydel, "Perspectives and visions for future SAR systems," *IEE Proceedings*, vol. 150, no. 3, pp. 97–103, 2003.
- [4] J. H. G. Ender, J. Klare, I. Walterscheid et al., "Bistatic exploration using spaceborne and airborne SAR sensors: a close collaboration between FGAN, ZESS and FOMAAS," in *Proceedings of the International Geoscience and Remote Sensing Symposium (IGARSS '06)*, pp. 1828–1831, Denver, Colo, USA, 2006.
- [5] T. Fujimura, H. Totsuka, N. Imai et al., "The bistatic SAR experiment with ALOS/PALSAR and Pi-SAR-L," in *Proceedings of the International Geoscience and Remote Sensing Symposium (IGARSS '11)*, pp. 4221–4224, Vancouver, Canada, 2011.
- [6] Z. Liu, J. Yang, X. Zhang, and Y. Pi, "Study on spaceborne/airborne hybrid bistatic SAR image formation in frequency domain," *IEEE Geoscience and Remote Sensing Letters*, vol. 5, no. 4, pp. 578–582, 2008.
- [7] M. Rodriguez-Cassola, S. V. Baumgartner, G. Krieger, and A. Moreira, "Bistatic TerraSAR-X/F-SAR spaceborne-airborne SAR experiment: description, data processing, and results," *IEEE Transactions on Geoscience and Remote Sensing*, vol. 48, no. 2, pp. 781–794, 2010.
- [8] U. Gebhardt, O. Loffeld, H. Nies, S. Knedlik, and J. Ender, "Bistatic airborne/spaceborne hybrid experiment: basic considerations," in *Sensors, Systems, and Next-Generation Satellites IX*, vol. 5978 of *Proceedings of SPIE*, Brügge, Belgium, 2005.
- [9] I. Walterscheid, T. Espeter, and J. H. G. Ender, "Performance analysis of a hybrid bistatic SAR system operating in the double sliding spotlight mode," in *Proceedings of the International Geoscience and Remote Sensing Symposium (IGARSS '07)*, pp. 2144–2147, Barcelona, Spain, 2007.
- [10] P. Zhou and Y. Pi, "Wide-beam mode and space-time synchronization of antenna footprints in hybrid bistatic SAR systems using sources of opportunity," *IEICE Transactions on Communications*, vol. E92-B, no. 4, pp. 1308–1317, 2009.
- [11] I. Walterscheid, J. Klare, A. R. Brenner, J. H. G. Ender, and O. Loffeld, "Challenges of a bistatic spaceborne/airborne SAR experiment," in *Proceedings of the European Conference on Synthetic Aperture Radar (EUSAR '06)*, Dresden, Germany, 2006.
- [12] G. Krieger, H. Fiedler, D. Hounam, and A. Moreira, "Analysis of system concepts for bi- and multi-static SAR missions," in *Proceedings of the International Geoscience and Remote Sensing Symposium (IGARSS '03)*, pp. 770–772, Toulouse, France, July 2003.
- [13] J. C. Curlander and R. N. McDonough, *Synthetic Aperture Radar—Systems and Signal Processing*, John Wiley & Sons, New York, NY, USA, 1991.

Research Article

Road Extraction from High-Resolution SAR Images via Automatic Local Detecting and Human-Guided Global Tracking

Jianghua Cheng, Wenxia Ding, Xishu Ku, and Jixiang Sun

College of Electronic Science and Engineering, National University of Defense Technology, Changsha 410073, China

Correspondence should be addressed to Jianghua Cheng, jianghua_cheng@nudt.edu.cn

Received 21 September 2012; Accepted 12 November 2012

Academic Editor: Gui Gao

Copyright © 2012 Jianghua Cheng et al. This is an open access article distributed under the Creative Commons Attribution License, which permits unrestricted use, distribution, and reproduction in any medium, provided the original work is properly cited.

Because of existence of various kinds of disturbances, layover effects, and shadowing, it is difficult to extract road from high-resolution SAR images. A new road center-point searching method is proposed by two alternant steps: local detection and global tracking. In local detection step, double window model is set, which consists of the outer fixed square window and the inner rotary rectangular one. The outer window is used to obtain the local road direction by using orientation histogram, based on the fact that the surrounding objects always range along with roads. The inner window rotates its orientation in accordance with the result of local road direction calculation and searches the center points of a road segment. In global tracking step, particle filter of variable-step is used to deal with the problem of tracking frequently broken by shelters along the roadside and obstacles on the road. Finally, the center-points are linked by quadratic curve fitting. In 1 m high-resolution airborne SAR image experiment, the results show that this method is effective.

1. Introduction

As a kind of microwave remote sensing system, synthetic aperture radar (SAR) data acquisition could operate during both day and night and is independent from the influence of sunlight and clouds. With the increasing availability of high resolution (HR) aerial and satellite SAR sensors (such as TerraSAR-X, AIRSAR, and RadarSAT-2), huge images are gotten everyday, which promote the urgent demand for analyzing and interpreting these data. Not only in photogrammetry and remote sensing field but also in computer vision and image understanding field; automatic target detection [1] and discrimination [2] from HR SAR images is a hot subject of research. As the typical man-made object in SAR images, road is one of the most important parts of modern transportation systems, which has important geographical, political, economic, and military values. Currently, road information are gaining popularity as a reference tool in locating important civilian and military targets and have an extensive application such as city planning, transportation controlling, GIS database updating, and assistant navigation.

Road network extraction from SAR images is in the growing emphasis by researchers around the world.

In low and medium resolution (>9 m) SAR images, road can be viewed as a line or curve with certain orientation, whose gray value is lower than other surrounding objects. Compared with low and medium resolution ones, high-resolution (<5 m) SAR images contain more details of the road. Road may be more precisely modeled as dark elongated areas surrounded by bright edges, which are due to double-bounce reflections by surrounding buildings or uniform backscattering by the vegetation [3, 4]. However, it is more difficult to extract road network from high-resolution SAR images, because the magnitude of noise is also magnified. The existence of various kinds of disturbances, layover effects, and shadowing are more vivid than in low and medium resolution SAR images.

Depending on whether a human being operator interacts with the process or not, it is generally acknowledged that road network extraction methods can be usually divided into two categories: automatic and semiautomatic. Different approaches have been proposed in the literature to address

the issue of automatic road extraction from high-resolution SAR images. Negri et al. [4] proposed a novel street candidate detection method, which was further specified into a multiscale feature fusion detector and a segment extractor, followed by optimization using a Markov random field description of the road network. Lisini et al. [5] thought that classical methods based on line detection do not use all the information available and presented a road extraction method which was based on the fusion of classification (statistical information) and line detection (structural information). Then, a modified Markovian approach was used for solving the global network optimization problem. Hedman et al. [6] combined two different approaches for automatic road extraction: one is more successful in rural areas and the other one is explicitly designed for urban areas. In order to get the best combination of both, a rapid mapping filter for discriminating rural and urban scenes was utilized. Finally, the results were fused on a feature level and connected by means of a network optimization. Amberg et al. [7] introduced context information (such as buildings, vehicles, etc.) detection result in the road extraction process to avoid false alarms in confusion areas and overcome difficulties of layover and bright objects.

However, viewed from the progress of current research, even if automatic road extraction from optical remotely sensed images is still difficult, let alone the SAR images which are relatively harder with the visual senses compared with the optical ones. Existing automatic road extraction algorithms cannot achieve satisfactory results in robustness, accuracy, and applicability and often requires setting lots of parameters and manual processing later, which does not give a great deal of enhancing efficiency in SAR images interpretation. Some researchers believe that the automatic road extraction method is not realistic in the foreseeable future. Semiautomatic methods can combine the rapid calculation of machine with human interpretation technique effectively. Therefore, the study of semiautomatic methods of manual intervention for quick and accurate extraction of the road is a more practical choice.

Numerous semiautomatic road extraction methods have been proposed from high-resolution remote sensing images [8–14], which are usually categorized into iterative two phases: local detection and global tracking. The local detection contents mainly include direction, width, and central point position in current local road region. Global tracking is an iterative line or center-point growing process, used to recover the network topology by connecting local detected outcomes and suppress false positives. Kim et al. [8] defined a rectangle window around a user-given input point, and then by matching the window along the orientation of the road under consideration. New match proceeded by shifting a matched target window further along road orientation once matching succeeded. By repeating the process above, a series of points were obtained. Zhou et al. [9] introduced a human-computer interaction system for robust and efficient road tracking. Extended Kalman filters and particle filters are used in conjunction with human inputs to estimate road axis points and update the tracking algorithms. Lin et al. [10] proposed a new combination strategy to extract the road

networks. One or more suitable road trackers were designed or combined for each type of roads based on the initialization information, such as the interlaced window matching, the profile matching, the rectangular window matching, and the parallelepiped angular texture signature (PATS).

The universal problems of these methods exist in that: (1) more than two human inputted initial seed points are needed to calculate the orientation and width of the road and (2) the tracking result is easily affected by the initial seed points (3) which are generally used in optical remote sensing images, seldom reports on their applicability on high resolution SAR images. Compared with optical remote sensing images, the signal-to-noise ratio (SNR) is lower in SAR images, which are disturbed by multiplicative speckle noise and often blocked by fences, crossovers, cars, and so forth on the road. The tracking methods mentioned above would be broken frequently and cannot be directly used in high resolution SAR images.

This paper presents a semiautomatic road center-point tracking method from high resolution SAR images, which consists of two iterative steps: (1) local double window detection model and (2) global particle filter tracking. Local double window detection only needs one input seed point, which has no impact on tracking. Global particle filter tracking can effectively jump over obstacles. Also, calculation efficiency is improved because of less human-computer interaction. Then, quadratic curve fitting is used to link the extracted road center-points into line. The remaining sections of this paper are organized as follows. In Section 2, a general scheme of road centerpoint tracking is introduced, and the local double window detection model is proposed. In Section 3, experiments are described and the performances of the road trackers are discussed. In Section 4, some conclusions are reached.

2. Methodology

2.1. Road Characteristics. Ideally, roads appear as a continuous strip region with constant width and can be modeled as dark elongated areas surrounded by bright edges (see Figure 1(a)) in high resolution SAR images. Actually, due to the interference of speckle noise and surrounding objects, the road shows the following characteristics in high-resolution SAR images.

- (i) Obstacles such as iron fences and vehicles would destroy the continuity of the border of road and contaminate it with a large number of bright points or small bright areas. Road surfaces may not have adequate contrast with adjacent areas. Sometimes even human beings cannot distinguish road areas from other object areas (see Figure 1(b)).
- (ii) Road conglutinating with parking areas or covered by buildings shadow would make original bright bilateral edges change into single edge (see Figure 1(c)). This makes the width inconsistent in the same road segment.
- (iii) High buildings shelter and trees shadow, make parts of road segment even have no edge (see Figure 1(d)).

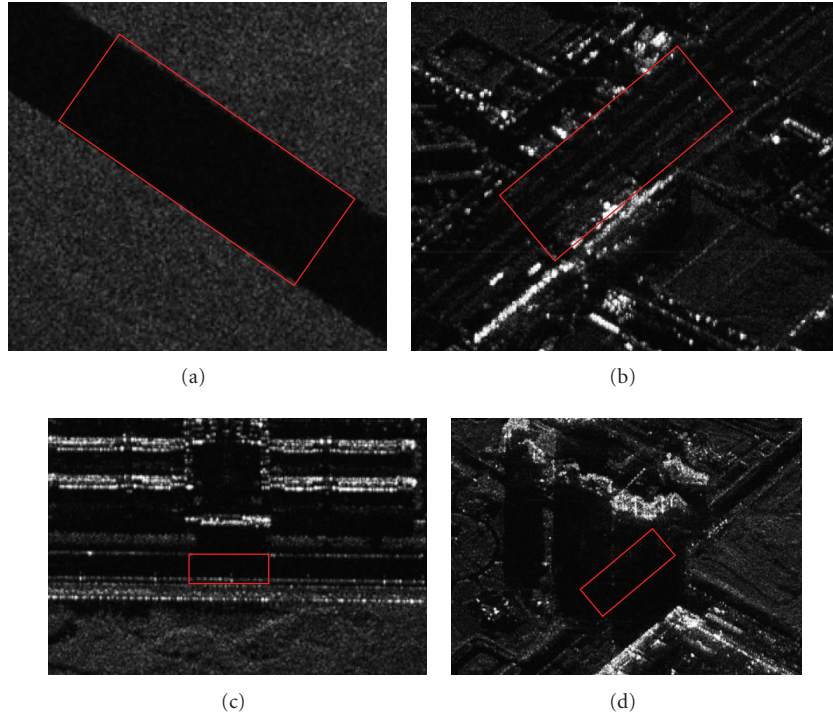


FIGURE 1: Road edges in high resolution SAR images. (a) Distinct bilateral edges. (b) Blurry road edges. (c) Single edge. (d) No edge.

As the actual complex circumstances of high-resolution SAR images, it is difficult to use a classical SAR edge detection method to extract road.

2.2. Framework. The framework of our semiautomatic road extraction algorithm consists of two components (see Figure 2).

- (1) *User.* The user is the master of the whole progress of the algorithm. He (or she) inputs an initial seed point when new high resolution SAR image provided, or an orientation leading point when the tracking cannot be carried on.
- (2) *Computer.* The computer extracts road center lines by three steps: local detection, particle filter tracking, and center-points fitting. Double window model is used to get the local road information such as orientation, width, and center point in local detection step. Particle filter tracking is used to predict and update the next road center point. When searching obstacle is met (such as end of road, border of image, tracking departure road area, crossroad, etc.), it hands over the control to the user.

2.3. Local Detection. The type of window sometimes plays a very important role in road detection. Several windows have been used to detect local road information from high resolution remote sensing images, such as circular window [11], rectangular window [8, 12] and interlaced window

[10]. Cheng et al. [11] proposed fixed size circular window to search the actual road center-point perpendicular to the road direction (see Figure 3(a)). This method needs not to rotate in window matching calculation. Rectangular window is frequently used in road center-point searching, orientation calculation, and window matching, because of its simpleness and practicality. Figure 3(b) shows road centerlines tracking by rectangular window least squares correlation matching. Figure 3(c) shows several rectangular windows rotating around a road centerline point, in order to compute the road direction. Interlaced window is composed of two parts: some cross-section profiles (i.e., each is a typical intensity profile perpendicular and symmetrical to the road axis) and some rectangular windows of road markings (i.e., some intensity rectangles whose width is as wide as lane markings). Lin et al. [13] used interlaced window to predict next most possible position of the road axis.

However, the windows mentioned above cannot adapt to different width road detection because of fixed size. This paper presents a novel double window type, which is composed of two windows: outer square window and inner rectangular window (see Figure 4(a)). The size of outer square window is fixed and chosen based on the resolution of the SAR sensor. Additionally, the outer square window cannot rotate anymore. It is used to calculate the local road direction. The inner rectangular window can shift (see Figure 4(b)), expand (see Figure 4(c)), and rotate (see Figure 4(d)) to adapt to different width and direction of road detection. It is used to search the center points and calculate the width of a road.

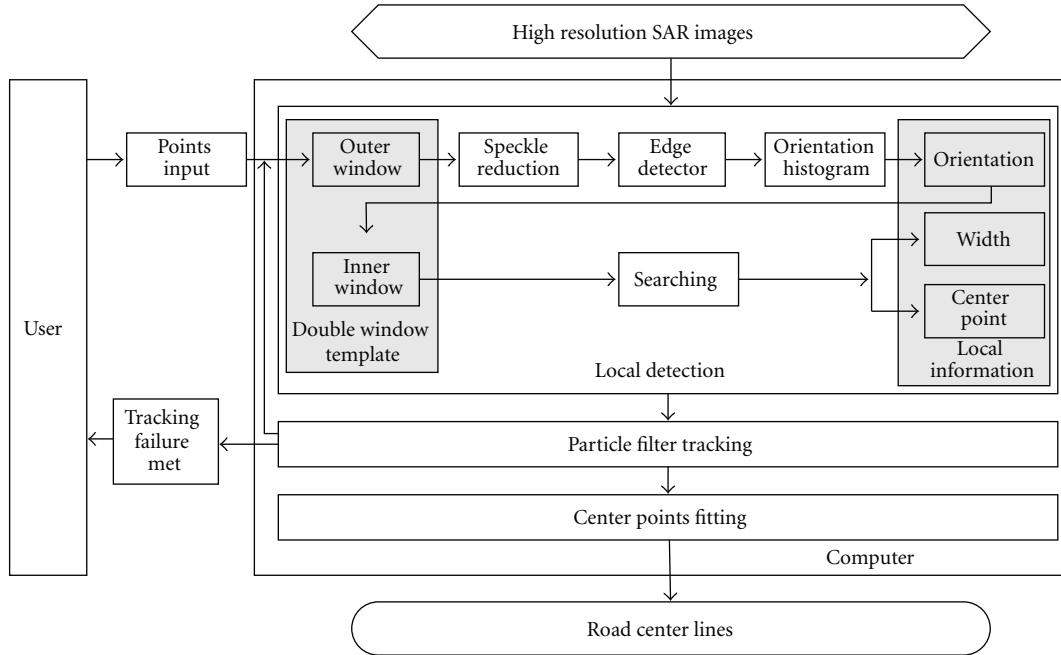


FIGURE 2: Semiautomatic road centerline extraction framework.

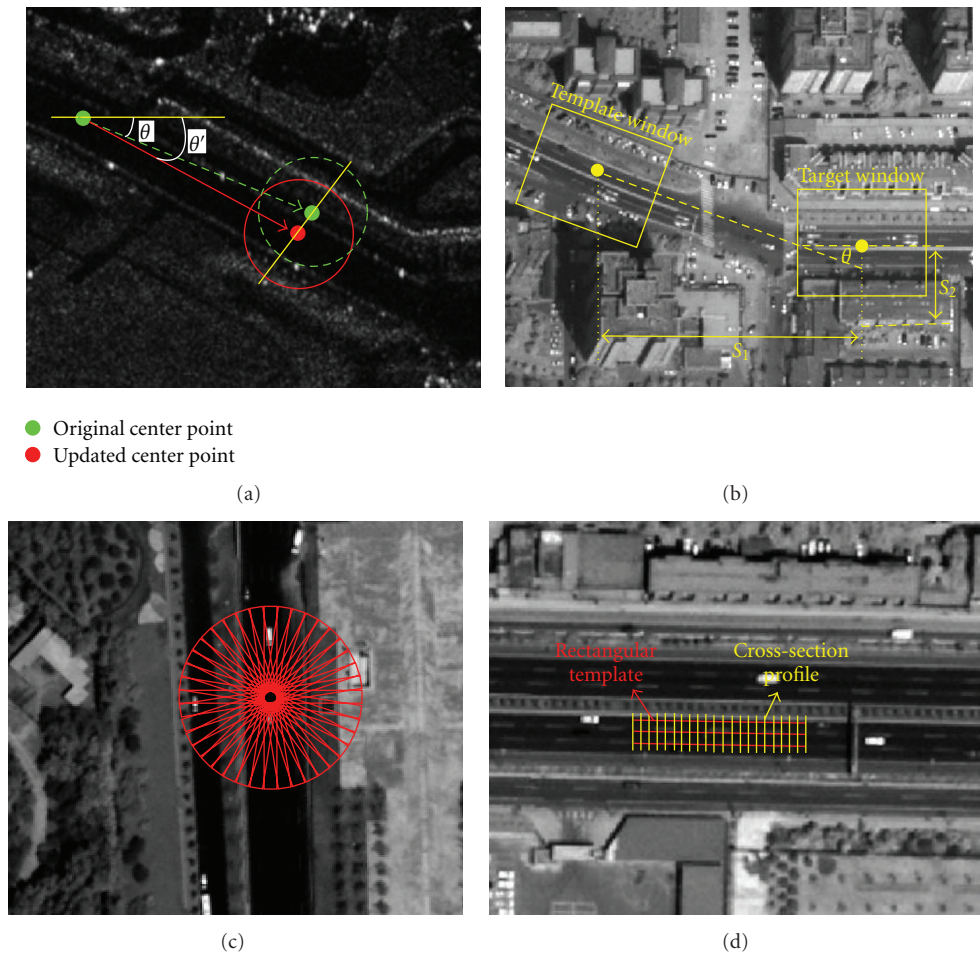


FIGURE 3: Local detection window. (a) Circle window. (b) Rectangular window. (c) Rotating rectangular window. (d) Interlaced window.

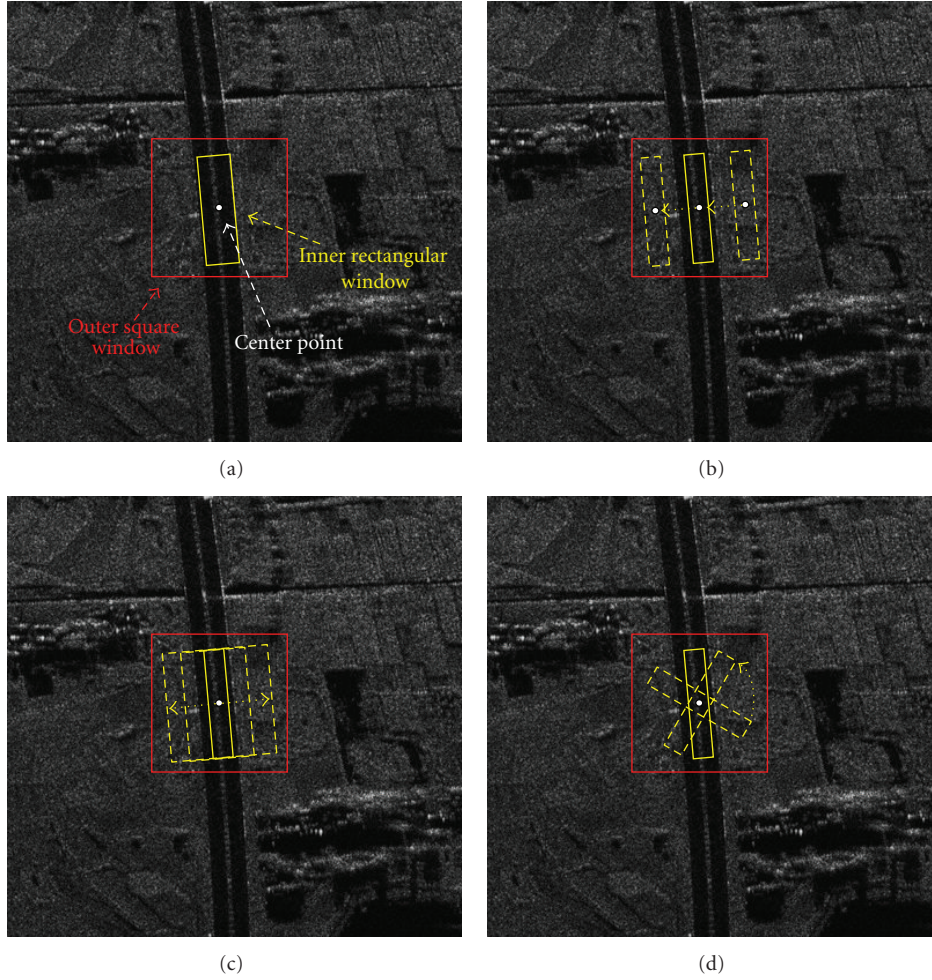


FIGURE 4: Double window. (a) Definition. (b) Inner window shifting. (c) Inner window expanding. (d) Inner window rotating.

2.3.1. Outer Square Window Orientation Estimation. After an initial seed center point is given by a human being, the outer square window size and position are fixed. And the main orientation is estimated within the outer square window. There exist several orientation estimation methods, such as edge direction histogram (EDH) [15], histograms of oriented gradients (HOG) [16], and tensor voting [17]. These methods cannot be directly used in SAR images because of the influence of multiplicative speckle noise. We firstly introduce the speckle reduction process before orientation estimation.

Many speckle reduction filters have been proposed in the literature for processing SAR images corrupted by multiplicative noise [18–20]. Among them, Frost filter [18] possesses better edge preserving properties and has shown superior performances for processing of speckle images.

Frost et al. [18] has proposed an optimum minimum mean-square error (MMSE) estimation starting from the following observed SAR image model:

$$I(x, y) = (r(x, y) \cdot n(x, y)) \otimes h(x, y), \quad (1)$$

where $h(x, y)$ is the system impulse response, \otimes is the convolution operation, $r(x, y)$ is the “ideal SAR image,”

and $n(x, y)$ is the multiplicative speckle noise. The impulse response $m(x, y)$ of the MMSE filter that provides an estimate of $r(x, y)$ from $I(x, y)$ is obtained by minimizing the mean square error ε given by

$$\varepsilon^2 = E[(r(x, y) - I(x, y) \otimes m(x, y))^2]. \quad (2)$$

The minimization leads to the MMSE filter with the following impulse response:

$$m(x, y) = \frac{k}{2} \left(\frac{\sigma_I}{\bar{I}} \right)^2 \exp \left[-k \left(\frac{\sigma_I}{\bar{I}} \right)^2 |D(x, y)| \right], \quad (3)$$

where k is a scale constant, \bar{I} and σ_I^2 are the mean and variance of the observed SAR image, respectively, and $D(x, y)$ is the distance from current point (x, y) to local center point.

After speckle reduction by Frost filter, canny operator [21] is used to detect road edges. Let $I(x, y)$ denote the SAR image, and $G(x, y)$ is the 2-D Gaussian function. We have the

following road edge intensity and orientation formulation, respectively:

$$C(x, y) = |\nabla G \otimes I(x, y)|, \quad (4)$$

$$\vec{n} = \frac{\nabla G \otimes I(x, y)}{|\nabla G \otimes I(x, y)|},$$

where ∇G is the gradient of G , and \otimes stands for the convolution operation.

Then, the histogram of every pixel orientation is carried out within the outer square window. The maximum of the orientation histogram is the main road direction. Figures 5 and 6 show the main road orientation estimation process within 100×100 the outer square window. Figures 5(d) and 6(d) are the orientation histogram of road edge.

2.3.2. Inner Rectangular Window Road Width and Center-Point Calculation. The center-point position of a road is determined by its width. In previous semiautomatic road tracking methods, the road width was typically confirmed by two [9] or three [10] human inputted seed points. Whereas in our system, the road width is calculated automatically by inner rectangular window shifting, expanding, or rotating. The width and center-point calculation algorithm is detailed as follows.

Step 1 (initialization). Take the main direction of outer square window as the inner rectangular window rotating orientation, and take the outer square window's center point as the initial inner rectangular window's center point. Define the fixed length of the inner rectangular window as L . Define the initial width of the inner rectangular window as W , which is changeable.

Step 2 (shifting). Perpendicular to the main road direction, and shift the inner rectangular window with fixed step length d_1 within the outer square window area, and compute the variations and means of series shifted inner rectangular windows.

Step 3 (expanding). Calculate the minimum variation and mean among the series shifted inner rectangular windows, and take corresponding inner rectangular window as the initial expanding window. Perpendicular to the main road direction, and expand the inner rectangular window with fixed step length d_2 within the outer square window area, and compute the variations and means of series expanded inner rectangular windows.

Step 4 (result). Calculate the minimum variation and mean among the series shifted inner rectangular windows, and take corresponding inner rectangular window as the best fitted window. Take its width as the local road width, and take its center point as the local road center point.

Our road width and center-point calculation algorithm only need one initial seed input.

2.4. Particle Filter Tracking. Particle filtering, specifically the *condensation* algorithm proposed by Isard et al. [22], is a

recursive procedure to estimate the parameters of a dynamic system and has been successfully used in modeling nonlinear and non-Gaussian road tracking system [9, 23, 24]. It starts from a seed point p_0 of the road and then moves along its direction.

2.4.1. State and Observation Model. The current state S_k is relative to the previous state and updated by the following nonlinear equation:

$$\mathbf{s}_k = \begin{bmatrix} x_k \\ y_k \\ \theta_k \end{bmatrix} = \begin{bmatrix} x_{k-1} + d_{k-1} \cdot \sin(\theta_{k-1}) + u_k^1 \\ y_{k-1} + d_{k-1} \cdot \cos(\theta_{k-1}) + u_k^2 \\ \theta_{k-1} + u_k^3 \end{bmatrix}, \quad (5)$$

where (x_k, y_k) is the current road center point, d_k is the current step length, θ_k is the current road direction, and u_k^i ($i = 1, 2, 3$) is the noise came from state transform. The tracking procedure is represented by an ordered state sequence $S_{0:k} = (S_0, \dots, S_k)$.

The current observation vector is represented by Z_k as follows:

$$\mathbf{z}_k = h(\mathbf{s}_k) + \mathbf{v}_k = \begin{bmatrix} 1 & 0 & 0 \\ 0 & 1 & 0 \\ 0 & 0 & 1 \end{bmatrix} \mathbf{s}_k + \mathbf{v}_k, \quad (6)$$

where \mathbf{v}_k is the measure noise. The observation sequence Z_k is formed from an ordered observed vectors $Z_{0:k} = (Z_0, \dots, Z_k)$.

2.4.2. Particle Filtering. To grow such a sequence, particle filtering approximates the posterior density $p(S_k/Z_k)$ by the particle set $\{S_k^i, w_k^i, i = 1, \dots, N\}$ in each time step k , where w_k^i is a weight used to characterize the probability of the particle S_k^i , N is the number of particles which is set by experience and selected as 100, and $\sum_{i=1}^N w_k^i = 1$. The posterior density function (pdf) can be approximated by

$$p\left(\frac{S_k}{Z_{1:k}}\right) \approx \sum_{i=1}^N w_k^i \delta(S_k - S_k^i), \quad (7)$$

where δ is the Dirac delta function. When we have enough samples from a pdf, the set of samples can be used to closely represent that distribution. However, the pdf of $p(S_k/Z_{1:k})$ is unknown in reality, and we can only generate samples from importance density function $q(\mathbf{s}_k/\mathbf{z}_{1:k})$ [24]. The choice of $q(\mathbf{s}_k/\mathbf{z}_{1:k})$ is an important issue in the design of the particle filtering. Generally, the transitional prior probability density function $p(\mathbf{s}_k/\mathbf{s}_{k-1}^i)$ is chosen as the importance density function. Based on this choice, the samples and weights update equation can be defined, respectively, as

$$s_k^i \sim p\left(\frac{\mathbf{s}_k}{\mathbf{s}_{k-1}^i}\right), \quad (8)$$

$$\omega_k^i = \omega_{k-1}^i \times p\left(\frac{\mathbf{z}_k}{\mathbf{s}_k^i}\right). \quad (9)$$

We assume that the observation is normally distributed, and the likelihood of the observation is

$$p\left(\frac{\mathbf{z}_k}{\mathbf{s}_k^i}\right) \propto \frac{1}{\sqrt{2\pi}} \exp\left(-\frac{l_i^2}{2\sigma^2}\right), \quad (10)$$

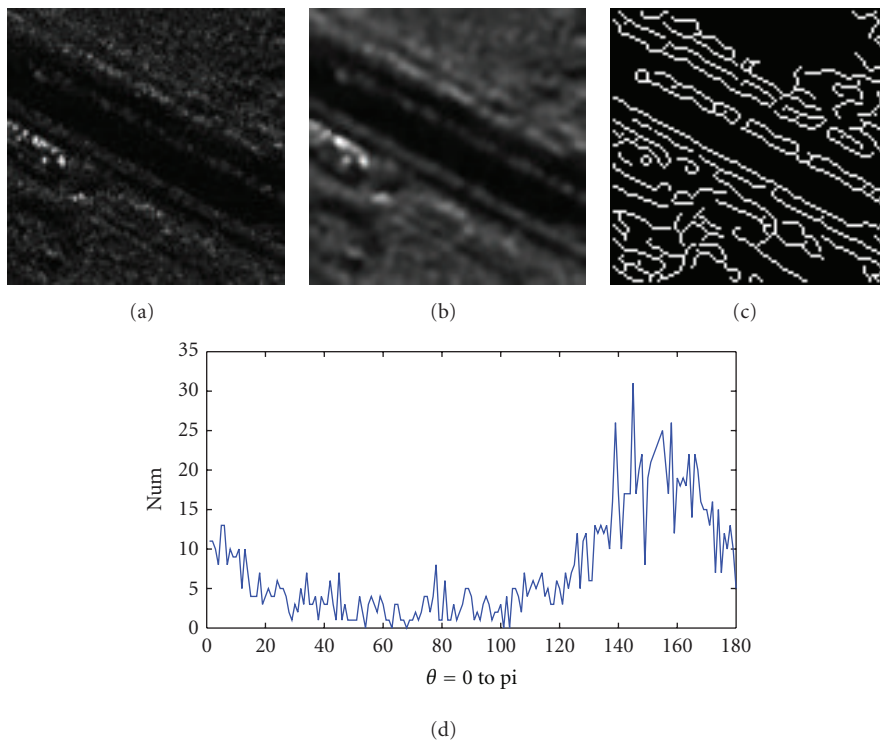


FIGURE 5: Orientation estimation 1. (a) Cropped SAR image. (b) Frost filter. (c) Canny edge detection. (d) Edge orientation histogram.

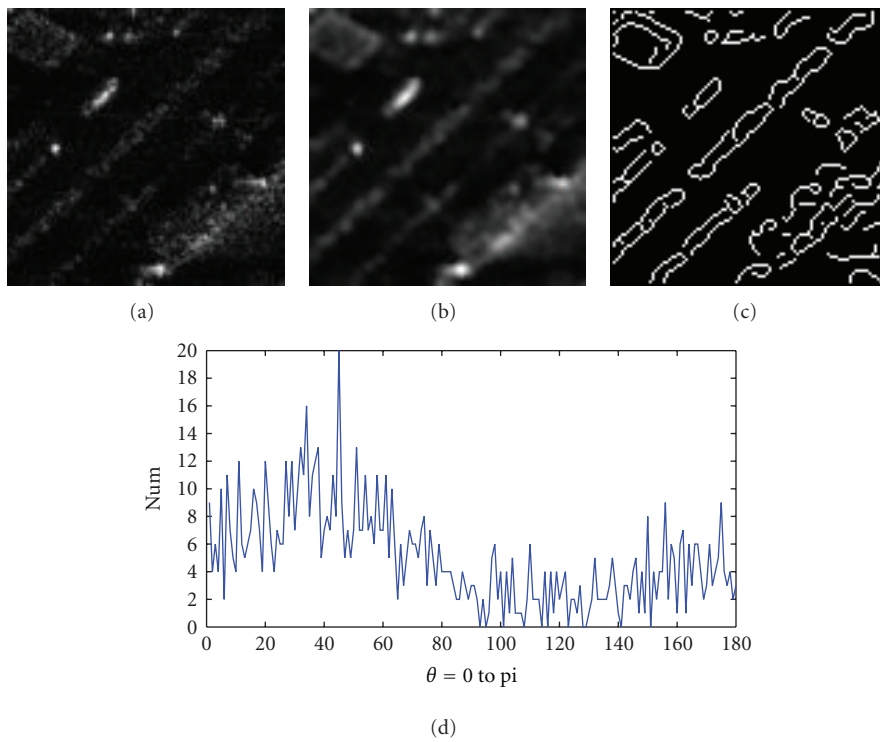


FIGURE 6: Orientation estimation 2. (a) Cropped SAR image. (b) Frost filter. (c) Canny edge detection. (d) Edge orientation histogram.

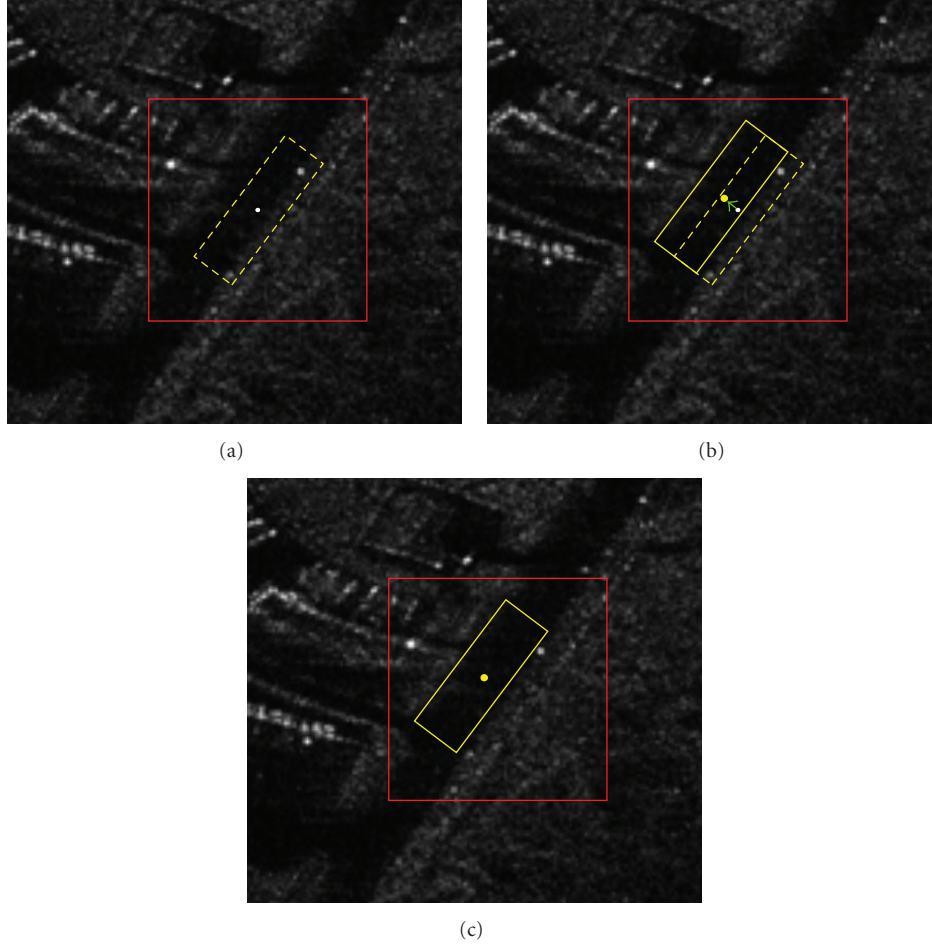


FIGURE 7: Initial seed point automatic update. (a) Input seed point. (b) The procedure of update. (c) Updated center-point.

where l_i is the Euclidean distance between the position of particle S_k^i and its corresponding observation.

The procedure of particle filter tracking is described as follows.

Step 1 (initialization). $\mathbf{s}_0^i \sim p(\mathbf{s}_0/\mathbf{z}_0) = p(\mathbf{s}_0)$ and $w_0^i = 1/N$, where $i = 1, \dots, N$.

Step 2 (prediction). Sample S_k^i from the importance density function $p(\mathbf{s}_k/S_{k-1}^i)$, and predict the next state vector S_{k+1} by using (5).

Step 3 (update). Calculate unnormalized weight w_k^i by using (9) and (10), and then normalize weight $\tilde{w}_k^i = w_k^i / \sum_{i=1}^N w_k^i$.

Step 4 (estimate output). $\hat{S}_k = \sum_{i=1}^N w_k^i S_k^i$.

Step 5 (resample). Calculate $\hat{N}_{\text{eff}} = (\sum_{i=1}^N (\tilde{w}_k^i)^2)^{-1}$. If $\hat{N}_{\text{eff}} < N_{\text{th}}$, $\{S_k^i, w_k^i\} = \text{RESAMPLE}[\{S_k^i, w_k^i\}]$.

Step 6 (return). Go to Step 2.

2.4.3. Starting Point Selection and Stopping Criteria. Before road center-point tracking procedure, the initial seed point is inputted by a human being. Then, the outer square window is set based on this inputted center point, and local main road direction is calculated. Subsequently, the inner rectangular window rotates to the local main road direction and searches the actual road center point. And then, particle filter tracking is carried out.

In real applications, the road characteristics are more complex in high resolution SAR images. The road center-point tracking procedure is broken frequently because of shelters along the road or obstacles on the road. For example, the outer square window cannot get the proper orientation because of shelters along the road, and the road width changes abruptly due to obstacles on the road. In this case, our particle filter tracking method makes another state update based on previous state, using a changeable step length d_k . When the tracking procedure goes continually, the step length d_k is a constant. When broken is met, d_k is increased to jump over shelters or obstacles. When contiguous jumps occur, the particle filter tracking recognizes that there is a tracking failure and returns control back to the

human being. Then, the human being restarts the tracking procedure by inputting another initial seed point.

2.5. Center-Points Fitting. Our particle filter tracking method can detect most center points despite small shelters or obstacles existing. When interference seriously exists, the extracted center points would deviate from the actual road central points. In order to lower the influence of interference, a method is applied to generate smooth road center lines by fitting all the extracted center points along one road segment.

Generally, the variety of a road centerline curvature is very small. A conic is sufficient to describe the road centerline. Define the extracted center points of a road are $\{x_i, y_i\}_{i=1}^{N_r}$. The conic is $y(x) = a_0 + a_1x + a_2x^2$. The error of fitting is

$$E = \sum_{i=1}^{N_r} (y(x_i) - y_i)^2. \quad (11)$$

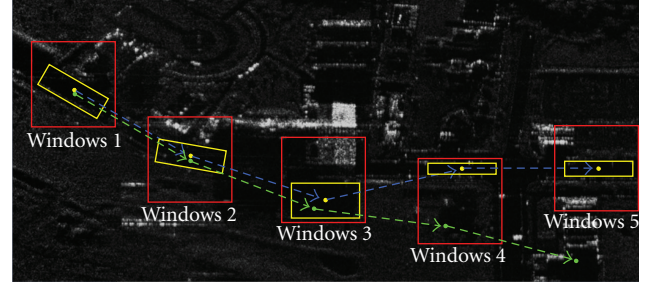
The parameters of a_0 , a_1 , a_2 are calculated by means of least square error.

3. Experimental Results and Analysis

To evaluate our proposed method, three different scale high resolution SAR images are chosen, which are taken by airborne in the region of Hefei, Anhui province, China. Figure 7 is zoomed in from the image with a ground pixel size of about 1 m. Figures 8 and 9 are normal scale with a ground pixel size of about 1 m. All the experiments are run on P(R) dual-core 2.8 GHz CPU, with 2 GB SDRAM, and the software platform is MATLAB R2007b.

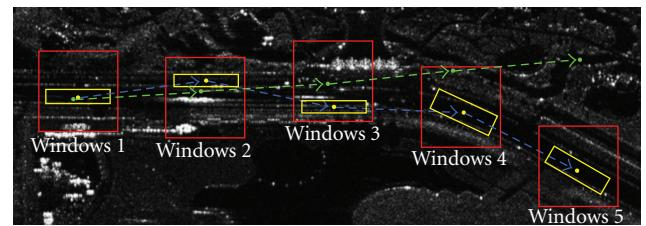
Figure 7(a) shows that an initial seed road center point is inputted by human being, which has a little bias from the true one. Red squares are outer window, and yellow rectangles are inner window. Our double windows can adjust automatically to the real position. In order to explore the effectiveness of our proposed method, the comparisons with other center-points extraction method are made like Kim's least squares correlation matching [8], which are shown in Figures 8 and 9. Yellow points are road center points extracted by our tracking method and connected by white lines. Green points are road center points extracted by the Kim's least squares correlation matching method and connected by green lines. In Figure 8, there exist shelters (Windows 3) along the roadside. Our tracking strategy can jump over it and come back to the normal road trajectory (Windows 5). But the center points extracted by the Kim's matching method are deviated from the normal road trajectory. In Figure 9, strong obstacles (Windows 2 and Windows 3) are on the road. Our tracking strategy can jump over these obstacles in the same way. However, the center points extracted by the Kim's matching method are deviated from the normal road trajectory too.

Figure 10 shows a large SAR scene also taken by airborne in the region of Hefei. Yellow points are road center points extracted by our tracking method and connected by white lines. Pink points are road center-points after fitting and connected by pink lines. In Figure 10, we can see that the



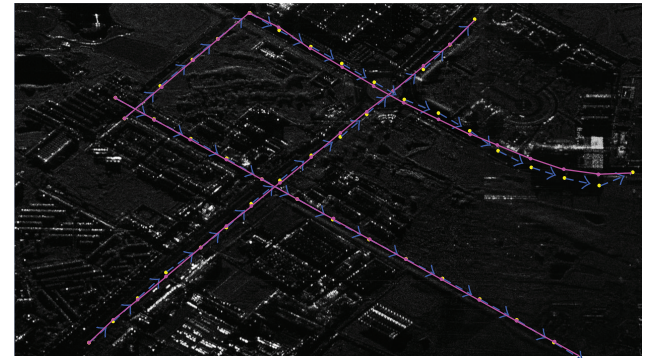
--> Center points extracted by our tracking method
--> Center points extracted by Kim's matching method

FIGURE 8: Road center-points extraction methods comparison 1.



--> Center points extracted by our tracking method
--> Center points extracted by Kim's matching method

FIGURE 9: Road center-points extraction methods comparison 2.



--> Center points extracted by tracking
— Quadratic curve fitted center lines

FIGURE 10: Extracted main road center-points fitting.

quadratic curve fitting method can link the discrete road center points into a line and smooth the abrupt changes. It is worth mentioning that our tracking method also can jump over the crossroad.

4. Conclusion

We have proposed a new double windows tracking method for extracting center points and center lines. This algorithm consists of two iterative steps, namely, local detection and global tracking. The local detection step uses double

windows, which can estimate the local road main direction and search the deviated center point automatically. The global tracking step makes use of particle filter, which can jump over shelters, obstacles, and crossroads. The presented method has been tested on three high resolution SAR images with 1 m spatial resolution. The experimental results validate the accuracy and efficiency of our method. The road center points are extracted by only using a single seed point to initialize the tracking. Moreover, this algorithm remains robust regardless of abrupt changes introduced by disturbs.

Acknowledgments

The authors wish to acknowledge the reviewers for their valuable suggestions and comments. This paper is supported by the National Natural Science Foundation of China (no. 41171316).

References

- [1] G. Gao, L. Liu, L. Zhao, G. Shi, and G. Kuang, "An adaptive and fast CFAR algorithm based on automatic censoring for target detection in high-resolution SAR images," *IEEE Transactions on Geoscience and Remote Sensing*, vol. 47, no. 6, pp. 1685–1697, 2009.
- [2] G. Gao, "An improved scheme for target discrimination in high-resolution SAR images," *IEEE Transactions on Geoscience and Remote Sensing*, vol. 49, no. 1, pp. 277–294, 2011.
- [3] G. Gao, "Statistical modeling of SAR images: a survey," *Sensors*, vol. 10, no. 1, pp. 775–795, 2010.
- [4] M. Negri, P. Gamba, G. Lisini, and F. Tupin, "Junction-aware extraction and regularization of urban road networks in high-resolution SAR images," *IEEE Transactions on Geoscience and Remote Sensing*, vol. 44, no. 10, pp. 217–221, 2006.
- [5] G. Lisini, C. Tison, F. Tupin, and P. Gamba, "Feature fusion to improve road network extraction in high-resolution SAR images," *IEEE Geoscience and Remote Sensing Letters*, vol. 3, no. 2, pp. 217–221, 2006.
- [6] K. Hedman, U. Stilla, G. Lisini, and P. Gamba, "Road network extraction in VHR SAR images of urban and suburban areas by means of class-aided feature-level fusion," *IEEE Transactions on Geoscience and Remote Sensing*, vol. 48, no. 3, pp. 1294–1296, 2009.
- [7] V. Amberg, M. Coulon, P. Marthon, and M. Spigai, "Improvement of road extraction in high resolution SAR data by a context-based approach," in *Proceedings of the IEEE International Geoscience and Remote Sensing Symposium (IGARSS '05)*, pp. 490–493, Seoul, Korea, July 2005.
- [8] T. Kim, S. R. Park, M. G. Kim, S. Jeong, and K. O. Kim, "Tracking road centerlines from high resolution remote sensing images by least squares correlation matching," *Photogrammetric Engineering and Remote Sensing*, vol. 70, no. 12, pp. 1417–1422, 2004.
- [9] J. Zhou, W. F. Bischof, and T. Caelli, "Road tracking in aerial images based on human-computer interaction and Bayesian filtering," *ISPRS Journal of Photogrammetry and Remote Sensing*, vol. 61, no. 2, pp. 108–124, 2006.
- [10] X. Lin, Z. Liu, J. Zhang, and J. Shen, "Combining multiple algorithms for road network tracking from multiple source remotely sensed imagery: a practical system and performance evaluation," *Sensors*, vol. 9, no. 2, pp. 1237–1258, 2009.
- [11] J. Cheng, Y. Guan, X. Ku, and J. Sun, "Semi-automatic road centerline extraction in high-resolution SAR images based on circular template matching," in *Proceedings of the International Conference on Electric Information and Control Engineering (ICEICE '11)*, pp. 1688–1691, Wuhan, China, April 2011.
- [12] Y. Yang and C. Zhu, "Extracting road centerlines from high-resolution satellite images using active window line segment matching and improved SSDA," *International Journal of Remote Sensing*, vol. 31, no. 10, pp. 2457–2469, 2010.
- [13] X. G. Lin, J. X. Zhang, Z. J. Liu, J. Shen, and M. Y. Duan, "Semi-automatic extraction of road networks by least squares interlaced template matching in urban areas," *International Journal of Remote Sensing*, vol. 32, no. 17, pp. 4943–4959, 2011.
- [14] X. G. Lin, R. Zhang, and J. Shen, "A template-matching based approach for extraction of roads from very high resolution remotely sensed imagery," *International Journal of Image and Data Fusion*, vol. 3, no. 2, pp. 149–168, 2012.
- [15] A. K. Jain and A. Vailaya, "Image retrieval using color and shape," *Pattern Recognition*, vol. 29, no. 8, pp. 1233–1244, 1996.
- [16] N. Dalal and B. Triggs, "Histograms of oriented gradients for human detection," in *Proceedings of the IEEE Computer Society Conference on Computer Vision and Pattern Recognition (CVPR '05)*, pp. 886–893, San Diego, Calif, USA, June 2005.
- [17] C. Poullis and S. You, "Delineation and geometric modeling of road networks," *ISPRS Journal of Photogrammetry and Remote Sensing*, vol. 65, no. 2, pp. 165–181, 2010.
- [18] V. S. Frost, J. A. Stiles, K. S. Shanmugan, and J. C. Holtzman, "Model for radar images and its application to adaptive digital filtering of multiplicative noise," *IEEE Transactions on Pattern Analysis and Machine Intelligence*, vol. 4, no. 2, pp. 157–166, 1982.
- [19] J. S. Lee, "Simple speckle smoothing algorithm for synthetic aperture radar images," *IEEE Transactions on Systems, Man and Cybernetics*, vol. 13, no. 1, pp. 85–89, 1983.
- [20] P. Bolon, J. Chanussot, I. Issa, and P. Lambert, "Comparison of prefiltering operators for road network extraction in SAR images," in *Proceedings of the International Conference on Image Processing (ICIP '99)*, pp. 924–928, October 1999.
- [21] J. Canny, "Computational approach to edge detection," *IEEE Transactions on Pattern Analysis and Machine Intelligence*, vol. 8, no. 6, pp. 679–698, 1986.
- [22] M. Isard and A. Blake, "Condensation—conditional density propagation for visual tracking," *International Journal of Computer Vision*, vol. 29, no. 1, pp. 5–28, 1998.
- [23] Q. Deng, Y. Chen, and J. Yang, "Joint detection of roads in multifrequency SAR images based on a particle filter," *International Journal of Remote Sensing*, vol. 31, no. 4, pp. 1069–1077, 2010.
- [24] S. Movaghghi, A. Moghaddamjoo, and A. Tavakoli, "Road extraction from satellite images using particle filtering and extended Kalman filtering," *IEEE Transactions on Geoscience and Remote Sensing*, vol. 48, no. 7, pp. 2807–2817, 2010.